

May 2013

# Probing Bonding and Dynamics at Heterogeneous Adsorbate/Graphene Interfaces

Eric Charles Mattson

*University of Wisconsin-Milwaukee*

Follow this and additional works at: <https://dc.uwm.edu/etd>

 Part of the [Materials Science and Engineering Commons](#), [Physical Chemistry Commons](#), and the [Physics Commons](#)

---

## Recommended Citation

Mattson, Eric Charles, "Probing Bonding and Dynamics at Heterogeneous Adsorbate/Graphene Interfaces" (2013). *Theses and Dissertations*. 728.  
<https://dc.uwm.edu/etd/728>

This Dissertation is brought to you for free and open access by UWM Digital Commons. It has been accepted for inclusion in Theses and Dissertations by an authorized administrator of UWM Digital Commons. For more information, please contact [open-access@uwm.edu](mailto:open-access@uwm.edu).

PROBING BONDING AND DYNAMICS AT HETEROGENEOUS  
ADSORBATE/GRAPHENE INTERFACES

by

Eric Mattson

A Dissertation Submitted in  
Partial Fulfillment of the  
Requirements for the Degree of

Doctor of Philosophy  
in Physics

at

The University of Wisconsin-Milwaukee

May 2013

ABSTRACT  
PROBING BONDING AND DYNAMICS AT HETEROGENEOUS  
ADSORBATE/GRAPHENE INTERFACES

by

Eric Mattson

The University of Wisconsin-Milwaukee, 2013  
Under the Supervision of Professor Carol Hirschmugl

Graphene-based materials are becoming an astoundingly promising choice for many relevant technological and environmental applications. Deriving graphene from the reduction of graphene oxide (GO) is becoming a popular and inexpensive route toward the synthesis of these materials. While the desired product from GO reduction is pristine graphene, defects and residual oxygen functional groups inherited from the parent GO render reduced graphene oxide (RGO) distinct from graphene. In this work, the structure and bonding for GO and RGO is investigated to the end of a working understanding of the composition and properties of these materials. *In situ* selected area electron diffraction and *ex situ* IR microspectroscopy are used to study, respectively, thermal and chemical reduction of GO. The residual oxygen functional groups are found to be predominantly epoxide, C-O-C, bonded oxygen. The role of these oxygen functional groups and the collective RGO in gas sensing applications is investigated by performing *in situ* IR spectromicroscopy studies of molecular adsorption onto RGO. NO<sub>2</sub> and NH<sub>3</sub> are the target molecules of interest; NH<sub>3</sub> due to its widespread use in industry and NO<sub>2</sub> is a common byproducts in combustion reactions. Following adsorption of both molecules, numerous species are identified on the surface due to the heterogeneity of the substrate. Residual epoxide groups participate in reactions with the target molecules to

produce additional surface species that have varying impacts on the conductivity of the substrate.



*to my grandfather, who valued knowledge above all*

# TABLE OF CONTENTS

<b>1. Background and Introduction</b> .....	1
1.1 Organization of the Dissertation.....	1
1.2 Nanomaterials.....	1
1.2.1 Graphene .....	2
1.3 Motivation .....	5
1.3.1 Development of IR spectromicroscopy and deconvolution with synchrotron radiation .....	5
1.3.2 Probing the structure of reduced graphene oxide .....	6
1.3.3 NH <sub>3</sub> /RGO and NO <sub>2</sub> /RGO Interfaces.....	6
1.4 Solid State Gas Sensors.....	7
1.4.1 RGO Sensor Design.....	9
1.5 References .....	11
<b>2. Methods and Instrumentation Background</b> .....	15
2.1 Infrared Spectroscopy.....	15
2.1.1 IR studies of adsorption on solid surfaces.....	18
2.2 IR Spectromicroscopy.....	19
2.2.1 IRENI.....	21
2.2.2 Detectors.....	24
2.2.3 Measurement Geometries.....	25
2.2.4 <i>In Situ</i> Spectromicroscopy.....	27
2.3 Transmission Electron Microscopy.....	29
2.3.1 Optics in the TEM.....	30
2.3.2 Bright-Field TEM.....	32
2.3.3 Selected Area Diffraction.....	33
2.3.4 High-Resolution TEM.....	35
2.3.5 Energy Dispersive x-ray spectroscopy.....	35
2.3.6 <i>In situ</i> Microscopy and Diffraction.....	36
2.4 References.....	37
<b>3. Toward Optimal Spatial Resolution in IR Spectromicroscopy with Synchrotron Radiation</b> .....	39
3.1 Introduction.....	40
3.2 Spatial Resolution.....	40
3.3 Hyperspectral Deconvolution.....	46
3.4 Evaluation the Deconvolution Method .....	52
3.5 Effect of Numerical Aperture, Spatial Oversampling, and Deconvolution on spatial resolution in Widefield Infrared Spectromicroscopy.....	60
3.6 Conclusions.....	71
3.7 References .....	72
<b>4. Probing the Structure and Composition of Graphene Oxide and Reduced Graphene Oxide</b> .....	74

4.1 Introduction.....	75
4.2 Characterization of Graphene Oxide.....	77
4.2.1 Sample Preparation.....	77
4.2.2 Transmission Electron Microscopy.....	77
4.2.3 IR Microspectroscopy.....	79
4.3 Vacuum Thermal Reduction of Graphene Oxide: Possible Evidence for Graphene Monoxide.....	84
4.3.1 Methods.....	85
4.3.2 Results and Discussion .....	87
4.3.3 Role of Molybdenum .....	103
4.3.4 Conclusions and Future Directions.....	108
4.4 Chemically Reduced Graphene Oxide .....	111
4.4.1 Introduction to the Chemical Reduction Method.....	111
4.4.2 Sample Preparation .....	112
4.4.3 Results and Discussion .....	113
4.4.3.1 Selected Area Diffraction .....	113
4.4.3.2 Electrical Transport .....	113
4.4.3.2 IR Spectroscopy.....	115
4.4.3.4 Electronic Structure.....	117
4.4.4 Conclusions.....	124
4.5 Dimensionality Effect on the Optical Properties of RGO; SnO <sub>2</sub> /RGO Heterostructures .....	124
4.5.1 Introduction.....	124
4.5.2 Methods and Synthesis .....	125
4.5.3 Results and Discussion.....	125
4.6 References.....	129
<b>5. Exploring Adsorption and Reactivity of NH<sub>3</sub> on Reduced Graphene Oxide.....</b>	<b>134</b>
5.1 Introduction.....	135
5.2 Methods.....	136
5.3 Results.....	138
5.3.1 IR Spectra of Bare and Adsorbate-covered RGO.....	138
5.3.2 Adsorption at Different Sites in RGO, Modeling, and Band Assignments.....	143
5.3.2.1 Case A: NH <sub>3</sub> /Graphene.....	144
5.3.2.2 Case B: NH <sub>3</sub> /Epoxide Groups in RGO.....	150
5.3.2.3 Case C: NH <sub>3</sub> /Carbon Vacancy.....	153
5.3.2.4 Case D: Hydrogen Bonding With other Functional Groups.....	154
5.3.3 Bands in the Far IR Region .....	155
5.3.4 Adsorbate-Substrate Electronic Interactions.....	159
5.3.4.1 Löwdin Population Analysis.....	159
5.3.4.2 Unusual Strength and Shape of the NH Stretching Band.....	161
5.3.5 Spatially-dependent Adsorption Distribution.....	163
5.4 Conclusions.....	166
5.5 References.....	166

<b>6. Bonding and Interactions at the NO<sub>2</sub>/Reduced Graphene Oxide Interface.....</b>	<b>171</b>
6.1 Introduction.....	172
6.2 Experimental .....	173
6.3 Results and Discussion.....	175
6.3.1 IR Spectra of Bare and Adsorbate-covered RGO .....	175
6.3.2 Correlating IR Measurements with Theoretical Modeling.....	179
6.3.3 Change in the Broadband Absorption.....	191
6.4 Conclusions.....	193
6.5 References.....	194
<b>7. Concluding Remarks.....</b>	<b>198</b>
7.1 References.....	200

## LIST OF FIGURES

Figure 1.1 Crystal Structure of Graphite and Graphene.....	3
Figure 1.2 Dispersion of valence and conduction states in graphene.....	4
Figure 1.3 Schematic diagram and SEM image of an RGO-based sensor.....	10
Figure 1.4 Sensing response of RGO to NO <sub>2</sub> and NH <sub>3</sub> .....	11
Figure 2.1 Schematic representation of the Schwarzschild optical arrangement.....	21
Figure 2.2 IRENI Schematic.....	22
Figure 2.3 Schematic diagram of the NIT measurement geometry.....	26
Figure 2.4 Schematics of the grazing incidence experimental setup and objective.....	27
Figure 2.5 Diagrams of the flow cell and its components.....	29
Figure 2.6 Schematic of electron optical components in the TEM illumination.....	31
Figure 2.7 Ray diagrams showing imaging and diffraction modes.....	32
Figure 2.8 Single-tilt heating holder.....	37
Figure 3.1 Diffraction from a circular aperture.....	42
Figure 3.2 Measured PSFs from IRENI using 74× objective.....	45
Figure 3.3 Comparison of PSFs for 74× and 36× objectives.....	46
Figure 3.4 Optical Transfer Function and Hanning windows.....	51
Figure 3.5 Transmission Images from a high-resolution USAF target.....	53
Figure 3.6 Original and Deconvoluted hyperspectral data of polymer samples.....	56
Figure 3.7 Raw and Deconvoluted spectromicroscopy of a mouse retina.....	59
Figure 3.8 Predicted and experimental resolutions of 36× and 74× objectives.....	64
Figure 3.9 Raw and deconvoluted images of a breast cancer cell.....	66
Figure 3.10 Line profiles through chemical images in Fig. 3.9.....	68

Figure 4.1 SAD pattern of unreduced GO.....	79
Figure 4.2 Absorbance spectra of GO in NIT and GIR geometries.....	81
Figure 4.3 Representative structural models of oxygen groups in GO.....	83
Figure 4.4 Temperature evolution of GO SAD patterns.....	90
Figure 4.5 Higher order SAD patterns in GO and TRGO.....	92
Figure 4.6 NIT and GIR absorption spectra of GO compared to TRGO.....	94
Figure 4.7 Structure and IR activity of GMO.....	100
Figure 4.8 HRTEM image of a TRGO edge region.....	101
Figure 4.9 Electronic structure of GMO.....	102
Figure 4.10 SAD temperature evolution of a Mo/GO sample on a Ni TEM grid.....	105
Figure 4.11 Comparison of IR spectra of GO and Mo/GO.....	106
Figure 4.12 IR spectra of TRGO and GO prepared on Mo Grid.....	106
Figure 4.13 EDS spectra of a GO sample treated with Mo before and after annealing.....	108
Figure 4.14 SAD pattern of hydrazine RGO multilayer film.....	113
Figure 4.15 Transport properties of RGO FET devices.....	115
Figure 4.16 NIT absorption spectra of RGO.....	116
Figure 4.17 Square of RGO absorption spectrum to determine the optical gap.....	118
Figure 4.18 IR Spectra of two RGO samples with different C=O content.....	119
Figure 4.19 Atomic and electronic structures of epoxide-decorated graphene.....	121
Figure 4.20 DOS of the structures in Figure 4.19.....	122
Figure 4.21 Comparison of broadband IR absorption of RGO and SnO <sub>2</sub> /RGO.....	128
Figure 5.1 IR spectra of RGO and differential absorbance following exposure to NH <sub>3</sub> .....	140
Figure 5.2 Square of broadband RGO absorption to find linear intercept.....	141

Figure 5.3 Application of FSD to emphasize bands in Fig. 5.1C.....	142
Figure 5.4 Time-dependent NH <sub>3</sub> /RGO differential absorption spectra.....	143
Figure 5.5 Structural models of the NH <sub>3</sub> /RGO system.....	144
Figure 5.6 DOS of graphene and NH <sub>3</sub> /graphene.....	147
Figure 5.7 Structural model of NH <sub>3</sub> adsorption adjacent to an epoxide group.....	148
Figure 5.8 Time-dependent intensity of the N-H stretching feature.....	149
Figure 5.9 DOS of graphene with an epoxide group before and after adsorption of NH <sub>3</sub> in different configurations.....	152
Figure 5.10 Adsorbate-substrate charge transfer diagrams.....	160
Figure 5.11 IR Spectral imaging of the NH <sub>3</sub> /RGO system.....	165
Figure 6.1 NO <sub>2</sub> /RGO differential absorption spectra.....	177
Figure 6.2 Gaussian curve fits of experimental absorption spectra.....	178
Figure 6.3 Structural models of RGO and the NO <sub>2</sub> /RGO system.....	179
Figure 6.4 DOS of graphene and NO <sub>2</sub> /graphene.....	181
Figure 6.5 DOS of graphene, graphene w/ one epoxide, and NO <sub>3</sub> /graphene.....	184
Figure 6.6 NO <sub>2</sub> /RGO differential absorption spectra from two different experiments.....	190
Figure 6.7 Subtraction of the two spectra in Fig. 6.6.....	191

## LIST OF TABLES

Table 3.1	Changes in Amide and Biomarker distribution following deconvolution.....	69
Table 4.1	Interplanar spacings of GO and TRGO measured from SAD.....	93
Table 4.2	Lattice spacings of graphene, GO, and the quasi-hexagonal GMO model.....	96
Table 5.1	Summary and assignment of NH <sub>3</sub> /RGO absorption bands.....	158
Table 6.1	Summary and assignment of NO <sub>2</sub> /RGO absorption bands.....	180



## Chapter 1: Background and Introduction

### 1.1 Organization of the Dissertation

The organization of the dissertation is as follows: Chapter 1 introduces the motivation of the dissertation and background information on the materials under consideration. Chapter 2 discusses the experimental techniques and details of the measurements used in the work. Chapter 3 discusses the development of synchrotron IR spectromicroscopy, characterizing the relationships between microscope optics, spatial resolution and deconvolution. Chapter 4 gives a characterization of the structure and properties of reduced graphene oxide prepared by vacuum thermal reduction on Molybdenum supports and by chemical reduction. Chapters 5 and 6 explore the adsorption of  $\text{NH}_3$  and  $\text{NO}_2$ , respectively, on chemically reduced graphene oxide (RGO).

### 1.2 Nanomaterials

The field of nanotechnology focuses on materials in which dimensionality (D) is limited to the nanoscale in one or more directions. In recent years, this field has been growing continuously on both fundamental and applied fronts. Examples of nanomaterials can include surfaces/films/single atomic layers (2D), nanowires and nanotubes (1D) and quantum dots or nanocrystals (0D). Nanostructuring of materials by tailoring atomic-scale structure and composition often leads to new and interesting properties that are often not observed in their bulk counterparts, opening entirely new disciplines of science. Their properties can be engineered to serve a desirable purpose through processes such as chemical modification, doping and

heterostructuring. This versatility has made nanotechnology a frontrunner in solving a variety of technological problems ranging from energy to medicine.

A key attribute of nanostructured materials is their extremely high surface-to-volume ratio; this property enables a number of attractive properties such as enhanced reactivity and ability to functionalize, grow on, or heterostructure with other materials. The work of this dissertation focuses on understanding the structure and bonding of various types of nanomaterials, their interfaces with atomic or molecular adsorbates and the effects that the different components of the interface have on one another.

### 1.2.1 Graphene

Graphene is a single atomic layer of graphite. Graphite is the most common allotrope of carbon, consisting layers of carbon atoms in a hexagonal honeycomb lattice stacked in a Bernal or AB stacking order. The crystal structure of graphite is shown in Fig. 1.1A. Graphene can be thought of as removing one of the layers in Fig. 1.1A. Each graphene layer has the atomic structure shown in Fig. 1.1B; the lattice constant of graphene is  $2.46 \text{ \AA}$  and the C-C bond length is  $1.42 \text{ \AA}$ . Although the concept of graphene has been used for many years, it was not until 2004 that a single graphene layer was successfully isolated [1]. This experimental breakthrough and the following characterization of the physical properties of graphene has led to an explosion of the field of carbon-based materials science, with tens of thousands of papers published in the field since 2004 and the award of the Nobel Prize in physics in 2010. Graphene has since intrigued materials scientists from both fundamental science and applied perspective. The appeal of graphene as a material for so many potential applications is driven from its many unique and exciting properties. The first and most obvious property is its high surface-to-volume ratio,

which is a defining characteristic of all nanomaterials. Since graphene is a single atomic layer, every atom in the crystal is present on the surface, leading to the highest possible surface-to-volume ratio. Second, graphene is remarkably strong, with the C-C bonds being the strongest of

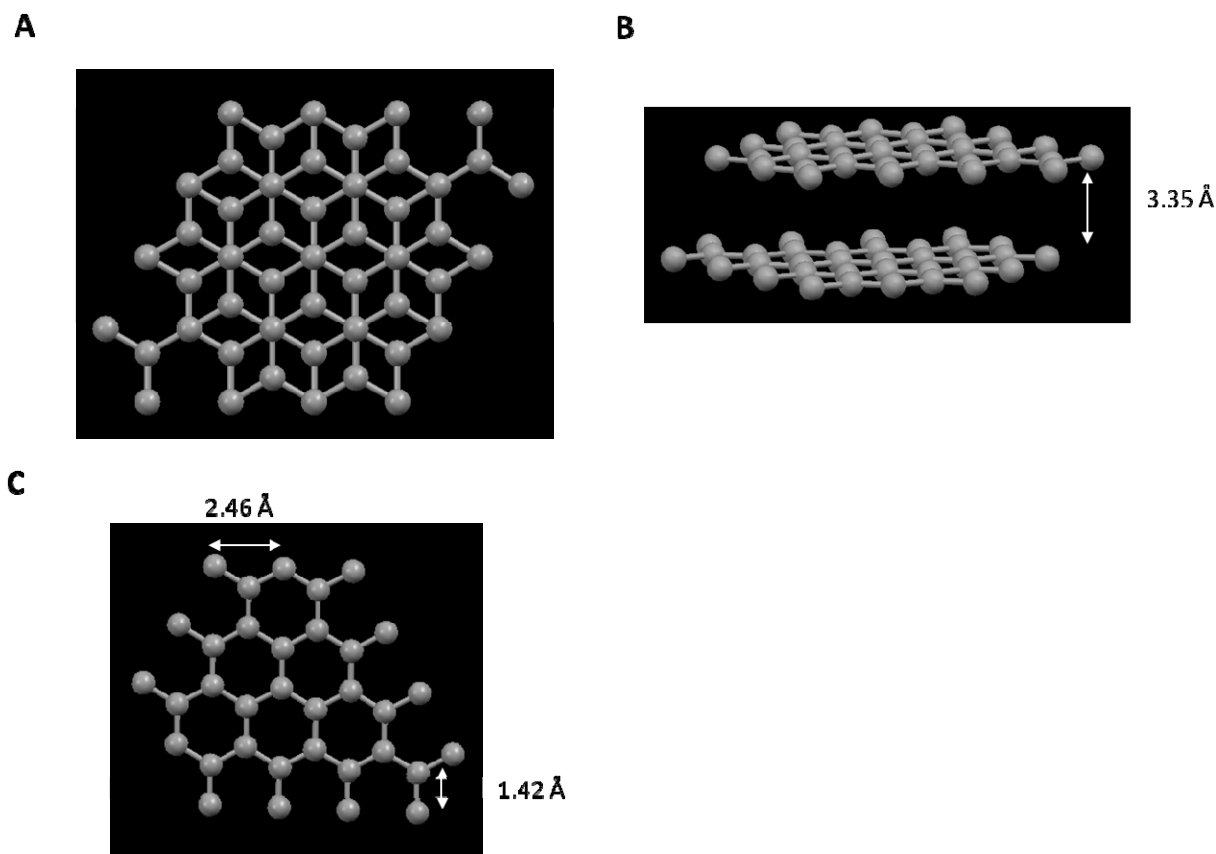


**Fig. 1.1:** Crystal structure of graphite seen from c-axis (A) and perspective (B) views. The crystal structure of a single graphite layer (graphene) is shown in (C). A graphite crystal is composed by stacking the individual hexagonal layers in an AB sequence with an interlayer spacing of  $3.35 \text{ \AA}$ .

any known material. The most sought after properties of graphene, however, are derived from its electronic structure. A schematic diagram of the band dispersion of a single graphene layer is shown in Fig. 1.2. The defining characteristic of graphene's electronic properties is the linear dispersion of the valence and conduction bands, which meet to form cones whose tips touch one

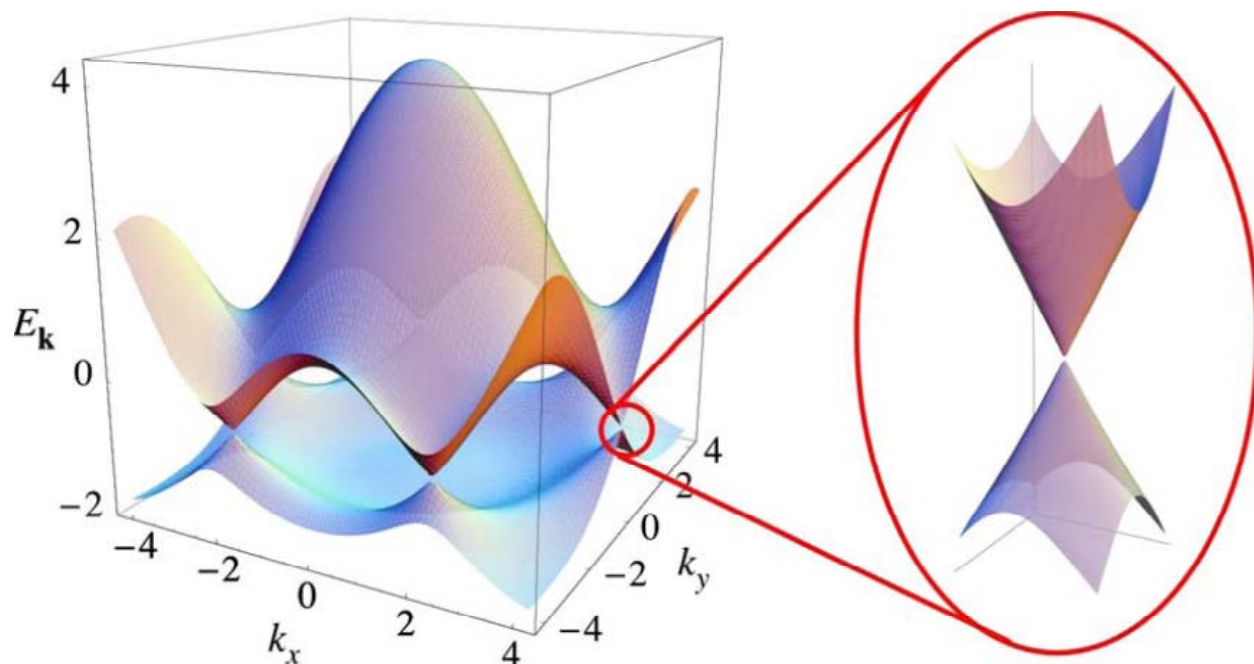


**Fig. 1.2:** Schematic diagram of the dispersion of the valence and conduction states in graphene. From [2].

another at the K-point of the Brillouin zone [2, 3]. The fact that the electronic states near the Fermi energy have a linear dispersion implies that the effective mass of the charge carriers is zero, leading to extremely high carrier mobility [1]. In intrinsic, free-standing graphene, the Fermi energy is located exactly at the point at which the valence and conduction bands touch one another, rendering graphene a zero-gap semiconductor or semimetal. The absence of a finite band gap makes it very easy to manipulate the population of the bands using electric fields, leading to ambipolar transport [1]. In addition, since every atom is in fact a surface atom, graphene lends itself superbly to chemical doping, and adsorption of atoms and molecules on its surface leads to a substantial modulation of the electronic properties. These characteristics make graphene an ideal component for solid-state sensing [4], in addition to numerous other applications. In addition, the structure and strength of graphene make it ideal as a support for

heterostructured materials that can combine the appealing properties of graphene with those of other materials.

### **1.3 Motivation**

Beyond the general motivation of "general scientific interest," there are aspects of the work that are technologically relevant in a number of fields. A few such applications are discussed.

#### **1.3.1 Development of IR Spectromicroscopy and Deconvolution with Synchrotron Radiation (Chapter 3)**

Infrared (IR) spectromicroscopy experiments at the recently developed IRENI beamline [5] are a central component to the work in this dissertation. The characterization of the beamline and instrumental performance are thus of central importance to the results presented here, as it was used for the largest body of work in this dissertation. The work in Chapter 3 evaluates the imaging characteristics of the beamline, and uses the determination of the point spread function (PSF) to develop deconvolution algorithms. In addition, the assessment of the instrument's imaging performance and development of deconvolution have motivation beyond the study of graphene-based systems. IR chemical imaging or spectromicroscopy is growing as a tool for many disciplines, particularly for studying biological systems.[6-8] Thus, the evaluation of the imaging characteristics of the instrument and the application of deconvolution is of relevance and is of general interest to the IR imaging community. In addition to the materials science applications presented here, the work in Chapter 3 has also been applied toward understanding Malaria infection in blood cells, the structure of spider silk, and the composition of dorsal root ganglion (DRG) neurons responsible for chronic pain.

### 1.3.2 Probing the Structure of Reduced Graphene Oxide (Chapter 4)

The largest component of this work focuses on the characterization of the properties of chemically modified graphene. Studying the properties of graphene oxide (GO) and different types of reduced graphene oxide (RGO) as in Chapter 3 is important for the development of these materials in electronic applications. The most imminent application in which this work is directly relevant is toward solid state gas sensors, discussed in detail below. Understanding the structure and bonding configuration of the RGO substrates is a critical first step toward an actual understanding of the adsorbate-substrate interactions and the mechanism of operation of sensors. In addition, RGO is being used increasingly as an electronic material and a catalyst support [9-17]. For these applications, it is critical to have a working knowledge of the composition and electronic structure of the materials in question, as these properties directly impact device performance. The correlation of bonding and concentration of oxygen functional groups to material properties goes directly to the use of the materials in technological applications. Particularly for the case of RGO, there have been many conflicting reports of the structure and composition of the reduced material following thermal and chemical treatments, reviewed in Chapter 4. The work presented here contributes to the gap in the knowledge on this subject through a combination of *in situ* electron diffraction studies and *ex situ* IR spectromicroscopy studies of RGO produced through different treatments.

### 1.3.3 NH<sub>3</sub>/RGO and NO<sub>2</sub>/RGO Interfaces (Chapters 5-6)

The interaction between the substrate and the adsorbate define the characteristics of a gas sensor or catalyst material. Although the interactions between graphene and GO substrates with relevant gas molecules have been considered to some extent theoretically [18-20], relatively little

experimental characterization of the gas-surface interactions has been reported. Bermudez and Robinson [21] used internal reflection IR spectroscopy under ambient atmospheric conditions to probe small molecules, including ammonia, on graphene; however, their sensitivity was not sufficient to observe the internal molecular vibrational modes and no conclusions regarding the bonding configuration of  $\text{NH}_3$  were drawn. Zhou et. al. [22] studied the adsorption of  $\text{NO}_2$  on epitaxial graphene using angle resolved photoemission measurements, but no connection to bonding or the interaction with defects was considered. The adsorption of  $\text{NO}_2$  and  $\text{NH}_3$  onto carbon nanotube (CNT) films was investigated using IR spectroscopy by Ellison et. al., [23] but the substrates in that case were structurally and chemically distinct from the materials under consideration here. This has been the driving motivation behind the *in situ* IR measurements of the gas-surface interfaces of sensor materials. The goal of these experiments has been to identify which molecular fragments are present on the substrates and their bonding configuration during realistic sensing conditions for  $\text{NH}_3$  and  $\text{NO}_2$  detection. In addition, broadband IR absorption measurements provide additional insight into the mechanism behind the conductivity changes and changes to the electronic states of graphene-based sensors during operation. In addition, the work impacts RGO as an electronic material; just as the current silicon based electronics industry relies heavily on the properties of doped silicon, the effects of chemical doping and adsorption onto graphene and RGO sheets are one means of realizing the electrical properties desired for a particular application.

#### 1.4 Solid State Gas Sensors

Gas sensors that are tuned to selectively detect a certain type of molecule with high sensitivity have a remarkably wide range of application including environmental monitoring,

medical diagnosis and security. While certain aspects of the actual operation/environmental interaction of different sensor materials remain controversial, driving the motivation of this work, the general mechanism of operation is well accepted. Solid state sensors consist of a semiconducting material that completes an electronic circuit. In the absence of any adsorbates, the semiconducting gate will have a certain free carrier density that determines the resistance of the circuit. For oxide semiconductors such as  $\text{SnO}_2$ ,  $\text{TiO}_2$  and  $\text{ZnO}$ , materials that are currently used in solid state sensors, the density of carriers available for conduction depends on the doping, impurities on the surface, surface stoichiometry and temperature. When a molecule approaches the surface of the semiconducting sensor component, adsorption can take place via one of several channels including 1) direct adsorption, 2) reaction with adsorbed species native on the surface, or 3) reaction with a surface oxygen vacancy. Depending on the oxidizing/reducing characteristics of the target molecules, the potential adsorption processes can either increase or decrease the number of free charge carriers.

Most existing gas sensors employ metal oxides such as  $\text{SnO}_2$  for the sensing material. The problem with this approach is that oxides typically have a fairly wide band gap, and elevated temperature is needed to create the number of free charge carriers required to achieve the signal-to-noise ratio (SNR) needed for high sensitivity. Under many circumstances, this is either impractical or dangerous. Materials scientists have employed many techniques to lower the operation temperature of solid state sensors while still maintaining the desired properties for sensing. One route that was explored involved the syndissertation of materials containing metal oxide nanocrystals that decorate a conducting carbon channel. For example, sensors based on  $\text{SnO}_2$ -decorated multi-walled carbon nanotubes (MWCNTs) have been shown [24] to produce



room temperature sensitivity to  $\text{NO}_2$  and  $\text{NH}_3$ . Silver nanocrystals added to the above materials were also shown to enhance the sensitivity toward  $\text{NO}_2$  and  $\text{NH}_3$  [25, 26].

More recently, it was demonstrated that reduced graphene oxide (RGO) without any metal or metal oxide component was also sensitive to  $\text{NO}_2$  and  $\text{NH}_3$  [27-30], and that sensitivity and selectivity toward a particular molecule could be tuned by applying a gate voltage or decorating with metal or metal oxide nanocrystals [29, 31-34]. Based on these recent breakthroughs, it is of paramount importance to identify the gas-surface interactions between target molecules and RGO for optimization and commissioning of actual devices. To this end, RGO and its interactions with gaseous environments is investigated in this work. While often RGO is combined with oxide nanocrystals for even further enhanced sensitivity, this work will only address molecular adsorption onto RGO, and not onto nanocrystal-decorated RGO.

#### 1.4.1 RGO Sensor Design

In this work, RGO and its interaction with the gases  $\text{NO}_2$  and  $\text{NH}_3$  are studied as a first step toward understanding the operation of RGO-based devices. The work is performed in collaboration with Prof. Junhong Chen, UW-Milwaukee Mechanical Engineering Dept. A schematic diagram of an RGO-based sensor is shown in Fig. 1.3A. The substrate consists of a Si wafer coated with a 200 nm layer of  $\text{SiO}_2$ . On top of the  $\text{SiO}_2$  layer, a set of interdigitated gold electrodes are deposited (Fig. 1.3B), which act as the source and the drain. Then, the RGO is deposited onto the electrodes to complete the circuit. The device offers the possibility also to gate the RGO using the Si wafer as the gate electrode. When a gas molecule adsorbs to the surface via one of the 3 channels discussed above, the carrier density in the RGO is modified and

a change in the resistance is measured. The sensing response is often given as the ratio of the resistance of the adsorbate covered sensor to that of the clean sensor,  $R_a/R_g$ .

RGO is considered to be a p-type semiconductor, meaning that the dominant charge carriers are holes. In the simplest picture, residual oxygen functional groups act as electron acceptor to leave free holes available for conduction. Therefore, adsorption of a reducing gas such as  $\text{NH}_3$  is expected to increase the resistance, and adsorption of oxidizing gases such as  $\text{NO}_2$  are expected to decrease the

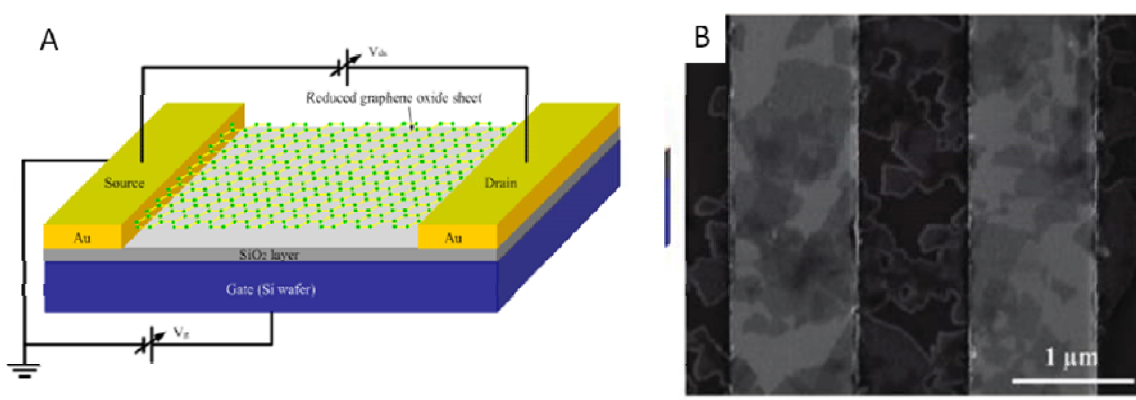


**Fig. 1.3:** A) Schematic diagram of an RGO-based gas sensor. From ref [27] B) Scanning electron microscopy (SEM) image of RGO deposited on Au electrodes. From ref [29].

resistance. This is indeed the response that is observed in actual sensors; Fig. 1.5 shows the response of an RGO gas sensor to 100 ppm  $\text{NO}_2$  and 1%  $\text{NH}_3$  diluted in air. It can be seen that the resistance  $R_g/R_a$  decreases when the sample is exposed to  $\text{NO}_2$ , and increases when the sensor is exposed to  $\text{NH}_3$  (note that the y-axis scales are opposite for the two cases).

Reported studies [28-30] have demonstrated that RGO can produce impressive results for sensing of small quantities of gases; however, an in-depth understanding of the actual interaction

between the adsorbate and the surface is needed in order to fully exploit RGO for technological purposes. Such an account of the gas-surface interactions could also shed light on the use of RGO for other applications.

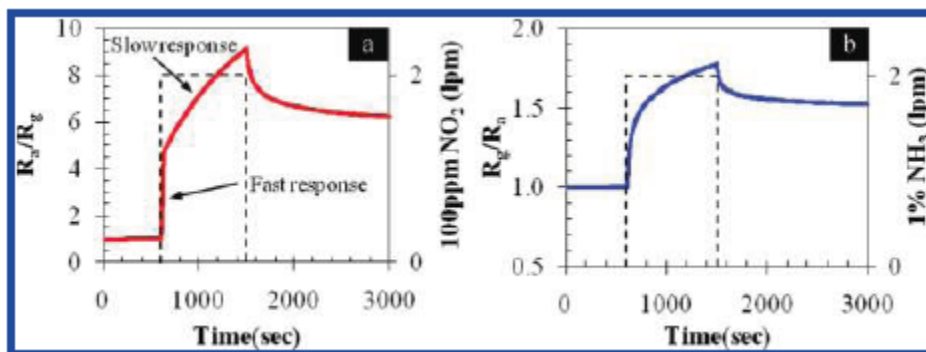


**Fig. 1.4:** Sensing response of RGO to NO<sub>2</sub> (A) and NH<sub>3</sub> (B). From ref [29].

## 1.5 References

1. Novoselov, K.S., et al., *Electric field effect in atomically thin carbon films*. Science, 2004. **306**(5696): p. 666-669.
2. Castro Neto, A.H., et al., *The electronic properties of graphene*. Reviews of Modern Physics, 2009. **81**(1): p. 109-162.
3. Geim, A.K. and K.S. Novoselov, *The rise of graphene*. Nature Materials, 2007. **6**(3): p. 183-191.
4. Schedin, F., et al., *Detection of individual gas molecules adsorbed on graphene*. Nature Materials, 2007. **6**(9): p. 652-655.
5. Nasse, M.J., et al., *High-resolution Fourier-transform infrared chemical imaging with multiple synchrotron beams*. Nature Methods, 2011. **8**(5): p. 413-U58.

6. Dumas, P., et al., *Imaging capabilities of synchrotron infrared microspectroscopy*. Faraday Discussions, 2004. **126**: p. 289-302.
7. German, M.J., et al., *Infrared spectroscopy with multivariate analysis potentially facilitates the segregation of different types of prostate cell*. Biophysical Journal, 2006. **90**(10): p. 3783-3795.
8. McNaughton, D. and B.R. Wood, *Synchrotron Infrared Spectroscopy of Cells and Tissue*. Australian Journal of Chemistry, 2012. **65**(3): p. 218-228.
9. Stankovich, S., et al., *Graphene-based composite materials*. Nature, 2006. **442**(7100): p. 282-286.
10. Eda, G., G. Fanchini, and M. Chhowalla, *Large-area ultrathin films of reduced graphene oxide as a transparent and flexible electronic material*. Nature Nanotechnology, 2008. **3**(5): p. 270-274.
11. Lightcap, I.V., T.H. Kosel, and P.V. Kamat, *Anchoring Semiconductor and Metal Nanoparticles on a Two-Dimensional Catalyst Mat. Storing and Shuttling Electrons with Reduced Graphene Oxide*. Nano Letters, 2010. **10**(2): p. 577-583.
12. Williams, G., B. Seger, and P.V. Kamat, *TiO<sub>2</sub>-graphene nanocomposites. UV-assisted photocatalytic reduction of graphene oxide*. ACS Nano, 2008. **2**(7): p. 1487-1491.
13. He, Q.Y., et al., *Centimeter-Long and Large-Scale Micropatterns of Reduced Graphene Oxide Films: Fabrication and Sensing Applications*. ACS Nano, 2010. **4**(6): p. 3201-3208.
14. Sudibya, H.G., et al., *Electrical Detection of Metal Ions Using Field-Effect Transistors Based on Micropatterned Reduced Graphene Oxide Films*. ACS Nano, 2011. **5**(3): p. 1990-1994.
15. Yang, M., et al., *Graphene Oxide: An Ideal Support for Gold Nanocatalysts*. Journal of Physical Chemistry C, 2012. **116**(42): p. 22336-22340.
16. Hernandez, R., et al., *Reduced Graphene Oxide Films as Solid Transducers in Potentiometric All-Solid-State Ion-Selective Electrodes*. Journal of Physical Chemistry C, 2012. **116**(42): p. 22570-22578.
17. He, Q.Y., et al., *Transparent, Flexible, All-Reduced Graphene Oxide Thin Film Transistors*. ACS Nano, 2011. **5**(6): p. 5038-5044.

18. Tang, S.B. and Z.X. Cao, *Adsorption and Dissociation of Ammonia on Graphene Oxides: A First-Principles Study*. Journal of Physical Chemistry C, 2012. **116**(15): p. 8778-8791.
19. Tang, S. and Z. Cao, *Adsorption of nitrogen oxides on graphene and graphene oxides: insights from density functional calculations*. J Chem Phys, 2011. **134**(4): p. 044710.
20. Leenaerts, O., B. Partoens, and F.M. Peeters, *Adsorption of H(2)O, NH(3), CO, NO(2), and NO on graphene: A first-principles study*. Physical Review B, 2008. **77**(12).
21. Bermudez, V.M. and J.T. Robinson, *Effects of Molecular Adsorption on the Electronic Structure of Single-Layer Graphene*. Langmuir, 2011. **27**(17): p. 11026-11036.
22. Zhou, S.Y., et al., *Metal to insulator transition in epitaxial graphene induced by molecular doping*. Physical Review Letters, 2008. **101**(8).
23. Ellison, M.D., et al., *Adsorption of NH3 and NO2 on single-walled carbon nanotubes*. Journal of Physical Chemistry B, 2004. **108**(23): p. 7938-7943.
24. Lu, G.H., L.E. Ocola, and J.H. Chen, *Room-Temperature Gas Sensing Based on Electron Transfer between Discrete Tin Oxide Nanocrystals and Multiwalled Carbon Nanotubes*. Advanced Materials, 2009. **21**(24): p. 2487-+.
25. Cui, S.M., et al., *Ag nanocrystal as a promoter for carbon nanotube-based room-temperature gas sensors*. Nanoscale, 2012. **4**(19): p. 5887-5894.
26. Cui, S.M., et al., *Fast and Selective Room-Temperature Ammonia Sensors Using Silver Nanocrystal-Functionalized Carbon Nanotubes*. ACS Applied Materials & Interfaces, 2012. **4**(9): p. 4898-4904.
27. Lu, G.H., L.E. Ocola, and J.H. Chen, *Gas detection using low-temperature reduced graphene oxide sheets*. Applied Physics Letters, 2009. **94**(8).
28. Lu, G.H., L.E. Ocola, and J.H. Chen, *Reduced graphene oxide for room-temperature gas sensors*. Nanotechnology, 2009. **20**(44).

29. Lu, G.H., et al., *Toward Practical Gas Sensing with Highly Reduced Graphene Oxide: A New Signal Processing Method To Circumvent Run-to-Run and Device-to-Device Variations*. *ACS Nano*, 2011. **5**(2): p. 1154-1164.
30. Robinson, J.T., et al., *Reduced Graphene Oxide Molecular Sensors*. *Nano Letters*, 2008. **8**(10): p. 3137-3140.
31. Lu, G.H., et al., *Facile, Noncovalent Decoration of Graphene Oxide Sheets with Nanocrystals*. *Nano Research*, 2009. **2**(3): p. 192-200.
32. Mao, S., et al., *Specific Protein Detection Using Thermally Reduced Graphene Oxide Sheet Decorated with Gold Nanoparticle-Antibody Conjugates*. *Advanced Materials*, 2010. **22**(32): p. 3521-+.
33. Mao, S., et al., *Tuning gas-sensing properties of reduced graphene oxide using tin oxide nanocrystals*. *Journal of Materials Chemistry*, 2012. **22**(22): p. 11009-11013.
34. Cui, S., et al., *Indium-doped SnO<sub>2</sub> nanoparticle-graphene nanohybrids: simple one-pot syndissertation and their selective detection of NO<sub>2</sub>*. *Journal of Materials Chemistry A*, 2013. **1**(14): p. 4462-4467.

## Chapter 2: Methods and Instrumentation Background

### 2.1 Infrared Spectroscopy

Infrared radiation consists of the portion of the electromagnetic spectrum spanning the broadband wavelength region from approximately 1-1000 micrometers, or 1.24 meV to 1.24 eV . Many fundamental excitations in condensed matter can occur within this wavelength region; in this work the transitions of interest consist of optical phonon modes, molecular vibrations of adsorbed species, and interband electronic excitations. For vibrational excitations, there exists a general selection rule for infrared/optical activity of any given mode: the transition must induce a so-called dynamical dipole moment, which is equivalent to requiring that the vibrational excited state must have the same symmetry as a component of the translation operator [1]. This selection rule follows directly from the evaluation of the matrix element in Fermi's Golden Rule for the transition rate [2]:

$$R_{i \rightarrow f} = \frac{2\pi}{\hbar} |\langle f^0 | H' | i^0 \rangle|^2 \delta(E_f^0 - E_i^0 - \hbar\omega) \quad (2.1)$$

Where  $f^0$  and  $i^0$  are the unperturbed initial and final states,  $H^1$  is the interaction Hamiltonian,  $E_f^0$  and  $E_i^0$  are the unperturbed energies of the states  $f^0$  and  $i^0$ , and  $\hbar$  is Planck's constant.

Evaluation of the matrix element in 1.1 for an electromagnetic perturbation leads to integrals of the form [1],

$$\int_{-\infty}^{\infty} \psi_f^* \mathbf{x} \psi_i d\tau \quad (2.2)$$

which is define the transition dipole moment of the excitation. Thus, the IR selection rule can be used as an intuitive guide for the interpretation of IR spectra: only vibrational excitations that produced a dynamical dipole moment are optically active.

In addition to vibrations of the atoms in a solid or a molecule, IR spectroscopy can also be used as a probe of the low-energy electronic structure of a solid. Two types of excitations are possible for a conducting solid; in the intraband transition process, free carriers are excited to a higher energy state within the same band, leading to a so-called Drude peak at zero frequency. For the case of a narrow-gap semiconductor or semimetal, absorption of an IR photon can also excite an electron from the valence band to the conduction band; *i.e.*, an interband transition. Interband transitions are of particular interest for the work presented here; in the case of graphene and graphite, the Drude peak is located in the far IR region, below the detectable range of the experimental setup discussed below. On the other hand, the interband transitions in graphene-based materials span the entire IR frequency region and extend into the visible region of the spectrum. The relationships between optically active electronic transitions, optical transmission and reflection were discussed by Dressel and Grüner [3]. Optically active electronic transitions can be directly correlated to measurements of IR reflectivity or transmission; in the thin film limit, the optical transmission is defined in terms of the real and imaginary parts of the refractive index, [3]

$$T \approx \left[ 1 - \frac{(1-n)^2 + k^2}{(1+n)^2 + k^2} \right]^2 \exp\{-\alpha d\} \quad (2.3)$$

where  $n$  and  $k$  are, respectively, the real and imaginary parts of the refractive index,  $d$  is the thickness of the film, and  $\alpha$  is the absorptivity defined by



$$\alpha = \frac{2k\omega}{c} \quad (2.4)$$

The complex refractive index, dielectric function, and optical conductivity are related quantities that describe the response of a material to an electromagnetic perturbation. The theory of excitations in a material is most commonly formulated in terms of the complex dielectric function  $\hat{\epsilon} = \epsilon_1 + i\epsilon_2$ , where the real component of the dielectric function describes dispersion and the imaginary part absorption. In a crystalline solid, the excitations of electrons between different bands is subject to a selection rule just as for the case of vibrational excitations. In this case, application of the Golden Rule leads to a similar selection rule where the absorption of radiation is proportional to the "dipole matrix element",

$$\mathbf{p}_{l'l} = \langle \mathbf{k}l' | \mathbf{p} | \mathbf{k}l \rangle = -\frac{i\hbar}{\Delta} \int_{\Delta} u_{l'}^* \nabla u_l d\mathbf{r} \quad (2.5)$$

for a transition between bands indexed  $l$  and  $l'$  at momentum  $\mathbf{k}$ . Here the  $\Delta$  is the area of the Brillouin zone and  $u_l$  are the coefficients of the Bloch wavefunctions for the states  $l$  and  $l'$ . The absorption coefficient is then given by

$$\alpha_{l'l}(\omega) = \frac{e^2}{\pi n c \omega m^2} \int_{BZ} |\mathbf{p}_{l'l}|^2 \delta\{\hbar\omega - \hbar\omega_{l'l}\} d\mathbf{k} \quad (2.6)$$

where  $e$  and  $m$  are the electron charge and mass, respectively, and the integral is taken over the Brillouin zone. The integral over the Brillouin zone appearing in the absorption coefficient can be recast into a different form known as the joint density of states (JDOS)[3]:

$$\int_{BZ} |\mathbf{p}_{l'l}|^2 \delta\{\hbar\omega - \hbar\omega_{l'l}\} d\mathbf{k} = \int_{\hbar\omega = \epsilon_{l'l}} \frac{dS_{\epsilon}}{|\nabla_{\mathbf{k}}[\epsilon_{l'}(\mathbf{k}) - \epsilon_l(\mathbf{k})]|^2} |\mathbf{p}_{l'l}|^2 \quad (2.7)$$

In this case, the integration is carried over a surface of constant energy in momentum space. Eq.

2.1.7 is particularly useful for understanding absorption lineshapes due to electronic interband

transitions. For example, a direct transition between parabolic valence and conduction bands with a band gap  $E_g$  yields a singularity in the JDOS, and evaluation of 2.1.7 gives for a three-dimensional solid,

$$D_{cv}(\hbar\omega) = \frac{1}{(2\pi)^2} \left(\frac{2\mu}{\hbar^2}\right)^{3/2} (\hbar\omega - E_g)^{1/2} \quad (2.8)$$

indicating a square-root dependence of the JDOS on the photon frequency for transitions near the band edge. Importantly, (2.8) was derived for a three-dimensional crystal, requiring that the integral over the Brillouin zone is a volume integral. In the case where the electronic states depend on only two components of the wavevector, for the same type singularity in the JDOS, the integral in (2.7) is carried out over the area of the Brillouin zone and reduces to a constant value that is independent of wavelength.

### 2.1.1 IR Studies of Adsorption on Solid Surfaces

IR studies of adsorption of atoms and molecules on solid surfaces can provide invaluable information on the adsorbate bonding configuration because the measured vibrational frequencies are directly correlated to the strength of a particular bond. In addition, the overall number of observed frequencies can be directly linked to the symmetry of the adsorbate/substrate system. A given adsorbate in the gas phase has  $3N$  degrees of freedom; following adsorption onto a surface, the degrees of freedom associated with translation and rotation in the gas phase become vibrations in the adsorbed state. For the case of molecular adsorbates, the vibrational spectrum will be composed of intermolecular vibrational modes as well as the frustrated translations and rotations of the entire molecule. The symmetry of the adsorption site and of the adsorbate will ultimately determine how many nondegenerate modes will be present, and the

rules of group theory can be applied to identify the number of IR active modes expected for a given system.

In a conventional surface-science experiment, [4, 5] the spectra from the gas-solid interface are sampled by an IR beam incident on the sample from a grazing angle. In a conducting sample, free carriers in the solid reflect the beam from the surface to amplify the electric field components perpendicular to the surface and eliminate the field components parallel to the surface in the region immediately neighboring the surface. The grazing incidence geometry is chosen [5, 6] to optimize the field components normal to the surface and hence optimize the sensitivity of the experiment. On a metal surface, image charges have the effect of cancelling dynamical dipole moments parallel to the surface, and consequently only vibrations that have a dipole component normal to the surface are allowed. In contrast, transparent samples lend themselves more so to transmission. In particular, thin films such as few layers of graphene allow an IR beam to be transmitted from arbitrary incidence and allow for the detection of all fundamentally active modes both parallel and perpendicular to the surface. Simultaneously, the change in transmittance due to contributions from the electronic absorption is recorded over a broadband frequency region. Thus in an IR transmission experiment sampling adsorption of molecules on graphene, both the adsorbate vibrational modes and the substrate interband transitions are sampled simultaneously.

## **2.2 Infrared Spectromicroscopy**

For studying samples which are microscopic in one or more dimensions or inhomogeneous at micrometer length-scales, it becomes necessary to perform IR Spectromicroscopy. While the emphasis in this work is on materials science of carbon-based

materials, IR Spectromicroscopy is also an unique tool for studying the chemistry of biological materials. This has been one of the driving factors in the development and characterization of IRENI and the construction and implementation of deconvolution algorithms, discussed in chapter 3. Conventional IR spectromicroscopy is performed by focusing an IR beam down to a micrometer-scale spot using a Cassegrain or Schwarzschild optical arrangement [7, 8] (Fig. 2.1) and performing measurements in a dual-aperture confocal geometry. Schwarzschild optics consist of two parabolic mirrors of different diameters, offset from one another. The primary concave mirror (larger, with hole in the center) collects the focused beam originating at the sample plane. The smaller, secondary convex mirror is positioned close to the focus of the concave mirror. Thus, the smaller mirror collects the radiation and focuses the beam so that it exits through the hole in the primary concave mirror. The use of apertures allows for the specific illumination of a particular region of the sample, which is then raster-scanned through the beam path to form a pixelated data set, consisting of an entire IR spectrum at each pixel. The data collected in this fashion are three dimensional "hyperspectral cubes" or maps of the absorbance as a function of position. Two dimensions of the cube represent position on the sample and the third dimension represents the spectral domain and consists of an absorption or transmission spectrum. IR or chemical images are then generated by considering the absorption at a particular wavelength/frequency for each pixel in the dataset. This allows for spatially resolved visualization of IR absorption over the region being imaged. The data presented as absorption as a function of position can be considered as projected images of the IR absorption of the sample and are referred to as chemical images since they provide a visualization of the chemistry of the sample. The challenge of this approach is to focus enough light through the aperture and onto the sample to achieve sufficient signal-to-noise ratio (SNR). Conventional

thermal sources have the undesirable qualities of large emittance (area-angle product) and low brightness, which corresponds to a low photon flux per solid angle. Synchrotron/storage ring sources, on the other hand, have a very low emittance and high brightness, which allows a much greater photon flux to be focused onto a small region of the sample [9]. Using this approach, illumination of sample areas down to  $3 \times 3 \mu\text{m}^2$  has been achieved using synchrotron sources [10]. Still, this approach remains prohibitive for high resolution imaging in reasonable acquisition times.

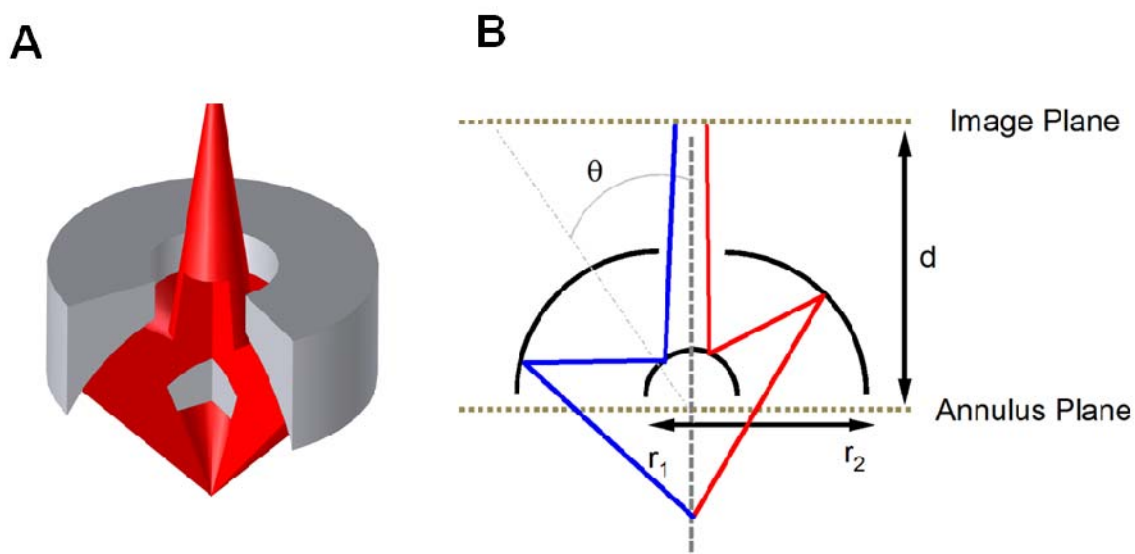


**Figure 2.1:** Schematic representation of the Schwarzschild optical arrangement. The optics consist of two parabolic mirrors (radii  $r_1$  and  $r_2$ ) offset from one another. The smaller secondary mirror effectively obscures the opening of the primary mirror, forming an effective annular aperture toward the incoming illumination. From [11]

### 2.2.1 IRENI

The synchrotron beamline IRENI (InfraRed ENvironmental Imaging) was recently developed [9, 12] to address the challenge of the tradeoff between spatial resolution, signal-to-noise ratio (SNR) and acquisition times in IR spectromicroscopy. Two unique components of this beamline differentiate it from other beamlines to overcome the resolution/SNR/acquisition

time tradeoffs. The first distinguishing aspect is the use of a commercial large area focal plane array (FPA) detector. An FPA detector acts as an array of individual MCT detectors aligned in a configuration similar to a charge coupled device (CCD) camera; each element of the detector acts as one pixel in an IR image and contains an entire mid-IR spectrum. The second is the extraction of a large swath ( $320 \text{ mrad} \times 27 \text{ mrad}$  of radiation) of radiation from a dedicated bending magnet that permits a homogeneous widefield illumination (approximately  $40 \times 40 \mu\text{m}^2$ ) of the FPA detector. In conventional synchrotron-based imaging, the SNR/spatial resolution/acquisition time tradeoff becomes prohibitive of acquiring IR data at high spatial resolution with practical SNR. Thermal sources coupled to FPA detectors, on the other hand, allow for rapid acquisition of large areas, but the large emittance of the source limits the amount of light that can be focused onto a given area. As a direct result of the high emittance, thermal sources can only effectively illuminate FPA detectors with effective geometric pixel sizes of  $\geq 5 \times 5 \mu\text{m}^2$  while still achieving reasonable SNR. In contrast, IRENI uses 12 low-emittance synchrotron beams, whose brightness are  $\approx 100$  times that of a conventional thermal source, to illuminate an FPA detector with an effective pixel size approximately one-tenth the value that is achievable with a thermal source.

A schematic of the beamline design of IRENI is shown in Fig. 2.2. The homogenous illumination of the detector is achieved by extracting a large swath of radiation from a dedicated bending magnet. The bending magnet source is coupled to an ultra-high vacuum (UHV) chamber containing 24 mirrors. The fan of radiation is extracted from the bending magnet source and projected onto 12 torroidal mirrors (denoted M1) which divide the swath into 12 independent synchrotron beams and focus the 12 beams onto 12 flat mirrors (M2). These 12 flat mirrors then direct the beam through 12 ZnSe windows that isolate the UHV chamber from the

ambient environment and onto 12 paraboloidal mirrors (M3). The paraboloidal mirrors redirect and refocus the diverging beams to onto a final set of 12 flat mirrors (M4). The flat mirrors direct the beams into a Bruker Vertex 70 Fourier transform spectrometer. After exiting the spectrometer, the beams directed into a Bruker Hyperion 3000 IR microscope. The beams are slightly defocused at the sample plane using a condenser lens with a numerical aperture (NA) matching that of the objective lens. Two objective lenses are routinely used: a 74 $\times$  (NA=0.65) and a 36 $\times$  (NA=0.5). Due to the higher NA of the former, a higher spatial resolution is achieved and it is thus the lens of choice for most applications, but the 36 $\times$  is more desirable for certain applications due to its larger working distance. While the 74 $\times$  objective has a working distance of only 1 mm, the 36 $\times$  has a working distance of several cm, and is thus optimal for applications which require greater flexibility in sample height, such as tomography.

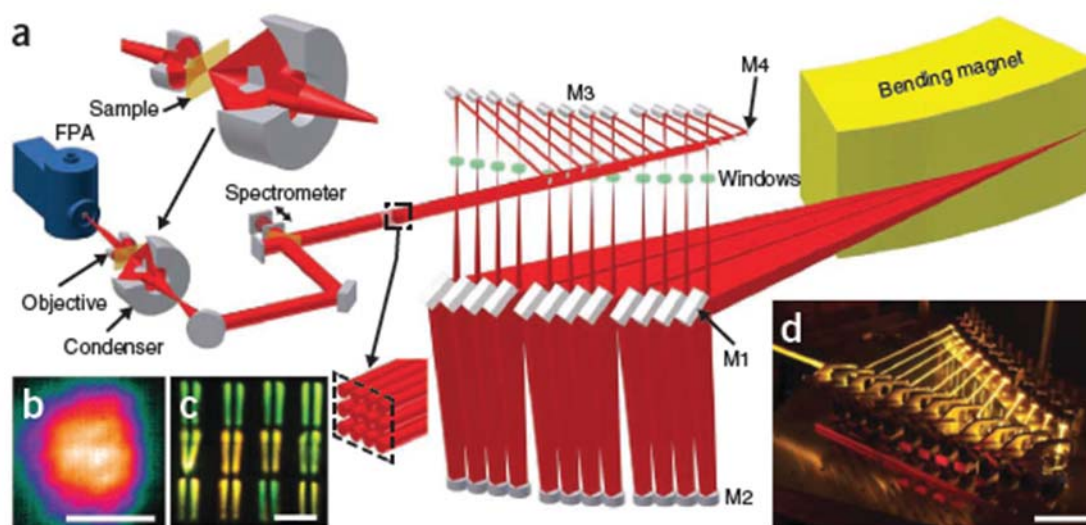


**Figure 2.2:** IRENI Schematic. A) IRENI Optical arrangement showing mirrors which direct the beam path from the bending magnet, to the spectrometer, through the condensing Schwarzschild, onto the sample, through the objective and onto the detector. B) Defocused illumination of the IR beams onto the FPA detector. C) Conventional image of the visible portion of the focused synchrotron beams. D)

visualization of the beam path through the M3 and M4 mirrors by a time-lapse photo generated by scattering the visible portion of the beams. From [9].

Based on the optics of the 74× objective, the effective geometric pixel size at the sample plane is  $0.54 \times 0.54 \mu\text{m}^2$ . The requirement for diffraction-limited spatial resolution follows from the criterion set by Stelzer,[13] which requires that to reach diffraction-limited spatial resolution for a given optical setup, each Airy disc must be sampled by at least 8 pixels. The size of the conventional Airy disc for unobstructed apertures is:

$$d = 1.22\lambda/NA \quad (2.9)$$

For the shortest wavelength in the mid-IR ( $2.5 \mu\text{m}$ ), the Stelzer criterion then says that diffraction-limited resolution is obtained by sampling with a pixel size no greater than  $0.59 \mu\text{m}$ , which is safely above the  $0.54 \mu\text{m}$  pixel sized used for the 74× (0.65 NA) objective. In contrast, the optical arrangement using the 36× (NA=0.5) objective has an effective pixel size of  $1.1 \mu\text{m}$  and is diffraction-limited only below  $2700 \text{ cm}^{-1}$ . These relationships between NA, pixelization, and spatial resolution are discussed in detail in Chapter 3.

### 2.2.2 Detectors

The two detectors are routinely used at IRENI are both mercury cadmium telluride (MCT) detectors. MCT is an alloy of HgTe and CdTe and falls under the category of quantum detectors [8] which are sensitive to the IR by a photoconductivity mechanism. MCT has a variable band gap based on the relative ratios of the constituent materials; with the right stoichiometry, MCT can have a band gap in the far IR region. This produces IR active excitations between the valence and conduction bands that excite carriers that can contribute to DC conduction and therefore produce a measureable response to IR light. Based on this



mechanism and the low band gap required for the IR sensitivity, there are an appreciable number of thermally excited carriers at room temperature that preclude any meaningful sensitivity. Consequently, the detectors are operated at liquid nitrogen temperatures to maintain their sensitivity.

The first detector, which is most desirable for imaging applications, is the FPA detector. The FPA is effectively an array of MCT detectors that acts as a spectrally-resolved CCD camera. The physical size of each detector element (pixel) is  $40 \times 40 \mu\text{m}^2$  and operates in the spectral range  $5400\text{-}850 \text{ cm}^{-1}$ . In addition to the FPA detector, the beamline is also equipped with a single-element MCT detector. The advantage of this detector is that, while it does not afford the high spatial resolution of the FPA, it has better SNR characteristics for individual spectra since it averages over a much larger area than a single element in the FPA. The single element detector also has the advantage of being able to probe a broader spectral range; with the right choice of beamsplitter, it functions between  $650\text{-}14000 \text{ cm}^{-1}$ .

### **2.2.3 Measurement Geometries**

Two experimental geometries with contrasting strengths were employed in this work. The first geometry is the normal incidence transmission (NIT) setup, depicted schematically in Fig. 2.3. In this experiment, the IR beam is focused onto a sample by a Schwarzschild objective that acts as a condenser lens with a NA that is matched to that of the objective. The sample is illuminated by a cone of radiation, with the effective range of incident angles determined by the NA of the condenser. The beam that is transmitted through the sample is then focused by the objective Schwarzschild and finally projected onto the detector.

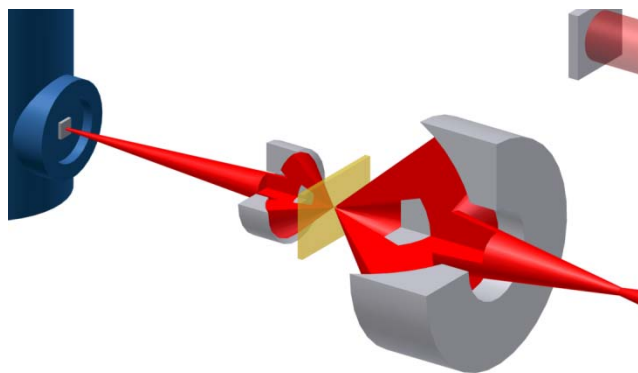


**Fig. 2.3:** Schematic diagram of the NIT measurement geometry

The illumination of the sample in the NIT geometry by a cone of radiation can be either desirable or undesirable depending on the application. For studying homogeneous samples, this is effectively irrelevant; however, for studying non-isotropic samples, there is not a well-defined polarization of the incident beam. While the majority of the radiation is polarized within the plane of the sample, a fraction of the radiation has components perpendicular to the sample as well. Thus for determining the orientation of functional groups on or in a sample, the NIT geometry provides less definitive information than the GIR geometry discussed below. On the other hand, for studying adsorption of molecules on surfaces, having both components of the polarization allows for the detection of all vibrational modes both parallel and perpendicular to the surface (in the absence of the metal surface selection rule).

In contrast, the grazing incidence reflection (GIR) geometry allows for measurements with a well-defined incident polarization. The general approach of this geometry is shown in Fig. 2.4A. A 15 $\times$  grazing angle objective (GAO) is designed for the Hyperion 3000 microscope. The objective focuses the beam onto the sample at an angle of incidence of approximately 84°. The beam reflects off of the sample surface, and is then refocused back onto the sample surface by another mirror, such that a double-pass measurement is made. The polarization of the

incident beam is controlled to be entirely parallel to the plane of incidence (p-polarization). The advantage of this polarization is that, due to the phase change upon reflection, the incident and reflected beams form a standing wave where the field components perpendicular to the surface are added constructively and parallel to the surface destructively. The measurement then selectively probes excitations that produce a dynamical dipole moment perpendicular to the reflecting surface. A schematic of the GAO in grazing operation mode is shown in Fig. 2.4B.

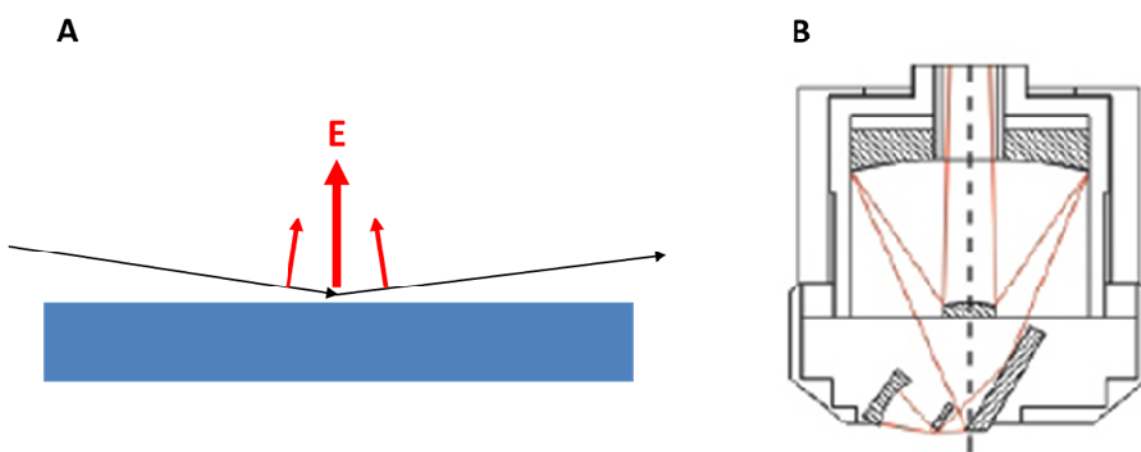


**Fig. 2.4:** A) Schematic of the GIR experimental setup. The polarization of the incident beam is within the plane of incidence, allowing for a well defined polarization normal to the reflecting surface. B) Schematic diagram of the GAO (provided by Bruker Optics).

### 2.2.4 *In situ* Spectromicroscopy

*In situ* IR Spectromicroscopy is performed using a custom flow cell that allows for IR measurements during exposure of the sample to gas or liquid flow [14]. In contrast to conventional surface science experiments, the measurements are performed under ambient atmospheric pressure, as such conditions are most closely aligned with actual sensing applications. The flow cell has a versatile design, allowing for measurements ranging from

living cells in liquid media to gas adsorption on solid films. A schematic diagram of the flow cell is shown in Fig. 2.5A-B with a photograph of the assembled device in Fig. 2.5C. The windows of the flow cell are IR transparent diamond cylindrical single crystals of 3 mm diameter and approximately 0.3 mm height that are embedded into 32 mm silicon or titanium wafer. In a typical experiment, the sample is deposited onto either the top or the bottom window of the flow cell prior to assembly. The base of the flow cell contains metal input and output tube that are connected to leur lock adaptors that interface with conventional plastic tubing. A rubber seal with holes for the input and output of the flow is placed between the base of the flow cell and the bottom window. Next, the top and bottom wafers are assembled as in 2.5A and separated by a Teflon spacer. A final seal is placed on the outside of the top window before the lid is screwed on. This flow cell is placed in the microscope, which is isolated and purged with a dry nitrogen source. In practice, the experiments are performed by first purging the flow cell with nitrogen to remove atmospheric components from the flow cell and tubes. Then, spectra and IR images of the sample are recorded prior to exposure. A background or reference spectrum is taken at the measurement position on the sample before the target gases are introduced to the cell. Then a controlled flow rate of the target gas is introduced using a mass flow controller connected to the input tube of the flow cell while differential transmission spectra are recorded. The output tube of the flow cell is connected to an external exhaust system that pumps on the flow cell to mimic a very weak vacuum environment. Typically, these measurements are performed in transmission mode. The relatively low thickness of the samples allows for sufficient transmitted intensity despite the continuum of substrate absorption over the entire MIR region. Importantly, the samples are illuminated with a cone of radiation (usually the  $NA=0.65$ ) such that vibrations whose dynamical dipole moments both parallel and perpendicular to the surface are excited.

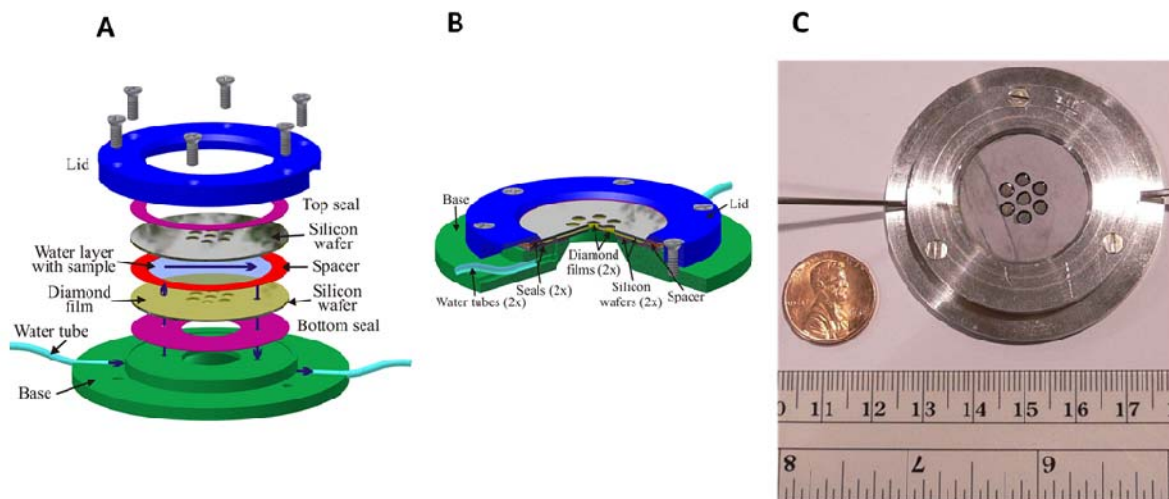


**Fig. 2.5:** A,B) Schematic diagrams of the flow cell and its components, C) Photograph of the assembled flow cell. From [14].

### 2.3 Transmission Electron Microscopy

Transmission electron microscopy (TEM) has become a workhorse of materials characterization, particularly in nanoscience. In a typical TEM experiment, electrons are accelerated to voltages that are typically 200-400 keV. The relativistic DeBroglie electron wavelength for an accelerating voltage of 300 keV (that used in this work) is 1.97 pm. Thus, the diffraction limit which plagues the long wavelength IR microscopy experiments is virtually nonexistent in TEM imaging, allowing for nanometer length scales to be explored at atomic resolution. Contrary to optical microscopy, however, the limiting factor in the spatial resolution in conventional TEMs is the lens aberrations, not diffraction effects. Even without the advent of aberration-correction, however, atomic resolution imaging in the TEM has become routine (high-resolution TEM or HRTEM). This capability coupled with the additional features of micro and nanodiffraction and electron spectroscopy have made TEM the single most widely utilized technique in the characterization of nanomaterials. In the proceeding sections [15], I will discuss

the aspects and techniques in TEM that are the most significant for the work done here.

### 2.3.1 Optics in the TEM

Figs. 2.6-2.7 shows a schematic diagram of the optical arrangement inside of the TEM. The source of electrons, the electron gun, is at the top of the column. In the Hitachi H900 NAR used in this work, the electron gun is a LaB<sub>6</sub> filament that operates through thermoelectronic emission. The operation principle is described by the Richardson Law, which states the relationship between the current density from the electron source, the operating temperature, and the work function of the material is given by [15]

$$J = AT^2 e^{-\Phi/kT} \quad (2.10)$$

where J is the current density, T is the temperature, k is the Boltzmann constant,  $\Phi$  the work function, and A is the Richardson constant of the material. For the case of the LaB<sub>6</sub>, the work function is 2.4 eV and the effective operating temperature is 1700 K. For LaB<sub>6</sub> electron guns, the LaB<sub>6</sub> crystal itself is used as the cathode in the electron gun to accelerate the electrons. Below the source is the Wehnelt cylinder situated above an anode plate with a hole in it, which together create a controllable beam of electrons in the following way: when a negative bias is applied to the Wehnelt cylinder, the electron beam is converged to “crossover”, allowing for optimum brightness in a small source size to be transmitted through the hole in the anode.

After transmitting through the anode, the electron beam diverges along the optic axis and is refocused by two condenser lenses whose purpose is to create a parallel beam of electrons incident on the sample. The condenser aperture allows the user to have control over the electron beam size. The last lens used to illuminate the sample is called the condenser/objective lens and allows for control of the beam convergence onto the sample. Thus, the sample is illuminated

with either a parallel or convergent electron beam, which is transmitted through and focused by the objective lens. A ray diagram of the optical paths taken following the specimen are shown in Fig. 2.7. Below the objective are two apertures, the objective aperture and the selected area aperture, located respectively at the back focal plane and the image plane; these are further discussed in the following sections. As the electron beam is focused by the objective lens, the diffraction pattern generated by the scattered electrons is formed in the back focal plane (BFP) of the objective. This can be seen in Fig. 2.7 by noticing that all of the rays scattered at the same angle are focused to the same point in the BFP of the objective. Lastly, the intermediate and projector lenses refocus and project images and diffraction patterns onto the viewing screen.

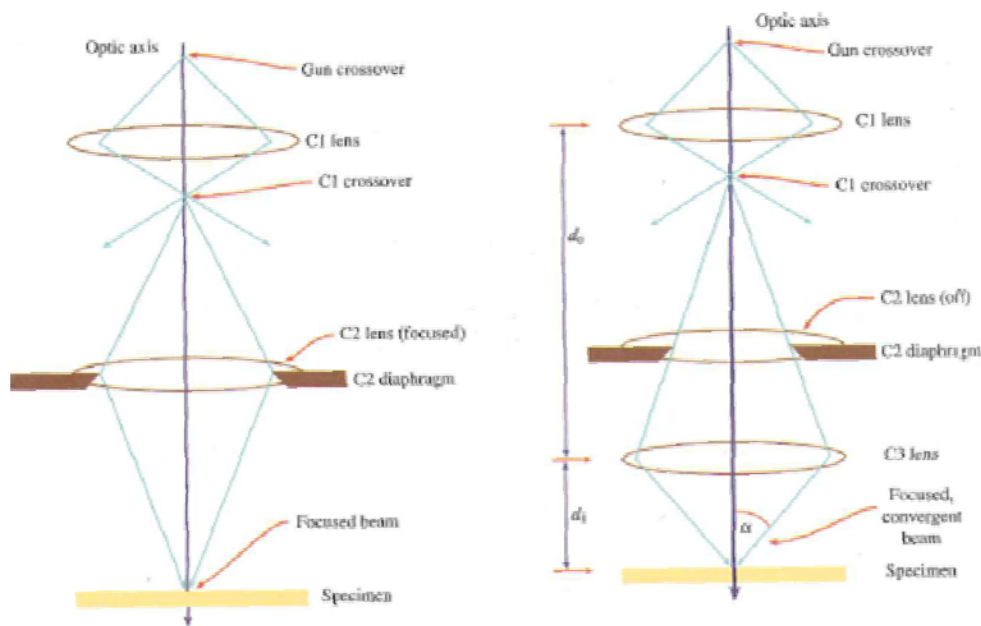


**Fig. 2.6:** Schematic diagram of the primary electron optical components in the TEM illumination. From [15]

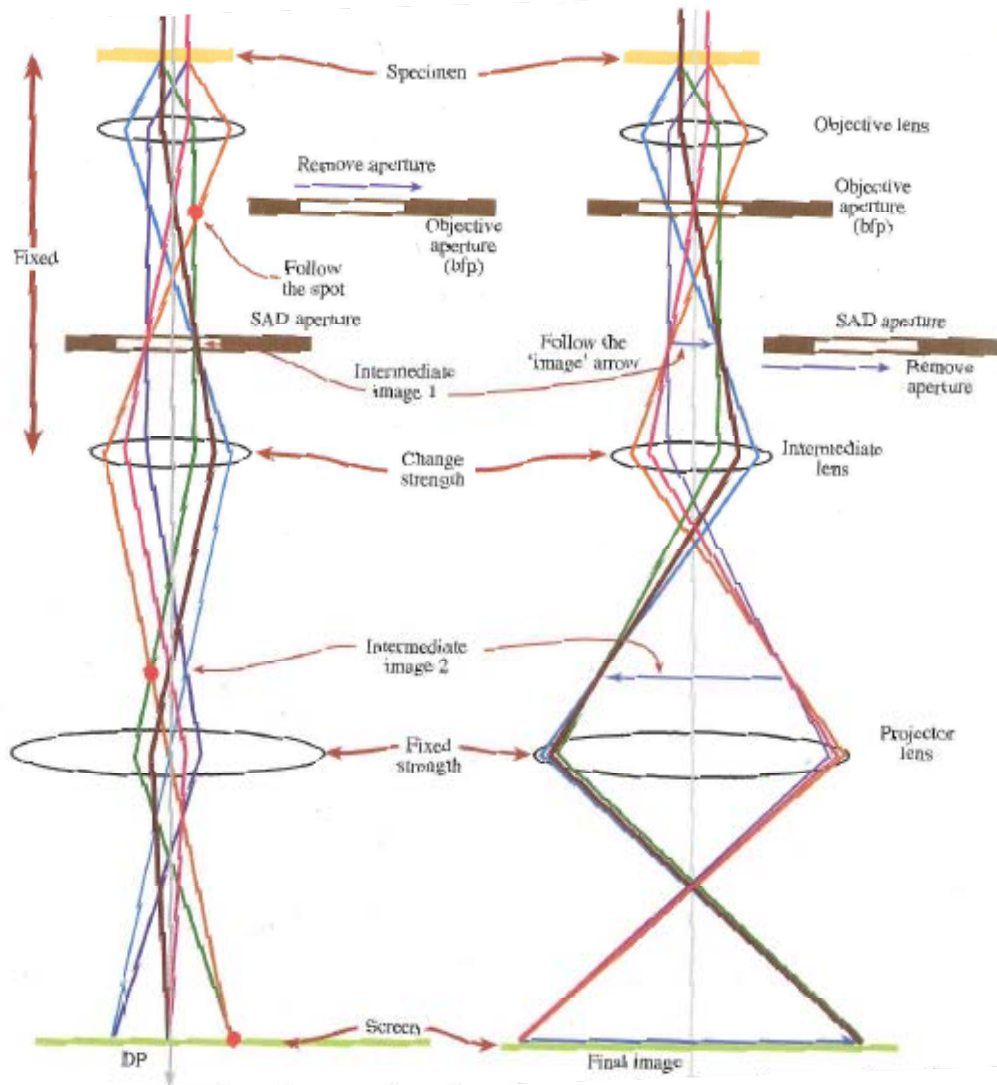


**Fig. 2.7:** Ray diagram showing image formation and optical paths taken in imaging and diffraction modes after the specimen. From [15]

### 2.3.2 Bright-Field TEM

Bright-field TEM (BFTEM) is the primary technique used to image and characterize the size, shape and morphology of a sample. The principle behind BFTEM imaging is shown in Fig. 2.7. After the electron beam passes through the sample, the scattered and transmitted electrons are focused by the objective lens. The electrons that scatter with the same angle with respect to the optic axis are focused to the same point in the BFP. To obtain a BFTEM image, an objective



aperture is placed at the BFP of the objective to block the scattered electrons, allowing only the transmitted electrons to pass through. The transmitted beam is then magnified and projected onto the viewing screen or ccd camera. The blocking of the scattered/diffracted electrons is what creates contrast in the resulting BFTEM images; the strength of the scattering by the sample is indicated by the number of counts on the viewing screen, causing scattering objects in the sample to appear dark. The more electrons that are scattered by the sample, the darker the contrast in the observed image. The principle behind dark-field TEM (DFTEM) imaging is essentially the same; the only difference is that the objective aperture is chosen to select the scattered/diffracted electrons rather than the transmitted beam. In this mode of operation, the scattering objects produce bright contrast in the resulting image, relative to a dark background.

### 2.2.3 Selected Area Diffraction

Selected area diffraction (SAD), also known sometimes as transmission high-energy electron diffraction (THEED), allows for characterization of the crystal structure of a specimen. The primary utility of SAD as compared to diffraction techniques performed outside of a microscope is the ability to collect diffraction patterns from sub-micrometer areas that can also be characterized subsequently using the various imaging and spectroscopic methods available in a TEM. The principle of SAD is shown in Fig. 2.7. The beam is spread over the sample to achieve a plane-wave illumination. As before, the electron beam is transmitted through the sample and focused by the objective lens. In this case, though, the selected area aperture is inserted at the image plane of the objective lens, rather than the BFP. In this way, only a certain effective area is allowed to transmit through to the intermediate lens. The current in the intermediate lens is adjusted in diffraction mode to have the BFP immediately before the

projector lens. In the BFP of the intermediate lens, the diffraction pattern is again formed from the selected region and focused onto the screen by the projector lens.

SAD patterns are formed based on the scattering and interference of the wavefunctions of the incident electron beam. The resulting diffraction pattern provides information that is analogous to x-ray diffraction patterns. Based on the wavelength of the incident beam, the scattering from a given crystallographic plane is determined by the Bragg Law:

$$n\lambda = 2d\sin\theta \quad (2.11)$$

where  $n$  is the order of the reflection,  $\lambda$  is the wavelength,  $d$  the interplanar spacing and  $\theta$  is the scattering angle. The interplanar lattice spacing for a given plane denoted by the Miller indices  $(h,k,l)$  is related to the lattice constant; for example, for a cubic material the lattice spacing  $d_{hkl}$  for a crystallographic plane is given by

$$d_{hkl} = \frac{a^2}{\sqrt{h^2+k^2+l^2}}, \quad (2.12)$$

where  $a$  is the lattice constant. In the case of the slightly more complicated hexagonal lattice structure, the interplanar spacing of a plane  $(h,k,l)$  is given by

$$d_{hkl} = \frac{a^2}{\sqrt{4/3(h^2+k^2+hk)+(c/a)^2l^2}}, \quad (2.13)$$

where  $a$  is the in-plane lattice constant and  $c$  the out-of-plane lattice constant.

So in principle, the SAD pattern of a material yields lattice spacings that can be correlated to its crystal symmetry and structure. In the most optimal conditions, Direct methods [16] can be applied to determine the phases of the Bragg beams and reconstruct the projected potentials. In more realistic circumstances, for example, a single-crystal sample is not available or a material is disordered or nonstoichiometric (*e.g.*, Chapter 4), the SAD pattern can still provide a valuable measure of the periodicity of the crystal lattice.

### 2.2.4 High Resolution TEM

High resolution TEM (HRTEM) exploits the wave properties of electrons to generate an image detailing information on the crystal structure of a crystalline sample. In brief, HRTEM involves imaging at very high magnifications without any apertures below the sample. The imaging characteristics of the objective lens then modify the electron wavefront in such a way that the phase and amplitude information are mixed with one another through the action of the transfer function of the microscope. The interference between the transmitted and diffracted beams from the sample leads to an image containing lattice fringes, or interference patterns whose periodicity represents that of the planes in the crystal lattice. This lattice-fringe imaging provides atomic resolution images of the crystal lattice(s) of the sample on the nanometer scale. In general, data collected this way produce images in which regions of dark contrast are representative of the positions of the atoms. The data are most commonly analyzed by taking the Fourier transform of the HRTEM images to produce a “diffractogram”. Diffractograms can be analyzed in a manner analogous to a single crystal diffraction pattern to obtain the spacings and angles of the planes in the crystal lattice. Periodic features in the HRTEM images produce spots or rings in the diffractogram with a spatial frequency equal to the inverse of the interplanar lattice spacing.

### 2.3.5 Energy Dispersive X-Ray Spectroscopy

Energy dispersive x-ray spectroscopy (EDS or EDX) is a spectroscopic technique performed in the TEM (or SEM) for the purpose of identifying the elemental components of a sample and their relative quantities. The excitation mechanism behind the principle of EDS occurs constantly.

When a high energy electron is incident upon atoms in a solid, a number of types of excitations can occur; the process relevant to EDS involves a core-level ionization. In this process, the

energy of the incident electron beam excites a core level electron out of the solid, leaving behind a hole. An energy from a higher occupied electron state than falls into the hole state, emitting an x-ray of the energy between the two levels. The allowed transitions between the core level states and the outer shell states are unique to each atom, providing a distinctive fingerprint of the elements being sampled. In practice, the measurement is performed by focusing the electron beam onto a small spot on the sample and tilting the sample toward the detector.

### 2.3.6 *In situ* Microscopy and Diffraction

*In situ* TEM and SAD experiments are used to probe the crystal structure of graphene oxide during thermal reduction. In these experiments, a commercial single-tilt heating holder is used to anneal the sample inside of the TEM. A schematic of the Gatan single-tilt heating holder is shown in Fig. 2.8. The holder uses a tantalum furnace with a thermocouple to control and monitor the temperature of the sample during heating. The time and temperature dependence of the structure of the sample is determined by recording the SAD pattern of the sample as a function of time. The Gatan Orius SC CCD camera permits the collection of TEM movies, and thus the evolution of the diffraction data as a function of time and/or temperature can be recorded as a movie.



**Fig. 2.8** Schematic diagram of the Gatan single-tilt heating holder (provided from Gatan website).

## 2.4 References

1. Sherwood, P.M.A., *Vibrational Spectroscopy Solids*. 1972: University Press.
2. Shankar, R., *Principles of Quantum Mechanics*. 1994: Springer.
3. Dressel, M. and G. Grüner, *Electrodynamics of Solids: Optical Properties of Electrons in Matter*. 2002: Cambridge University Press.
4. Zangwill, A., *Physics at Surfaces*. 1988: Cambridge University Press.
5. Tolstoy, V.P., I. Chernyshova, and V.A. Skryshevsky, *Handbook of Infrared Spectroscopy of Ultrathin Films*. 2003: John Wiley & Sons.
6. Hirschmugl, C.J., *Frontiers in infrared spectroscopy at surfaces and interfaces*. Surface Science, 2002. **500**(1-3): p. 577-604.
7. Carr, G.L., O. Chubar, and P. Dumas, *Multichannel Detection with a Synchrotron Light Source: Design and Potential*, in *Spectrochemical Analysis Using Infrared Multichannel Detectors*. 2007, Blackwell Publishing Ltd. p. 56-84.
8. Griffiths, P. and J.A. De Haseth, *Fourier Transform Infrared Spectrometry*. 2007: Wiley.
9. Nasse, M.J., et al., *High-resolution Fourier-transform infrared chemical imaging with multiple synchrotron beams*. Nature Methods, 2011. **8**(5): p. 413-U58.
10. Dumas, P., et al., *Imaging capabilities of synchrotron infrared microspectroscopy*. Faraday Discussions, 2004. **126**: p. 289-302.
11. Mattson, E.C., et al., *Restoration and Spectral Recovery of Mid-Infrared Chemical Images*. Analytical Chemistry, 2012. **84**(14): p. 6173-6180.
12. Nasse, M.J., et al., *Multi-beam synchrotron infrared chemical imaging with high spatial resolution: Beam line realization and first reports on image restoration*. Nuclear Instruments &

- Methods in Physics Research Section a-Accelerators Spectrometers Detectors and Associated Equipment, 2011. **649**(1): p. 172-176.
13. Stelzer, E.H.K., *Contrast, resolution, pixelation, dynamic range and signal-to-noise ratio: fundamental limits to resolution in fluorescence light microscopy*. Journal of Microscopy-Oxford, 1998. **189**: p. 15-24.
  14. Nasse, M.J., et al., *Demountable Liquid/Flow Cell for in Vivo Infrared Microspectroscopy of Biological Specimens*. Applied Spectroscopy, 2009. **63**(10): p. 1181-1186.
  15. WILLIAMS, D.B.A. and C.B. Carter, *Transmission Electron Microscopy: A Textbook for Materials Science. Basics*. 1996: Plenum Press.
  16. Marks, L.D., et al., *Direct methods for surfaces*. Surface Review and Letters, 1998. **5**(5): p. 1087-1106.

## **Chapter 3: Toward Optimal Spatial Resolution in IR Spectromicroscopy with Synchrotron Radiation**

The imaging performance of the IR beamline IRENI has been evaluated. Measurements of the point-spread-function (PSF) have been performed to understand the response of the imaging system over a broadband frequency range. The spatial resolution of the raw data that is achievable with this experimental approach for different IR wavelengths has been determined by the measurements of a number of test samples. As a step toward achieving optimal spatial resolution in IR spectromicroscopy, methods have been developed to deconvolute the measured PSF from IR hyperspectral data sets over the entire mid-IR region. Several examples have been selected to explore the relationships between numerical aperture, pixelization, deconvolution, and spatial resolution.

### 3.1 Introduction

Fourier Transform Infrared (FTIR) microspectroscopy is a powerful technique for label-free chemical imaging that has supplied important chemical information about heterogeneous samples for many problems across a variety of disciplines.[1-6] State-of-the-art synchrotron based infrared (IR) microspectrometers can yield high-resolution images, but are truly diffraction limited for only a small spectral range. Furthermore, a fundamental trade-off exists between the number of pixels, acquisition time and the signal-to-noise ratio, limiting the applicability of the technique. The recently commissioned infrared synchrotron beamline, Infrared Environmental Imaging (IRENI), [7] overcomes this trade off and delivers 4096-pixel diffraction limited IR images with high signal-to-noise ratio in under a minute. The spatial oversampling for all mid-IR wavelengths makes the IRENI data ideal for spatial image restoration techniques. Here, we measured and fitted wavelength-dependent point-spread-functions (PSFs) at IRENI for a 74x objective between the sample plane and detector. Noise-free wavelength-dependent theoretical PSFs are deconvoluted from images generated from narrow bandwidths ( $4\text{ cm}^{-1}$ ) over the entire mid-infrared range ( $4000 - 900\text{ cm}^{-1}$ ) using a Fourier filtering-based approach. The stack of restored images is used to reconstruct the spectra.

### 3.2 Spatial Resolution

Many factors impact the spatial resolution of an imaging system. As microscopy is performed at increasingly smaller length scales, the probing wavelength limits the obtainable resolution by the so-called diffraction limit. The diffraction limit arises because of the finite NA of an imaging system, *i.e.*, the limited angular region from which the objective can collect the light from the object being imaged. Consequently, imaging a point source of radiation with a



finite objective results in a blurring of the point within the resulting image; *i.e.*, the point spread function (PSF). When the distance between the observation point of the measurement is much greater than the object being imaged, diffraction effects become relevant, and the blurring of the point source can be considered physically as arising from diffraction of the plane waves radiating from the source from the aperture of the objective. The physical characteristics of the PSF determine the resolution of the resulting images generated from the optical system since each object being imaged is in essence a superposition of point sources. This is equivalent to saying that the measured image is a convolution of the true image with the PSF [8],

$$I_{\text{meas}} = I_{\text{true}} * \text{PSF} \quad (3.1)$$

The so-called "Rayleigh Criterion" frames the resolution of the optical system within the characteristics of the PSF. The Rayleigh Criterion states that the lowest achievable resolution corresponds to the point at which the central maximum of one PSF overlaps with the first zero-crossing of another PSF. For conventional lenses, this requirement can be recast into an equation for the resolution achievable with a given objective; however, for obstructed Schwarzschild objectives used in this work there is no closed form analog. Rather, the contrast difference for conventional lenses is used as the standard for resolution; [9] specifically, for conventional lenses the contrast difference for two PSFs at the Rayleigh criterion is exactly 26.4%. This is the so-called Stelzer or contrast resolution criterion. In this work, two objects are considered resolved if the contrast difference between them is  $\geq 26.4\%$ .

As the obtainable resolution is directly related to the characteristics of the PSF, understanding data from IRENI critically depends on understanding the PSF of the microscope used. As a model for the PSF, the image formation is considered in terms of Kirchoff's scalar

diffraction theory. The object is treated as a radiating point source at the sample plane; the source is considered sufficiently far from the focusing objective that the spherical waves emanating from the point source are approximately plane waves. The conventional treatment of plane wave illumination of a circular aperture is shown in Fig. 3.2 [8]. The Kirchoff integral for the electric field at the observation point P is given by [8]:

$$\tilde{E} = \frac{\varepsilon_A e^{i(\omega t - kR)}}{R} \int_0^a \int_0^{2\pi} \exp\{i(k\rho q/R) \cos\phi\} \rho d\rho d\phi \quad (3.2)$$

Where  $\varepsilon_A$  is the electric field amplitude,  $\rho$  is the radial coordinate of the aperture,  $R$  is the distance from the center of the aperture to the observation point,  $k$  is the wavenumber and  $\phi$  is

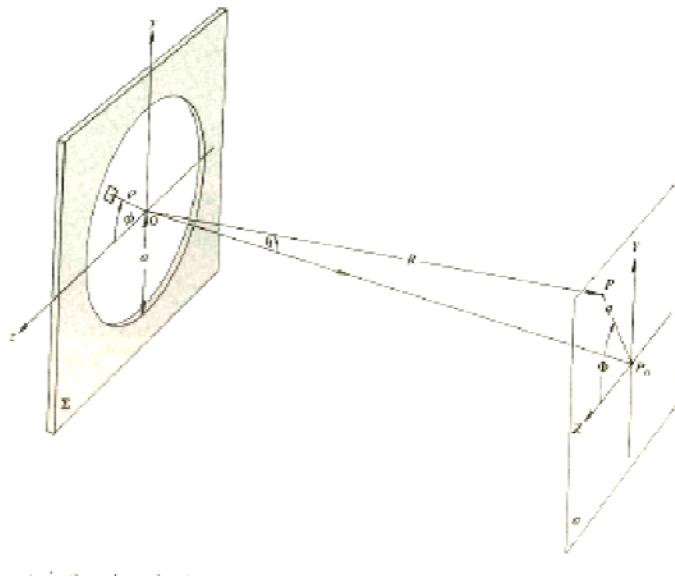


**Fig. 3.1:** Diffraction from a circular aperture. From [8].

the angular coordinate of the aperture. Evaluation of the angular integral using the definition of the Bessel function gives ultimately gives:

$$\tilde{E} = \frac{\varepsilon_A e^{i(\omega t - kR)}}{R} 2\pi \int_0^a J_0(k\rho q/R) \rho d\rho \quad (3.3)$$

For the case of the Schwarzschild optic, the secondary mirror obscures the beam path leading to an effectively annular aperture. Thus equation 3.3 is modified by placing a lower bound on the integral. For inner radius  $r_1$  and outer radius  $r_2$ , the result of 3.3 reduces to:

$$\tilde{E} \propto \frac{J_1\left(\frac{kr_2q}{R}\right)}{kr_2q/R} - \frac{J_1\left(\frac{kr_1q}{R}\right)}{kr_1q/R} \quad (3.4)$$

so that the light intensity is

$$I \propto \left[ \left( \frac{J_1\left(\frac{kr_2q}{R}\right)}{kr_2q/R} \right)^2 + \left( \frac{J_1\left(\frac{kr_1q}{R}\right)}{kr_1q/R} \right)^2 - 2R^2 \frac{J_1\left(\frac{kr_1q}{R}\right)J_1\left(\frac{kr_2q}{R}\right)}{k^2r_2r_1q^2} \right] \quad (3.5)$$

Thus the intensity distribution of the PSF can effectively be described by 3 parameters specific to the imaging optic: the inner and outer radii of the annular objective and the distance between the plane of the annulus to the plane at which the image is formed. A more convenient form of (3.5) recasts these three variables into the ratio of the inner to outer radii,  $\epsilon$ , and the angular position at the image plane with respect to the optical axis,  $\theta$ :

$$I(\theta) = I_0 \left( \frac{2J_1(x)}{x} - \frac{2\epsilon J_1(x)}{x} \right)^2 \quad (3.6)$$

where  $x = k r_2 \sin \theta$ . Since this objective is a three-dimensional object, and the obscuration due to the secondary mirror is not coplanar with the image plane, there are small deviations from this ideal theory that are wavelength dependent. They are absorbed into an “effective  $r_1$ ” as described below.

The PSF of IRENI is measured by measuring the transmission through a 2  $\mu\text{m}$  pinhole at the sample plane, yielding images of the PSF from 1500-4000  $\text{cm}^{-1}$ . Next, to obtain noise-free

idealized PSFs, the measured data is fit by a model described by a variant of eq. 3.6. In practice, when characterizing the wavelength-dependence of the PSF,  $d$  and  $r_2$  are fixed to their known physical dimensions, and the trend for the effective size of the obscuration (effective  $r_1$ ) is obtained by fitting the measured data to a function describing an annular diffraction pattern over a range of wavelengths. Deviations from the ideal annulus model, such as the optical path differences introduced from the curvature of the primary optic, are absorbed into the effective obscuring mirror radius (effective  $r_1$ ) in the annular model. The obscuring mirror amplifies the intensity of the diffraction maxima in the PSF, while narrowing the central maximum as compared to the conventional Airy function.[10, 11] Fig. 3.2A shows the measured PSFs for a 74× objective lens on the Bruker Hyperion IR microscope, as observed at 3 different locations in the field of view at three different wavelengths. The overall similarity of the PSF across the field of view indicates that the PSF is shift invariant; as expected a broadening is observed with increasing wavelength. A comparison of the PSFs simulated by reproducing eq. 3.6 using the values obtained from the fits with the measurement is shown in Fig. 3.2B for 3 different frequencies. The data are center profiles through the experimental and simulated PSFs.

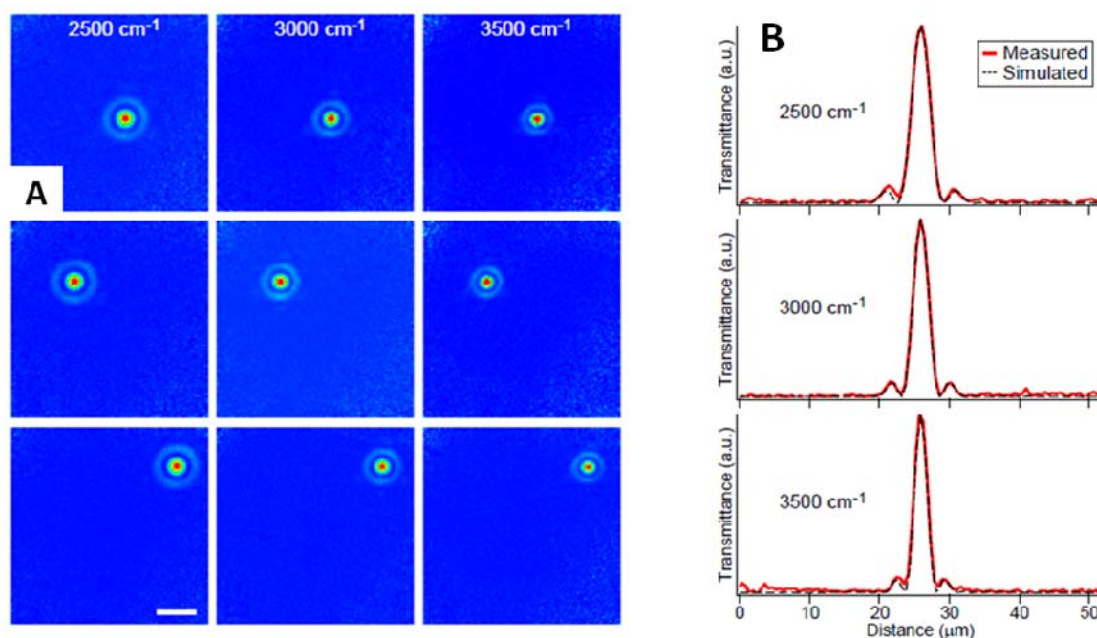


**Fig. 3.2:** A) Measured PSFs observed at 3 different frequencies and 3 different locations in the field of view. B) Comparison of center profiles from measured and simulated PSFs at 3 different frequencies. From ref [12].

The PSF of the 36× (NA=0.5) objective was characterized as well; the significance of this lower magnification objective is its utilization in tomography experiments. The much larger working distance of this objective makes it possible to rotate a sample of finite dimension without interfering with the objective; furthermore, the lower NA is more similar to plane wave illumination assumed in the reconstruction algorithms. A comparison between measured and fitted PSFs for the two objectives is shown in Fig. 3.3. As can be seen from the center profiles, the lower NA of the 36× results in a larger spatial extent of the PSF in addition to the coarser sampling (1.1 μm geometric pixel size at the sample plane).

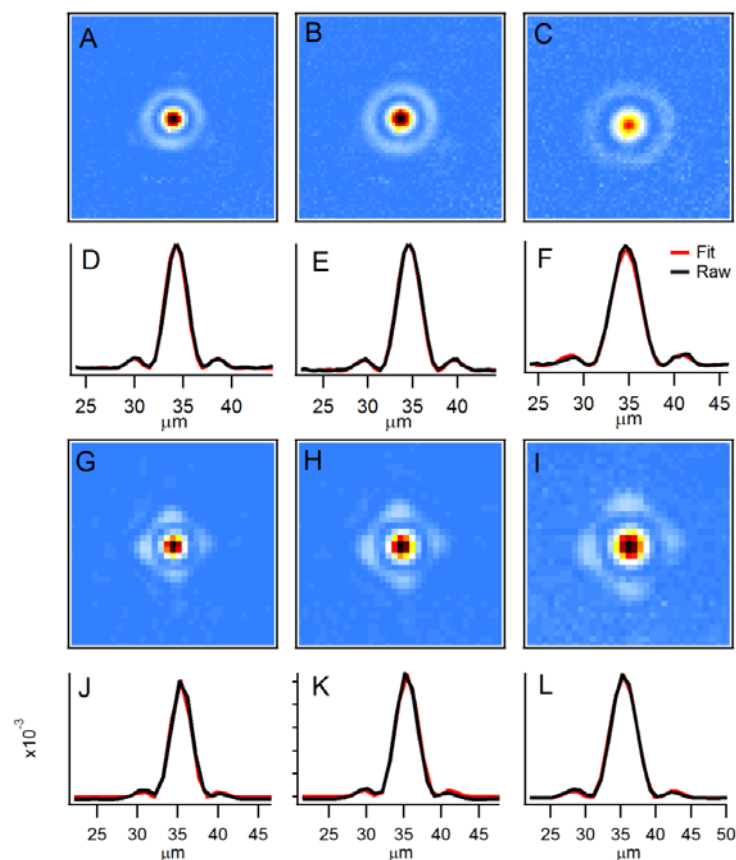


**Fig. 3.3:** Comparison of measured and fitted PSFs for the two objectives. A-F) 74 $\times$  (NA=0.65) PSFs, G-L) 36 $\times$  (NA=0.5) PSFs

### 3.3 Hyperspectral Deconvolution

For the IR imaging community, it has long been a goal to perform spatial and spectral deconvolution of hyperspectral cubes. The problem of deconvolution is substantially more complicated for IR data than for conventional visible microscopy due to the broadband nature of the data. The PSF is strongly dependent on wavelength, and every image in the hyperspectral cube needs to be reconstructed such that the resulting spectra at each pixel are reasonable and faithful. Other approaches to deconvolution of IR hyperspectral data sets [13] have applied the well-known method of Fourier Self-Deconvolution (FSD) to the spectral domain as well as the

spatial domain. These methods, implemented in commercial software packages, deconvolute arbitrary (user-defined) Lorentzian lineshapes from the spectra, as well as from the two dimensional images in the hyperspectral cube. The fundamental difference in the method presented here is that this work has focused on deconvolving a PSF which truly represents the response of the imaging system to a point light source and thus correctly describes the mechanism of image formation. No deconvolution is applied in the spectral domain. Rather, a two-dimensional restoration method is applied to an IR image at every wavelength which is then scaled as described below. Then these images are reassembled into a hyperspectral cube, from which the reconstructed spectra are extracted. The approach taken for the deconvolution is as follows: the measured image is assumed to be a convolution of the true image and the PSF (Eq. 3.1). The true image is then recovered through Fourier inversion:

$$I_{\text{true}} = \text{FT}^{-1} \left[ \frac{\text{FT}(I_{\text{meas}})}{\text{FT}(\text{PSF})} \right] = \text{FT}^{-1} \left[ \frac{\text{FT}(I_{\text{meas}})}{\text{OTF}} \right] \quad (3.6)$$

The term in the denominator is the Fourier transform of the PSF, or the optical transfer function (OTF). Any discrete image,  $I(\mathbf{x})$ , may be decomposed into an infinite series of complex exponentials:

$$I(\mathbf{x}) = \frac{1}{(2\pi)^2} \sum_{\mathbf{q}} I_{\mathbf{q}} e^{2\pi i \mathbf{q} \cdot \mathbf{x}} \quad (3.7)$$

where  $\mathbf{q}$  is the Fourier-space coordinate or spatial frequency and  $\mathbf{x}$  is the real-space coordinate.

The coefficients  $I_{\mathbf{q}}$  are given by the discrete Fourier Transform (FT):

$$I_{\mathbf{q}} = \sum_{\mathbf{x}} I(\mathbf{x}) e^{-2\pi i \mathbf{q} \cdot \mathbf{x}} \quad (3.8)$$

The PSF,  $P(\mathbf{x})$  may be expressed as a Fourier series just as the image in (3.8):

$$P(\mathbf{x}) = \frac{1}{(2\pi)^2} \sum_{\mathbf{q}} P_{\mathbf{q}} e^{2\pi i \mathbf{q} \cdot \mathbf{x}} \quad (3.9)$$

Each  $I_{\mathbf{q}}$  determines the extent to which a given spatial frequency  $\mathbf{q}$  contributes to the image.

In terms of the Fourier components  $I_{\mathbf{q}}$  and  $P_{\mathbf{q}}$  of the image and PSF, respectively, the true image may be obtained by combining (2.7-9):

$$I_{\text{true}}(\mathbf{x}) = \frac{1}{(2\pi)^2} \sum_{\mathbf{q}} \left( \frac{I_{\mathbf{q}}}{P_{\mathbf{q}}} \right) e^{2\pi i \mathbf{q} \cdot \mathbf{x}} \quad (3.10)$$

Thus the approximate solution for the "true" image is given by (3.10). While this problem is commonly encountered in Fourier analysis, the direct solution for the true image becomes intractable due to the fact that the OTF approaches zero at high spatial frequencies (i.e., the  $P_{\mathbf{q}}$  approach zero for large  $\mathbf{q}$ ). Stable solutions to such inverse problems are routinely obtained by applying a low-pass filter to the data. In practice, these filters allow all spatial frequencies below a certain threshold, above which the OTF becomes zero, to contribute to the reconstructed image. The filter is brought continuously to zero by a smoothly varying function, so that spatial frequencies at which the OTF is nearly zero are not included in the reconstructed image. This Fourier Inversion approach to image deblurring is employed in this work; however, there are certain inherent drawbacks to this method. For example, there is a loss of high spatial frequency information, which is determined by the high-frequency content in the PSF. Furthermore, the use of discrete FTs can cause oscillatory "ringing" artifacts near physical boundaries) and discontinuities of objects. Despite its drawbacks, this method has distinct advantages over other methods: it is robust and computationally inexpensive. In contrast, more



sophisticated methods which implement an iterative, variational or statistical approach are subject to long computation times and user subjectivity; however, they do not employ a low-pass filter and therefore do not involve an inherent loss in high spatial frequency components in the image.

The approach taken is as follows: to avoid ringing artifacts at the image boundaries, the image was placed in an array with the original image in the center and additional images reflected about each axis on the edges before applying the FT ("reflexive" boundary conditions[14]). A Hanning apodization kernel of the following form was applied to the Fourier

$$\text{data: } H(k) = \begin{cases} 1 & k < k_{\min} \\ \frac{1}{2} \left[ 1 + \cos \left( \frac{\pi(k - k_{\min})}{k_{\max} - k_{\min}} \right) \right] & k_{\min} < k < k_{\max} \\ 0 & k > k_{\max} \end{cases} \quad (3.11)$$

Here  $k$  is the radial coordinate in the Fourier domain,  $k_{\max}$  is the cutoff frequency, where the OTF approaches zero, and  $k_{\min}$  is an effective smoothing parameter. The Hanning function is equal to 1 for all frequencies less than  $k_{\min}$  and is equal to 0 for frequencies greater than  $k_{\max}$ . At frequencies between  $k_{\min}$  and  $k_{\max}$ , the filter smoothly approaches zero by using a function with a sinusoidal dependence. Ringing artifacts associated with discontinuities in the image are mitigated by smoothly approaching zero,  $k_{\min}$  is chosen to optimize image sharpness and suppress edge-ringing artifacts that could arise from the discrete FT. Universally acceptable values for the parameters  $k_{\max}$  and  $k_{\min}$  were determined empirically over a wide spectral range using a four-step process. First, a phantom test image was blurred by the known PSF. Second, the deconvolution routine was applied with different  $k_{\min}$  and  $k_{\max}$  values and the optimal choices

for the two parameters were inferred based on the fidelity of the resulting images. Third, the second step was repeated for images spanning the entire mid-IR spectral range to establish variation of the parameters as a function of wavelength. Fourth, a polynomial curve was fitted to the wavelength-dependent  $k_{\min}$  and  $k_{\max}$  values. The latter depend only on the PSF, and are thus generally applicable to all spectrochemical data sets.

Importantly, due to the normalization convention used for the PSFs, the resulting images will have arbitrary absorption intensity scales. Since it is important to recover meaningful spectra from the deconvoluted hyperspectral cube of data, the arbitrary scaling is compensated for in each deconvoluted image. To find the correct scaling, the zero-frequency component in the FT of the original and deconvoluted images at a given wavelength are required to be equal, modifying 2.11 as:

$$I_{\text{true}}(\mathbf{x}) = \frac{1}{(2\pi)^2} \frac{I_0}{P_0} \sum_{\mathbf{q}} \left( \frac{I_{\mathbf{q}}}{P_{\mathbf{q}}} \right) e^{2\pi i \mathbf{q} \cdot \mathbf{x}} \quad (3.12).$$

Next, the total transmitted light reaching the detector is required to be equal for both the original and deconvoluted images. In practice this latter correction was a small contribution to the results from (2.13). This scaling leads to high-quality, faithful, and chemically meaningful spectra. The OTF of the measured PSF is shown in Fig. 2.2.3.1 for 2 different wavelengths with the appropriate Hanning apodization kernels overlaid. As can be seen from the image, the spatial frequencies in which the OTF has appreciable intensity correspond to the Hanning filter being equal to one. The filter then smoothly approaches zero in the vicinity of the frequencies for which the OTF approaches zero.

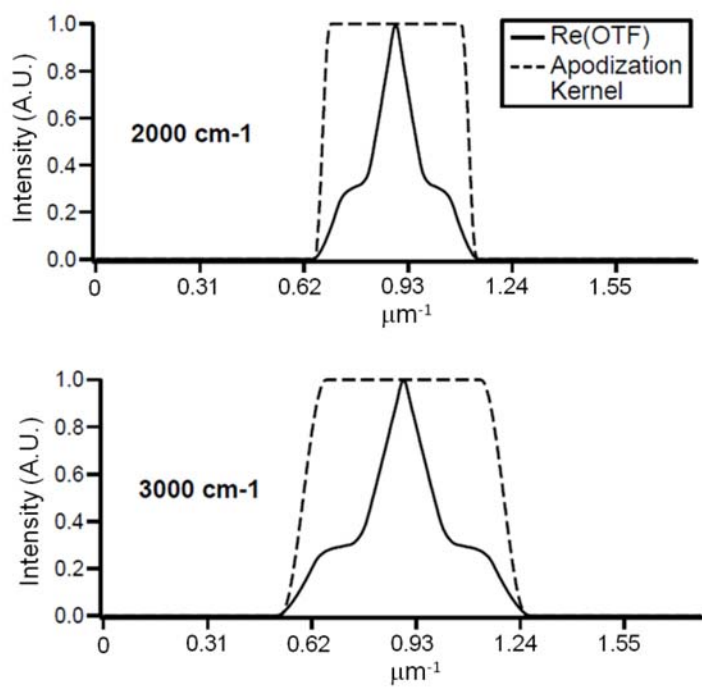


**Fig. 3.4:** Real part of the OTF overlaid with the Hanning apodization kernel for 2 different frequencies. From [12]

### 3.4 Evaluating the Deconvolution Method

As a demonstration of the deconvolution method, several applications are considered. United States Air Force (USAF) targets have proven to be an effective tool for probing spatial resolution in infrared microspectroscopy[15, 16]. The targets consist of chrome strips of various sizes evaporated onto glass; the chrome constitutes an absorbing object on a transparent substrate for frequencies above  $2500\text{ cm}^{-1}$ , below which point the glass also becomes opaque to IR light. Group 7 elements 4-6 and groups 8 and 9 with pitches of 228 and 256-645 line pairs/mm, respectively, were imaged. These correspond to chrome strips that are, respectively, 2.2 and  $1.95 - 0.775\text{ }\mu\text{m}$  wide, separated by the same distance. Hybrid polymer structures were constructed to test the preservation of spectral features following the deconvolution process. Polystyrene (PS) beads, with diameters of 1, 2 and  $6\text{ }\mu\text{m}$ , were mixed in solution with polyurethane (PU). A  $10\text{-}\mu\text{m}$  layer of the PU/PS bead solution was spin-coated onto a glass slide. The films were removed and mounted free-standing on stainless steel washers. Finally, in order to evaluate the suitability of this method for real-life heterogeneous samples, the deconvolution algorithm was also applied to IRENI spectrochemical images acquired from a cryosectioned mouse retina mounted on a  $\text{BaF}_2$  window. Sample preparation and data collection protocols are reported elsewhere [17].

As a first consideration on the improvement in resolution following deconvolution, the USAF targets are shown before and after deconvolution in Fig. 3.5. These images represent the raw IR absorbance of the 3-bar USAF targets for groups 8-9 ( $256\text{--}645\text{ cycles / mm}$ ) at two different wavelengths:  $2.63\text{ }\mu\text{m}$  ( $3,800\text{ cm}^{-1}$ ) and  $3.70\text{ }\mu\text{m}$  ( $2,700\text{ cm}^{-1}$ ), respectively. Images in Fig. 2.7 C-D show the patterns from (A) and (B) after deconvolution with measurement-based PSFs. Line profiles (Fig. 2.7 E-H) have been extracted from along the dashed lines in Fig. 2.7.

A-D to demonstrate the improvement in contrast and resolution following application of the deconvolution algorithm to these single wavelength IR images. The pairs of dashed gray lines in

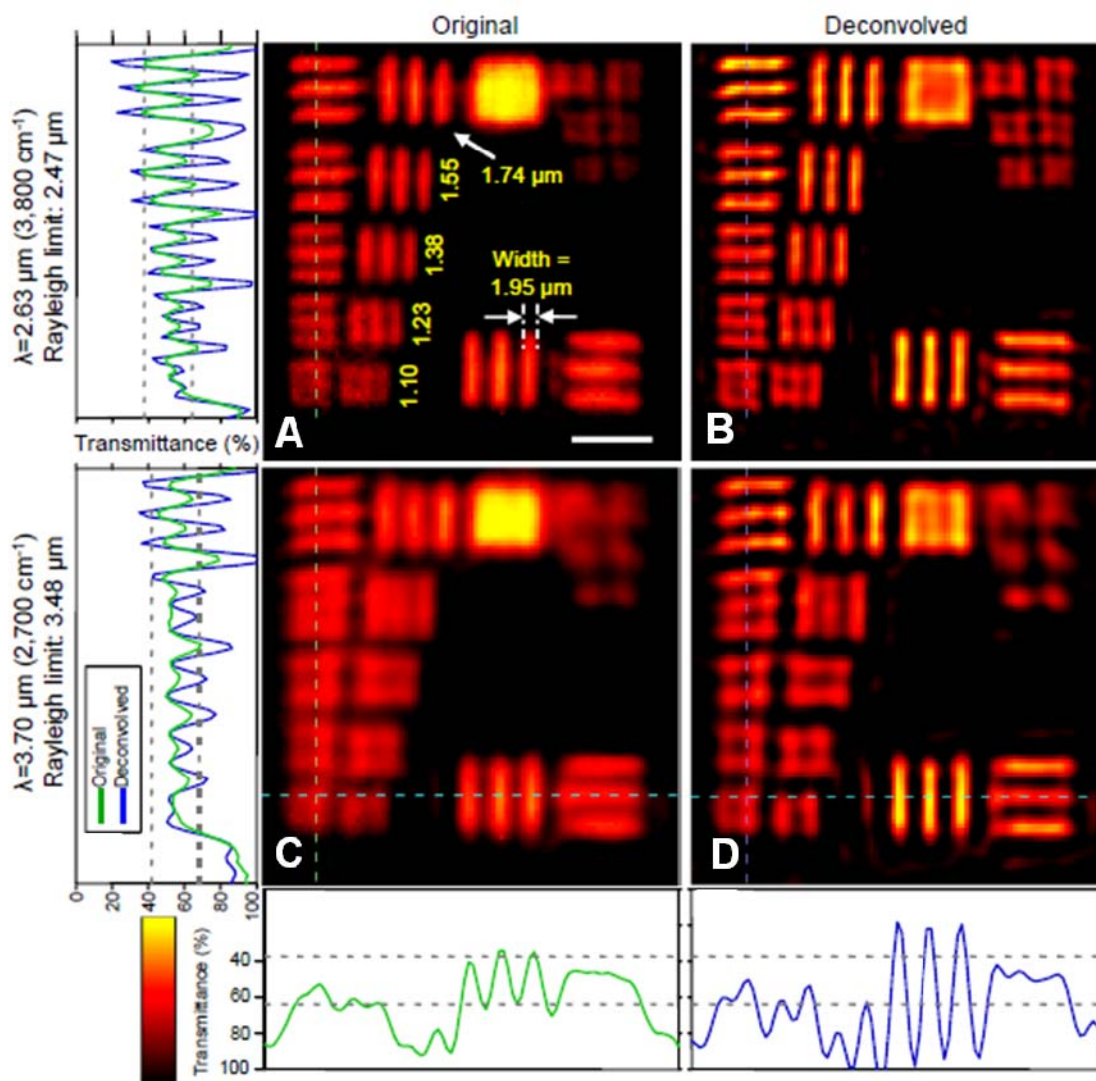


**Figure 3.5:** Transmission images of a high-resolution 1951 USAF test target. Panels A) and B) show unprocessed images in transmittance at a wavelengths of  $2.63\mu\text{m}$  ( $3,800\text{ cm}^{-1}$ ) and  $3.70\mu\text{m}$  ( $2,700\text{ cm}^{-1}$ ), respectively. Panels C) and D) show the same patterns after deconvolution with the measurement-based PSFs (see text). Intensity profiles extracted along the dashed lines in (A-D) are shown in (E-H); green = original, blue = deconvolved. White scale bar in a:  $10\mu\text{m}$ . From [7]

Fig. 3.5 E-H define a contrast range of 26.4%, corresponding to the Rayleigh resolution limit. Analysis of the line profiles indicates that this imaging system exceeds the theoretical Rayleigh resolution ( $2.47 \mu\text{m}$  and  $3.48 \mu\text{m}$  for A and B, respectively, since the  $1.74 \mu\text{m}$  pattern is clearly resolved (contrast=30.7%) in (A), as is the  $1.95 \mu\text{m}$  pattern (contrast=29.1%) in B); while the  $1.55 \mu\text{m}$  pattern in A is almost resolved (contrast=23.8%. The resolution improvement upon deconvolution with the instrument's PSF is clearly apparent in the images and in the line profiles. The contrast of the patterns with a width of  $1.38 \mu\text{m}$  increases from 14.1% (unresolved) in A) to 30.9% (resolved) in C), and from 13.7% (unresolved) in B) to 40.2% (resolved) in D), respectively.

Naturally, the effects of blurring due to sampling beyond the diffraction limit are manifested in the spectra and in spectrochemical images, as illustrated in the analysis of a chemical image of the PS/PU mixed sample, Fig. 3.6. Closely spaced  $5.9 \mu\text{m}$  spheres, as well as smaller  $1$  and  $2 \mu\text{m}$  spheres throughout the field of view (schematic in Fig. 3.6), were imaged by integrating each spectrum over a PS-specific CH stretching band ( $3007\text{-}3041 \text{ cm}^{-1}$  with same baseline), to reveal the location of PS in the PU matrix (Fig. 3.6A). The PS absorption signal observed near the interface of the two central beads should be smaller than the absorption signal observed at the centers of the beads, since the optical path length traversed is predominantly through PU, and the path length of PS is much smaller near the interface. Similarly, the optical path length through the PU should be reduced at the top of a bead, yet nearly equal amounts of PS are detected all across the interface of the two beads. Fig. 3.6B shows the C-H stretching region of spectra taken along the line connecting the two spheres, Reference spectra of PS and PU are shown below as red and black, respectively. In the spectra along the line joining the two spheres, there is very little variation in the intensity of the PS-specific bands. Fig. 3.6C, which

shows the variation in the intensity of the PS band at  $3026\text{ cm}^{-1}$ , indicates that this value is nearly constant along the line. This is in contrast to the expectation that the PS signal should be strongest immediately on top of the spheres, and much weaker in between them. In addition, the intensity of the PU-specific band at  $2960\text{ cm}^{-1}$  remains nearly constant along the line as well. These data demonstrate how imaging at the diffraction limit produces IR spectra contaminated with signals from neighboring pixels, and concomitantly blurred images.

The deconvolution algorithm is applied for every wavelength in this data set, and all of the resulting chemical images are reassembled the deconvoluted images in a hyperspectral cube to thus produce a reconstructed spectrum for every pixel. Reconstructed spectra are compared to original spectra from the same positions in Fig. 3.6D-E, taken from the PU background and on top of a PS bead, respectively. The reconstructed spectra follow the unprocessed spectra closely, maintain all spectral features and show that the deconvolution process does not introduce additional artifacts. The baseline fringes come from multiple reflections in the PU film. Fig. 3.6F shows an image generated from the restored data set integrated over the same spectral range as that used in Fig. 3.6A for comparison. Enhanced contrast and a reduction of blurring are immediately obvious, particularly evident at the interface of the two beads. Smaller  $1$  and  $2\ \mu\text{m}$  beads scattered throughout the field of view become more apparent. Fig. 3.6G shows the reconstructed spectra taken from the sample pixels used to generate the spectral stack in Fig. 3.6 F. While in the original data the absorbance signatures in the spectra from every point along the line contain very similar absorption strengths (Fig. 3.6H, green), much stronger variation is observed in the restored data set. These spectra more accurately reflect the expected absorption strengths for PS and PU function groups across the interface of the two beads. Moving from the left bead to the center of the interface, one observes that the absorption strength detected from



the PS decreases as expected, while the absorption strength from the PU is smaller directly at the center of the bead, and gradually increases near the center of the interface. Fig. 3.6H compares the absorption strength of the PS band at  $3026\text{ cm}^{-1}$  as a function of position along the indicated line for both the original and restored data. The changes in PS absorption along the line are clearly resolved in the deconvoluted data, whereas little change is observed in the raw data. Thus, the improvements in spatial resolution are observable not only in the deconvoluted images, but also in the faithfulness of the resulting spectra.

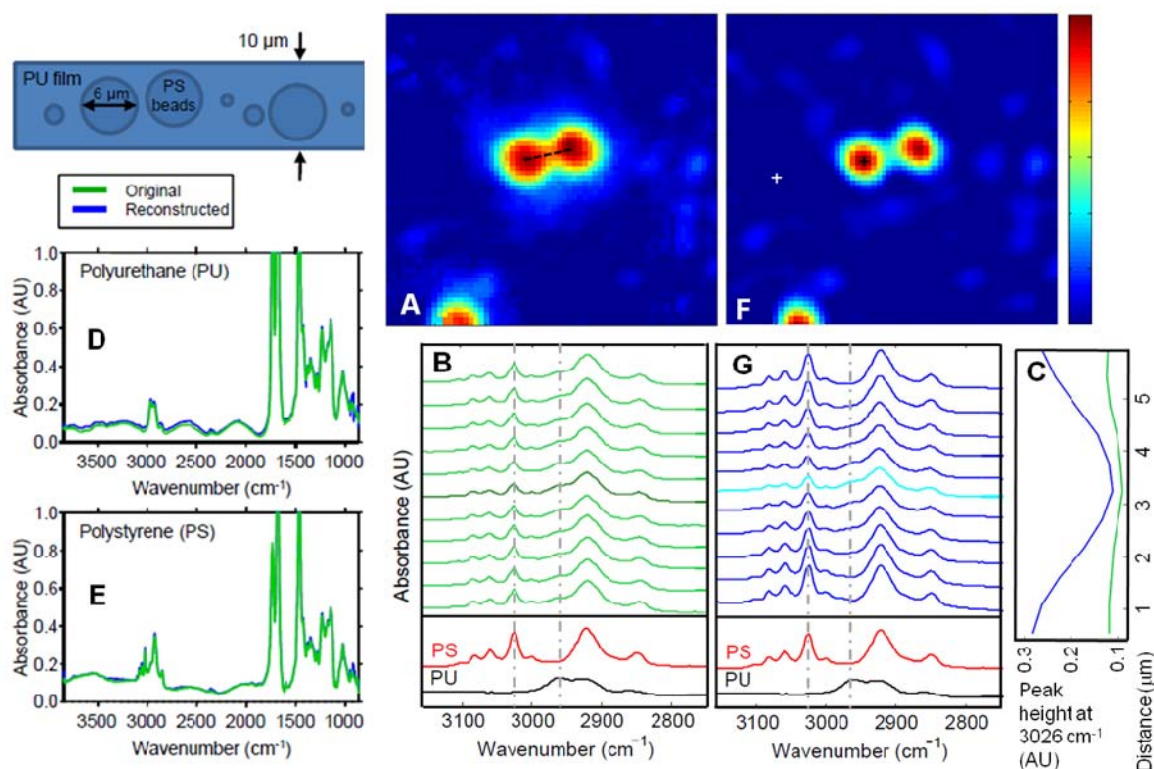


**Figure 3.6:** Original and Deconvoluted hyperspectral data from 1.0, 2.1, and 5.9 μm diameter PS beads dispersed in a 10 μm thick PU film. A) unprocessed and F) deconvoluted absorbance images integrated over the PS peak at  $3020\text{ cm}^{-1}$  (aromatic CH stretch). Three 5.9 μm PS beads are clearly visible, the weaker signal in the background stems from several 1.0, 2.1 μm PS beads, some of which are out of focus. D,E) Comparison of original and reconstructed spectra from the PU background (D) and from one of the PS beads (E). F,G) Stacked spectra taken along the black line in A), between the centers of the 5.9 μm PS beads, illustrating the effect of the reconstruction process on the spectra. While the original spectra



in F) all show a very similar PS/PU mixture (compare reference spectra on the bottom), the reconstructed spectra in G) clearly exhibit the PS–PU–PS transition demonstrating the spatial resolution enhancement in the spectra achieved with the deconvolution algorithm. [12]

The PS/PU composite sample provides a clear and effective demonstration of the power of the restoration algorithm; however, much of the material imaged with FTIR is heterogeneous and components are distributed in irregular patterns. For example, the retina, a biological tissue that is composed of several highly distinct layers, presents an excellent real-world test case for evaluating improvements in resolution. In a recent paper [17], high-resolution IRENI images of mouse retina tissue were reported. The deconvolution algorithm is now applied to data from that study. The visual signaling pathway through the retina includes three main types of neurons: photoreceptors (containing the rods or cones), bipolar cells and ganglion cells, connected approximately end to end. Images and data, before and after deconvolution, are shown for the region that includes the photoreceptor nucleus and outer plexiform layers (Figure 3.7).

The nucleus layer is composed of the nuclear bodies of photoreceptor neurons, while the outer plexiform layer is composed of dendrites and synapses. The former layer is therefore rich in nucleic acids while the latter, composed primarily of cell membranes, are rich in phospholipids. Typical IRENI spectra extracted from well within each region are shown in Figure 3.7A. The CH stretch peak intensities are much greater in the plexiform layer; the polyunsaturated fatty acid (PUFA) peak at  $3012\text{ cm}^{-1}$  and the phospholipid carbonyl peak at  $1740\text{ cm}^{-1}$  are also considerably elevated relative to the same bands in the nuclear layer. Distinguishing spectral features of the photoreceptor nucleus layer include the appearance of a small peak at  $1712\text{ cm}^{-1}$ , associated with nucleic acids, and decreased intensity in all phospholipid bands. The photoimage of a near-by section, nuclei stained deep blue with

hematoxylin, (Fig. 3.7B) may be compared to the spectrochemical false-color images for the area inside the white box, created from the intensity of the  $1712\text{ cm}^{-1}$  nucleic acid peak, before and after the deconvolution process (Fig. 3.7 C,D, respectively). In each case, the image processing allows one to distinguish between the layers, but, prior to deconvolution, the sharp demarcation between nuclei and axons is blurred by poor spatial resolution.

To show the improvement in spectral purity, a stack of 25 spectra spanning the transition region was extracted from the original and restored data sets (Fig. 3.7 C,D, white line). Baseline-corrected areas of several biomarker peaks were measured and plotted (Figure 3.7 E,F). Plots of the intensity of peaks corresponding to distinct tissue constituents (marked in 3.7A) that vary between the two morphological layers show that the transition is sharper and stronger in each case, following deconvolution (solid lines) compared to the original data (dashed lines). The deconvolution algorithm is thus successful in increasing the spatial resolution and spectrochemical contrast of IRENI images.

This demonstration has important implications for the value of this restoration process. Many biochemical and biomedical studies are focused on changes at the cellular and sub-cellular level. The deblurring capability offered by this deconvolution method represents a significant practical step forward, retaining the true chemical information through achieving the best spatial and chemical contrast from the raw data.

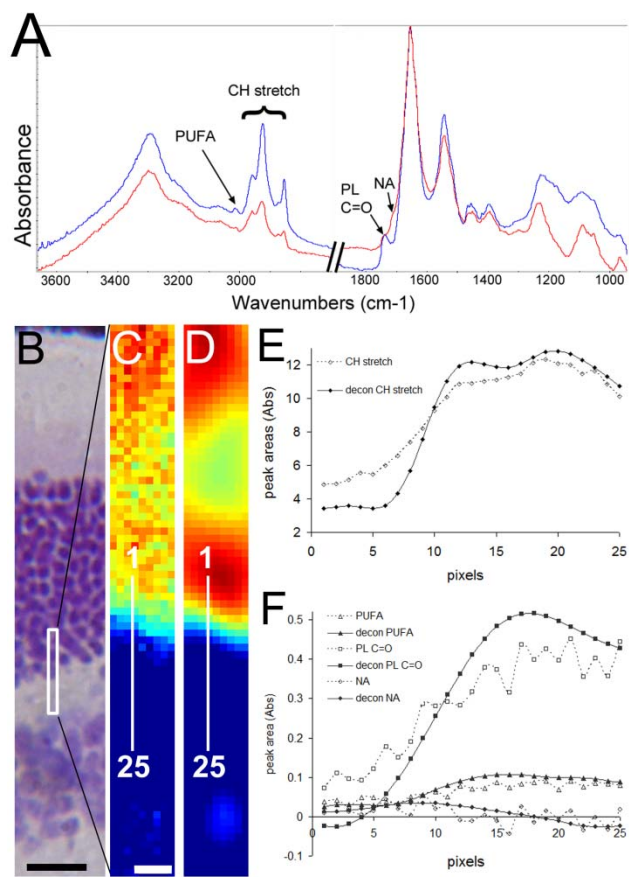


**Figure 3.7:** Deconvolution of IRENI data resolves biological details. A) Representative single-pixel IRENI spectra of the photoreceptor nucleus layer (red) and outer plexiform layer (blue) from mouse retina. B) Photomicrograph of a hematoxylin-stained serial section. The white box indicates the approximate location of the IRENI images. (Scale bar = 50  $\mu\text{m}$ ). C and D) False-color spectrochemical images created by integrating the area of the nucleic acid peak at  $1712\text{ cm}^{-1}$  for (C) the original IRENI FTIR-FPA data and (D) data after hyperspectral deconvolution (red=high, yellow-green=medium, blue=low spectral intensity, scale bar = 5  $\mu\text{m}$ ). White lines in (C) and (D) denote the exact locations of the stack of spectra extracted from the 25 pixels for analysis. E, F) Peak areas for region-specific marker peaks, plotted from data in each stack. [12]

### **3.5 Effect of Numerical Aperture, Spatial Oversampling and Deconvolution on Spatial Resolution in Widefield Infrared Spectromicroscopy**

The contrast resolution for confocal, dual aperture systems is predicted to be superior to one aperture systems, since the point spread function (PSF) is a multiplicative effect of two Schwarzschild objective PSFs, and results in a narrower central peak and suppressed sidelobes at each wavelength.[11] Reports of the contrast resolution determined from sufficiently spatially oversampled, raster-scanned data for confocal microscope optics with no apertures illuminated with a synchrotron beam were similar [15, 16] to the predicted values with dual apertures. For the widefield geometry employed in the present experiment, which is also apertureless, the pixel size, and thus spatial oversampling is based on the magnification of the objective that projects a certain area of the sample onto the detector pixels. Here the combination the spatial oversampling and NA influence the resolution of synchrotron-based widefield imaging. Results employing an array detector are compared to results in the literature[11, 15, 16] for synchrotron-based confocal, dual aperture, raster-scanning systems. It is shown that they are, within the noise, identical for deconvoluted image data and raster-scanned data from the confocal microscope, which is significant since samples are measured more quickly with the array detector. Spectrochemical images from two Schwarzschild objectives with varying magnification and NA (36 $\times$ , 0.5 NA and 74 $\times$ , 0.65 NA), both used in the Bruker Hyperion 3000 microscope, will be used to demonstrate this. While the highest magnification is likely desirable in most cases, experimental constraints sometimes require the inherently larger working distance (i.e. environmental controlled stages) and or the lower numerical aperture (i.e. tomography) that are available with the lower magnification and lower NA objective. The comparison between the

different magnifications and NAs allows an examination of the impact of spatial oversampling on the contrast resolution.

To address the relationship between numerical aperture, pixelisation, deconvolution, and spatial resolution, several studies have been performed. The performance of the 36× and 74×-based imaging systems is first evaluated from measurements of United States Air Force (USAF) targets. The performance of these imaging systems following deconvolution of the corresponding instrumental PSFs as determined from transmission measurements of a 2 μm diameter pinhole placed at the sample plane [12] is considered next. This is followed by studies of a sample of a single MDA-MB-231 hormone independent breast cancer cell labelled with an exogenous metal-carbonyl derivative (Re(CO)<sub>3</sub>N<sub>3</sub>)[18] is analyzed as a demonstration of the impact of oversampling and deconvolution in a biologically relevant sample. IR-specific biomarkers, such as metal-carbonyl derivatives, show intense absorptions in the transparent window of biological media between 2000-1850 cm<sup>-1</sup>. Such markers are important in spectromicroscopy applications, as they allow for the unambiguous determination of the localization of cellular organelles in IR microscopic data sets. For example, the Re(CO)<sub>3</sub>N<sub>3</sub> biomarker used here on single breast cancer cells specifically labels the Golgi Apparatus (GA). [18]

The samples are measured in transmission mode with two different Schwarzschild objectives. When the 74× Schwarzschild objective is used for focusing, a 20× Schwarzschild condenser (0.58 NA) is used to illuminate the sample. The objective effectively projects 0.54 × 0.54 μm<sup>2</sup> of the sample area onto each 40 × 40 μm<sup>2</sup> detector pixel.[7, 19] Typically, lower magnification and smaller NA objectives provide larger working distances, which is also the case for Schwarzschild objectives. Thus, when experimental limitations require larger working

distances than the limiting range of 1 mm for the 74× objective, or require a smaller numerical aperture, other options can be employed.

In Figure 3.8, simulated resolutions based on the parameters determined from the experimental PSFs [7] for both objectives are compared with the experimentally-determined wavelength-dependent resolution of both objectives. The PSF contrast resolution (PSFCR), which is similar to the Rayleigh criterion for the Airy function, is first considered for the 2 objectives (solid lines, right axis). Here full width at 73.6% maximum is calculated because two objects are considered resolved if the contrast difference between them exceeds 26.4%. [9] As for the case of the FWHM, the PSFCR is substantially smaller for the 74× than for the 36× objective, particularly at the longest wavelengths and is likely due to the difference in the NA of the objectives. Next, the experimental spatial resolutions of the objectives were determined from transmission measurements of high-resolution USAF targets, as described elsewhere [7, 12, 19]. The results from the original experimental (open circles) and deconvoluted (solid triangles) data are compared to the simulated PSFCRs; the experimentally resolved features from the original USAF target data (grey circles) for the 74× is only slightly above that predicted by the simulated PSFCRs, most likely due to experimental uncertainty in the measurements. In contrast, the 36× results show a substantially poorer agreement with the predicted PSFCR, likely due to the coarser spatial sampling employed with the 36× geometry. The raw data collected with 74× magnification ( $0.54 \times 0.54 \mu\text{m}^2$  projected sample area/pixel) is sufficient to retrieve resolutions similar to the simulated PSFCR. The original data measured with the 36× magnification, with inherently coarser sampling ( $1.1 \times 1.1 \mu\text{m}^2$  projected sample area/pixel), is unable to achieve the optimal resolution due to the spatial sampling. In order to achieve optimal spatial resolution, the data must be sampled with at least 8 pixels spanning the dimension of the airy disk for any given

wavelength. Using the conventional Rayleigh criterion for the shortest wavelength in the mid-IR (2.5  $\mu\text{m}$ ), this corresponds to a pixel size no larger than 0.6  $\mu\text{m}$  for the 74 $\times$  objective, which is larger than the effective pixel size in the geometry employed here. Conversely, this sampling criterion for the 36 $\times$  objective requires a pixel spacing no larger than 0.76  $\mu\text{m}$ , which is smaller than the effective pixel size. Thus the optical setup for the 36 $\times$  geometry is undersampled for wavelengths below 3.6  $\mu\text{m}$  (2770  $\text{cm}^{-1}$ ). Following deconvolution, however, both objectives yield resolutions exceeding the predicted PSFCR criterion, yet still retain their dependence on NA as expected. This suggests that instrumental broadening is successfully removed through deconvolution, and a more faithful image is recovered in both cases.

Next, these results are compared to previously published works performed with analogous objectives. Carr [11] explored resolution limits using a confocal synchrotron-based IR microscope with NA=0.65, while Levenson et. al. [15, 16] used a similar approach to study spatial resolution limits with a 32 $\times$  objective with NA=0.65. For a direct comparison to the results shown here, two lines are included in Figure 1 that correspond to the reported [15, 16] PSFCR trends for the confocal dual aperture microscope with similar NAs (0.47 $\lambda$  describes the confocal Rayleigh Criterion resolution for a NA=0.65 objective, [16] while 0.61 $\lambda$  describes the same quantity for a NA=0.5 objective). This is appropriate because the objective NA is the primary contribution to the achievable resolution. The PSF contrast resolution results presented here for the original (undeconvoluted) data with the 74 $\times$  objective (NA=0.65) show resolution limits ranging from comparable (3000-4000  $\text{cm}^{-1}$ ) to poorer (2000-2500  $\text{cm}^{-1}$ ) to those described previously [11] for the dual aperture confocal setup. Upon deconvolution using measured PSFs of the 36 $\times$  and 74 $\times$  objectives, however, the resolution of the 74 $\times$  exceeds the resolution of the confocal geometry with a similar NA, while that of the 36 $\times$  geometry becomes comparable to or

slightly better than the predicted resolution for a NA=0.5 confocal geometry.[11, 15, 16] In sum, with the correct oversampling, and therefore projected sample pixel size that is matched to the NA of the objective, one achieves similar spatial resolution results for dual aperture confocal mapping and FPA based imaging. Application of PSF deconvolution allows for the resolution of wide-field FPA-based microscopy to exceed that of confocal microscopy.

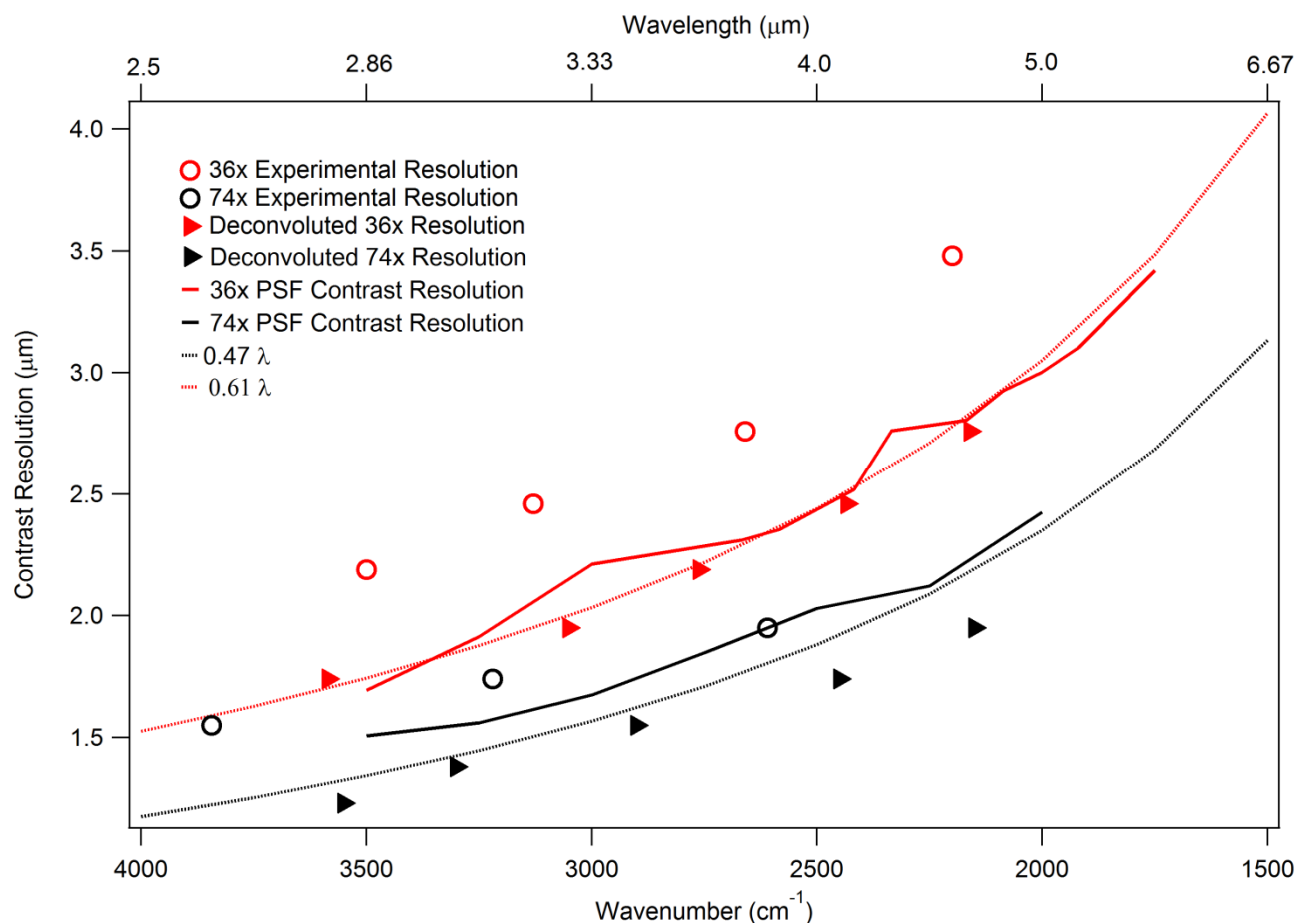


**Fig. 3.8** Predicted and experimental spatial resolutions of original and deconvoluted data. Contrast resolution (solid lines) of the PSF for the 36×(NA 0.5) and 74×(NA 0.6NA) objectives compared to the experimentally determined resolution limit for the 36×(NA 0.5) and 74×(NA 0.6NA) objectives before (open circles) and after (filled triangles) deconvolution, and with reported NA dependent trends for confocal, raster scanning resolution limits (dotted lines).



These results are now considered within the context of a realistic biological specimen, namely, a breast cancer cell labelled with a metal carbonyl biomarker ( $\text{Re}(\text{CO})_3\text{N}_3$ ). This label has been shown to selectively bind to the GA[18]; therefore, chemical images showing its localization within the cell should indicate a spatial distribution displaced from that of the nucleus, which is indicated by the region with the highest Amide absorption [18]. Fig. 3.9 shows integrated images of the Amide I and metal carbonyl functional groups within the cell generated from both the raw and deconvoluted data sets taken with the  $36\times$  and  $74\times$  objectives. The following parameters were used to generate the integrated images: For the Amide I band, the integration was performed over  $1600\text{-}1690\text{ cm}^{-1}$ , with the same baseline. Integration of the biomarker signature was performed over the  $\text{C}=\text{O}$  stretching feature from  $2005\text{-}2040\text{ cm}^{-1}$  with the same baseline. In the raw data taken with both objectives, the distribution of the Amide shows a slight displacement from the localization of the biomarker signature, which is discussed further below. Upon comparison of the raw and deconvoluted data from both objectives, it is clear that in all cases the deconvolution produces images show sharper, more well-defined features with enhanced contrast.

To more qualitatively address the effect of deconvolution on the data from both objectives, intensity profiles through the same position of the cell are shown for both datasets (Fig. 3.10). The location of the profile used for the  $74\times$  data set is indicated by the white line in Fig. 3.9B; all of the  $74\times$  profiles in Fig. 3.10 from the different functional groups are extracted from the exact same location. The location from which the profiles from the  $36\times$  data are extracted is shown by the white line in Fig. 3.9H. The relative distributions of the Amide I and the biomarker

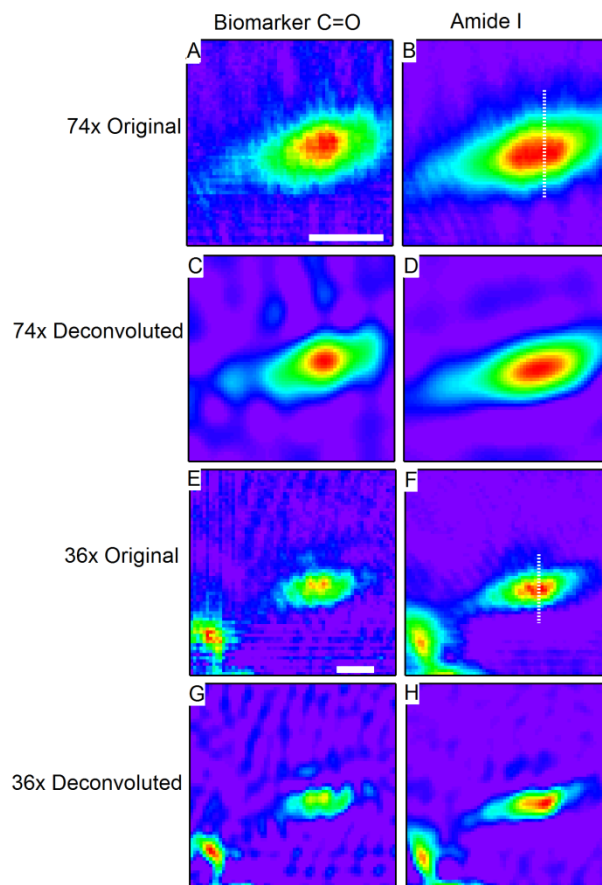


**Fig. 3.9:** Original and Deconvoluted images of a breast cancer cell labelled with a metal-carbonyl marker taken with both 74 $\times$  and 36 $\times$  objectives. A-B) show original chemical images NOTE: (color scales: purple (low intensity) – red (high intensity)) of the cell as measured with the 74 $\times$  objective generated by integrating under C=O stretching of the biomarker (A), and Amide I (B). Scale bar in A is 20  $\mu$ m. C-D) show the results of deconvolution of the data used to generate A-B). E-F) show the analogous data of A-B) as measured with the 36 $\times$  objective. Scale bar in E is 20  $\mu$ m. G-H) show the results of deconvolution of the data used to generate C-D).

features within the cell as indicated by the original and deconvoluted 36 $\times$  data (Fig. 3.10A) are first considered. A comparison of the profiles from the Amide I chemical images from the original and deconvoluted datasets shows that the deconvolution results in a narrowing of the Amide distribution and a sharper edge at the periphery of the cell. Several informative quantities will be considered to evaluate the data. The first is the effective spacing between the Amide and Biomarker distributions as measured from the distance between the peak values of the Amide

and Biomarker profiles, as shown in Fig. 3.10. Next, to quantify subcellular distances in this sample, a figure of merit is introduced; namely, the distance between the peak value of the integrated intensity to the point where it reaches its minimum value (*e.g.*, the peak-to-edge distances) for all of the profiles shown in Fig. 3.10. Lastly, to explore the relationship between error propagation and spatial oversampling, a simple error analysis of the conclusions drawn on the Amide and Biomarker distributions is discussed.

The relative displacements between the Amide and Biomarker signatures in the 36 $\times$  and 74 $\times$  datasets are considered first. In Fig. 3.10A, both the original and deconvoluted data sets show that the distance between the maximum values of the Amide and Biomarker signals is 2 pixels, or 2.2  $\mu\text{m}$  given the effective geometric pixel size at the sample plane for the 36 $\times$  objective. The same quantity for the 74 $\times$  objective in Fig. 3.10B is exactly 3 pixels, corresponding to an effective geometric distance of 1.62  $\mu\text{m}$  at the sample plane. This discrepancy between the 2 objectives is a direct result of the coarser sampling of the 36 $\times$  objective. While the difference between the two values is only 0.58  $\mu\text{m}$ , this difference is a significant deviation of 35.8% from the Amide/biomarker separation measured between the 74 $\times$  objective and corresponds to, nearly identically, the effective geometric size of one pixel using the 74 $\times$  objective geometry (0.54  $\mu\text{m}$ ). Thus, these data indicate that sufficient spatial oversampling is critical in applications such as subcellular microscopy of biological specimens.

Next, the peak-to edge distances in the profiles shown in Fig. 3.10 are used to evaluate the change between raw and deconvoluted data for the two objectives. These distances for the Amide I and Biomarker signatures before and after deconvolution are summarized in Table I. First, for the Amide profiles derived from the 36 $\times$  objective (Fig. 3.10A); the distance from the centre of the cell (the point of highest intensity in the Amide profile) to the bottom edge of the

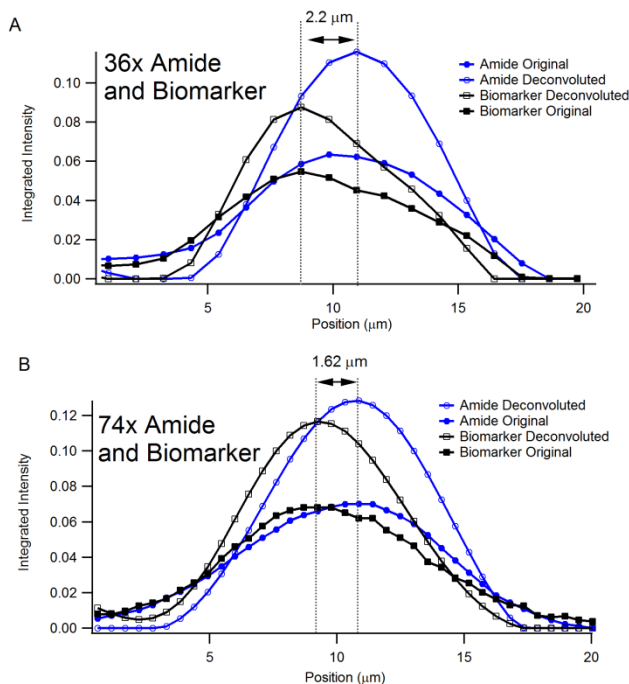


**Fig. 3.10** Line profiles through chemical images of the labelled cell shown in Fig. 3.9. A) original and deconvoluted line profiles of the Amide and biomarker chemical images shown in Fig. 3H-I and K-L. The profiles all come from the location indicated by the white line in Fig. 3H. The displacement between the Amide and biomarker signatures is measured to be  $2.2 \mu\text{m}$ . B) Original and deconvoluted line profiles of the Amide and biomarker chemical images shown in Fig. 3.9B-C and E-F. The profiles all come from the location indicated by the white line in Fig. 3.9B. The displacement between the Amide and biomarker signatures is measured to be  $1.62 \mu\text{m}$

cell (where the intensity profile approaches its minimum value) is  $7.8 \mu\text{m}$  in the original data set and  $6.4 \mu\text{m}$  in the deconvoluted dataset, indicating a decrease of approximately 18% in the peak-to-edge spatial distribution of the Amide. In the case of the biomarker, the distance from the point of highest intensity of the biomarker to the bottom edge of the cell where the biomarker signal drops to zero changes from  $10 \mu\text{m}$  in the original intensity profile to  $7.7 \mu\text{m}$  in the deconvoluted profile. This corresponds to a decrease of 23% in the spatial distribution of the biomarker following the application of deconvolution. For the case of the  $74\times$  objective, shown in Fig. 2.12B, a similar trend showing a narrowing of the Amide and biomarker distributions

Objective	Amide I Peak-to-edge Intensity			Biomarker Peak-to-edge Intensity		
	Orig. ( $\mu\text{m}$ )	Deconv. ( $\mu\text{m}$ )	% Difference	Orig. ( $\mu\text{m}$ )	Deconv. ( $\mu\text{m}$ )	% Difference
36 $\times$	7.8	6.4	18.0	10.0	7.7	23.0
74 $\times$	8.7	6.6	24.0	10.8	8.1	25.0

**Table 3.1:** Changes in Amide and Biomarker distribution for both objectives following deconvolution

is observed following deconvolution. In this case, the Amide peak-to-edge distance decreases from 8.7  $\mu\text{m}$  in the original data to 6.55  $\mu\text{m}$  in the deconvoluted data, corresponding to a change of 24.7%. Similarly, the peak-to-edge distance of the biomarker signature decreases from 10.8  $\mu\text{m}$  in the raw data to 8.1  $\mu\text{m}$  in the deconvoluted data, a change of 25%. These data give a direct demonstration of the impact of spatial oversampling on the effectiveness of deconvolution deconvolution; the decrease in the effective distribution of the biomarker and Amide signatures shows a greater improvement for the case of the 74 $\times$  oversampling than that of the 36 $\times$ . For example, the change in peak-to-edge distance of the Amide I and biomarker distributions following deconvolution are 18% and 23%, respectively, for the 36 $\times$  geometry. The same values for the 74 $\times$  geometry are 24% and 25%; as before, these data indicate that the application of deconvolution has a greater impact in the case of sufficiently oversampled data. The relatively similar improvements between the Amide I and biomarker signatures in the 74 $\times$  geometry upon deconvolution (24% and 25%) are consistent with the very similar wavelengths that the biomarker and Amide absorptions occur. With twice the pixel spacing of the 74 $\times$  geometry, the 36 $\times$  geometry has a measurement uncertainty that is 0.56  $\mu\text{m}$  greater than that of the 74 $\times$  geometry. This uncertainty, though small, can have a large impact on the assessment of

distances and overall image detail when performing microscopy at the diffraction limit. This uncertainty is likely accountable for the comparatively large discrepancy in the changes in the peak to edge distances of the Amide I and biomarker distributions following deconvolution (18% and 23%, respectively).

Next this measurement uncertainty is discussed in more detail. Consider first the measurement of the change in peak to edge distance in the Amide I distribution in the cell following deconvolution (decrease from  $7.8 \mu\text{m}$  to  $6.4 \mu\text{m}$  in the  $36\times$  data). A measurement error of  $1.1 \mu\text{m}$  in the peak to edge distances in the original and deconvoluted data will give a contribution of 4% toward the measurement error of the percent change in this distance, giving an error of  $18\pm 4\%$ . Similarly, the error in the peak to edge measurement of the biomarker in the  $36\times$  data is  $23\pm 4.1\%$ . The corresponding errors for the  $74\times$  data are  $24.7\pm 2.6\%$  and  $25\pm 2.1\%$  for the Amide and biomarker changes, respectively. These data show that spatial oversampling has an important, measurable effect on both overall spatial resolution as well as measurement error, and underline the critical importance of spatial oversampling when performing diffraction-limited spectromicroscopy.

### 3.6 Conclusions

The PSF, which defines the imaging characteristics of the IR microscope at IRENI, is determined by the geometric structure of the focusing Schwarzschild objective. This PSF has been determined throughout the mid-IR region for the 74× and 36× objectives used for the Bruker Hyperion 3000 microscope. Methods have been developed to deconvolute the known PSFs from measured datasets using a Fourier spectral filtering approach. The results of this method show the potential for enhanced spatial resolution and contrast in IR images, with the achievable resolution well below the conventional Rayleigh limit. The role of the factors contributing to the overall spatial resolution, namely the numerical aperture, oversampling and deconvolution are evaluated and discussed within the context of a biological specimen. In general, it is most desirable to perform imaging experiments with the highest possible numerical aperture and oversampling beyond the Stelzer criterion [9].

### 3.7 References

1. Li, Z.Q., et al., *Infrared imaging of the nanometer-thick accumulation layer in organic field-effect transistors*. Nano Letters, 2006. **6**(2): p. 224-228.
2. Heraud, P. and M.J. Tobin, *The emergence of biospectroscopy in stem cell research*. Stem Cell Research, 2009. **3**(1): p. 12-14.
3. German, M.J., et al., *Infrared spectroscopy with multivariate analysis potentially facilitates the segregation of different types of prostate cell*. Biophysical Journal, 2006. **90**(10): p. 3783-3795.
4. Holman, H.Y.N., et al., *Real-time molecular monitoring of chemical environment in obligate anaerobes during oxygen adaptive response*. Proceedings of the National Academy of Sciences of the United States of America, 2009. **106**(31): p. 12599-12604.
5. Fogarty, S.W., et al., *Sub-cellular spectrochemical imaging of isolated human corneal cells employing synchrotron radiation-based Fourier-transform infrared microspectroscopy*. Analyst, 2013. **138**(1): p. 240-248.
6. Holman, H.Y.N., et al., *Synchrotron IR Spectromicroscopy: Chemistry of Living Cells*. Analytical Chemistry, 2010. **82**(21): p. 8757-8765.
7. Nasse, M.J., et al., *High-resolution Fourier-transform infrared chemical imaging with multiple synchrotron beams*. Nature Methods, 2011. **8**(5): p. 413-U58.
8. Hecht, E., *Optics*. 2002: Addison-Wesley.
9. Stelzer, E.H.K., *Contrast, resolution, pixelation, dynamic range and signal-to-noise ratio: fundamental limits to resolution in fluorescence light microscopy*. Journal of Microscopy-Oxford, 1998. **189**: p. 15-24.
10. Carr, G.L., O. Chubar, and P. Dumas, *Multichannel Detection with a Synchrotron Light Source: Design and Potential*, in *Spectrochemical Analysis Using Infrared Multichannel Detectors*. 2007, Blackwell Publishing Ltd. p. 56-84.
11. Carr, G.L., *Resolution limits for infrared microspectroscopy explored with synchrotron radiation*. Review of Scientific Instruments, 2001. **72**(3): p. 1613-1619.



12. Mattson, E.C., et al., *Restoration and Spectral Recovery of Mid-Infrared Chemical Images*. Analytical Chemistry, 2012. **84**(14): p. 6173-6180.
13. Lasch, P. and D. Naumann, *Spatial resolution in infrared micro spectroscopic imaging of tissues*. Biochimica Et Biophysica Acta-Biomembranes, 2006. **1758**(7): p. 814-829.
14. *4. Structured Matrix Computations*, in *Deblurring Images*. p. 33-54.
15. Levenson, E., P. Lerch, and M.C. Martin, *Infrared imaging: Synchrotrons vs. arrays, resolution vs. speed*. Infrared Physics & Technology, 2006. **49**(1-2): p. 45-52.
16. Levenson, E., P. Lerch, and M.C. Martin, *Spatial resolution limits for synchrotron-based infrared spectromicroscopy*. Infrared Physics & Technology, 2008. **51**(5): p. 413-416.
17. Kastyak-Ibrahim, M.Z., et al., *Biochemical label-free tissue imaging with subcellular-resolution synchrotron FTIR with focal plane array detector*. Neuroimage, 2012. **60**(1): p. 376-383.
18. Clede, S., et al., *A rhenium tris-carbonyl derivative as a single core multimodal probe for imaging (SCoMPI) combining infrared and luminescent properties*. Chemical Communications, 2012. **48**(62): p. 7729-7731.
19. Nasse, M.J., et al., *Multi-beam synchrotron infrared chemical imaging with high spatial resolution: Beam line realization and first reports on image restoration*. Nuclear Instruments & Methods in Physics Research Section a-Accelerators Spectrometers Detectors and Associated Equipment, 2011. **649**(1): p. 172-176.

## Chapter 4: Probing the Structure and Composition of Graphene Oxide and Reduced Graphene Oxide

Graphene Oxide (GO) has been characterized using TEM, SAD, and IR Microspectroscopy. The average structure and predominant oxygen functional groups have been identified. Two methods of reduction, thermal reduction and chemical reduction via hydrazine monohydrate, have been studied by TEM, SAD, HRTEM, IR Microspectroscopy, and first-principles calculations. The composition and final structure of reduced GO (RGO) have found to be highly dependent on the reduction method. For the case of vacuum thermal reduction of GO on Mo TEM grids, experiments and calculations have shown that an unexpected ordering of the oxygen functional groups takes place, forming a quasi-hexagonal lattice of double-epoxide groups known as graphene monoxide (GMO). Reduction via hydrazine treatment followed by a mild thermal anneal in air does not result in formation of double-epoxide groups, but rather leaves only single epoxide groups and carbonyl groups, with minority carbonyl groups. The electronic properties of these materials are investigated using IR/Optical measurements, FET measurements, density functional theory (DFT) calculations. The optical properties of RGO multilayers and SnO<sub>2</sub> nanocrystal-intercalated RGO multilayer heterostructures are contrasted.

## 4.1 Introduction

Graphene is a single atomic layer of graphite, consisting of carbon atoms arranged in a honeycomb lattice. Since its first isolation in 2004[1-3], a number of astounding properties of graphene have been identified, particularly related to its electronic structure. Because of its symmetry and structure, the band structure of graphene near the Fermi level becomes nearly linear at the K-point of the Brillouin zone, implying that the charge carriers have effective mass equal to zero. Such electronic structure leads to extremely high electron mobility, in addition to many other exotic effects not seen in other materials. Because of its electronic properties and high surface-to-volume ratio, materials based on graphene have demonstrated tremendous potential for future electronic devices.

Large-scale production of graphene has, however, remained a problem. The first method used for isolation of graphene, mechanical exfoliation (*e.g.*, peeling off of graphite with scotch tape) is labor intensive and impractical for scaled-up production. Another method involves thermal decomposition of SiC (0001), where after heating to temperatures exceeding 1000° C, one or more layers of graphene are formed on top of a carbon buffer layer on the SiC surface. The largest drawback of this method is the extremely high cost of SiC substrate, which becomes cost-prohibitive of large scale production. Growth on metal substrates by chemical vapor deposition (CVD) by decomposition of hydrocarbons at high temperatures represents another growth modality that lies somewhere in the middle of the spectrum of impracticality and expense of large-scale production.[4-6] The last major option for large-scale production of graphene is through reduction of GO. The advantages of this approach are that GO can be produced cost-effectively in solution from graphite and easily dispersed in large quantities monolayer or multilayer form. Deposition from solution is also attractive from an applications standpoint.

Reduction of GO is also scalable; chemical reduction via hydrazine monohydrate can be performed directly on GO suspensions, and thermal reduction easily performed for GO mounted on a suitable substrate. Thermal reduction also has the advantage that the degree to which the GO is reduced may largely be tuned using predefined annealing temperatures and times. There are, however, many drawbacks to this approach. The first is that the precise structure of GO is something that is poorly defined and understood. The process of oxidation of graphite to form graphite oxide and subsequently GO produces a material that is disordered and non-stoichiometric, with numerous species of oxygen functional groups decorating the carbon basal planes. Second, RGO is never fully reduced by reduction treatments; some degree of residual oxidation, for better or worse, always remains. Lastly, reduction of GO introduces large quantities of defects into the lattice, as the desorption products during reduction are often CO and CO<sub>2</sub>. These defects can span the entire spectrum of lattice vacancies to extended  $sp^3$  regions to large holes in the film. As such, RGO differs dramatically from the desired graphene, yet comprises an entirely new classes of materials. The work in this chapter focuses on understanding the atomic structure and composition of GO and RGO, such that these properties may be correlated to synthesis and ideally be tailored as desired.

## 4.2 Characterization of Graphene Oxide

### 4.2.1 Sample Preparation

GO samples, obtained by our collaborators, were prepared in aqueous solution by a modified Hummers method [7]. Samples for TEM were prepared by dropping 1  $\mu\text{L}$  of the resulting suspension onto a lacey carbon coated Cu TEM grid and were dried in air overnight. Samples for IR spectroscopy were prepared by depositing approximately 10  $\mu\text{L}$  of GO solution onto IR transparent diamond windows and gold-coated microscope slides and were dried in air overnight. The same technique was used for deposition of chemically reduced GO samples.

### 4.2.2 Transmission Electron Microscopy

TEM and SAD was performed on the GO samples using a Hitachi H9000 NAR TEM operating at an accelerating voltage of 300 kV. BFTEM images of the film showed, not surprisingly, a uniform intensity distribution and were not of any use in subsequent analysis and are not shown here. SAD patterns of the sample were much more valuable for structural analysis. A representative SAD pattern of a GO sample is shown in Fig. 4.1. The pattern is collected at a 0.5 m camera length; at this camera length, two rings are present in the field of view corresponding to lattice spacings of 0.213 nm and 0.123 nm. For ease of interpretation, the hypothetical SAD pattern of a single crystal graphene samples is overlaid. Several conclusions can be immediately drawn by comparison of the measured GO SAD pattern with the hypothetical graphene pattern. First, the sample presents a ring pattern rather than a spot pattern; this type of a pattern generally indicates that the sample consists of randomly oriented grains (or sheets). Based on the planar nature of the sample, this ring pattern indicates that the sample has a multilayer morphology with no stacking order between the layers; *i.e.*, the sheets in the multilayer are randomly oriented.

Second, the two observed rings have the spacings of the [10-10] and [11-20] family of reflections in the graphene lattice. From this it can be concluded that the ordered component GO sample has, on average, the same lattice spacing as graphene. In addition, the lack of any spacings other than those corresponding to graphene indicates that the oxygen functional groups present in the GO sample do not form any superlattice ordering. Lastly, the pattern shows that the inner [10-10] reflection has a greater intensity than the outer [11-20] reflection. For the case of graphene and graphite, it was shown [8] that for samples with ordered stacking, any sample thicker than one monolayer (*e.g.*, one graphene bilayer and thicker) will show greater diffracted intensity in the [11-20]-type reflections than in the [10-10]-type reflections. The fact that the latter reflections are brighter in this pattern indicates that the sheets comprising the multilayered sample are in fact graphene monolayers, rather than few-layer graphene/graphite with ordered stacking. Overall, the conclusions drawn from the SAD analysis presented here are in good agreement with previously published diffraction data on GO. [9]

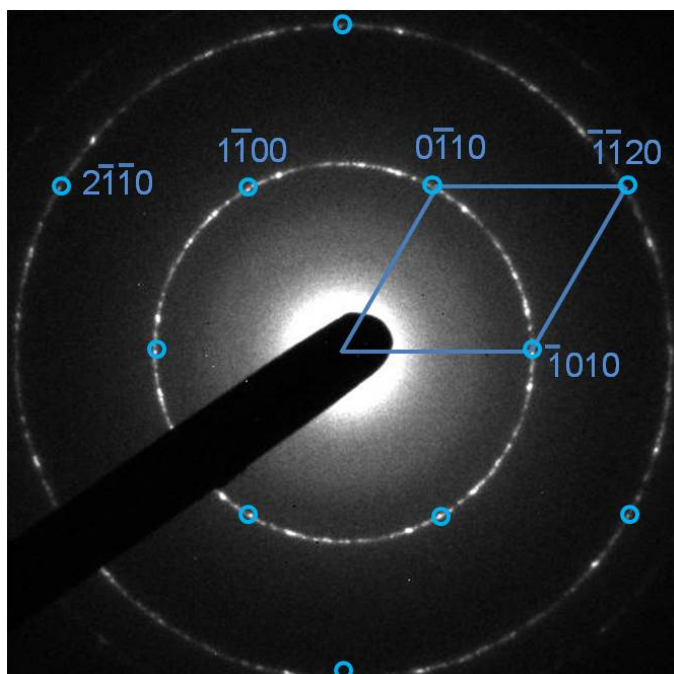


**Fig. 4.1** SAD pattern of unreduced GO overlaid with a hypothetical single crystal graphene SAD pattern (blue).

#### 4.2.2 IR Microspectroscopy

While many studies have performed IR measurements on GO, the overall band assignments are extremely complicated and remain controversial due to the many types of oxygen functional groups in GO. As an attempt of deriving some further structural information about our samples and identifying which functional groups are present prior to reduction, IR absorption studies of GO samples were performed using the IRENI beamline at SRC using two different experimental geometries. Normal incidence transmission (NIT) measurements were performed on GO samples mounted on diamond windows and grazing incidence reflectance (GIR) measurements were performed with the films mounted onto the gold-coated slides. The rationale for this approach was to try to extract some orientation about the oxygen groups in the samples by controlling the direction of the electric field of the probe. While the NIT geometry has field

components both in-plane and out-of-plane, in the GIR experiment the components are strictly normal to the surface. The IR absorption spectra of GO as determined from these two experimental geometries are shown in Fig. 4.2. Upon comparison of the spectra, several similarities and differences are immediately obvious. First, in the OH stretching region (3000-3600  $\text{cm}^{-1}$ ), the NIT absorption spectrum has absorption bands at 3250, 3360, and 3520  $\text{cm}^{-1}$ , whereas the GIR absorption spectrum has bands at 3300, 3420, and 3570  $\text{cm}^{-1}$ . This spectral region comprises absorptions due to intercalated water and various species of hydroxyl and carboxylic groups. Due to the complexity of the possible bonding sites and the additional complication of hydrogen bonding, a precise interpretation for the bands in this region is elusive; however, bands below 1800  $\text{cm}^{-1}$  are more readily assignable. First, the band observed at 1740  $\text{cm}^{-1}$  in both the NIT and GIR spectra is assigned to the carbonyl C=O bond stretching. The



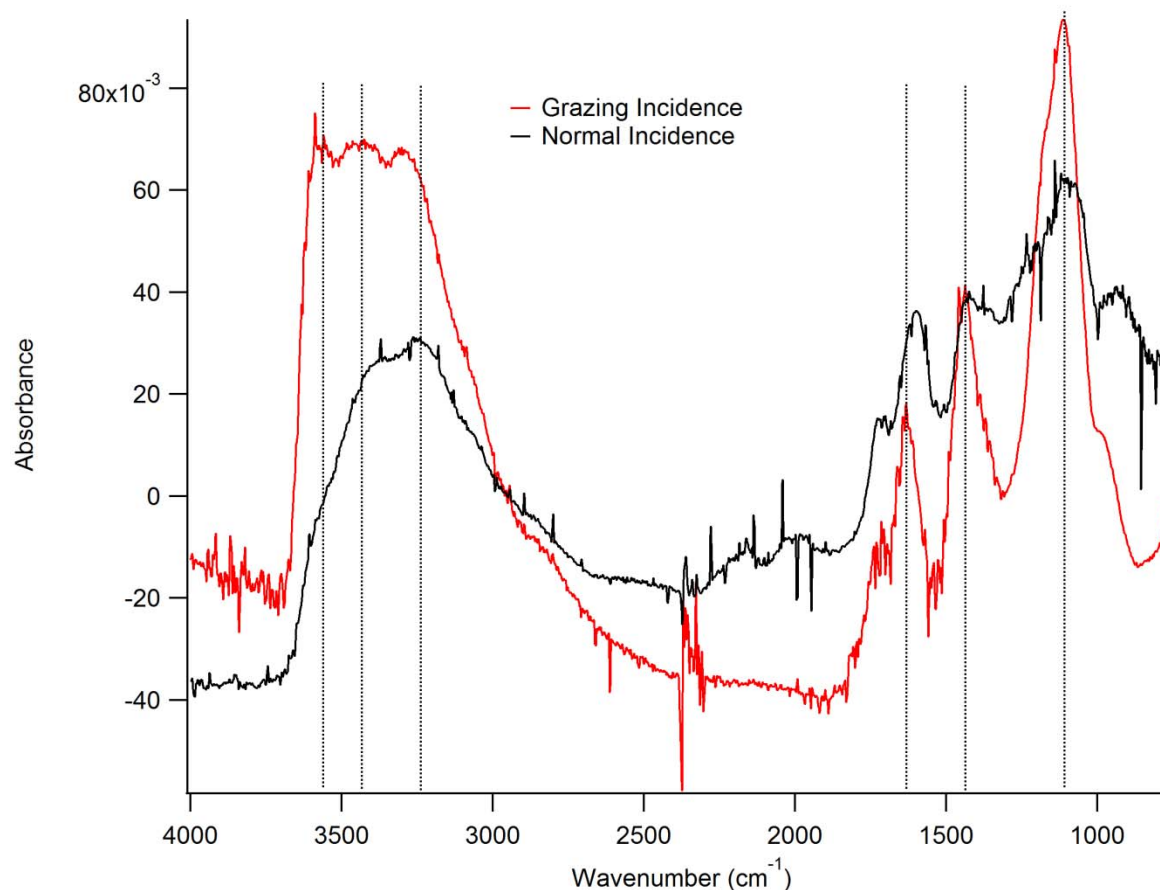


**Fig. 4.2:** Absorbance spectra of unreduced GO as determined from the NIT (black) and GIR (red) geometries. In the NIT spectrum, the reference used is the clean diamond window, and in the GIR geometry the reference is the clean gold.

clear activity of this band in both experimental geometries suggests that the C=O bond has components both parallel and perpendicular to the carbon basal planes. In the normal incidence geometry, the next band is observed is  $1600\text{ cm}^{-1}$ ; this band corresponds to the C=C stretching vibrations of the underlying carbon skeleton. The next band observed is located at  $1640\text{ cm}^{-1}$  and corresponds to the OH bending mode of the intercalated water molecules. The enhanced absorption of this mode in the GIR geometry suggests an alignment of the intercalated water molecules with their molecular axes perpendicular to the carbon planes. A band at between  $1300\text{-}1500\text{ cm}^{-1}$  is active in both the normal and grazing incidence experimental geometries and appears to be a superposition of several bands. Three specific vibrations are likely to contribute

in this spectral region; first, absorption due to the C=C bond stretching of the C atoms hosting the oxygen atom in the epoxide group likely gives a contribution. The presence of the COC bond in this case is responsible for the redshifted frequency, and the IR activity in the GIR geometry arises because expansion/compression of the C=C bonds causes an oscillation of the oxygen atom perpendicular to the basal planes. The second contribution likely comes from the C-O-H angle bending of the adsorbed hydroxyl groups and COOH bending of carboxylic groups. Third, the carboxylic C=O stretches are likely to also fall in this region. Finally, a band centered at  $1100\text{ cm}^{-1}$  is observed in both geometries and also is clearly a superposition. The first mode to give a contribution in this region is the adsorbate/substrate bond stretching of the hydroxyl groups. The second mode would be the asymmetric and symmetric stretching vibrations of the epoxide groups, each of which will give a contribution both normal and parallel to the carbon basal planes, as discussed in more detail in section 4.4. The overall bonding scheme of the majority functional groups in GO derived from the combined experiments and theoretical calculations is shown in Fig. 4.3.

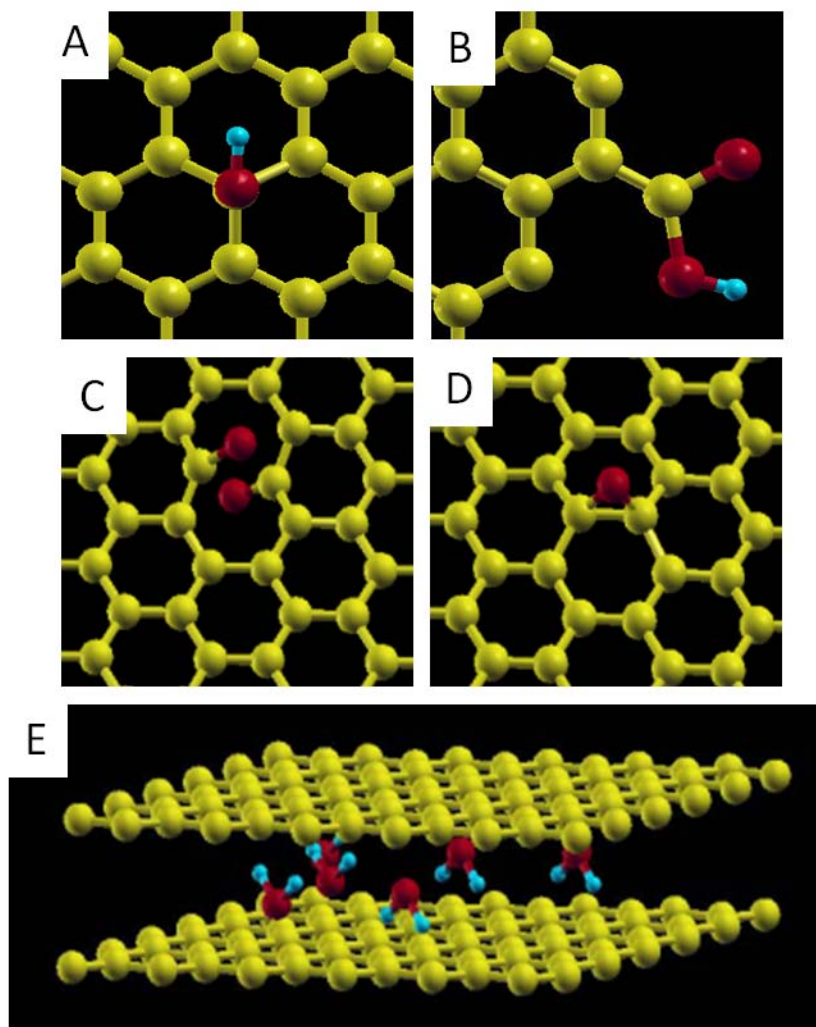


**Fig. 4.3:** Representative structural models of the primary oxygen functional groups in GO. A) Hydroxyl group. B) Carboxyl group C) Carbonyl pair at a defect D) Epoxide group E) Intercalated water.

### **4.3 Vacuum Thermal Reduction of GO: Possible Evidence of Nanocrystalline graphene monoxide**

Graphene has demonstrated great potential for novel electronic technologies;[10-12] however, many emerging applications require atomically thin films with a substantial band gap. One route toward the manipulation of the electronic properties of graphene-based materials is through chemical modification. Chemically-modified graphene or graphene oxide (GO) [13-17] has already found various applications such as supercapacitors,[18] sensors[19, 20] and flexible transparent conductive electrodes. [21] However, GO is a non-stoichiometric, partially disordered material[9, 22] with poor electronic properties. While studies have indicated that on average the hexagonal lattice constant of graphene is preserved in GO,[22, 23] amorphous regions coexist with the crystalline carbon lattice, with a number of oxygen functional groups, such as hydroxyl, carboxyl, carbonyl, epoxide, and intercalated water,[23-25] bonded with no long range order.[22] These disordered qualities of GO make it an unappealing candidate for application in modern electronics. Thus, GO is most commonly modified by various chemical<sup>[15]</sup> and thermal reduction treatments[23-25] with the goal of removing oxygen functional groups from GO and producing graphene. While the quality of the resulting materials can in general be improved via chemical vapor deposition (CVD),[4] these treatments generally fail to form graphene and produce yet another nonstoichiometric partially reduced GO where oxygen remains disordered.

Here it is proposed that a stoichiometric carbon oxide could be formed by vacuum annealing of multilayered GO, a method commonly used to make thermally reduced graphene oxide (TRGO). Studies of TRGO, however, have primarily focused on reduction of monolayer or few layer systems,[23-25] with little attention paid to thermal reduction of systems with a

large number of layers. There are also no reports of the use of catalysts to aid the thermal reduction process. While previous reports[25] have shown that the chemistry of intercalated water in multilayer GO is significant, no investigations have reported the effect of vacuum annealing a large number of GO layers to high temperature. One interpretation of the data in this chapter is that the multilayer structure of GO thin films with intercalated water results in a previously unobserved atomic structure and morphology when annealed in vacuum: a two-dimensional phase segregation produces graphitic regions with little or no oxidation that coexist with oxidized regions with an unusually high oxygen content. This work combines *in situ* selected area electron diffraction (SAD) studies with synchrotron-based infrared microspectroscopy (IRMS) and density functional theory (DFT) calculations to attempt to understand the reduction process. From DFT modeling guided by experimentally-derived structural data, a structure called Graphene Monoxide (GMO) was derived in an attempt to understand the SAD and IR data. GMO consists of a quasi-hexagonal unit cell with two carbon atoms bridged by a double-epoxide pair. GMO is of interest because of its appealing transport properties. Additional theoretical work on GMO [26] suggests that its electronic structure could potentially be tuned over a wide range, motivating work on understanding the synthesis of the proposed GMO.

#### 4.3.1 Methods

GO suspensions were synthesized using a modified Hummers method, as described in previous work [7]. GO multilayer samples were prepared by drop-casting 2  $\mu$ l of the resulting suspension onto bare 200 mesh Mo TEM grids. The individual GO monolayers became stacked after water evaporation, forming self-supporting multilayer structures that span the grid holes.

Monolayer GO samples were prepared by drop-casting diluted suspensions into Si TEM grids with an ultrathin Si<sub>3</sub>N<sub>4</sub> membrane.

TEM studies were performed *in situ* using a Gatan tantalum-cup heating holder inside a Hitachi H9000NAR TEM operating at an accelerating voltage of 300 keV. The column pressure of the TEM was maintained at approximately 10<sup>-7</sup> torr. The TEM is equipped with a Gatan Orius SC CCD, which was used to record diffraction movies with 1 frame (1s exposure time) per 4 seconds. An SAD pattern of the GO film was recorded during the vacuum annealing process, allowing structure to be correlated with temperature that was detected with a thermocouple. An SAD movie (see Supplementary Information) was recorded at the same region of the sample and the electron beam intensity was fixed throughout the experiment. Importantly, SAED patterns were recorded both during and after annealing of the sample, indicating that the structural changes observed during the experiment were stable upon cooling the sample to room temperature. A radially averaged profile of diffraction intensity (such as displayed in the insets of Fig. 4.4) was extracted from each frame of the SAD movie corresponding to the temperature of the sample, and subsequently combined as Fig. 3.4B, thus indicating the evolution of the reciprocal space positions (y-axis) of the diffracted electrons with increasing temperature (x-axis). During annealing and after being cooled, the samples were studied using SAD, CBED, HRTEM, and bright-field TEM. In other *in situ* experiments, a CBED pattern, taken with a 17 nm convergent beam electron probe, was examined as the samples were reduced.

After TEM analysis, IRMS was performed on the same TRGO samples. IR measurements were performed at the Synchrotron Radiation Center (SRC, Stoughton, WI) at the IRENI beamline [27]. The films as prepared on TEM grids were measured in a Bruker Hyperion 3000 IR Microscope coupled to a synchrotron source. Normal incidence transmittance and

reflectance measurements were performed on the *free standing* films supported on TEM grids. By repeating the experiments with objectives of different numerical aperture, measurement effects resulting from convergence of the synchrotron beam being focused by the Schwarzschild focusing optics were ruled out. The films were subsequently removed from the grids and placed on microscope slides with an IR reflective coating (Kevelly Technologies). This enabled the films to be measured at a grazing incidence using a Bruker Grazing Angle IR microscope objective lens. GI measurements were performed with an IR polarizer to emphasize only radiation polarized parallel to the plane of incidence.

The density functional calculations were carried out using the all-electron Full-potential Linearized Augmented Plane Wave method, as implemented in flair. [28] The GMO and graphene calculations used the generalized gradient approximation (GGA) of Perdew, Burke, and Ernzerhof for exchange-correlation; sphere radii of  $1.2 a_B$  for both C and O; plane wave basis and charge/potential representation cutoffs of 275 and 2700 eV, respectively;  $12 \times 12 \times 2$  to  $36 \times 36 \times 2$  k-point sets; and vacuum regions of 15 Å. The internal coordinates were relaxed to a force criterion of  $10^{-4}$  eV/Å. Other C:O ratios and configurations were modeled starting from  $2 \times 2$  hexagonal cells with 8 carbon atoms.

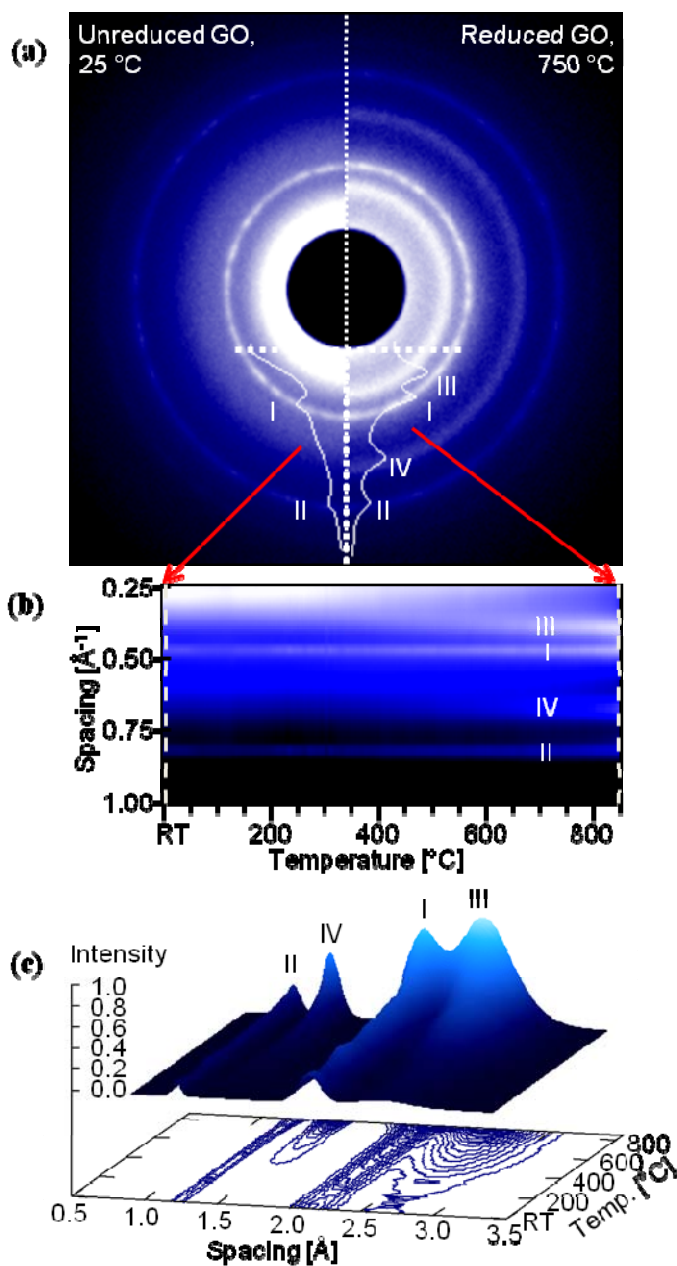
#### 4.3.2 Results and Discussion

Figure 4.4A compares SAD patterns of a multilayer GO film before (left) and during (right) *in situ* vacuum annealing, at  $750^\circ$  C. Before annealing, the primary features evident in Figure 3.4A are the diffraction rings (labeled as I and II) from spacings of 0.213 nm and 0.123 nm, respectively, corresponding to the [100]- and [110]-type reflections of graphene. A ring pattern is observed rather than a spot pattern due to the fact that the sample consists of a large

number of randomly oriented layers. Analysis of the relative intensities show that the [100] type reflections produce a greater diffracted intensity than the [110] reflections, indicating that the layers are monolayers with disordered stacking, as opposed to few-layer Bernal-stacked graphite oxide.[9] Moreover, SAD patterns (Fig. 4.5, Table 4.1) recorded at higher scattering angles (i.e., smaller lattice spacing), clearly indicate weaker higher order rings also consistent with crystalline graphene. In addition, SAD patterns recorded before annealing (Fig. 4.4A, left) show two broad, seemingly amorphous rings centered at about 0.27 and 0.52  $\text{\AA}^{-1}$  (0.370 nm and 0.185 nm in real space). The amorphous rings can be attributed to first- and second-order reflections from nearest-neighbor disordered species. While annealing the multilayer GO film, two prominent rings (labeled as III and IV) develop corresponding to spacings of about 0.260 nm and 0.152 nm, respectively, while the graphene rings (I and II) remain largely unchanged (Fig. 4.4A) in reciprocal-space position. Thus the SAD data demonstrates that a new crystalline phase develops upon annealing. A visualization of the complete temperature-dependent evolution of SAD patterns from the GO film annealing (extracted from a real time movie; see Supplementary movie) is shown in Fig. 4.4B. Diffraction rings in a conventional SAD pattern (Fig. 4.4A) appear as horizontal lines in the representation of Fig. 4.4B. From Fig. 4.4B, it is evident that the graphene rings, I and II, grow in intensity as the sample is annealed, but that they remain essentially fixed in reciprocal space position. The new crystalline phase characterized by peaks III and IV, however, shows a qualitatively different behavior with temperature. The broad amorphous peak (associated with the disordered functional groups) initially centered at about 0.27  $\text{\AA}^{-1}$  appears to split into two bands, one of which evolves in position and intensity into the crystalline reflection of the new phase labeled as III. The remaining amorphous contributions shift closer to the reciprocal space origin and suffer a dramatic reduction in intensity, most



evident in the 300-500 °C temperature range, with similar behavior observed in band IV. This structural ordering does not produce visible features in bright field TEM images, indicating that the multilayer morphology is preserved and that the new phase has 2D structure. The evolution of the SAD patterns was observed across the entire sample and was constant upon cooling the sample, thus ruling out effects related to sample drift. These observations were reproducible in numerous experiments.



**Figure 4.4.** Evolution of Electron Diffraction patterns with temperature. (a) SAD patterns of G-O sample before (left) and after (right) vacuum reduction anneal. Overlay is the radial average of intensity showing peaks at ring positions I and II before annealing, and the addition of peaks III and IV after annealing. (b) Radially averaged profiles from SAD patterns as a function of temperature. Profiles displayed as overlay in top panel are equivalent to profiles along the corresponding dashed lines (arrowed) in middle panel of figure. Peaks III and IV, evolve continuously from the broad background, most notably in the temperature range from 500 °C to 700 °C. (c) Temperature-dependent evolution of unwrapped SAD patterns. As temperature is increased, new peaks appear with indicated spacings and grow in intensity. Peaks I and II are attributed to graphene regions of the sample, while peaks III and IV are attributed to the new phase. From [29].

To quantify the temperature evolution of the diffraction data, individual profiles of Fig. 4.4B over the complete temperature range were fit with a set of Gaussians. Figure 4.4C shows the fitting results for the crystalline diffraction bands I-IV without the background and amorphous contribution where several key features of the structural evolution of the GO film are observed. First, the integrated intensity of the graphene peaks I and II, related to the volume fraction of scattering material, more than doubles. Similarly, the integrated intensity of peaks III and IV (new phase) grows rapidly from zero in the starting material to more than 1.5 times that of the graphene phase at the end of the annealing. These integrated intensities may be considered in terms of qualitative increases and decreases in quantity of material, as an absolute determination of the volume fraction would require knowledge of the intensity contained in the transmitted beam, unobtainable due to the beam stop. Second, from the results shown in Fig. 4.4C, the ratio of peak positions for the graphene phase (peaks I and II) maintains the value  $\sqrt{3}$  (with absolute deviation due to thermal expansion less than 0.1%), as would be expected for an ideal hexagonal structure. The thermal evolution of the new peaks III and IV, while nearly  $\sqrt{3}$  in ratio, deviate 1-2% (depending on temperature) from the ideal hexagonal crystalline symmetry. This deviation from hexagonal symmetry, too large to be associated with thermal expansion, clearly indicates that the crystalline phase associated with the diffraction rings III and IV is centered rectangular, albeit nearly hexagonal (quasi-hexagonal), and is distinct from the graphene phase characterized by diffraction rings I and II.

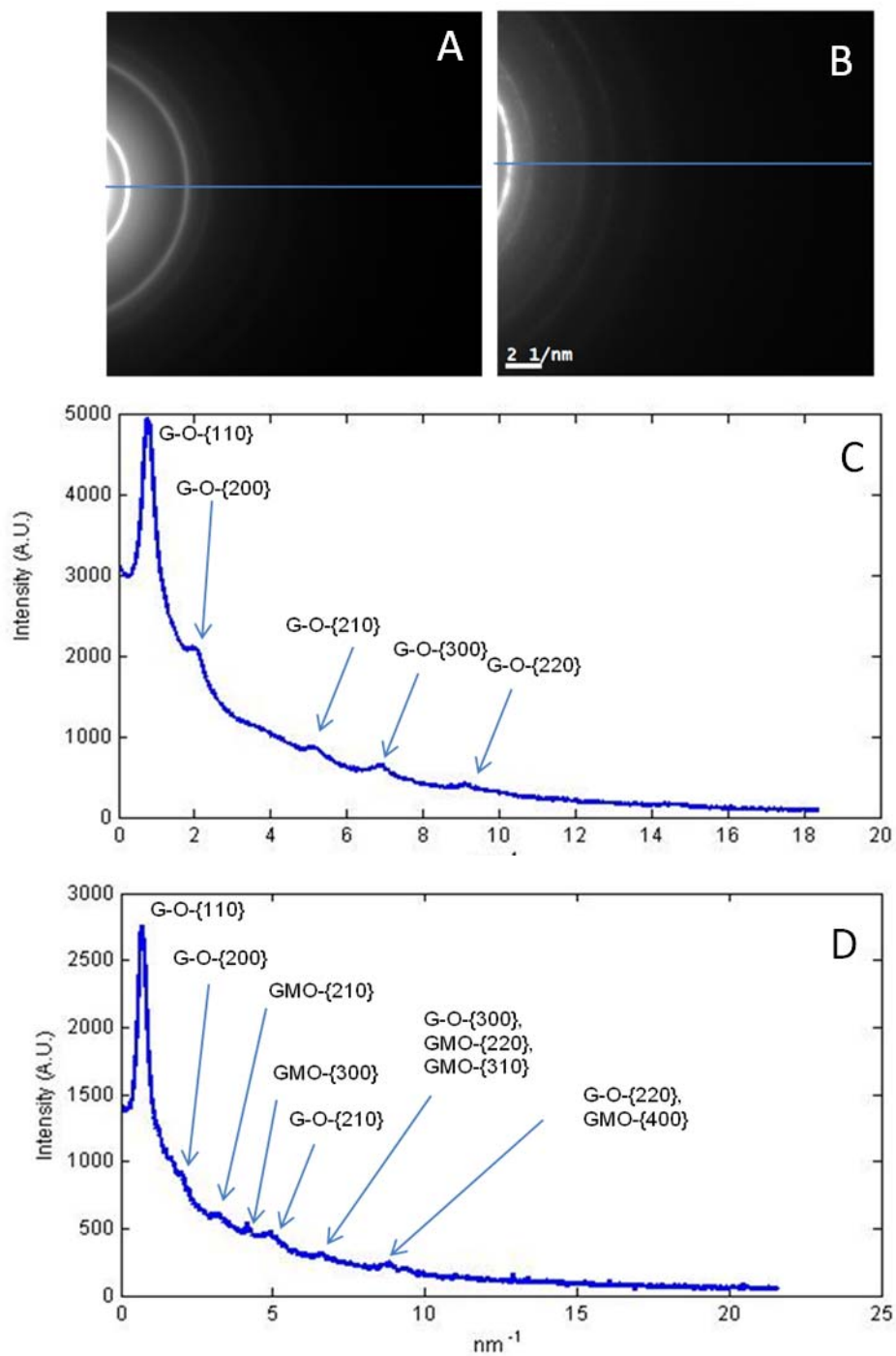


**Fig. 4.5:** Higher order SAD reflections in GO (A) and TRGO (B). Line profiles through the patterns in A) and B) are shown in C) and D), respectively. [29]

Measured spacings for G-O before annealing [nm]	Measured Spacings after annealing [nm]
	0.26
0.213	0.213
	0.152
0.123	0.123
0.107	0.107
	0.095
	0.085
0.081	0.081
0.071	.071
0.065	.062
0.059	.059

**Table 4.1:** Measured interplanar spacings of GO and TRGO derived from SAD patterns in Fig. 3.5. [29]

To elucidate the *in situ* SAD observations, the geometrical bonding of the films before and after annealing was investigated by IRMS. Using two experimental geometries with-normal incidence (NI) transmission and grazing incidence (GI) reflectance – vibrational modes with dynamic dipole moments predominantly parallel or perpendicular to the basal plane of the films, respectively, are emphasized. Figure 4.6A-D shows IR absorbance of the samples before and after annealing as measured in NI and GI. The features in the NI spectrum of GO (Fig 4.6A) indicate the presence of oxygen functional groups including hydroxyl ( $3,300\text{ cm}^{-1}$ ), carbonyl

(1,708  $\text{cm}^{-1}$ ), carboxyl (1,425  $\text{cm}^{-1}$ ), epoxide (1,245  $\text{cm}^{-1}$ , 900  $\text{cm}^{-1}$ ), and alkoxy (1,080  $\text{cm}^{-1}$ ), consistent with existing literature.[30] The feature at 1,580  $\text{cm}^{-1}$  is assigned to the C=C stretch of the underlying carbon lattice which is activated in GO due to oxygen functional groups and defects. The GIR (Fig. 4.6C) absorbance spectrum of GO also indicates the presence of O-H from intercalated water (stretching modes at 3,300-3,600  $\text{cm}^{-1}$ , bending mode at 1,645  $\text{cm}^{-1}$ ), as well as carbonyl (1,708  $\text{cm}^{-1}$ ) and hydroxyl (C-OH stretching at 1,070  $\text{cm}^{-1}$ ). Importantly, two peaks were observed at  $\sim 900$  and 960  $\text{cm}^{-1}$ , and at the time of publication were assigned to C-O-C bending modes.

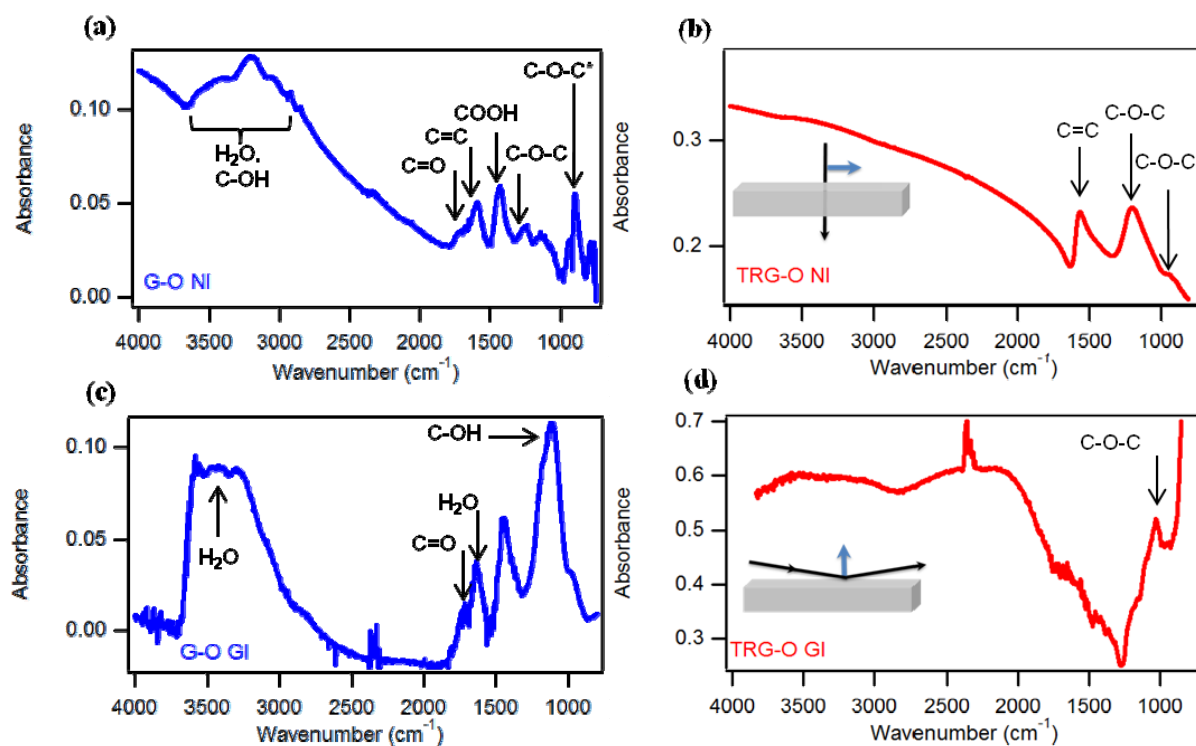


**Figure 4.6.** IRMS of GO and TRGO. Normal Incidence (NI) transmission probes vibrations with dipole moments predominantly parallel to the film's basal plane as the E-field vector (blue arrow) is within this plane, while GI probes those with a dipole moment perpendicular to the basal plane. (a) NI IR absorbance of unreduced GO with contributing functional groups assigned to spectral regions. (b) NI IR absorbance spectrum of TRGO samples with functional groups assigned. (c) GI IR absorbance spectrum of GO. (d) GI IR absorbance spectrum of TRGO. [29]

After annealing, many of the oxygen functionalities including carbonyl, carboxyl, intercalated water, and hydroxyl are no longer present in the NIT spectrum of TRGO (Fig. 4.6B).

The C=C stretching mode softens in frequency and evolves into an asymmetric Fano[31] lineshape, indicating a continuum of electronic transitions with symmetries parallel to the C=C vibrational excitation spanning at least 0.18-0.21 eV. The C=C stretching mode, which is inactive in pure graphene and graphite due to symmetry considerations, is activated due to defects and neighboring oxidized regions. The C-O-C stretching mode, whose overall intensity increases dramatically, is softened by about  $25\text{ cm}^{-1}$ . Analysis of this mode from the same position of the same sample before and after annealing showed that the integrated intensity of the C-O-C asymmetric stretching band increased by a factor of approximately 20 after the annealing process. The doublet assigned to C-O-C bending has diminished intensity and only appears as a single peak in the annealed spectrum. GI IR absorption spectra from samples after annealing are also shown in Fig. 4.6D, where many oxygen features are missing, including notably, those associated with water. While the C-O-C mode at  $1,205\text{ cm}^{-1}$  is very weakly active in this geometry, a prominent new mode is seen at  $1,050\text{ cm}^{-1}$ . Thus, we conclude that the nanocrystalline phase contains structures that give rise to only two distinct vibrational modes involving C-O displacements that were active in the NI geometry, and one C-O mode that was active in the GI geometry.

The electron diffraction data presented in Fig 4.4 show that the vacuum thermal reduction of multilayered GO results in a two-phase nanoscale system containing regions of graphene and a new (as yet undetermined) crystalline phase. Phase segregation has been theoretically predicted [32] and experimentally observed in reduced graphene oxide but with little information provided about the structure. [33] In reference, a C:O ratio of 2:1 was observed through XPS measurements, with slowly varying stoichiometry across the sample. An extensive search of possible unit cells for C-O-C groups bonded to a primarily unperturbed graphene lattice

concluded that no configuration of epoxide groups attached to such a graphene lattice produces SAD reflections in agreement with those measured. Moreover, careful examination of high camera length diffraction patterns from the carbon-oxide phase, which probes reciprocal spacings closer to the origin, indicated that the 0.260 nm spacing is the lowest order reflection of the crystalline unit cell, corresponding to a unit cell about 20% larger than graphene. Therefore, the electron diffraction data indicate a quasi-hexagonal unit cell. This was further confirmed by closely examining the higher order SAD reflections from Fig. 4.5. To verify the proposed symmetry and periodicity of the unit cell, all of the interplanar spacings for a quasi-hexagonal structure were calculated, assuming the spacing of 0.26 nm as the lowest order reflection. The results, shown in Table 4.2, show that measured spacings of the TRGO material are consistent with the quasi-hexagonal unit cell.

GMO Index	GO/G Index	GO measured spacings, nm	Quasi-hexagonal model spacings, nm
[100]			.256
[1-10]			.273
	[100]	.213	
[2-10]			.154
[110]			.145
[200]	[110]	.123	.128
	[200]	0.1065	
[210]			0.095
[300]			0.085
	[210]	0.081	
[220]	[300]	0.071	0.073
[310]			0.070
[400]	[220]	0.062	0.064

**Table 4.2.** Comparison of measured GO spacings, known graphene spacings and quasi-hexagonal model interplanar spacings. [29]



DFT calculations demonstrated that adding oxygen to graphene is energetically favorable, leading to the proposed quasi-hexagonal double-epoxide structure (Fig. 4.7; C:O=1:1) with a binding energy of 4.36 eV/O. This is significantly higher than previously reported GO configurations with high epoxide coverage, [34] where ordered epoxide groups in a C<sub>2</sub>O structure yield a binding energy of 3.73 eV/O in our calculation. This structure has some similarities to models proposed in previous calculations. [35] The calculated lattice parameters of this centered-rectangular (quasi-hexagonal) structure are given in Fig. 4.7B. Compared with graphene, the magnitude of the primitive lattice vectors increases to 3.09 Å (from 2.46 Å) and the angle between them is 124° versus the 120° of an ideal hexagonal lattice. Although this structure no longer has the 3-fold symmetry of the graphene lattice, there are three sets of mirror planes, corresponding to D<sub>2h</sub> symmetry, which implies that there are three IR-active vibrational modes (Fig. 4.6C); two C-O-C modes are active in the NI geometry and one C-O-C mode in GI, consistent with the number of modes observed experimentally. The correlation between the atomic structure and normal modes of all models considered was performed as follows: The number of allowed IR vibrational modes was determined by carrying out a factor group analysis of the unit cell. After identifying the symmetry of each proposed model, the number of modes belonging to each irreducible representation was determined using the equation:

$$n^{(\gamma)} = \frac{1}{g} \sum_j \chi_j^{(\gamma)*} \chi_j \quad (4.1)$$

where  $\chi_j$  is the character for a group operation  $j$ ,  $\chi_j^{(\gamma)}$  is the character of the irreducible representation for group operation  $j$ , and  $g$  is the order of the group. The usual selection rules for infrared absorption and the Raman effect were then applied to the resulting representation, after subtracting off the acoustic modes. The normal modes of vibration corresponding to the IR active irreducible representations were then calculated. This allowed the component of the

dipole moment vector associated with each vibration to be determined, and thus its activity in normal or grazing incidence geometries established. The GMO regions, with a  $D_{2h}$  symmetry, have IR active modes represented by  $\Gamma=B_{1u}+B_{2u}+B_{3u}$ . As the components of the dipole moment vector, which transform in the same way as the translation vector components within the basal plane ( $T_x$  and  $T_z$ ), belong to  $B_{1u}$  and  $B_{3u}$ , we expect two IR active modes in the NI geometry. The  $T_y$  component belongs to  $B_{2u}$ , and we thus expect that only this mode will be active in the GI geometry. This analysis was in agreement with the measured spectra (Fig. 4.6). The normal modes of vibration of GMO are shown in Fig. 4.7C. Figs. 4.7A-B shows the undistorted molecular structure of the repeat GMO unit as viewed from different perspectives, while the atomic displacements corresponding to each normal mode are shown in Figs. 4.7C. The displacement of the oxygen and carbon atoms produces a dynamic dipole moment within the basal planes for the vibrations  $B_{1u}$  and  $B_{3u}$ , and normal to the basal planes for  $B_{2u}$ , giving rise to the observed spectral features in different experimental geometries.

Various configurations of C-O-C groups were considered; however, only the double-epoxide structure produces the correct number of allowed vibrational modes in each experimental geometry. Thus, the structure suggested by DFT calculation is consistent with the experimental diffraction and infrared spectroscopic data. The O to C ratio in the oxidized regions is significantly higher than previously reported values in unreduced multilayer G-O where the average chemical compositions vary from  $C_1O_{0.17}H_{0.08}$  to  $C_1O_{0.49}H_{0.2}$  depending on the oxidation time and methods.[36, 37] As graphene-like islands spread across the G-O film,[32] the local oxidation level has been reported to be as high as  $C_1O_{0.5}$  to  $C_1O_{0.75}H_{0.75}$  for monolayer GO.[34] Here, the higher ratio of 1:1 can be realized by converting oxygen species present initially in GO to the double-epoxide structure. Initially, there are not enough epoxide or

cyclic ether-type oxygen groups in GO to create GMO. However, conversion of the remaining oxygen-containing functional groups to a C-O-C configuration could provide a viable path. The spectroscopic evidence that suggests this transformation is the changes of the integrated intensities of all the oxygen-containing functional groups before and after annealing, including the absence of the H<sub>2</sub>O, OH, and carbonyl absorption bands and the increase in the C-O-C asymmetric stretching peak (Fig. 4.6B) after annealing. Meanwhile, experimentally we observe an increase in diffracted intensity of the original GO/graphene reflections, which indicates a concurrent increase in the crystalline areas of graphene-like islands that are oxygen-free regions. The increase in stoichiometry is only localized to small crystalline regions of GMO, and that the overall oxygen content of the entire sample has not increased. The formation of the new composite nanomaterial is likely a consequence of the large number of layers in the starting material and the diffusion-limited nature of the reduction process.

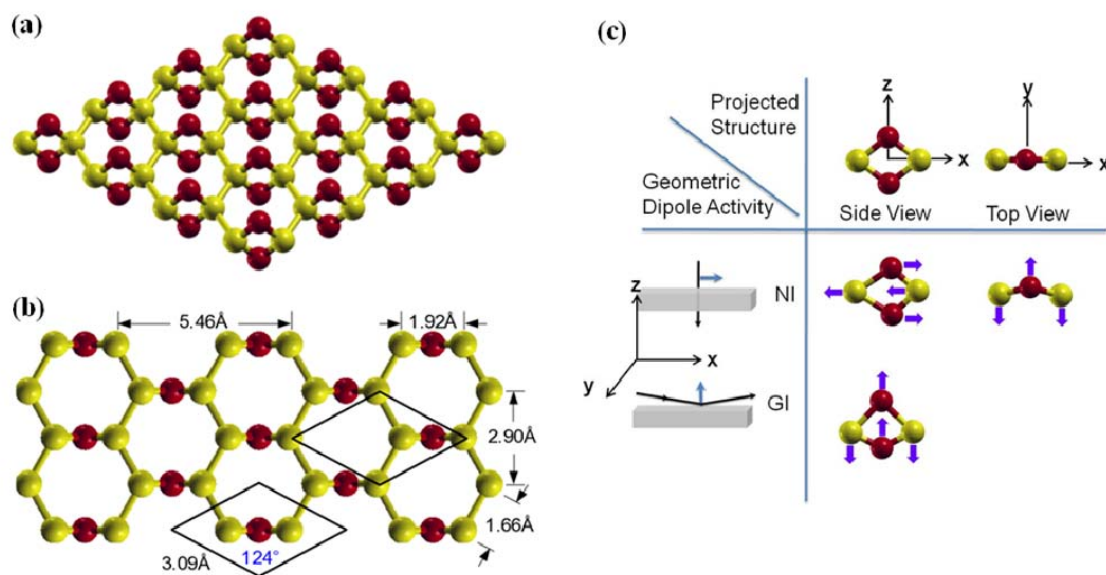


**Figure 4.7.** Proposed GMO structure. (A) Perspective view of 4x4 unit cells. Carbon (oxygen) atoms are yellow (red). (B) Top view of GMO with the unit cell and various calculated structural parameters. (C) Schematic of the IR active vibrational modes for this model. Two modes produce a dipole moment within the carbon basal planes, and one mode produces a dipole moment perpendicular to the basal planes, and are thus active in the NI and GI geometry, respectively. [29]

The proposed structural model was further investigated using HRTEM. While the majority of the sample was much too thick to obtain atomic resolution images, we were able to locate a very thin region where the TRGO sheets tore during annealing that enabled imaging of the lattice planes of individual GMO domains. HRTEM images of such a region are shown in Fig. 4.8. The HRTEM image in Fig. 4.8A shows that lattice fringes from individual GMO domains can be resolved in thin regions of the sample edges. Fig. 4.8B shows an enlargement of a single GMO domain from the HRTEM image in Fig. 4.7A, with the numerical diffractogram from the same region shown in Fig. 4.8C. In Fig. 4.8B, high frequency components of the image beyond the lattice resolution of the microscope have been filtered out, as this data contains no real information. In the diffractogram of this region, two reflections are observed with measured

spacings of .25 nm and .254 nm, corresponding to both the [100] and [010]-type reflections of GMO. Measurement of the angle between then sets of lattice fringes yields an angle  $55^\circ$ . This is in excellent agreement with DFT predictions from the relaxed GMO model structure which suggests an angle of  $56^\circ$  between the GMO [100] and [010] planes. These results further support the structural conclusions based on all SAD, IRMS, and DFT analyses.

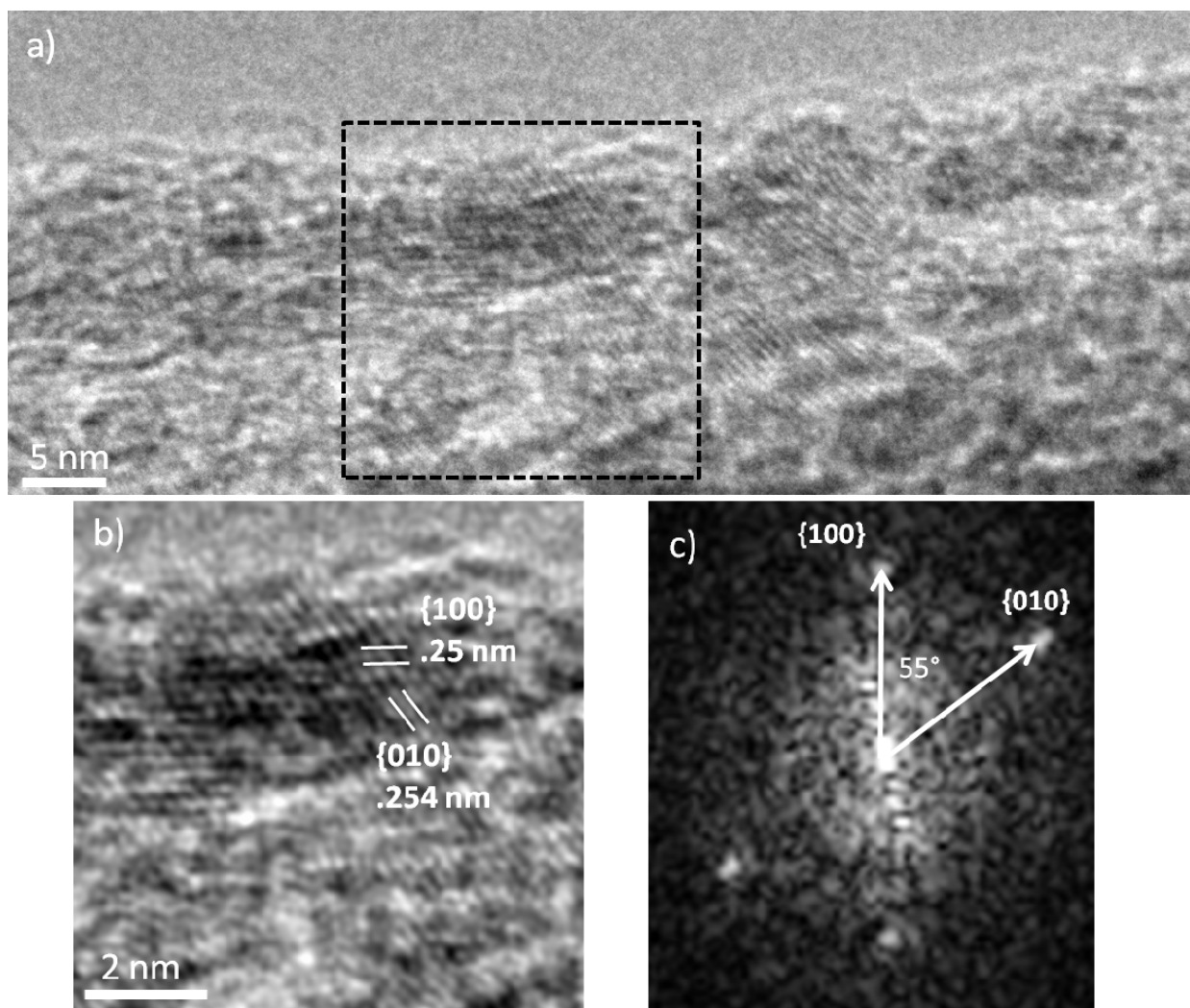


**Figure 4.8.** HRTEM images of a TRGO film. (a) HRTEM image of a thin region of the sample (b) Enlargement of the marked region from the image in (a) illustrating a GMO domain with denoted lattice spacings. (High frequency noise has been filtered out as described in the main text). (c) Numerical

diffractogram from the indicated region in (a), showing two prominent reflections with measured spacings in agreement with the GMO [100] and [010]-type reflections. The measured angle between the spots is  $55^\circ$ . [29]

The new GMO is predicted to be a semiconductor, with a direct band gap of  $\sim 0.9$  eV at the X point (Fig. 4.9). The size (and existence) of the gap is dependent on the distortion of the lattice away from the ideal hexagonal lattice: constraining GMO to be hexagonal (*i.e.*, an angle of  $120^\circ$ ) results in a zero gap semiconductor. The overall shapes and magnitudes of the density of states (DOS) of GMO and graphene within  $\pm 2$  eV of the Fermi level (beyond the gap) are very similar. The sensitivity of the electronic properties to subtle changes in the structure could potentially lead to the ability to tailor the band gap.

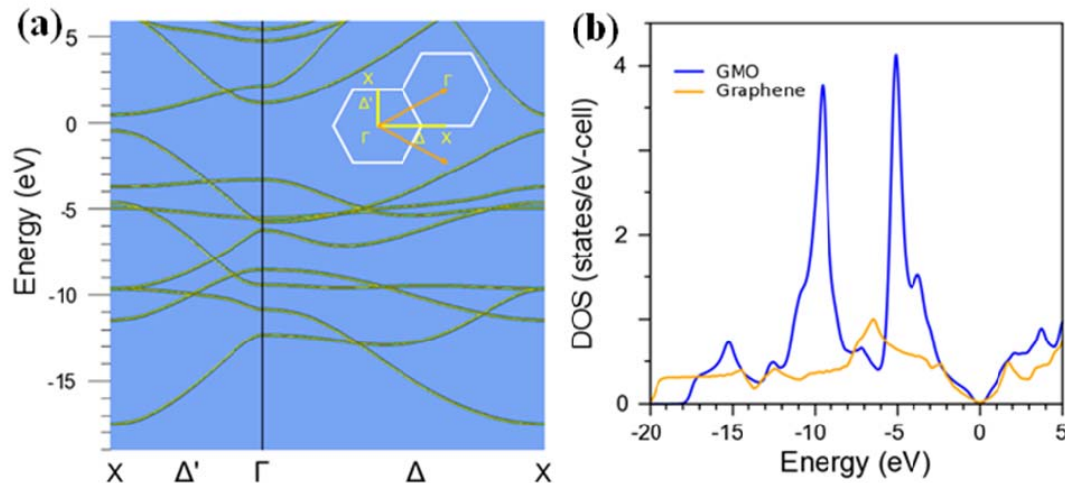


**Figure 4.9.** Calculated band structure and density of states (DOS) for GMO. (a) Band structure along the high symmetry directions (inset). (b) Comparison of DOS for GMO and graphene. [29]



### 4.3.3 Role of Molybdenum

Following the initial discovery of GMO, numerous further studies were performed, with attempts to scale up the production. In the process of doing so, several different TEM grid materials- Cu, Ni, and Pt- were used to attempt to synthesize GMO. Surprisingly, these experiments revealed that GMO could only be synthesized using Mo as the grid material. Immediately, this raised many questions about the validity of the proposed interpretation of GMO. The measured spacings were compared to various forms of Molybdenum oxides and carbides; however, no known form of Mo matched the measured spacings. The question then became in what fashion is Mo contributing to the new rings observed in the SAD experiments. Subsequently, the IR spectra of the GO prepared on Mo TEM grids was revisited. It was determined that the peaks at 900 and 960  $\text{cm}^{-1}$  (GO spectra from NIT measurements, Fig. 4.6A) were likely not assignable to C-O-C modes, but rather to the Mo-O stretching modes of  $\text{MoO}_2$  (molecular modes located at 900 and 950  $\text{cm}^{-1}$ )[38]. Interestingly, comparison of IR transmission measurements of samples before and after annealing to form the GMO phase showed that after heating, the intensity of the  $\text{MoO}_2$  bands dramatically decreased and were barely present following annealing, as seen by comparing Fig. 4.6 A-B. More surprisingly, a comparison IR transmission measurement of GO samples measured on Mo TEM grids (Fig. 4.6) and on diamond windows (Fig. 4.2) indicated that the effect of the Mo was to partially reduce the GO (this is discussed further below).

To further identify the interaction between Mo and GO, samples of GO were treated with Mo in partially controlled ways: the aqueous solution of GO was mixed with a commercially ordered Mo powder sample, or a Mo TEM grid was allowed to partially dissolve in a GO solution. This solution was then used to prepare Mo-intercalated GO on Ni TEM grids and

diamond windows. When the Mo-intercalated GO samples were prepared this way and then heated *in situ* in the TEM, the evolution of the SAD patterns was the same as before, and clearly showed the evolution of the rings assigned to the GMO phase. Fig. 4.10 shows SAD patterns of a sample of prepared by mixing 50 mg of the Mo powder with 0.5 mL of the aqueous GO solution (.2 mg/mL GO) at room temperature (A) after heating to 755 C (B). The pattern clearly shows the spacings that emerge due to the new ordered phase after the annealing. To probe the chemical changes induced by the presence of Mo, Fig. 4.11 compares NIT IR spectra from pure GO and GO prepared with a Mo TEM grid soaked in the solution for 2 weeks. The spectra have been scaled for clarity. The overall absorption of the pristine GO appears lower than that treated with the Mo TEM grid; however, this is only due to the quantity of sample being measured. Indeed, as was the case for GO prepared on TEM grids, the GO mixed with Mo powder appears partially reduced as compared to the pure GO. The intensity of OH features relative to the bands in the fingerprint region is lower in the case of the Mo-treated GO, and the frequency of the C=C stretching mode has shifted from 1615 to 1580  $\text{cm}^{-1}$ . This shift is routinely observed in reduced GO samples that have been reduced by other means (see, *e.g.*, the hydrazine-reduced GO in the next section, where the C=C stretch is at  $\approx 1580 \text{ cm}^{-1}$ ). There are also bands observed at 905 and 952  $\text{cm}^{-1}$  due to the  $\text{MoO}_2$  stretching modes (gas-phase/molecular values at 900 and 949  $\text{cm}^{-1}$  [38]). Similar results were obtained for GO treated with Mo powders rather than Mo TEM grids. While it is likely that the surfaces of the grids (or powders) as obtained are oxidized, the reduction of the GO by the Mo suggests that the powders may dissolve to yield Mo in solution, which then reacts with the oxygen groups in the GO to form adsorbed  $\text{MoO}_2$  and partially reduce the GO. Despite this large quantity of  $\text{MoO}_2$  present following exposure to either a controlled source of Mo, such as a powder, or an uncontrolled source, such as a TEM grid, the peaks



assigned to  $\text{MoO}_2$  are substantially reduced and very nearly absent in the GMO phase. A close comparison of the Mo-O stretching region for the GMO and GO phases prepared on Mo grids is shown in Fig. 4.12.

Having observed the very large reduction in the overall number of Mo-O bonds in the sample following preparation of the GMO phase, the presence or absence of Mo in the final samples was investigated using energy dispersive x-ray spectroscopy (EDX). In this experiment, aqueous GO suspensions were exposed to Mo and then deposited onto a Ni TEM grid. The use of the Ni grid eliminates the possibility of spurious Mo signals arising from the grid material. Then, EDX was performed on the sample before and after vacuum annealing to form the GMO phase. The resulting EDX spectra obtained from the sample are shown in Fig. 4.13. In both the spectra measured before and after heating, the distinctive Mo peaks at 2 and 17 keV are clearly visible, and do not show any significant changes relative to the O peak.

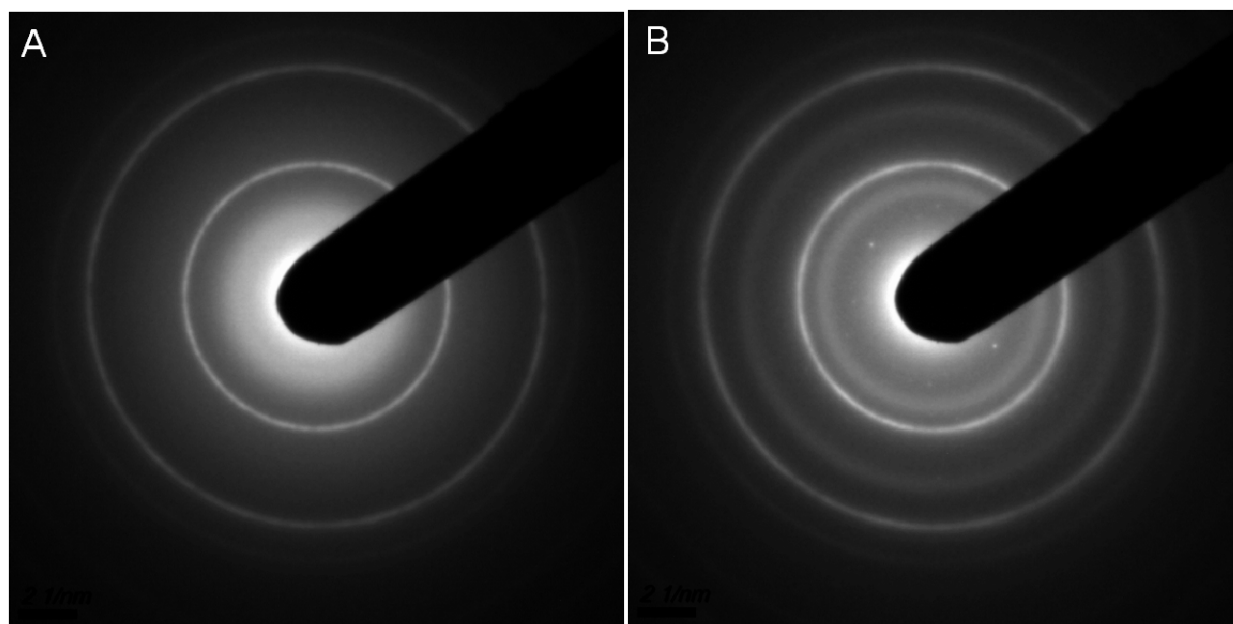


**Fig. 4.10:** SAD pattern of a sample of GO mixed with Mo powder at room temperature (A) and after heating to 755° C (B).

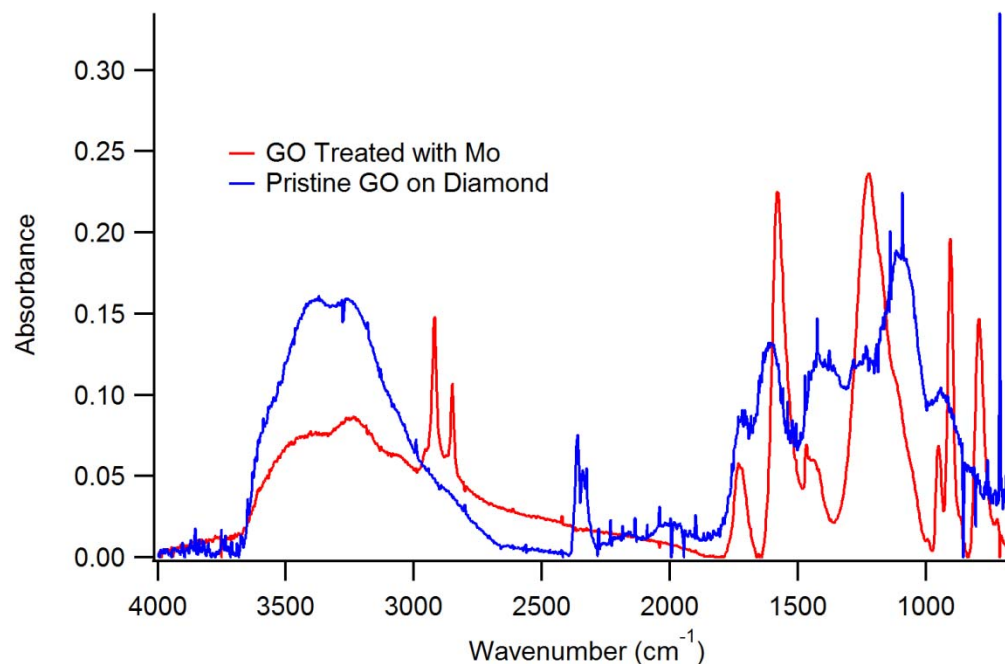


**Fig. 4.11:** IR absorption spectra of GO treated with Mo, and pristine GO as deposited onto a diamond window. The spectrum of the clean diamond window is used as the reference spectrum.

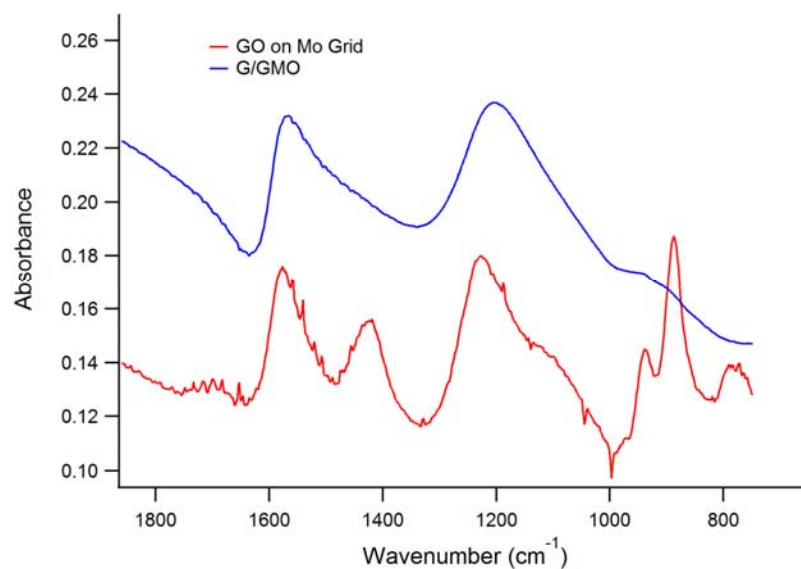


**Fig. 4.12:** Comparison of pure GO deposited on a Mo TEM grid and the GMO phase prepared from GO deposited on a Mo grid.

Thus it is apparent that while the annealing process depletes the quantity of MoO<sub>2</sub> present in the sample, the overall quantity of Mo present remains largely unchanged.

Based on these data two possible conclusions may be drawn: either Mo is a catalyst that creates GMO or Mo is a contaminant and the ordered phase observed in SAD is not GMO but rather an ordered structure into which Mo is incorporated. The first conclusion is as follows: following exposure to Mo via a TEM grid, the aqueous GO solution incorporates atomic Mo. This Mo reacts with the oxygen functional groups in GO to form aqueous MoO<sub>2</sub>, which becomes intercalated between the GO layers during the drying process. During annealing, a large strain is introduced following removal of some of the oxygen functional groups; this strain is relieved by the MoO<sub>2</sub> giving up its oxygen to the carbon to form the double epoxide structures and ultimately ordered GMO. The Mo then remains atomically adsorbed within the multilayer. The second interpretation is as follows: following exposure to Mo via a TEM grid (or other means), the aqueous GO solution incorporates atomic Mo. This Mo reacts with the oxygen functional groups in GO to form aqueous MoO<sub>2</sub>, which becomes intercalated between the GO layers during the drying process. During annealing, both the Mo and the carbon in the GO give up their O atoms, and the remaining Mo atoms form an ordered overlayer on the graphene template. The periodicity of the new phase identified in the SAD and HRTEM data are in agreement of the in-plane spacings of Mo<sub>2</sub>C and Mo<sub>3</sub>C<sub>2</sub>, but lack the c-axis spacings of these structures. The answer to these two questions is still largely being investigated and additional experiments are being developed to address the role of Mo in the ordered structures observed in SAD patterns (see section 4.3.4).

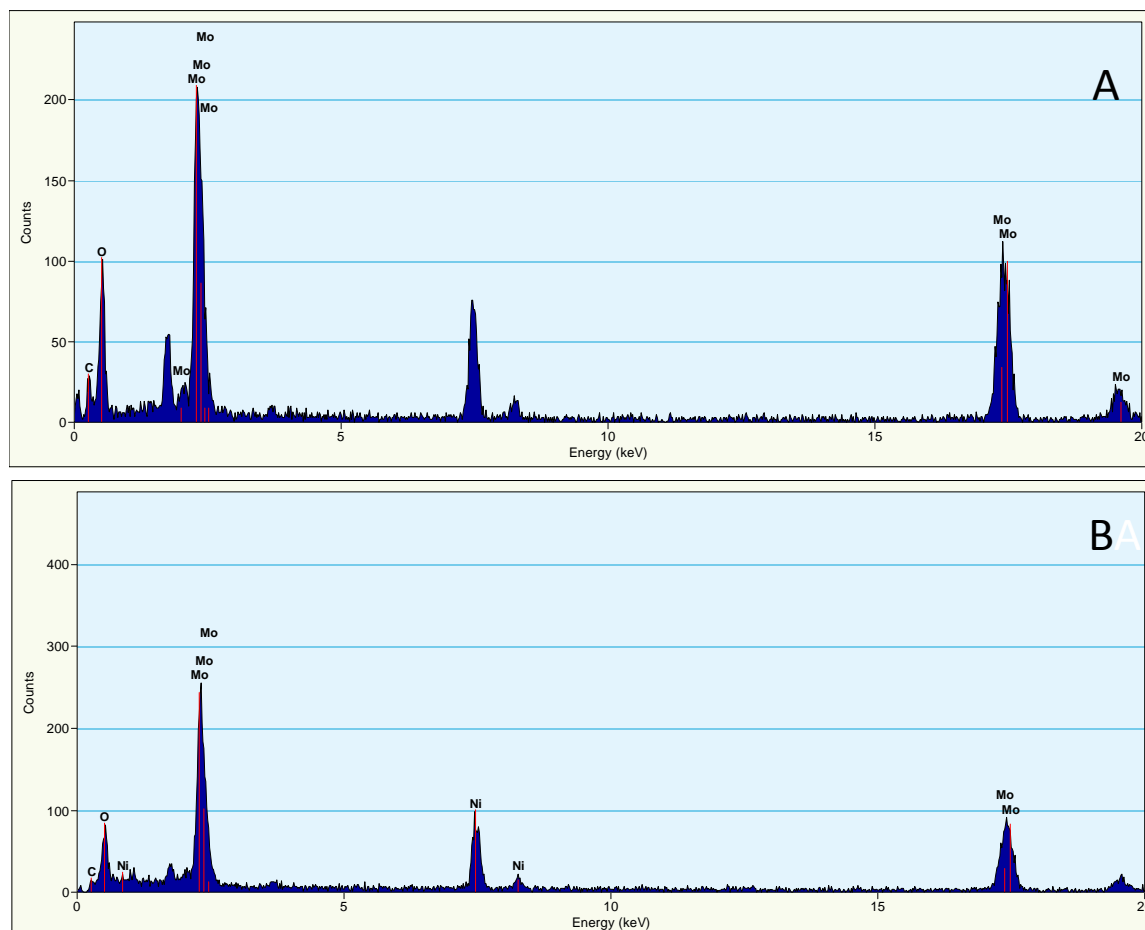


**Fig. 4.13:** EDS spectra of a GO sample treated with Mo before (A) and after (B) heating the sample to form the GMO phase.

#### 4.3.4 Conclusions and Future Directions

It has been proposed that the vacuum thermal reduction of multilayer GO films yields a composite material containing graphene and graphene monoxide nanocrystalline regions. The atomic structure of GMO is consistent with all experimental evidence from electron diffraction and IRMS and possesses an O:C = 1:1 stoichiometry, with double-epoxide GMO units arranged on a 2D quasi-hexagonal lattice. The semiconducting properties of GMO, predicted by *ab initio*

calculations, suggest that this new material, if it exists, might be useful for various electronic applications such as sensors, transistors, and optoelectronic devices, particularly considering its compatibility with graphene. This discovery of nanocrystalline GMO is a critical step to seeking methods to develop band gap controlled, crystalline, monolayered graphene oxide that do not rely on multilayered materials. An important question remains, however, namely the role of Mo in GMO formation, and whether the experimental evidence conclusively indicates the presence of GMO at all.

To summarize, SAD and HRTEM experiments conclusively indicate that an ordered phase develops following annealing of GO that has been exposed to Mo in some fashion. The data lends itself to interpretation, but experiments have yielded several indisputable facts regarding the evolution of the GMO phase: first, the ordered phase that develops has a periodicity that is consistent with the relaxed lattice spacings of GMO as predicted by DFT. Second, IR experiments confirm that epoxide groups are present in the samples following the annealing treatments. Third, Mo is still largely present in the sample following the formation of GMO. Last, at present, it has not been possible to synthesize GMO without the presence of Mo. Both hypothesis on the role of Mo in the evolution of the SAD rings, namely that Mo either acts as a catalyst for the reaction of GMO growth or it incorporates itself into the final structure as a carbide, can explain all of these observations. Regarding the measurement of the observed lattice spacings, both GMO and two Mo compounds including  $\text{Mo}_2\text{C}$  and  $\text{Mo}_3\text{C}_2$ , have spacings that are consistent with those observed in the SAD patterns. These compounds have other reflections with contributions from the c-axis order in the crystal structure that are not observed. This could be due to the lack of orientational order in the template GO material, resulting in misoriented 2D molybdenum carbide layers. With regard to the second observation, the

presence of epoxide groups in the final samples is consistent both with the presence of GMO and with there being residual oxygen (epoxides) that persists following the reduction treatments. Third, it is clear that the Mo remains in the sample in some form following annealing to produce the new rings. The presence of Mo in the final state of the samples could suggest either that Mo has changed its oxidation state and remains bonded at disordered sites in the multilayer or that the remaining Mo is in fact ordered and responsible for the development of the new rings. Lastly, the need for the presence of Mo can be explained either by Mo acting as a catalyst for the formation of GMO or by Mo becoming incorporated into the final structure that gives rise to the new SAD rings. In addition, the two interpretations are not mutually exclusive and both interpretations could be correct and contributing to the results.

A focused experiment that could directly address this question is an anomalous x-ray scattering measurement. In this experiment, the use of a synchrotron source allows one to vary the wavelength of the incident x-ray beam. This allows for identification of elements contributing to the reflections in a diffraction pattern based on the dispersion of the material's dielectric function near an absorption edge. The scattering factor for incident x-ray energies above the absorption edge picks up an imaginary component that affects the scattered intensity of a given reflection. For example, by performing this experiment on the TRGO samples prepared with Mo, collecting an x-ray diffraction pattern using an incident x-ray energy above and below the Mo K-edge will indicate if Mo makes a contribution to the diffraction rings assigned to GMO. If Mo is incorporated into the diffracting structure, the intensity of the GMO reflections will change relative to the graphene reflections as the x-ray energy is varied above and below the absorption edge. These experiments are currently in the planning phase.

## 4.4 Chemically Reduced Graphene Oxide

### 4.4.1: Introduction to the Chemical Reduction Method

Chemical reduction of GO was one of the first explored routes toward the goal of large-scale synthesis of graphene. In the most commonly employed technique, which is the one employed here, aqueous GO suspensions are treated with *N,N*-dimethylformamide (DMF) for the purpose of dispersion, and are then exposed to hydrazine monohydrate at a slightly elevated temperature ( $\sim 80^\circ\text{C}$ ) for 12 hours. This process yields dispersions of monolayer RGO that can be deposited on arbitrary substrates. Following drop-casting of the solution, the resulting films were dried and then subjected to a  $200^\circ\text{C}$  anneal for 1 hour to remove the remnant solvent. Despite the extremely wide use of this method and the realm of application of the resulting materials, contradictory reports on the degree of residual oxidation, the nature of the remaining oxygen functional groups, and the electronic properties of the resulting material continue to inspire debate on this material. In the work by Stankovich et. al., [39] the chemical reduction method was pioneered and the resulting material characterized. Based on elemental analysis and core-level photoemission measurements, the authors suggested that the oxygen content in RGO was lowered to a final C:O ratio of 10.7, with the predominant oxygen species the carbonyl group. This determination was based largely upon peak fitting of the C 1s peak in the XPS spectrum of the reduced material, and the assignment of the largest peak as being due to a C-N bond resulting from the hydrazine treatment. This peak, however, was displaced by only 0.6 eV from the C 1s peak due to C-O bonds, and thus their assignment of the remaining oxygen groups to carbonyls seems dubious. Perhaps the most useful structural information on RGO prepared by chemical treatments has come from high resolution electron microscopy. Using low-voltage aberration-

corrected TEM, two groups investigated the structure of RGO [32, 40]. In both cases, it was found that the reduced GO had a substantially more ordered carbon network than GO, but was still riddled with defects ranging from residual oxidation to extended topological defects and even large quantities of etch holes. Based on the HRTEM images alone, however, it was not possible to determine the type of remaining oxidation. Eda et. al. [21] characterized the electronic properties of RGO films, and found that while monolayer RGO films showed the characteristic ambipolar transport of graphene, thicker films showed a semimetallic behavior. In contrast, field effect transistor (FET) measurements performed within our group (Fig. 3.13) showed that the RGO films as prepared by our method showed a p-type semiconducting behavior. To this end, experiments have been performed on RGO films to further elucidate the structure of the remaining oxygen functional groups and their effect on the materials electronic properties. Normal incidence IR transmission measurements were performed to probe the bonding and low energy electronic structure of this material.

#### **4.4.2 Sample Preparation**

Reduction of GO was achieved by a chemical treatment using hydrazine monohydrate. The process has been described previously [41]; in brief, GO suspensions were prepared in aqueous solution as described above. DMF was added to the aqueous solution for a volume fraction DMF:water=9 to achieve stability of the solution. Lastly, hydrazine monohydrate was added and stirred for 12h at 80° C. Samples for TEM were prepared by drop casting approximately 1  $\mu$ L of the resulting suspension onto a lacey carbon-coated Cu TEM grid.



### 4.4.3 Results and Discussion

#### 4.4.3.1 Selected Area Diffraction

SAD measurements were performed on RGO multilayer films prepared as described above. A representative SAD pattern of such a sample is shown in Fig. 4.14. The pattern resembles the SAD pattern of unreduced GO multilayers shown in Fig. 4.1. As before, only the in-plane reflections of graphene are observed, and a coarse ring pattern is present due to the random orientation of the samples. This again yields the important information that on average the periodicity of graphene is preserved, and there is no stacking order along the c-axis.

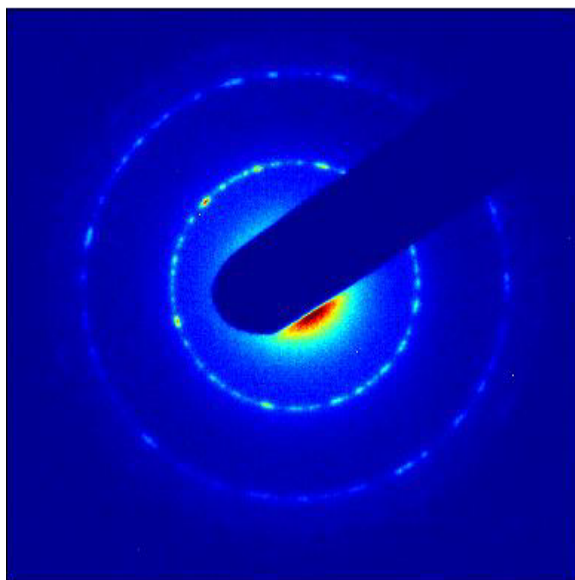


**Fig. 4.14:** SAD pattern of an hydrazine-treated RGO multilayer.

#### 4.4.3.2 Electrical Transport

Field effect transistor (FET) measurements have been performed on RGO produced by the chemical method to identify the majority charge carriers. In this experiment, the RGO is deposited onto the interdigitated gold electrode substrate (Chapter 1), which is supported by a

300 nm SiO<sub>2</sub> film on a Si wafer. The Si wafer is used as the back gate and a circuit is connected to the gold electrode assembly. When a voltage is applied to the back gate, the RGO sample is subjected to an electric field; this field has the potential to change the position of the Fermi energy of the sample. Application of a negative voltage to the back gate causes a decrease in the Fermi level, while a positive voltage has the opposite effect. As the gate voltage is modulated, the source-drain current is measured, providing an indication of the conductivity at a particular voltage. FETs made with graphene show ambipolar transport, meaning that the current as a function of applied voltage is V-shaped and symmetric about 0V [1]. This indicates that in pristine graphene, the charge carriers can easily be converted from electrons to holes. Some reports on the transport properties of RGO have shown a similar behavior to graphene, where ambipolar transport is observed at room temperature [21, 42]. In contrast, our RGO samples show transport properties as seen in Fig. 4.15. In this case, the source-drain current has its maximum value at the lowest gate voltage, and decreases continuously as the gate voltage increases. The continual decrease of I<sub>SD</sub> even above 0V indicates that our RGO samples do not, in fact, show ambipolar transport. Rather, they behave as a p-type semiconductor. The application of a negative gate voltage lowers the Fermi level, increasing the number of holes available for conduction, whereas a positive gate voltage has the opposite effect. As shown below, the reason for this behavior is residual oxygen groups that effectively open a gap in the density of states, leading to p-type transport.

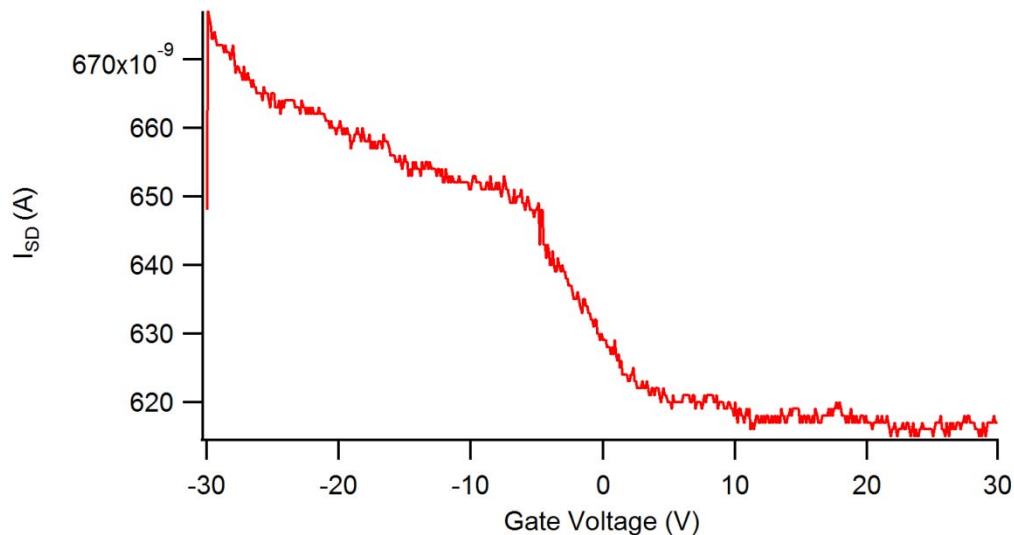


**Fig. 4.15:** Transport properties of RGO FET devices. The source-drain current,  $I_{SD}$ , increases with decreasing gate voltage, indicating p-type conduction is dominant.

#### 4.4.3.3 IR Spectroscopy

IR transmission measurements of RGO were performed on samples prepared on diamond windows. Fig. 4.16A shows a representative absorption spectrum from a thin film of RGO measured in the transmission geometry from  $7500\text{--}650\text{ cm}^{-1}$ , with an enlargement of the  $1200\text{ cm}^{-1}$  band in 4.15B. Throughout the mid-IR region, there are three prominent absorption bands with peak positions at  $1735$ ,  $1580$ , and  $1238\text{ cm}^{-1}$ . The band at  $1735\text{ cm}^{-1}$  is unambiguously assigned to the C=O bond stretching mode of the carbonyl groups. The  $1580\text{ cm}^{-1}$  band is due to the C=C stretching of the graphitic part of the substrate, and the  $1238\text{ cm}^{-1}$  is assigned to the epoxide C-O-C stretching vibrations. Examination of the lineshape of this mode reveals an asymmetric profile, with additional intensity on the low-frequency side of the band. For a bridge-bonded atomic adsorbate, such as the epoxide group,

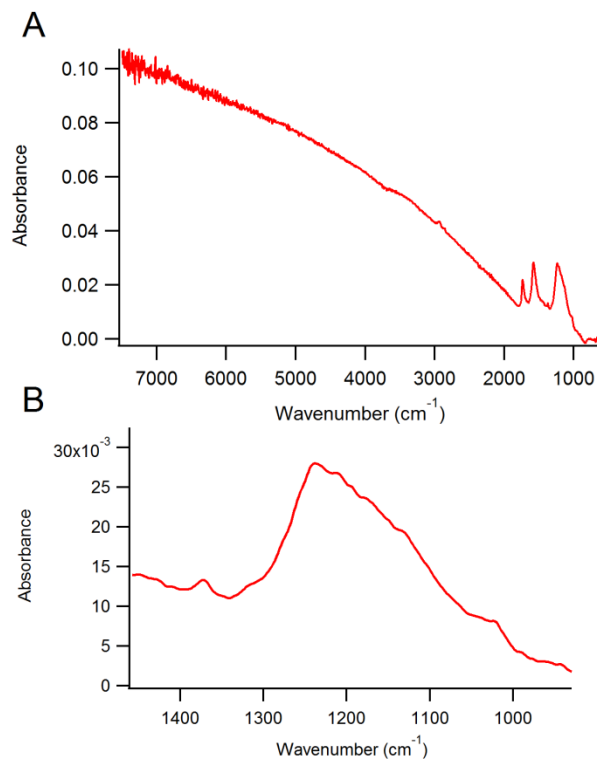


**Fig. 4.16:** IR spectra of RGO as determined from NIT measurements. The measurements are performed with RGO samples deposited onto diamond windows, with the spectrum of the clean window used as the reference. B) shows an enlargement of the  $1200\text{ cm}^{-1}$  band in (A).

two bond-stretching vibrational modes are expected corresponding to the symmetric and asymmetric stretching modes. These two modes, which are close in energy, are clearly superimposed on the broad band at  $1200\text{ cm}^{-1}$ . Additionally, it is possible that the band is comprised of more than just the two peaks corresponding to symmetric and asymmetric stretching. Assignment of the origin of these bands is a formidable task; since the C-O-C modes are so close in energy to the phonons of the substrate, the vibrations of the epoxide group couple strongly to the vibrations of the lattice. Thus, any attempt to calculate the normal modes of vibration using first-principles computations leads to a nearly intractable set of IR active modes in which the modes of the substrate dominate. In addition, the tendency of oxygen groups in GO and RGO to cluster, discussed below, further complicates the interpretation of the normal modes

that are possible. Of the numerous attempts made to identify the symmetric and asymmetric stretching vibrations using DFT modeling, the relative energies of the symmetric and asymmetric stretching frequencies were strongly dependent on the symmetry of the unit cell or cluster chosen for the calculation. Depending on the initial structure and level of theory chosen, the symmetric stretching frequency could be either higher or lower than that of the asymmetric stretch. In addition, the stretching of the two carbon atoms which hosts the epoxide oxygen atom also produces an IR active mode that would have no analogy for, *e.g.*, a metal substrate. All of these modes likely contribute to the absorption between 1000-1300  $\text{cm}^{-1}$ .

#### 4.4.3.4 Electronic Structure

The spectrum in Fig. 4.16 shows, in addition to vibrational absorption, a strong background absorption that increases with increasing frequency. Broadband absorption in the mid IR in graphene-based materials has been studied extensively in the context of its electronic structure. Interband transitions between the valence and conduction bands in intrinsic monolayer graphene produce a flat, "universal" absorption over the entire mid-IR [43]; electrostatic doping produces a threshold to the absorption at  $2E_f$  [44]. The broadband absorption seen in Fig. 4.16 can also be assigned to interband excitations; however, it does not have the characteristic constant absorption value of monolayer graphene. Rather, there is a low energy threshold above which the absorbance continues to rise monotonically. Based on the transport measurements and IR spectra discussed above, it is reasonable to attribute this absorption to an M-type critical point resulting from a gap in the density of states. In the vicinity of such a critical point, the JDOS has a characteristic dependence proportional to  $\sqrt{\hbar\omega - E_g}$  (see Ch. 2). Optical measurements of the band gap are carried out by calculating the square of the absorbance, which produces a linear dependence of the absorption on photon frequency in the vicinity of the gap. The value of the

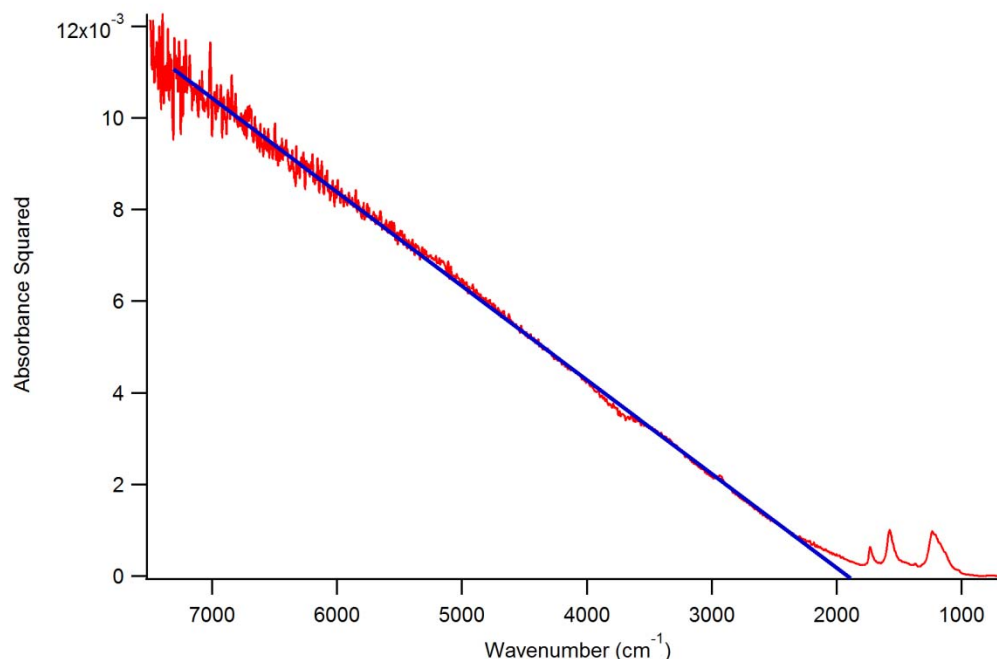


**Fig. 4.17:** Frequency dependence of the absorption squared for RGO transmission measurements. The intercept indicates the magnitude of the gap.

energy gap is then determined by finding the intercept of the linear dependence. The method is shown in Fig. 4.17 for the spectrum in Fig. 4.16. The square of the absorbance produces a very nearly linear dependence throughout the mid IR and the extracted value of the energy gap is approximately  $1900 \text{ cm}^{-1}$  ( $\approx 0.24 \text{ eV}$ ). Thus the observed lineshape is consistent with the absorption expected with a direct-gap semiconductor. The measurements provide an overall estimation of the average electronic behavior in this inhomogeneous material at mesoscopic length scales

Next, it is logical to inquire into the origin of the gap observed in the measurements. The oxygen dopants, in the form of epoxide and carbonyl functional groups, both have the potential to perturb the electronic structure. Measurements done on a number of samples indicate,

however, that the presence and amount of carbonyl groups (as well as  $\text{CH}_x$  groups) are not constant from one sample to the next. These groups most likely are present at edges and defects in the samples. Fig. 4.18 compares

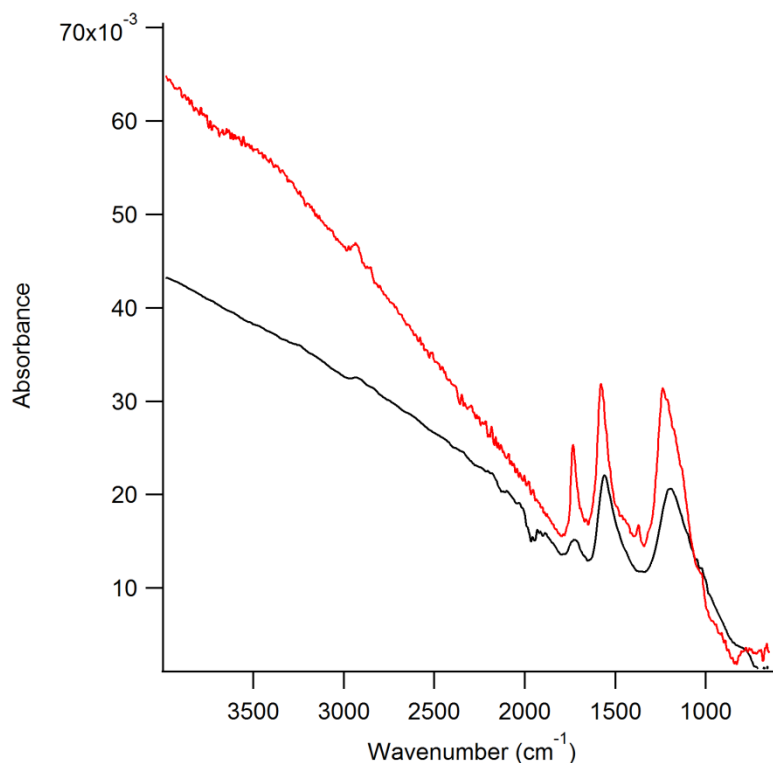


**Fig. 4.18:** Comparison of the spectrum in Fig. 4.15 with a spectrum from another sample in which the relative C=O content was lower. A qualitatively similar behavior of the background absorption is observed.

the IR spectra from two different samples; the spectrum from Fig. 4.16 is compared to a spectrum from a sample that had a much lower concentration of C=O. The ratios of the integrated intensity of the C=O peak to the C=C peak of the two spectra are 0.13 and 0.32, indicating a significant change in the overall concentration of C=O. The thickness and therefore the background absorption strength is different for the two samples, yet qualitatively they show the same trend in the background absorption and yield very similar values of the optical gap.

This suggests that the carbonyl groups are not the dominant contributor in determining the optical properties. This is not surprising; the carbonyl groups are likely to be present at edges and defects, where localized states would be expected, and would likely have minimal effect on the optical properties even in the absence of the carbonyl termination.

Having identified the epoxide group as the most likely contributor to the optical gap, DFT calculations were performed to model the substrate. Some theoretical data already existed in the literature at the time of this work [35, 45-47]; however, it was important to produce calculations closely aligned to experimental measurements that could be used as a comparison and for modeling adsorption at the RGO surface, as discussed in the subsequent chapters. The results indicated that the overall substrate electronic structure is acutely sensitive to the concentration of oxygen functional groups. The calculations are performed using a  $3\times 3$  graphene supercell with different numbers of oxygen atoms. Fig. 4.19 shows the results for two representative structures: a  $3\times 3$  supercell with a single epoxide group at the center of the cell (B), and a  $3\times 3$  supercell with two epoxide groups decorating opposite sides of the basal plane (C). The bare supercell with only graphene is shown for comparison in (A). The calculated band dispersions along the high symmetry directions for the structures in 4.19 A-C) are shown in Figs. 4.19 D-F), respectively. The total densities of states (DOS) for the three structures are shown in Fig. 4.20 A-C). The data show that for the  $C_{18}O$  stoichiometry (4.19 B), the material remains a gapless semiconductor with the valence and conduction bands touching at the K-point, as for the case of pure graphene. Doubling the oxygen concentration as in Fig. 4.19 C, however, does open a gap at the K-point of approximately 0.7 eV. These features are also reflected in the calculated total DOS in Fig. 4.20, where only the structure from 4.18 C shows an actual gap.



Establishing that the epoxide groups can induce a gap in the DOS is consistent with previously published experimental data. Hossain et.al. [48] showed that when epitaxial graphene samples were exposed to atomic oxygen, low coverages of epoxide groups were formed to permit examination of single epoxide groups using scanning tunneling microscopy (STM). The

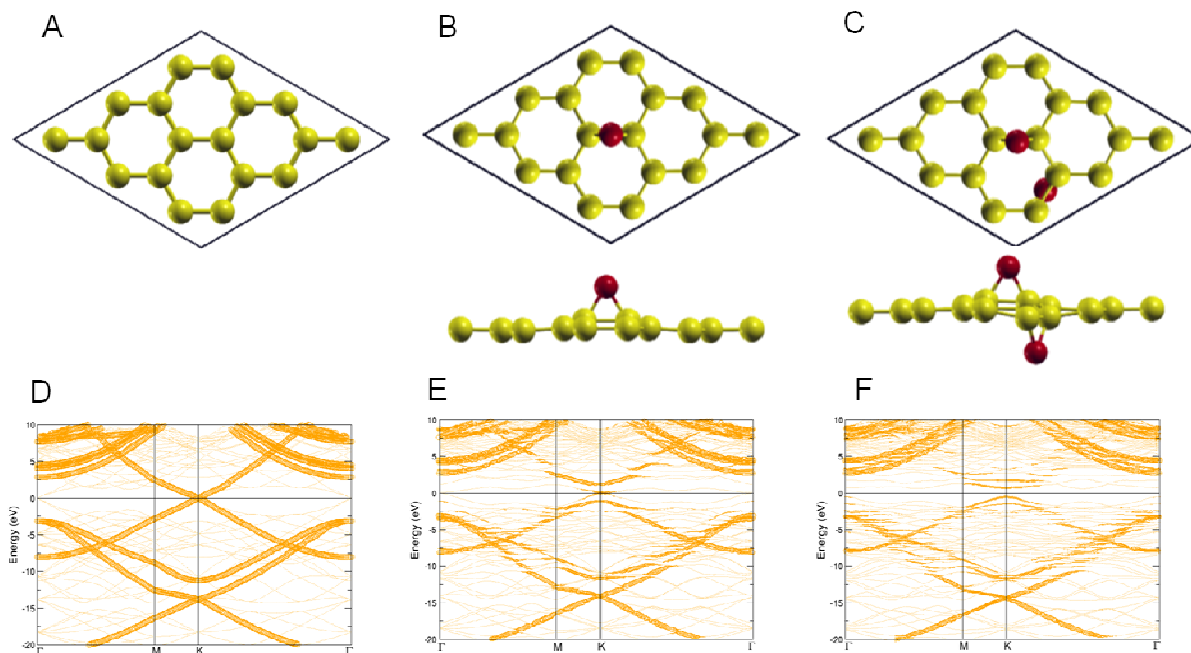


**Fig. 4.19:** Atomic structures of graphene (A) and graphene with one (B) and two (C) epoxide groups in a  $3 \times 3$  supercell. The band dispersions of the structures in A-C) are shown along the high symmetry directions in D-F), respectively.

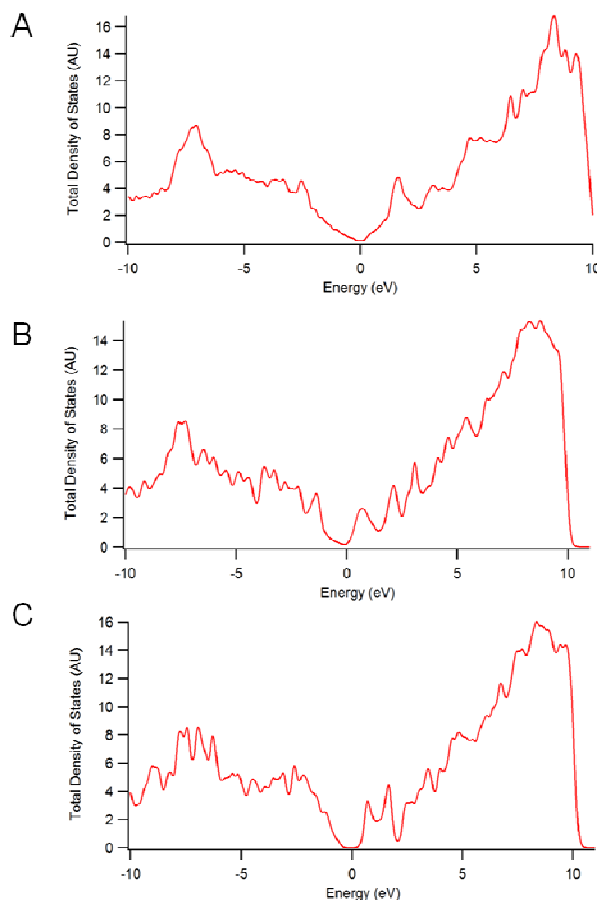


**Fig. 4.20:** Calculated total DOS for the structures in Fig. 4.19. A)  $3 \times 3$  graphene supercell, B) with 1 epoxide group, C) with 2 epoxide groups.

STM images showed that a single epoxide group caused a significant change in the density of states extending over regions as large as 1.2 nm ( $\approx 5$  graphene lattice constants or 8 C-C bond lengths). In addition, valence band photoemission measurements showed that the oxidation substantially reduced the density of states near the Fermi level, consistent with the calculations and experiments shown here.

It is important to note that it is highly unlikely that the actual material contains ordered or even stoichiometric oxidation. Previous experimental [9, 29, 32, 40, 49] and theoretical [47]

works have shown that oxygen atoms in GO and RGO have a propensity to cluster, leaving segregated graphitic and oxidized regions. A single oxygen adsorbate on an otherwise pristine graphene lattice introduces a large amount of local strain to the neighboring carbon atoms [22, 47, 48], causing a protrusion normal to the carbon basal planes. This strain is stabilized when additional oxygen functional groups are located on the opposite side of the basal plane. Consequently, configurations of the type in Fig. 4.19B in which oxygen atoms are adjacent but on opposite sides of the basal plane have a much higher binding energy [50] and are thus more likely to represent the configuration of the oxygen functional groups that persist following reduction. The IR measurements probe a micrometer-scale area, and effectively average over the oxidized regions, graphitic regions, and intermediate regions. A more realistic comparison of the theoretical modeling to the actual measurement would be to apply a substantial broadening to the DOS plots shown in 4.20. This interpretation is justified: in the limit of total disorder, amorphous semiconductors often reflect electronic properties similar to their ordered counterparts, but with an overall broadening in the DOS [51] and hence the optical properties. In light of this correspondence, the gap discussed in the context of RGO may not be a *bona fide* "band gap", since the oxygen adatoms are not ordered, but rather a gap in the DOS across which optically active excitations exist. Thus, the calculations are intended only to show that, at sufficient concentrations, the epoxide groups can open a gap in the density of states and also to assess how the occupation of the electronic states change upon adsorption of small molecules.

#### 4.4.4 Conclusions

Following chemical reduction of GO, the resulting RGO material has oxygen functional groups including carbonyl and epoxide. The epoxide groups make the perturbation to the electronic structure, and depending on the oxygen concentration, can open a gap of variable size in the DOS, as suggested by DFT calculations. This is supported by IR measurements that show on average, the energy gap is  $\approx 0.2-0.25$  eV. The presence of the epoxide groups renders the collective RGO material a p-type semiconductor.

### 4.5 Dimensionality Effect on the Optical Properties of RGO; SnO<sub>2</sub>/RGO

#### Heterostructures

##### 4.5.1 Introduction

Heterostructures consisting of RGO decorated with SnO<sub>2</sub> nanocrystals were investigated experimentally using electron microscopy and IR microspectroscopy. These materials are of interest from several technological viewpoints; first, the addition of the SnO<sub>2</sub> to the RGO enhances its sensitivity to NO<sub>2</sub> [52, 53]. Second, SnO<sub>2</sub>/graphene composites can be used in energy applications such as supercapacitors [54] and lithium ion batteries [55]. Lastly, the electronic and optical properties of nanocrystal/graphene hybrids are of fundamental interest, particularly in the IR region where the most significant features of graphene's electronic structure are found. Here, the structure of SnO<sub>2</sub>/RGO hybrids is considered in conjunction with the low-energy spectral properties of the composite system.

### 4.5.2 Methods and Synthesis

SnO<sub>2</sub>/RGO heterostructures were described as follows: GO was synthesized using as described above. Sn<sup>4+</sup> ions were introduced into the GO solution and electrostatically adsorb onto the GO surfaces [53]. Subsequently, the solution was centrifuged, the precipitate was collected and washed, and air-dried overnight at 80°C. The final SnO<sub>2</sub>/RGO hybrid was obtained by annealing the dried material at 350°C in an Ar atmosphere for 1 hour. This material was then resuspended in aqueous solution and sonicated. Normal incidence IR transmission measurements were performed at IRENI using samples deposited on diamond windows.

### 4.5.3 Results and Discussion

The observed behavior of the broadband optical absorption of RGO near the energy gap showed the characteristic behavior of a three dimensional material in the vicinity of an M<sub>0</sub>-type critical point (Fig. 4.16, 4.17). As was discussed in Chapter 2, when the electronic structure depends on three components of the electronic wavevector, the resulting form of the JDOS has a  $\sqrt{\hbar\omega - E_g}$  dependence. The three-dimensional behavior of the optical properties arises because of the multilayer structure of the samples being considered; the interaction of a given RGO layer with the adjacent layers causes the energy to depend on all three components of the wavevector. This is notably different from the case of monolayer graphene, in which the electrons are confined to a single atomic layer resulting in a frequency independent ("universal") value of the conductivity and hence the absorption above the band gap [43, 44]. This effect of multilayer structure has resulted in deviation from the ideal universal absorbance even for the case of a single bilayer [56, 57], as well as graphene samples containing more than 2 layers [58].

Multilayer structures of RGO with SnO<sub>2</sub> nanocrystals decorating the individual sheets are different in this respect; the SnO<sub>2</sub> nanocrystals lying on the basal planes have the effect of decoupling the layers, so that even when multilayer structures of the SnO<sub>2</sub>/RGO are fabricated by drop-casting from solution, the distance between the individual carbon layers is sufficiently large so as to render each layer as an independent 2D sheet. Fig. 4.21 compares the IR absorption spectrum of pure RGO (A) with that of an SnO<sub>2</sub>/RGO multilayer structure (B). The vibrational absorption features in the SnO<sub>2</sub>/RGO structure are essentially the same as those in the chemically-prepared RGO. Bands are observed at 1730, 1580 and 1230 cm<sup>-1</sup> within a few wavenumbers of the band positions observed in undecorated RGO (4.21A). This indicates that despite a fairly different route toward reduction, the RGO component of the SnO<sub>2</sub>/RGO heterostructure has the same functional groups as the hydrazine-reduced RGO. The spectrum in 4.21B also shows a peak at 670 cm<sup>-1</sup> due to the IR active  $E_u$  mode of the SnO<sub>2</sub> nanocrystals. The largest difference between the two spectra is the overall broadband absorption, which shows a notably different character throughout the IR region. Rather than an absorption threshold that increases continuously with wavelength, as observed in Fig. 4.21A, the spectrum of the SnO<sub>2</sub>/RGO shows a sharp absorption threshold that levels to a constant value throughout the IR region. This is a direct manifestation of the dimensionality effects induced by the SnO<sub>2</sub> nanocrystals; rather than having a three-dimensional multilayered graphitic structure where adjacent layers interact to modify the optical properties, the finite size of the SnO<sub>2</sub> nanocrystals intercalated into the structure effectively decouples every layer. Since each layer is effectively independent, no interlayer hopping can occur and the electron energy levels in the RGO depend only on two components of the wavevector. Consequently, the composite structure demonstrates an absorption profile consistent with a 2D JDOS, which is the case observed in graphene

monolayers [43, 44]. Thus while the two pieces of data consistently indicate the presence of a gap in RGO, dimensionality effects ultimately dictate the functional dependence of the broadband absorption. The primary difference in the electronic structure of the multilayer RGO versus the decoupled SnO<sub>2</sub>/RGO is most likely a difference in the dispersion of the  $\pi$  bands around the K-point. This is the case observed for the evolution of the bands of intrinsic graphene from a single to an ordered bilayer; in both cases the material has zero band gap, but the band dispersion becomes parabolic in the bilayer case.

Lastly, note that misoriented graphene multilayers (*e.g.*, twisted bilayer graphene and multilayer extensions) have additional bands that could potentially produce optically active electronic transitions. For a twisted bilayer, the electronic structure can be thought of as a misorientation of two hexagonal Brillouin zones; the region in K-space where the  $\pi$  bands overlap produces an additional band that would not be otherwise observed in the case of monolayer graphene. Tabert and Nicol [59] reported that this effect is likely to manifest itself in the optical spectra as additional peaks. Such features are not observed in our data most likely because the twist angles between each adjacent layers is sufficiently large that these transitions are outside of the IR frequency range. Additionally, since the layers are randomly oriented, all possible twist angles coupled with translations are possible in the real samples, and the possible optical transitions due to the interlayer coupling are effectively averaged out.

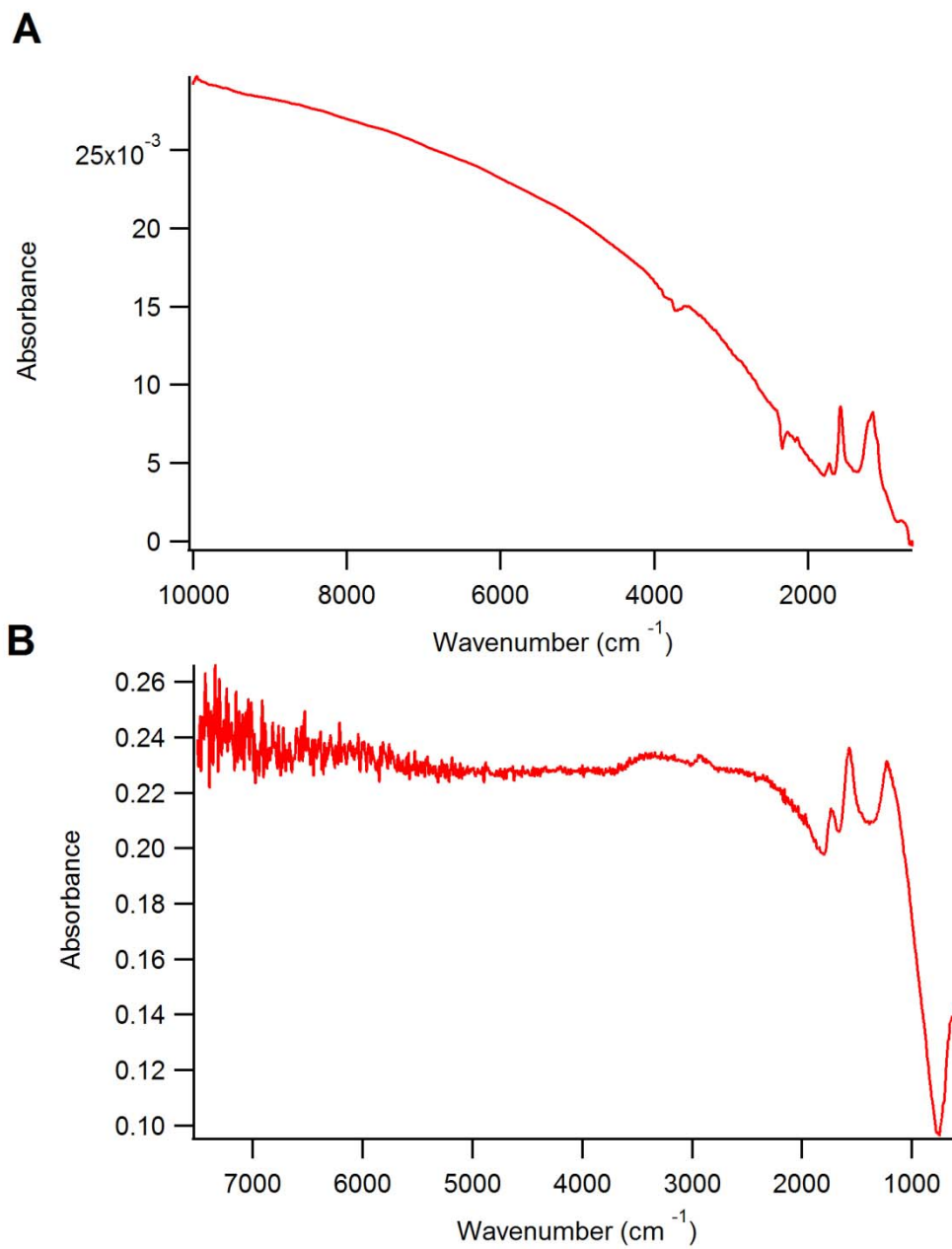


**Fig. 4.21:** Comparison of the IR absorption of RGO (A) and SnO<sub>2</sub>/RGO (B). In both cases, the reference is the clean diamond window.



## 4.6 References

1. Novoselov, K.S., et al., *Electric field effect in atomically thin carbon films*. Science, 2004. **306**(5696): p. 666-669.
2. Geim, A.K. and K.S. Novoselov, *The rise of graphene*. Nature Materials, 2007. **6**(3): p. 183-191.
3. Novoselov, K.S., et al., *Two-dimensional gas of massless Dirac fermions in graphene*. Nature, 2005. **438**(7065): p. 197-200.
4. Lopez, V., et al., *Chemical Vapor Deposition Repair of Graphene Oxide: A Route to Highly Conductive Graphene Monolayers*. Advanced Materials, 2009. **21**(46): p. 4683-4686.
5. Li, X.S., et al., *Large-Area Synthesis of High-Quality and Uniform Graphene Films on Copper Foils*. Science, 2009. **324**(5932): p. 1312-1314.
6. Halasi, G., G. Schubert, and F. Solymosi, *Photodecomposition of Formic Acid on N-Doped and Metal-Promoted TiO<sub>2</sub> Production of CO-Free H<sub>2</sub>*. Journal of Physical Chemistry C, 2012. **116**(29): p. 15396-15405.
7. Park, S., et al., *Aqueous Suspension and Characterization of Chemically Modified Graphene Sheets*. Chemistry of Materials, 2008. **20**(21): p. 6592-6594.
8. Meyer, J.C., et al., *On the roughness of single- and bi-layer graphene membranes*. Solid State Communications, 2007. **143**(1-2): p. 101-109.
9. Wilson, N.R., et al., *Graphene Oxide: Structural Analysis and Application as a Highly Transparent Support for Electron Microscopy*. Acs Nano, 2009. **3**(9): p. 2547-2556.
10. Novoselov, K.S., et al., *Electric Field Effect in Atomically Thin Carbon Films*. Science, 2004. **306**(5296): p. 666-669.
11. Li, D. and R.B. Kaner, *Materials Science - Graphene-Based Materials*. Science, 2008. **320**(5880): p. 1170-1171.
12. Zhang, Y.B., et al., *Experimental observation of the quantum Hall effect and Berry's phase in graphene*. Nature, 2005. **438**(7065): p. 201-204.

13. Dikin, D.A., et al., *Preparation and Characterization of Graphene Oxide Paper*. Nature, 2007. **448**(7152): p. 457-460.
14. Dreyer, D.R., R.S. Ruoff, and C.W. Bielawski, *From conception to realization: An historical account of graphene and some perspectives for its future*. Angewandte Chemie-International Edition, 2010. **49**(49): p. 9336-9344.
15. Dreyer, D.R., et al., *The chemistry of graphene oxide*. Chemical Society Reviews, 2010. **39**(1): p. 228-240.
16. Li, D., et al., *Processable Aqueous Dispersions of Graphene Nanosheets*. Nature Nanotechnology, 2008. **3**(2): p. 101-105.
17. Gao, W., et al., *New insights into the structure and reduction of graphite oxide*. Nature Chemistry, 2009. **1**(5): p. 403-408.
18. Zhu, Y., et al., *Carbon-based supercapacitors produced by activation of graphene*. Science, 2011. **332** (6037 ): p. 1537-1541.
19. Lu, G.H., et al., *Toward Practical Gas Sensing with Highly Reduced Graphene Oxide: A New Signal Processing Method To Circumvent Run-to-Run and Device-to-Device Variations*. ACS Nano, 2011. **5**(2): p. 1154-1164.
20. Mao, S., et al., *Specific Protein Detection Using Thermally Reduced Graphene Oxide Sheet Decorated with Gold Nanoparticle-Antibody Conjugates*. Advanced Materials, 2010. **22**(32): p. 3521-+.
21. Eda, G., G. Fanchini, and M. Chhowalla, *Large-area ultrathin films of reduced graphene oxide as a transparent and flexible electronic material*. Nature Nanotechnology, 2008. **3**(5): p. 270-274.
22. Mkhoyan, K.A., et al., *Atomic and electronic structure of graphene-oxide*. Nano Letters, 2009. **9**(3): p. 1058-1063.
23. Acik, M., et al., *Unusual infrared-absorption mechanism in thermally reduced graphene oxide*. Nature Materials, 2010. **9**(10): p. 840-845.

24. Bagri, A., et al., *Structural evolution during the reduction of chemically derived graphene oxide*. Nature Chemistry, 2010. **2**(7): p. 581-587.
25. Acik, M., et al., *The Role of intercalated water in multilayered graphene oxide*. ACS Nano, 2010. **4**(10): p. 5861-5868.
26. Pu, H.H., et al., *Strain-induced band-gap engineering of graphene monoxide and its effect on graphene*. Physical Review B, 2013. **87**(8): p. 085417.
27. Nasse, M.J., et al., *Multi-beam synchrotron infrared chemical imaging with high spatial resolution: Beam line realization and first reports on image restoration*. Nuclear Instruments & Methods in Physics Research Section a-Accelerators Spectrometers Detectors and Associated Equipment, 2011. **649**(1): p. 172-176.
28. Weinert, M., et al., *FLAPW: applications and implementations*. Journal of Physics-Condensed Matter, 2009. **21**(8): p. 084201.
29. Mattson, E.C., et al., *Evidence of Nanocrystalline Semiconducting Graphene Monoxide during Thermal Reduction of Graphene Oxide in Vacuum*. ACS Nano, 2011. **5**(12): p. 9710-9717.
30. Stankovich, S., et al., *Graphene-based composite materials*. Nature, 2006. **442**(7100): p. 282-286.
31. Fano, U., *Effects of configuration interaction on intensities and phase shifts*. Physical Review, 1961. **124**(6): p. 1866.
32. Erickson, K., et al., *Determination of the Local Chemical Structure of Graphene Oxide and Reduced Graphene Oxide*. Advanced Materials, 2010. **22**(40): p. 4467-4472.
33. Ekiz, O.O., et al., *Reversible Electrical Reduction and Oxidation of Graphene Oxide*. ACS Nano, 2011. **5**(4): p. 2475-2482.
34. Boukhalov, D.W. and M.I. Katsnelson, *Modeling of graphite oxide*. Journal of the American Chemical Society, 2008. **130**(32): p. 10697-10701.
35. Xiang, H.J., S.H. Wei, and X.G. Gong, *Structural motifs in oxidized graphene: A genetic algorithm study based on density functional theory*. Physical Review B, 2010. **82**(3): p. 035416.

36. Cassagneau, T., F. Guerin, and J.H. Fendler, *Preparation and characterization of ultrathin films layer-by-layer self-assembled from graphite oxide nanoplatelets and polymers*. Langmuir, 2000. **16**(18): p. 7318-7324.
37. Szabo, T., et al., *Evolution of surface functional groups in a series of progressively oxidized graphite oxides*. Chemistry of Materials, 2006. **18**(11): p. 2740-2749.
38. *NIST Chemistry Webbook*. NIST Chemistry Webbook, 2012.
39. Stankovich, S., et al., *Synthesis of graphene-based nanosheets via chemical reduction of exfoliated graphite oxide*. Carbon, 2007. **45**(7): p. 1558-1565.
40. Gomez-Navarro, C., et al., *Atomic Structure of Reduced Graphene Oxide*. Nano Letters, 2010. **10**(4): p. 1144-1148.
41. Park, S., et al., *Colloidal Suspensions of Highly Reduced Graphene Oxide in a Wide Variety of Organic Solvents*. Nano Letters, 2009. **9**(4): p. 1593-1597.
42. Gomez-Navarro, C., et al., *Electronic transport properties of individual chemically reduced graphene oxide sheets*. Nano Letters, 2007. **7**(11): p. 3499-3503.
43. Mak, K.F., et al., *Measurement of the Optical Conductivity of Graphene*. Physical Review Letters, 2008. **101**(19).
44. Li, Z.Q., et al., *Dirac charge dynamics in graphene by infrared spectroscopy*. Nature Physics, 2008. **4**(7): p. 532-535.
45. Yan, J.A. and M.Y. Chou, *Oxidation functional groups on graphene: Structural and electronic properties*. Physical Review B, 2010. **82**(12).
46. Yan, J.A., L.D. Xian, and M.Y. Chou, *Structural and Electronic Properties of Oxidized Graphene*. Physical Review Letters, 2009. **103**(8).
47. Topsakal, M. and S. Ciraci, *Domain formation on oxidized graphene*. Physical Review B, 2012. **86**(20): p. 205402.
48. Hossain, M.Z., et al., *Chemically homogeneous and thermally reversible oxidation of epitaxial graphene*. Nature Chemistry, 2012. **4**(4): p. 305-309.

49. Mao, S., H.H. Pu, and J.H. Chen, *Graphene oxide and its reduction: modeling and experimental progress*. Rsc Advances, 2012. **2**(7): p. 2643-2662.
50. Huang, B., et al., *Overcoming the Phase Inhomogeneity in Chemically Functionalized Graphene: The Case of Graphene Oxides*. Physical Review Letters, 2013. **110**(8).
51. Dressel, M. and G. Grüner, *Electrodynamics of Solids: Optical Properties of Electrons in Matter*. 2002: Cambridge University Press.
52. Mao, S., et al., *Tuning gas-sensing properties of reduced graphene oxide using tin oxide nanocrystals*. Journal of Materials Chemistry, 2012. **22**(22): p. 11009-11013.
53. Cui, S., et al., *Indium-doped SnO<sub>2</sub> nanoparticle-graphene nanohybrids: simple one-pot synthesis and their selective detection of NO<sub>2</sub>*. Journal of Materials Chemistry A, 2013. **1**(14): p. 4462-4467.
54. Mao, S., et al., *A General Approach to One-Pot Fabrication of Crumpled Graphene-Based Nanohybrids for Energy Applications*. Acs Nano, 2012. **6**(8): p. 7505-7513.
55. Wen, Z.H., et al., *Binding Sn-based nanoparticles on graphene as the anode of rechargeable lithium-ion batteries*. Journal of Materials Chemistry, 2012. **22**(8): p. 3300-3306.
56. Li, Z.Q., et al., *Band Structure Asymmetry of Bilayer Graphene Revealed by Infrared Spectroscopy*. Physical Review Letters, 2009. **102**(3).
57. Kuzmenko, A.B., et al., *Infrared spectroscopy of electronic bands in bilayer graphene*. Physical Review B, 2009. **79**(11).
58. Mak, K.F., et al., *The evolution of electronic structure in few-layer graphene revealed by optical spectroscopy*. Proceedings of the National Academy of Sciences of the United States of America, 2010. **107**(34): p. 14999-15004.
59. Tabert, C.J. and E.J. Nicol, *Optical conductivity of twisted bilayer graphene*. Physical Review B, 2013. **87**(12): p. 121402.

## Chapter 5: Exploring Adsorption and Reactivity of NH<sub>3</sub> on Reduced Graphene Oxide

The adsorption of Ammonia on RGO was studied through a combination of *in situ* IR spectromicroscopy experiments and density functional theory (DFT) calculations. The measurements were performed under realistic sensor operation (ambient pressure and temperature) to correlate observations with behavior in actual devices. The extremely heterogeneous substrates lead to a large number of absorption configurations and a rich vibrational spectrum. To understand the origin of these bands, DFT modeling of the interaction between the adsorbate and different representative sites in the substrate was performed. Based on comparison of the predictions of the theoretical models and experimental vibrational band frequencies, the overall behavior following adsorption on RGO is determined.

## 5.1 Introduction

Graphene is increasingly being utilized for applications such as gas sensing and heterogeneous catalysis that require good electrical conductivity, high surface area, and potentially reactive substrates. For example, single atomic layers of graphene produced by mechanical exfoliation of graphite have demonstrated single molecule sensitivity towards target gas molecules in ultrahigh vacuum (UHV) conditions.[1] Despite this impressive performance at low pressures, many applications would require sensitivity towards extremely low quantities of gases diluted in air. The relatively weak interaction between intrinsic graphene and most molecules would produce an intractably small signal under normal working conditions, thus hindering the implementation of graphene in ambient pressure sensing conditions. The interaction between graphene and most molecules of interest can, however, be enhanced by the introduction of chemically active defects. Materials such as graphene oxide (GO)[2, 3] and reduced graphene oxide (RGO)[4] are rich with such defects,[5, 6] including residual oxygen functional groups and a host of structural defects to the carbon lattice. In contrast to GO, RGO is highly conductive,[7] thus allowing for sufficient signal-to-noise ratio to detect low concentrations of target gases. Indeed, gas sensors that employ RGO have demonstrated impressive sensitivity, selectivity, and recovery time under realistic working conditions toward  $\text{NH}_3$ , a chemical of particular industrial and environmental relevance,[8-11] including as a means for storage and transportation of hydrogen.[12] Despite these demonstrations of the advantage of using RGO in sensing applications, and its potential in the closely related field of catalysis, little experimental evidence exists to elucidate the nature of the interaction between the RGO substrates and target gases. Furthermore, adsorption of small

molecules is a possible method of molecular doping to engineer electronic properties of graphene.[13-15] Thus it is important to study the adsorption of these molecules onto RGO to gain a fundamental understanding and to optimize RGO for real applications.

IR microspectroscopy is ideally suited to probe these processes. Unlike many other surface sensitive techniques, IR can be performed under ambient atmospheric pressure, *i.e.*, realistic working conditions, and it does not require well-ordered surfaces and/or interfaces to extract useful structural and chemical information. Here we report *in situ* IR microspectroscopy studies of NH<sub>3</sub> adsorption on RGO in conjunction with density functional theory (DFT) calculations to model the adsorption under various scenarios. We find evidence for molecular species adsorbed on the surface, and experiment and calculations are correlated to identify the chemical nature of these adsorbates. In particular, oxygen species and carbon vacancies can facilitate surface reactions with NH<sub>3</sub>, resulting in strongly chemisorbed adsorbates, in contrast to the case of pure graphene in which physisorption occurs with comparatively minimal effect on the substrate electronic properties.

## 5.2 Methods

RGO suspensions in *N,N*-dimethylformamide (DMF) were prepared as described previously[4]. Samples for IR microspectroscopy were prepared for transmission experiments by depositing a small quantity of the RGO dispersion onto IR transparent diamond windows. For the *in situ* measurements, the substrates were placed in a custom flow cell[16] that employs 0.5 mm IR transparent diamond windows for transmission measurements. IR microspectroscopy was performed at the synchrotron radiation center, using the multi-beam Infrared Environmental



Imaging (IRENI)[17, 18] beamline in the spectral range 7,000-650  $\text{cm}^{-1}$ . The beamline employs a Bruker Hyperion 3000 IR microscope equipped with both a Mercury Cadmium Telluride (MCT) single point detector and a focal plane array (FPA) detector. The flow cell was pumped on by an external exhaust system, producing a weak vacuum environment. 1%  $\text{NH}_3$  diluted in Ar was subsequently pumped through the flow cell at a flow rate of 28 mL/min. Ar was chosen as an inert balance gas of the diluted mixture to mimic UHV conditions and highlight only the surface chemistry of the target gases and not that of ambient atmospheric components.

Transmission measurements were performed *in situ* by collecting background single beam spectra on the sample using a 74 $\times$  objective of NA=0.65, effectively illuminating the samples with a cone of radiation with field components both parallel and perpendicular to the sample. Single beam spectra were recorded at the exact same position as the reference spectra to produce differential absorption spectra during exposure to the gases, highlighting only changes due to the adsorption. Individual spectra were collected for approximately 3 minutes.

Plane-wave density functional theory (DFT) calculations and geometry optimization were performed with the QUANTUM ESPRESSO package[19] using the Perdew-Zunger local density approximation (LDA)[20] for the exchange-correlation potential. Ultrasoft pseudopotentials with a plane-wave cutoff of 30 Ry ( $\sim 408$  eV) for the wavefunction and 300 Ry ( $\sim 4082$  eV) for the charge density were used to represent the interaction between ionic cores and valence electrons. A convergence threshold of  $10^{-8}$  eV was set for the energy self-consistency and the forces were relaxed to 0.005 eV/Å. Integration over the Brillouin zone was performed on a regular  $12 \times 12 \times 1$  Monkhorst-Pack  $\mathbf{k}$ -point grid. The computational unit cell consists of a  $3 \times 3$  graphene supercell with a single  $\text{NH}_3$  molecule adsorbed at different sites. The unit cell for defective graphene has one vacancy and that for RGO has one epoxide group in a  $3 \times 3$  supercell. A vacuum region of 12

Å was considered to separate the layer and its image in the direction perpendicular to the graphene plane. The adsorption energy,  $E_a$ , is defined as the difference between the energy of the system with a bound  $\text{NH}_3$  molecule and the sum of the energy of the isolated molecule and the graphene layer. The charge transfer from  $\text{NH}_3$  to graphene, defective graphene and RGO was calculated on the basis of Löwdin population analysis.[21]

## 5.3 Results

### 5.3.1 IR Spectra of Bare and Adsorbate-Covered RGO

The structure and composition of RGO was discussed in Chapter 4. To summarize, the properties of RGO can vary dramatically based on the preparation method, but it is generally accepted [22] that RGO is not the same as graphene, and that residual oxygen functional groups are always present to some extent, as previously reported for the case of the hydrazine-reduced GO presented here.[4] To understand the nature and effect of residual oxygen groups in our chemically RGO samples, an IR absorption spectrum of few-layer RGO for  $5000\text{-}650\text{ cm}^{-1}$  is shown in Fig. 5.1A. Several vibrational absorption bands indicate the average chemical status of the reduced material. The band at  $1200\text{ cm}^{-1}$  is assigned to the COC stretching modes of the remaining epoxide groups, and the band at  $1730\text{ cm}^{-1}$  is due to remaining carbonyls. The band at  $1580\text{ cm}^{-1}$  is due to the C=C stretch of the graphene lattice, which becomes IR active due to the presence of defects. Throughout the mid-IR region, strong background absorption is observed that approaches zero at lower energies and monotonically increases at higher energies.

Absorption in the mid IR region has previously been ascribed to direct interband transitions between valence and conduction bands for the case of monolayer graphene, [23] and interband transitions between the nearly parallel valence and conduction bands for the case of multilayer

graphene. [24-27] When comparing the absorption spectrum of few-layer RGO to that of pure graphene, [28] the decrease in the absorption at lower photon energies is due to oxygen functional groups that effectively open a band gap and suppress interband transitions at lower photon energies. This gap is particularly evident in the functional dependence of the broadband IR absorption. For the case of an  $M_0$ -type critical point, the joint-density of states (JDOS) coefficient is proportional to the square root of the photon frequency. [29] Squaring the absorption coefficient and finding the intercept of the linear trend gives the value of the band gap. Fig. 5.2 shows the square of the absorption coefficient of the sample for  $6000\text{-}650\text{ cm}^{-1}$  with the linear dependence of the absorption. The energy gap is found by the intercept of the linear dependence to the data at  $E_g=0.25\text{ eV}$  ( $2000\text{ cm}^{-1}$ ). This behavior clearly indicates the semiconducting nature of RGO, one of the features that make it particularly attractive as a sensing material. Due to the wide variability and inhomogeneity of substrate structure and composition though, it is likely that a range of values for the local energy gap exists based on domain sizes and local oxidation.

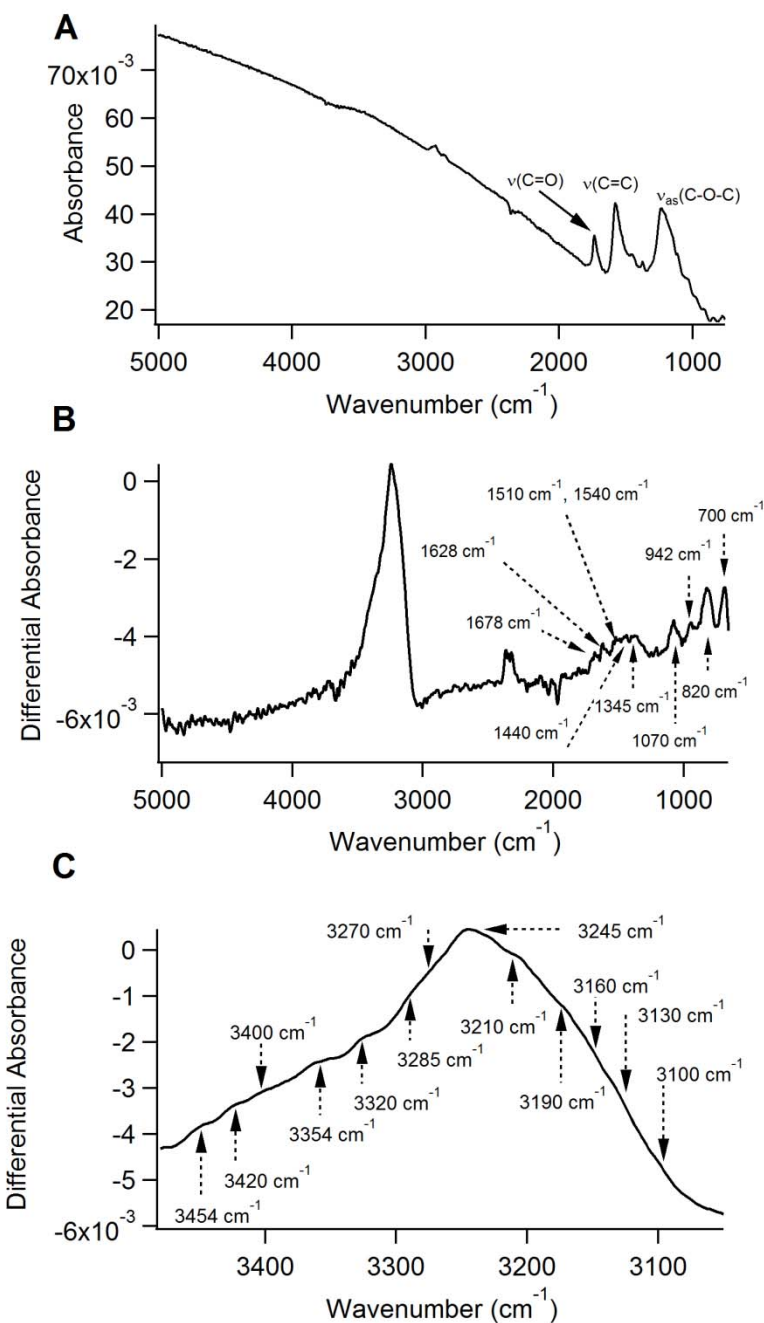


**Figure 5.1:** Absorption spectra of RGO and  $\text{NH}_3/\text{RGO}$ . A) IR absorption spectrum of RGO. The primary functional groups are due to epoxide (C-O-C,  $1200 \text{ cm}^{-1}$ ) and carbonyl (C=O,  $1740 \text{ cm}^{-1}$ ) groups, with few minority CH ( $2800\text{-}3000 \text{ cm}^{-1}$ ) and OH ( $3000\text{-}3600 \text{ cm}^{-1}$ ) groups. In this spectrum, the clean diamond window is used as the reference. B) Differential IR absorption spectrum of RGO exposed to 1%  $\text{NH}_3$  diluted in Ar at a flow rate of 28 mL/min. In this spectrum, the RGO sample before exposure to  $\text{NH}_3$  is used as the reference for the measurement. C) Enlargement of the N-H stretching region from B) to show the different components of the broad band from  $3000\text{-}3500 \text{ cm}^{-1}$ .

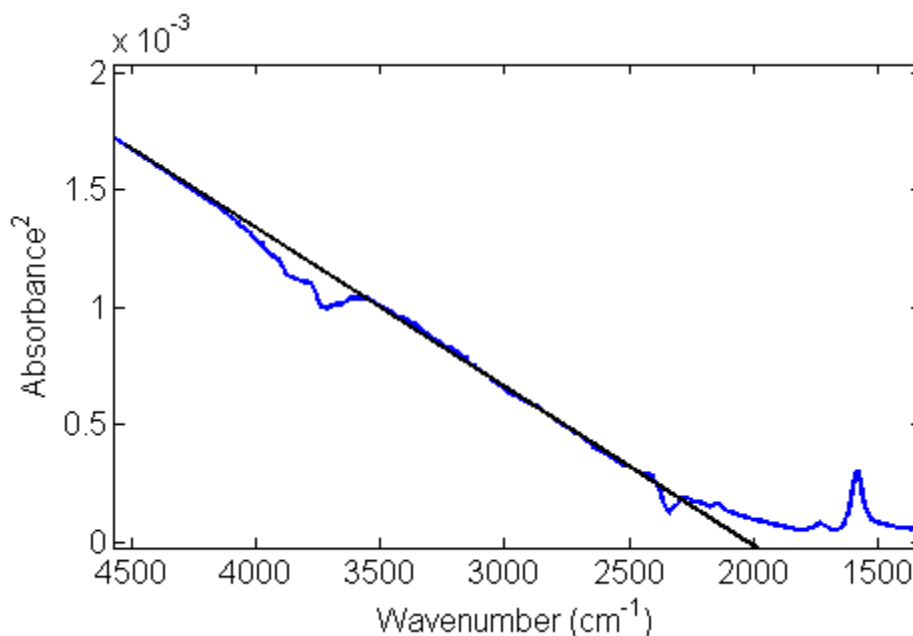


**Figure 5.2:** IR absorption of RGO (from Fig. 5.1) squared overlaid with a linear extrapolation to the intercept. The best agreement is obtained for  $E_g=0.25$  eV ( $2000\text{ cm}^{-1}$ ). The feature at  $\sim 3700\text{ cm}^{-1}$  is due to incomplete water vapor cancellation during the measurement.

The interaction of  $\text{NH}_3$  with RGO is now considered. Fig. 5.1B shows a representative differential IR absorption spectrum of RGO collected following 30-minute exposure to 1%  $\text{NH}_3$  diluted in Ar at a rate of 28 mL/min at atmospheric pressure. A broad, intense band is observed in the N-H stretching region ( $3000\text{-}3500\text{ cm}^{-1}$ ), with several other bands observed in the N-H deformation region ( $900\text{-}1700\text{ cm}^{-1}$ ), and two bands in the far IR region ( $<900\text{ cm}^{-1}$ ). A close observation of the NH stretching band reveals the presence of numerous overlapping bands, evidenced by shoulders and irregular changes in slope comprising the primary peak. To emphasize these features, an enlargement of the stretching region is shown in Fig. 5.1C. The most pronounced features are observed at 3100, 3136, 3160, 3190, 3208, 3230, 3245, 3270, 3285, 3320, 3360, 3400, 3420, and  $3453\text{ cm}^{-1}$ . Fourier Self Deconvolution (FSD) is applied (Fig.

5.3) to the raw spectral data to emphasize these bands and more clearly demonstrate their presence.

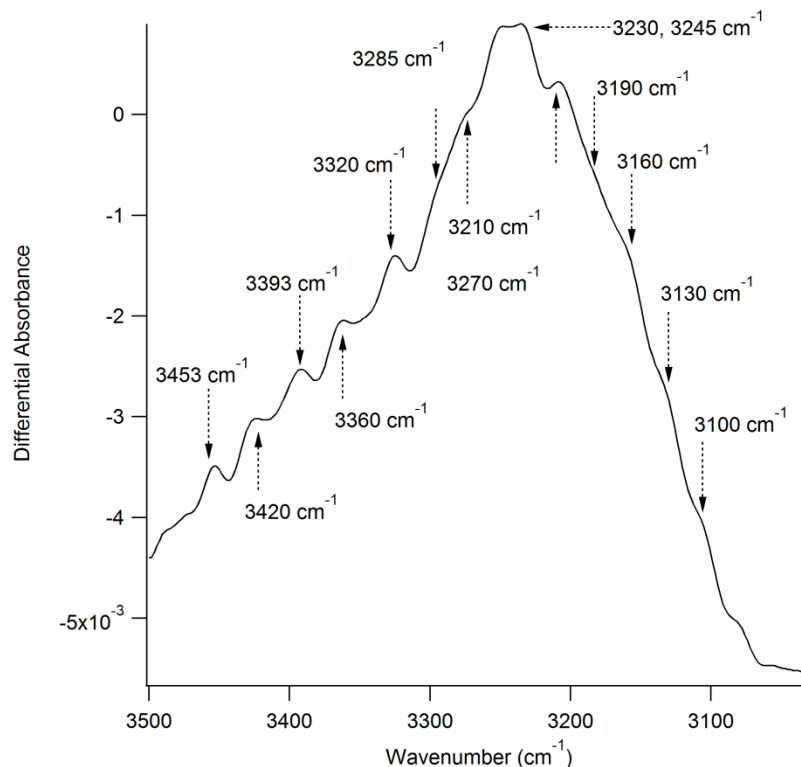


**Figure 5.3:** Application of FSD to  $\text{NH}_3/\text{RGO}$  differential spectra to emphasize the presence of the peaks given in the main text.

In the bending region, peaks are observed at 1682, 1623, 1540, 1508, 1440, 1374, 1300, 1158, 1070, and 942  $\text{cm}^{-1}$ ; the far IR region shows bands at 820 and 700  $\text{cm}^{-1}$ . Additionally, a reduction of intensity at the frequency of the COC stretch of the substrate is observed at 1225  $\text{cm}^{-1}$ . This change is slightly obscured due to the presence of other nearby absorption bands, but nevertheless clearly shows that the intensity of the frequency falls below the spectral baseline. This decrease is particularly evident from spectra taken at shorter exposure times, corresponding to lower coverage (Fig. 5.4).

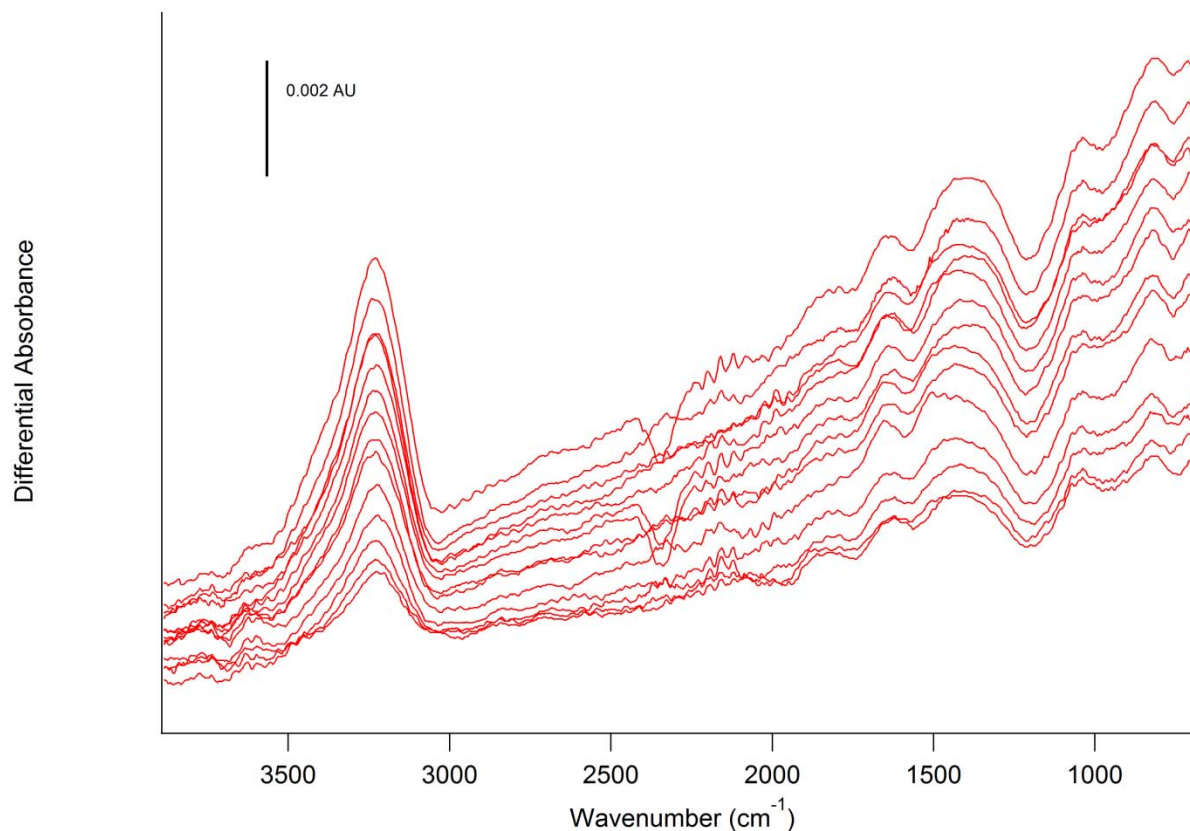


**Figure 5.4:** Time-dependent  $\text{NH}_3/\text{RGO}$  differential absorption spectra for exposure times ranging from 1 to 20 minutes (bottom to top, respectively) at a flow rate of 28 mL/min.

To better understand the origin of these absorption bands, the adsorption process was modeled using DFT calculations. Existing experimental data was considered to model the substrate atomic structure. High-resolution electron microscopy studies[6] have shown that RGO is quite heterogeneous, and contains regions that are basically graphene-like (graphitic) with minimal defects and dopants; contaminated or oxidized regions; and various types of structural defects including carbon vacancies, etch holes, and extended topological defects. Additionally, the IR data in Fig. 5.1 indicates that the majority oxygen species is the epoxide group. Whereas GO is commonly thought of as containing randomly distributed oxygen groups, theoretical studies have suggested that oxygen groups likely aggregate in island-like regions,[30,

31] consistent with published data [6]. Thus, to model molecular adsorption on the RGO surface, three structural models were considered with and without  $\text{NH}_3$  (Fig. 5.5): Case A (Figs. 5.5 A, D) graphitic regions; Case B (Figs. 5.5B, E) oxidized regions containing a single epoxide group; and Case C (Figs. 5.5C, F) defective regions with a carbon vacancy. While RGO is in reality far more complicated than any simple combination of the aforementioned models, the approach is to identify simple but realistic models containing the dominant interactions between  $\text{NH}_3$  and the RGO substrate in order to help identify the most significant features in the IR absorption spectra from  $\text{NH}_3/\text{RGO}$ . Although RGO contains carbonyl groups, as evidenced in the IR spectra in Fig. 5.1A, the interaction of  $\text{NH}_3$  with carbonyl groups was not modeled theoretically, but adsorption at these sites (Case D) was still considered on the basis of empirical evidence. Each of these types of bonding sites are considered in turn below and correlated with families of peaks observed in the IR data.

### 5.3.2 Adsorption at Different Sites in RGO, Modeling and Band Assignments

#### 5.3.2.1 Case A: $\text{NH}_3/\text{Graphene}$

First consider case A, the  $\text{NH}_3$  adsorption on pristine graphene. To find the most favorable adsorption configuration, the  $\text{NH}_3$  molecule is initially placed at different positions and in different orientations on the graphene sheet. The optimized structure has an adsorption energy of -0.12 eV, with the  $\text{NH}_3$  molecule adsorbed at the 6-fold hollow sites, 2.94 Å above the carbon basal planes with the H atoms pointing away from the graphene sheet, as depicted in Fig. 5.5D. The optimized structure with  $\text{NH}_3$  adsorbed at the 6-fold hollow site and H atoms pointing toward the graphene sheet has adsorption energy of -0.11 eV. For the  $\text{NH}_3$  molecule adsorbed either on a C-top or bridge site, the adsorption energy is -0.1 eV, irrespective of the orientation of



the H atoms, and the molecular geometries are essentially unchanged upon structural relaxations. In the actual sample, which is disordered and complex, a combination of these respective adsorption sites is likely due to the very small energy difference between the different configurations. The calculated results indicate a weak interaction for this configuration, suggesting that NH<sub>3</sub> molecules physisorb at the surface. The calculated density of states (Fig. 5.6) is nearly identical to a superposition of graphene and gas-phase NH<sub>3</sub>, and shows that NH<sub>3</sub> adsorption has little effect as a dopant, and the optimized adsorbate-substrate geometry (Table 5.1) shows that adsorption at such regions has a minimal effect on the molecular geometry as compared with the free molecule. Thus only minor changes to the vibrational frequencies compared to the gas phase values are expected. This scenario is consistent with the bands observed in the *in situ* experiments in the bending region at 942 and 1623 cm<sup>-1</sup> and in the stretching region at 3320, 3420, and 3453 cm<sup>-1</sup>. The bands at 3420 and 3453 cm<sup>-1</sup> are assigned to the degenerate asymmetric stretch, with the symmetric stretch at 3320 cm<sup>-1</sup>. The bands at 1623 and 942 cm<sup>-1</sup> are due to the asymmetric and symmetric deformation modes. The experimental gas phase values of the symmetric and asymmetric stretches are 3337 and 3444 cm<sup>-1</sup>, the experimental asymmetric deformation is at 1626, and the symmetric deformations (split due to inversion doubling) are at 932 and 968 cm<sup>-1</sup>. [32] The observation of two bands rather than one on either side of the gas phase value of 3445 cm<sup>-1</sup> in our spectra arises due to the splitting of the doubly degenerate *E* vibration following the lowering of the molecular symmetry upon adsorption. These values are in agreement with previously calculated values for fundamental frequencies of NH<sub>3</sub> on graphite. [33] While this model suggests adsorption at the high-symmetry 6-fold hollow sites is favorable, the real samples are not pristine graphene, and adjacent defects

can lower the effective site group symmetry and lead to the observed splitting, such as the case for  $\text{NH}_3$  molecules that adsorb at the carbon atoms adjacent to epoxide groups (Fig. 5.7).

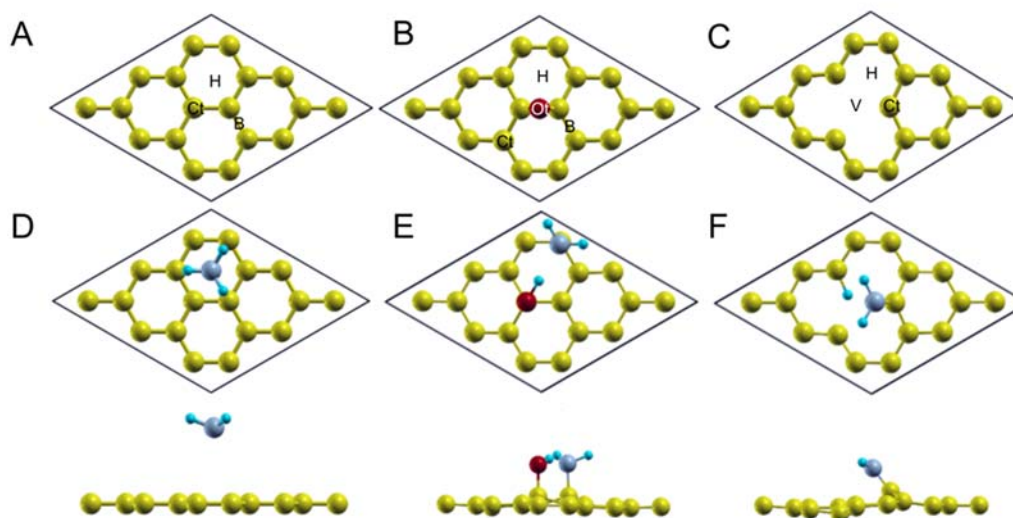


**Figure 5.5:** Structural models of RGO and  $\text{NH}_3$  adsorption on graphene and RGO. A-C)  $3 \times 3$  supercells used to model bare RGO containing (A) pristine graphene (Case A of main text), B) graphene with a single epoxide group (Case B) and C) graphene with a carbon vacancy (Case C). The relevant sites for which  $\text{NH}_3$  can adsorb are carbon-top (Ct), 6-fold hollow (H), bridge (B), vacancy (V), and oxygen-top (Ot). D-F) Optimized geometries for  $\text{NH}_3$  adsorption on the constituent regions in RGO. D) Case A:  $\text{NH}_3$  molecules adsorb molecularly on pristine graphene at the 6-fold hollow sites. E) Case B:  $\text{NH}_3$  molecules that adsorb near epoxide groups dissociate, resulting in  $\text{NH}_2$  and  $\text{OH}$  groups sitting at opposite C-top sites. F) Case C:  $\text{NH}_3$  molecules adsorbed at defects are dissociated into  $\text{NH}_2$  and H bonded to next nearest neighbor carbon atoms.

The adsorption of  $\text{NH}_3$  multilayers on graphite has been previously investigated by infrared reflection-absorption spectroscopy under conditions used for most surface science experiments (single crystal in UHV).[34] The reported stretching bands due to  $\text{NH}_3$  were located at  $3300$  and  $3380 \text{ cm}^{-1}$ , notably lower in frequency than the values reported here. These bands were attributed to the formation of crystalline  $\text{NH}_3$  multilayers, similar to solid  $\text{NH}_3$ , after dosing the surface at  $95 \text{ K}$ , and were removed entirely at  $105 \text{ K}$ . These conditions are certainly

significantly different than the case observed here. In addition, in the experiments shown here the  $\text{NH}_3$  absorption bands eventually saturated in intensity as the  $\text{NH}_3$  exposure time continued (Fig. 5.8). This suggests a Langmuir-type adsorption is dominant, rather than a Brunauer Emmett Teller (BET)-type multilayer adsorption.

The band observed in the deformation region at  $1440\text{ cm}^{-1}$  is also considered here. This band is in a frequency region characteristic of the NH deformation vibration of  $\text{NH}_4^+$  (gas-phase vibrational frequency of  $1447\text{ cm}^{-1}$ ). In addition, the peaks observed in the stretching region at  $3136$  and  $3160\text{ cm}^{-1}$  are very close to the gas phase  $\text{NH}_4^+$  stretching value of  $3145\text{ cm}^{-1}$  and arise due to the splitting of the degenerate  $T_2$  vibration.[32] The formation of  $\text{NH}_4^+$  from  $\text{NH}_3$  under the given experimental conditions is not surprising since the studies are performed under ambient atmospheric conditions, where these ions are likely formed following reaction of the  $\text{NH}_3$  with atmospheric or adsorbed water molecules or minority residual hydroxyl groups.

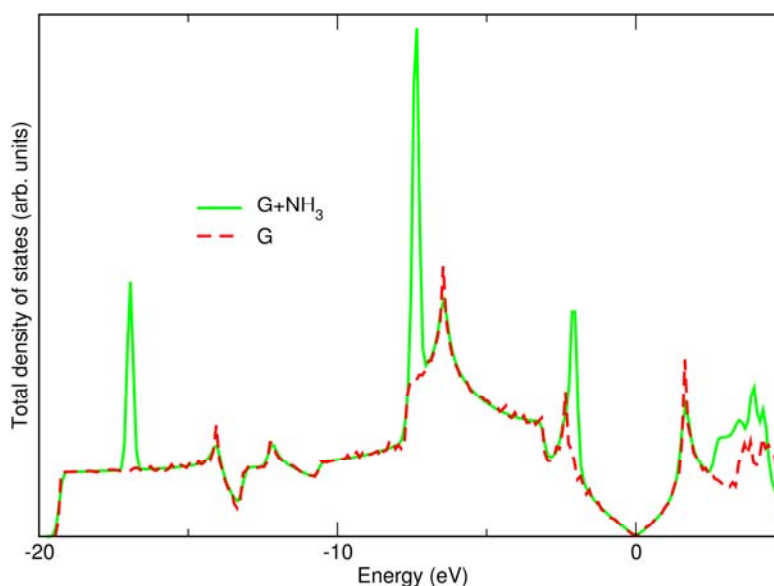


**Figure 5.6:** Comparison of the density of states for pristine graphene and graphene with a single  $\text{NH}_3$  molecule adsorbed at the 6-fold hollow site in a  $3 \times 3$  unit cell. A Gaussian broadening of  $0.13\text{ eV}$  ( $0.01\text{ Ry}$ ) has been used.

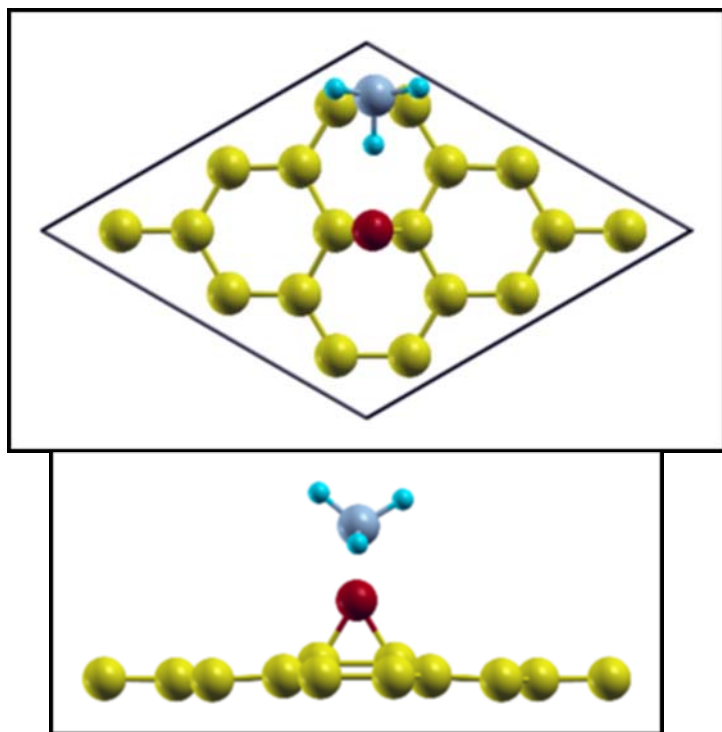


**Figure 5.7:** Optimized geometry of the most favorable site adjacent to an epoxide group for  $\text{NH}_3$  adsorbed on graphene with a single epoxide group.

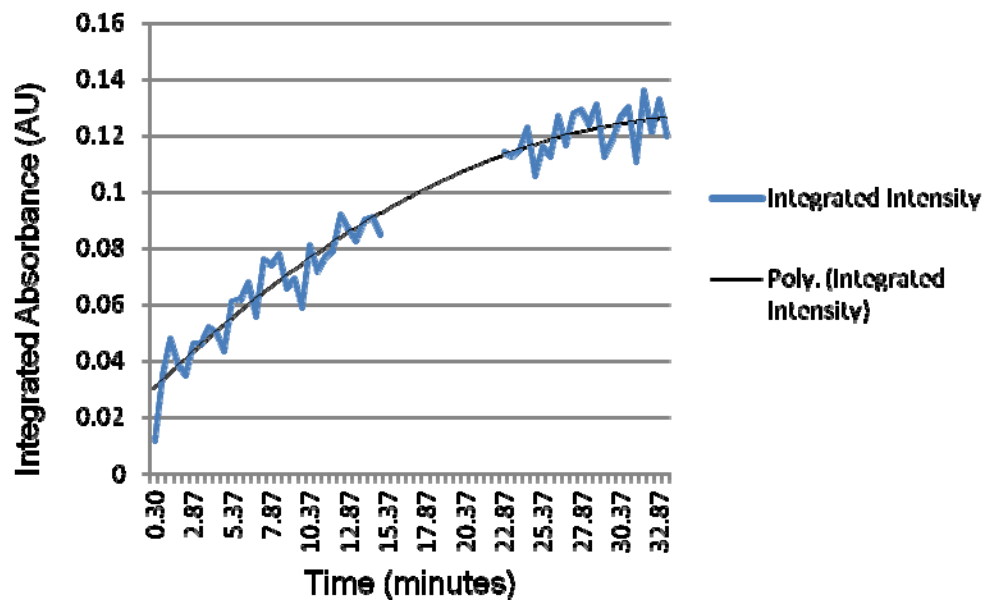


**Figure 5.8:** Integrated intensity of the NH stretching region as a function of exposure time. A particularly thin sample was used for this analysis, as thicker samples continued to intercalate continuously and would take much longer to saturate in intensity. The data is overlaid with a polynomial fit to show the plateau in intensity as a function of time. A gap of 8 minutes in the data is due to the examination of several portions of the sample during the experiment. During the time gap, another region of the sample was examined, and we then returned to the original region.

Structure	N-H bond length (Å)	H-N-H angle (degrees)
NH <sub>3</sub> isolated molecule	1.02	108
NH <sub>3</sub> on graphene (Fig. 3a)	1.02	108
NH <sub>3</sub> dissociated on graphene vacancy to form NH <sub>2</sub> +CH (Fig. 3c)	1.02	117
NH <sub>3</sub> on graphene with an epoxide group (Fig. S5)	1.02,1.03	108,109
NH <sub>3</sub> dissociated on graphene with epoxide group to form NH <sub>2</sub> + OH (Fig. 3b)	1.03	108
NH <sub>2</sub> isolated molecule	1.04	103

**Table 5.1:** NH bond angles and bond lengths of optimized NH<sub>x</sub> surface species on different sites in RGO.

### 5.3.2.2 Case B: NH<sub>3</sub>/Epoxide Groups in RGO

Next, consider Case B, where the interaction with the substrate plays a more significant role when NH<sub>3</sub> adsorbs onto a region containing a single epoxide group. DFT calculations show that for this case physisorption is again favored; in this case the calculated adsorption energy at bridge sites is -0.28 eV. (As before, adsorption at the other sites neighboring the epoxide group is likely to take place in the actual samples due to the similar adsorption energies). Nevertheless, relatively little effect on the molecular geometry and the substrate and adsorbate electronic states

is observed for this configuration (Table 5.1, Fig. 5.9). Thus the vibrational frequencies of 942, 1623, 3320, 3420, and 3453  $\text{cm}^{-1}$  are also representative of this type of adsorption. It is important to note that even when the initial adsorption site for the  $\text{NH}_3$  molecule is on a C-top site or the 6-fold hollow site, upon structural relaxations the molecule has a tendency to move toward the bridge site, which is the energetically favorable configuration. The  $\text{NH}_3$  molecule is now about 2.7 Å above the RGO layer with two of the H atoms facing away from the graphene sheet and the third H atom facing toward the O of the epoxide group. This configuration is a reaction intermediate preceding molecular dissociation. It is energetically favorable for the H atom that points toward the epoxide group to ultimately bond to the oxygen, resulting in the breaking of the NH bond and opening of the epoxide ring. This reaction resulting in dissociation of the  $\text{NH}_3$  molecule is favored over molecular adsorption by -0.37 eV. The process results in the formation of chemisorbed OH and  $\text{NH}_2$  groups bonded at opposite C-top sites (Fig. 5.5E), consistent with previously reported calculations and with *ex situ* IR spectra collected for graphite oxide treated with ammonia.[35, 36] The peaks that most closely correspond with this scenario are those at 1510  $\text{cm}^{-1}$  in the bending region and 3208, 3270, and 3400  $\text{cm}^{-1}$  in the stretching region. The frequencies at 3208 and 3270  $\text{cm}^{-1}$  are assigned to the symmetric and asymmetric stretches of adsorbed  $\text{NH}_2$ , respectively, and the 1510  $\text{cm}^{-1}$  band is assigned to the symmetric deformation. These assignments were made based on the optimized adsorbate geometry (Table 5.3.2.1), which shows only minimal perturbations relative to the gas phase bond lengths and angles. The frequencies of 1510, 3210, and 3270  $\text{cm}^{-1}$  are very close to the  $\text{NH}_2$  frequencies in the gas-phase (1497, 3220, and 3301  $\text{cm}^{-1}$ )[32] and are also in agreement with the relationship between the symmetric and asymmetric stretching frequencies for amino complexes as formulated by

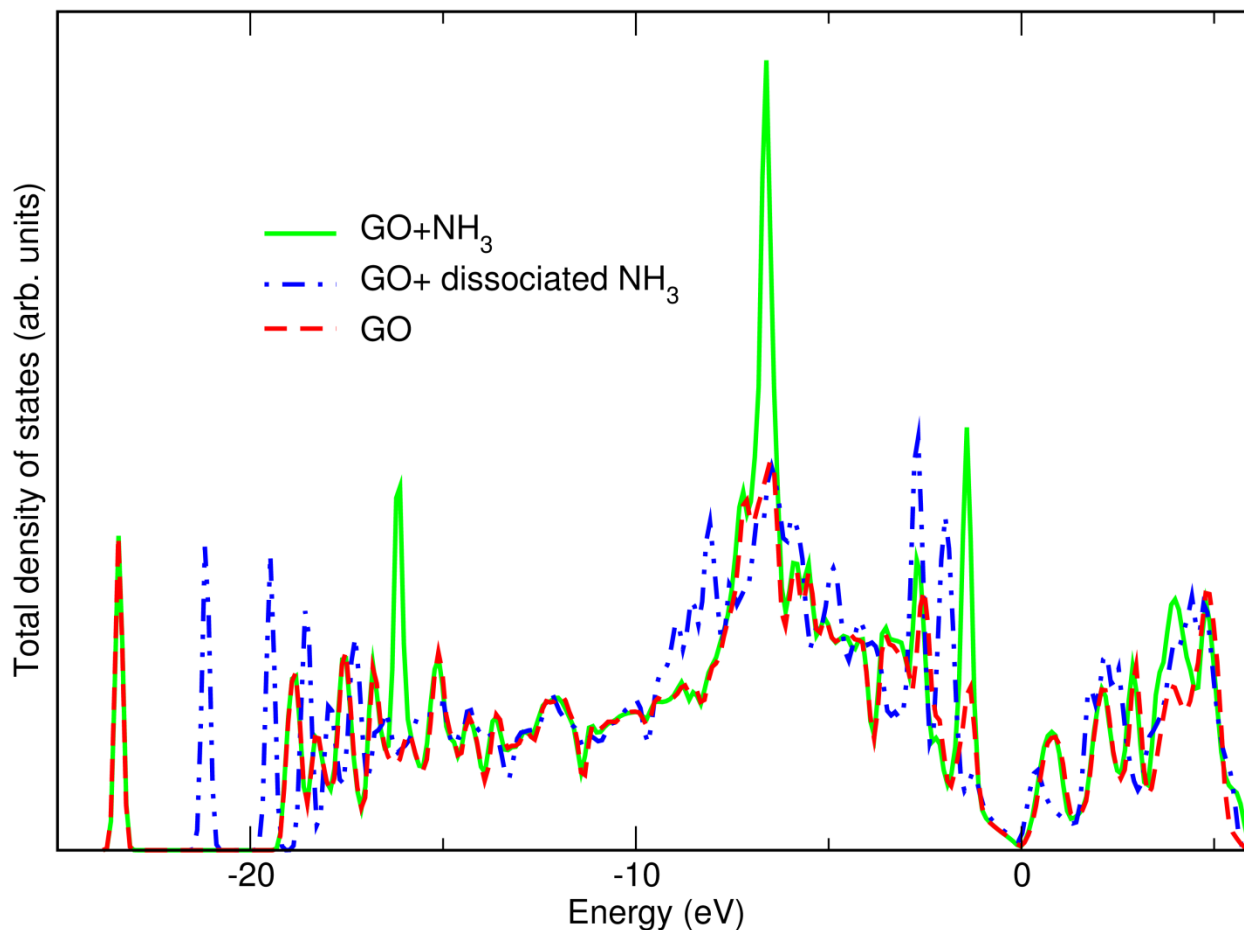


**Figure 5.9:** Calculated total density of states for graphene with a single epoxide group (Fig. 5.5B), graphene with a single epoxide group and a single  $\text{NH}_3$  molecule physisorbed (Fig. 5.7), and graphene with adsorbed  $\text{OH}$  and  $\text{NH}_2$  radicals (Fig. 5.5E). Importantly, significant changes are observed in the O and N 2s states for the case of the dissociated molecule. Such changes would produce measurable signals in a complementary *in situ* x-ray photoelectron spectroscopy (XPS) experiment, which would further support the work presented here.

Bellamy and Williams, [37]  $\nu_s = 0.876 \nu_{as} + 345.5 \text{ cm}^{-1}$ . Treating the  $3270 \text{ cm}^{-1}$  band as the asymmetric stretch in this equation yields a value for the symmetric stretch of  $3210 \text{ cm}^{-1}$ , in close agreement with the experimental data. The band at  $3400 \text{ cm}^{-1}$  is assigned to hydroxyl groups formed following the dissociation of  $\text{NH}_3$  and epoxide bond breaking (Fig. 5.5E). A decrease in the intensity of the COC stretching mode at  $1200 \text{ cm}^{-1}$  (Figs. 4.1B, 4.4) also provides evidence for the reduction in the number of epoxide bonds. The bands in the  $1300\text{-}1400 \text{ cm}^{-1}$  region are



assigned to the rocking mode of the O-H bond perpendicular to the surface. Note that in reality the samples are heterogeneous and may not result in exactly the structure shown in Fig. 4.5E; however, the experimental data definitively provide evidence for the reaction between  $\text{NH}_3$  and epoxide groups to form adsorbed  $\text{NH}_2$  and OH groups.

### 5.3.2.3 Case C: $\text{NH}_3$ /Carbon Vacancy

Now we consider case C that comprises  $\text{NH}_3$  interacting with carbon defect sites, which we find extremely reactive toward  $\text{NH}_3$ . The chemical activity of these and similar defect sites are consistent with previous experimental and theoretical works. Previous scanning tunneling microscopy (STM) studies [38] have reported an extremely high local density of states near the Fermi level localized to the dangling bonds, indicating high potential reactivity of these sites. DFT calculations showed that following the adsorption of  $\text{NH}_3$  at vacancy sites (adsorption energy of -1.71 eV), it is energetically favorable to dissociate into  $\text{NH}_2+\text{H}$ . These fragments bond to the  $\sigma$  bonds of opposing carbon atoms, resulting in adjacent C- $\text{NH}_2$  and C-H functional groups (Fig. 4.5F, adsorption energy of -2.85 eV). The optimized adsorbate geometry (Table 5.1) indicates a shorter N-H bond length for this configuration than the gas phase value, and a larger H-N-H bond angle. These observations suggest charge transfer out of the  $\text{NH}_2$  lone pair orbitals, and would blueshift the vibrational frequencies of both the stretching and bending modes with respect to the gas phase values (symmetric and asymmetric stretching respectively at 3220 and 3301  $\text{cm}^{-1}$  and bending at 1497  $\text{cm}^{-1}$ ) due to the shorter bond lengths. This is observed in the experimental spectra by the bands at 1540, 3100, 3285, and 3360  $\text{cm}^{-1}$ . The bands at 3285 and 3354  $\text{cm}^{-1}$  are assigned to the symmetric and asymmetric  $\text{NH}_2$  stretches, respectively, and the band at 1540  $\text{cm}^{-1}$  is due to the symmetric deformation. The energy separation between the NH stretching bands (3354 and 3285  $\text{cm}^{-1}$ ) is in good agreement with the equation previously noted

for the spacing between symmetric and asymmetric  $\text{NH}_2$  stretching vibrations, and is consistent with the expectations for the frequency shifts as compared with the gas phase value. For example, when the effective population of the  $\text{NH}_2$   $1b_1$  lone pair orbital is increased, the stretching frequencies are redshifted, as is the case for the amino anion,[32] and opposite to the behavior observed here. The deformation at  $1540\text{ cm}^{-1}$  is too low in frequency to be assigned to  $\text{NH}_3$ . The significant blue-shift of the stretching frequencies relative to the gas phase is indicative of strong electron donation to the substrate. The band at  $3100\text{ cm}^{-1}$  is due to the formation of C-H bonds following the dissociation of the molecule. This frequency for a C-H stretch on graphene coordinated via the  $\sigma$  bonds is a reasonable value, and is similar to the C-H stretching frequencies for aromatic hydrocarbons and unsaturated CH functional groups.[39] These peaks could also be assigned to  $\text{NH}_2$  groups bonded at other types of defects containing dangling  $\sigma$  bonds, such as unreconstructed holes and edges, divacancies, etc.

#### 5.3.2.4 Case D: Hydrogen Bonding with Other Functional Groups

There remain several bands in the deformation ( $1070$  and  $1678\text{ cm}^{-1}$ ) and stretching ( $3190$  and  $3245\text{ cm}^{-1}$ ) regions that are unaccounted for by the theoretically considered models. While the interaction with residual oxygen has mostly been considered through adsorption at epoxide sites in RGO, experimental IR spectra (Fig. 5.1A) and other reports[40-42] indicate that there are other minority species present in RGO as well, particularly carbonyl groups, with significantly fewer hydroxyls and hydrogen-terminated carbon edges. All three of these groups are likely to behave as active adsorption sites for  $\text{NH}_3$ . For carbonyl groups, adsorption is likely to occur through hydrogen bonding coordinated via the H atoms in  $\text{NH}_3$ , forming an  $\text{H}_2\text{NH}\cdots\text{O}$  bonding configuration. For  $\text{CH}_x$  groups  $\text{NH}_3$  adsorption will occur via hydrogen bonding coordinated by the nitrogen atom and for OH groups could occur either by coordination of the N

in  $\text{NH}_3$  to the H in the hydroxyl group or coordination of one of the H atoms in  $\text{NH}_3$  to the O in the hydroxyl group. Since previous theoretical studies have shown that hydroxyl groups can lead to  $\text{NH}_3$  dissociation followed by desorption of  $\text{H}_2\text{O}$  molecules, [36] it is unlikely that intact  $\text{NH}_3$  is adsorbed at the OH sites. Thus, as these bands suggest molecularly adsorbed  $\text{NH}_3$ , they are most likely due to  $\text{NH}_3$  hydrogen-bonded to the carbonyl groups. This assignment to hydrogen bonding at carbonyl groups, rather than at hydrogen-terminated edges, is due to the fact that oxygen is more electronegative than nitrogen, so hydrogen bonding of  $\text{NH}_3$  to carbonyl groups (coordinated by hydrogen in  $\text{NH}_3$ ) will be more energetically favorable than hydrogen bonding of  $\text{NH}_3$  to CH groups (coordinated by nitrogen). This does not, however, rule out the possibility of  $\text{NH}_3$  hydrogen-bonded to the hydrogen-terminated edges. The bands at 3245 and 3190  $\text{cm}^{-1}$  are assigned to the asymmetric and symmetric N-H stretches. The shifted values of the NH stretching and deformation vibrations relative to the gas phase values are characteristic of hydrogen bonding, which in general redshifts the stretching vibrations and blueshifts the symmetric deformation vibration.[39, 43] The band at 3230  $\text{cm}^{-1}$  is assigned to the first overtone of the symmetric deformation vibration.

The assignments given for the four cases A-D are not meant to represent *exactly* the models shown in Fig. 5.5, but rather to provide a simplistic description of the physical situation that occurs in the representative regions on the highly heterogeneous substrates.

### 5.3.3 Bands in the Far-IR Region

The assignments of  $\text{NH}_2$  groups in the representative configurations of Figs. 5.5E-F shed light on the bands in the far IR region at 821 and 700  $\text{cm}^{-1}$ . These bands are assigned to C- $\text{NH}_2$  stretching vibrations of the  $\text{NH}_2$  groups coordinated by the  $\sigma$  and  $\pi$  bonds, respectively, based on

the following observations: First, these bands cannot be assigned to any internal mode of molecularly adsorbed  $\text{NH}_3$ , as this frequency is much too low to be associated with the lowest frequency  $\text{NH}_3$  internal mode, the symmetric deformation vibration. Second, they also cannot be assigned to a C- $\text{NH}_3$  stretch for the following reason: our calculations suggest that there is no adsorption site, apart from carbon vacancies, at which chemisorption between the carbon substrate and  $\text{NH}_3$  takes place. Even at these vacancy sites, the presence of stable  $\text{NH}_3$  groups is unlikely, as dissociation is favored by 1.14 eV. Lastly, the 821 and 700  $\text{cm}^{-1}$  frequencies are too high in frequency to be the C- $\text{NH}_3$  stretch of the physisorbed  $\text{NH}_3$  molecules. To demonstrate this, consider Badger's rule, which relates the bond stretching force constants of two molecules with their bond length based on the periodic table. The system is treated as a carbon atom bonded to the  $\text{NH}_3$  molecule with a bond length of 2.94 Å. Application of Badger's rule then suggests 158  $\text{cm}^{-1}$  for the C- $\text{NH}_3$  stretching frequency. As an additional demonstration of the approximate frequency of such a vibration, a calculation of the force constant was performed based on the calculated energy of the system as a function of the height of the adsorbate above the graphene plane, extracted from the DFT calculation steps from the model in Fig. 5.5D. The molecule is initially started at 1.5 Å above the carbon plane, and rises to a height of 2.94 Å upon structural relaxations. The second derivative of the adsorption energy as a function of the height of  $\text{NH}_3$  above the graphene layer gives the adsorbate-substrate stretching force constant. Based on the extracted force constant, the C- $\text{NH}_3$  stretching frequency is 129  $\text{cm}^{-1}$ , in relative agreement with the frequency derived from Badger's rule. This is not meant to be a rigorous attempt to calculate the actual frequency of such a mode, but simply to demonstrate the overall frequency region in which the C- $\text{NH}_3$  stretching mode for the model in Fig. 4.5D is expected to be. As the determined frequency range for the graphene- $\text{NH}_3$  bond stretching mode is far below

the spectral range under consideration, the bands at 820 and 700  $\text{cm}^{-1}$  are assigned to the adsorbate-substrate stretches of two different amino species present on RGO following exposure to  $\text{NH}_3$ . The substantial difference in vibrational frequency of the two C-NH<sub>2</sub> stretch suggests a significant disparity in the bond strength of the adsorbate-substrate bond for the two amino species. The amino groups bonded at the defects via the carbon  $\sigma$  bonds, which are notoriously strong, are likely to produce a stronger-adsorbate substrate bond than those coordinated by the  $\pi$  electrons. Such a stronger bond will result in a higher C-NH<sub>2</sub> stretching frequency for the NH<sub>2</sub> groups coordinated via  $\sigma$  bonds (Fig. 5.5F) than via  $\pi$  bonds (Fig. 5.5E). The band at 820  $\text{cm}^{-1}$  corresponds to a higher vibrational frequency, indicating a stronger bond, and is assigned to the former leaving the band at 700  $\text{cm}^{-1}$  assigned to the amino groups coordinated via the  $\pi$  bonds. A summary of all band assignments is given in Table 5.2.

Functional Group	Bands Observed	Assignment to Absorption Fundamentals
Case A: Physisorbed NH <sub>3</sub> and NH <sub>4</sub> <sup>+</sup>	942 cm <sup>-1</sup> 1623 cm <sup>-1</sup> 3320 cm <sup>-1</sup> 3420, 3453 cm <sup>-1</sup> 3136 cm <sup>-1</sup> 3160 cm <sup>-1</sup> 1440 cm <sup>-1</sup>	NH <sub>3</sub> Symmetric Deformation NH <sub>3</sub> Asymmetric Deformation NH <sub>3</sub> Symmetric Stretch NH <sub>3</sub> Split asymmetric stretch NH <sub>4</sub> <sup>+</sup> Degenerate Stretch NH <sub>4</sub> <sup>+</sup> Degenerate Stretch NH <sub>4</sub> <sup>+</sup> Deformation
Case B: Chemisorbed NH <sub>2</sub> +OH	700 cm <sup>-1</sup> 1345 cm <sup>-1</sup> 1510 cm <sup>-1</sup> 3208 cm <sup>-1</sup> 3270 cm <sup>-1</sup> 3400 cm <sup>-1</sup>	C-NH <sub>2</sub> Stretch OH Rocking NH <sub>2</sub> Symmetric Deformation NH <sub>2</sub> Symmetric Stretch NH <sub>2</sub> Asymmetric Stretch OH Stretch
Case C: Chemisorbed NH <sub>2</sub> +H at defects	820 cm <sup>-1</sup> 1540 cm <sup>-1</sup> 3100 cm <sup>-1</sup> 3285 cm <sup>-1</sup> 3360 cm <sup>-1</sup>	C-NH <sub>2</sub> Stretch NH <sub>2</sub> Symmetric Deformation CH Stretch NH <sub>2</sub> Symmetric Stretch NH <sub>2</sub> Asymmetric Stretch
Case D: Hydrogen Bonded NH <sub>3</sub>	1070 cm <sup>-1</sup> 1678 cm <sup>-1</sup> 3190 cm <sup>-1</sup> 3245 cm <sup>-1</sup>	NH <sub>3</sub> Symmetric Deformation NH <sub>3</sub> Asymmetric Deformation NH <sub>3</sub> Symmetric Stretch NH <sub>3</sub> Asymmetric Stretch

**Table 5.1:** Summary of absorption bands observed in experimental IR spectra and their band assignments.

### 5.3.4 Adsorbate-Substrate Electronic Interactions

#### 5.3.4.1 Löwdin Population Analysis

To explore the effect of these groups on the substrate, the effective charges on each atom in the unit cell following adsorption were calculated using Löwdin population analysis.[21] These charges, in conjunction with the calculated density of states (DOS), demonstrate how the adsorbates dope the substrate and affect the nearby atoms, and also how the vibrational frequencies of the adsorbate may be modified. Fig. 5.10A-C shows the change in the effective valence charge on each atom in the unit cells shown in Figs. 5.5 and 5.7 relative to its value in an isolated  $\text{NH}_3$  molecule. Here, blue/red represents a depletion/gain of valence charges relative to the calculated nominal value in the isolated molecule. First, the calculated DOS for the  $\text{NH}_3$  molecule on graphene and graphene with a single epoxide group (Fig. 5.6, Fig. 5.9) shows that the adsorbate has almost no observable effect on the position of the Fermi energy relative to the Dirac point, indicating that such a scenario would produce little effect on the conductivity of the substrate. This negligible interaction is indicated in the diagram of Fig. 4.10A. All of the carbon atoms neighboring the adsorption site, and the atoms in the  $\text{NH}_3$  molecule, have valence charges that are very close to their nominal values, with a change in the valence charge of the  $\text{NH}_3$  of  $< 0.01 e$  as compared with the free molecule. The final structure for  $\text{NH}_3$  dissociated by an epoxide group (Fig. 5.5E) results in much stronger charge transfer. In the representation shown, the nitrogen atom is light blue, indicating some charge donation to the substrate. The oxygen atom in the hydroxyl group and the carbon atom below it are red, indicating acceptor behavior. This acceptor behavior is also indicated by the calculated DOS (Fig. 5.9), which shows an

increase at  $E_f$  following dissociation of the molecule relative to the initial DOS of the unit cell containing only an epoxide group. Similarly, for the  $\text{NH}_2$  and  $\text{CH}$  groups following  $\text{NH}_3$  dissociation at defect sites, the nitrogen atom is deep blue, indicating significant charge donation to the substrate. The carbon atom that hosts the dissociated hydrogen atom gains a substantial amount of charge. Several other atoms in the supercell also acquire small fractions of electronic charge. This charge depletion from the  $\text{NH}_2$  lone pair orbitals ultimately results in the decreased bond length, strengthening of the  $\text{N-H}$  bonds, and blueshift of the vibrational frequencies.

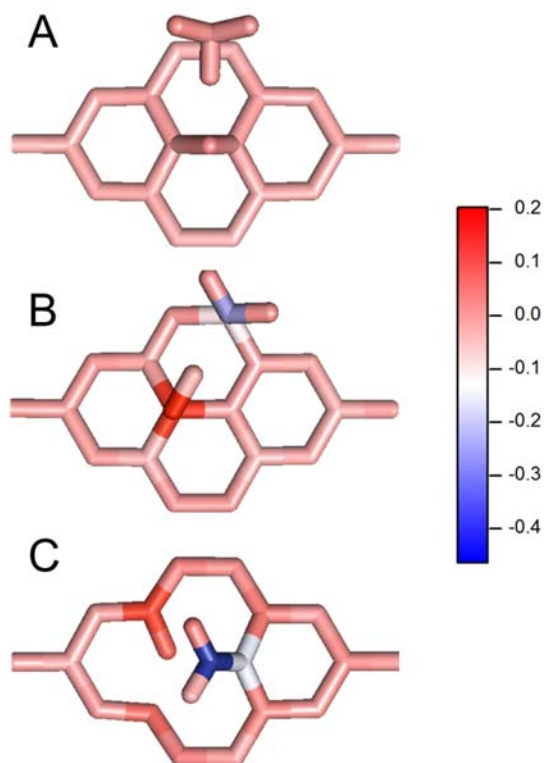


**Figure 5.10:** Adsorbate/substrate charge transfer in graphene supercells. A) Valence charge difference diagram for  $\text{NH}_3$  adsorbed on a bridge site in a supercell containing a single epoxide group. Very little difference from the nominal values is observed due to the weak interaction between the physisorbed  $\text{NH}_3$  group and the substrate. B) Valence charge difference diagram for  $\text{NH}_3$  dissociated by an epoxide to form chemisorbed  $\text{NH}_2$  and  $\text{OH}$  radicals. The nitrogen atom is blue, indicating charge is lost and donated to the



substrate. The adsorbed hydroxyl group and the carbon atom below it are red, indicating acceptor behavior. C) Valence charge difference diagram for  $\text{NH}_3$  dissociated by a C vacancy to form chemisorbed  $\text{NH}_2$  and H. The color bar shows the difference in valence charge in units of e.

This donation effect can also explain the observation of the overall negative broadband differential absorption observed in Fig. 5.1. The breaking of the epoxide bonds and strong electron donation of the various  $\text{NH}_x$  fragments has the effect of both raising the chemical potential above the Dirac point as well as suppressing the strong optical excitations associated with the epoxide-doping of the RGO. The net effect is a negative differential absorption.

#### 5.3.4.2 Unusual Strength and Shape of the NH Stretching Band

The anomalously large absorption strength of the N-H stretching band, as compared with the NH symmetric and asymmetric bending vibrations, is now addressed. Whereas in the gas-phase for both  $\text{NH}_3$  and  $\text{NH}_2$  the symmetric deformation mode is the most intense vibration, here the N-H bending region produces the strongest absorption. This absorption band also has an overall asymmetric shape, with a suppressed negative spectral weight relative to the background absorption on the low wavenumber side and a long absorption tail on the high wavenumber side. The suppression of the background absorbance on the low wavenumber side suggests that this feature cannot be assigned simply to inhomogeneous broadening. These asymmetric lineshapes, as previously observed for the case of CO on Cu(100)[44] and H on W(100),[45] are indicative of resonant coupling of the adsorbate vibration to the continuum of low energy substrate excitations. The effect has previously been attributed to adsorbate vibrational coupling to substrate electron-hole pair excitations.[46, 47] In this picture, the adsorbed molecule provides unoccupied electronic levels into which the substrate electrons can tunnel and occupied

electronic levels from which electrons can tunnel into the vacant electronic bands of the substrate. As the molecule vibrates, the position of this level oscillates relative to the Fermi energy, resulting in charge oscillations between the substrate and adsorbates. This process happens out of phase with the adsorbate vibration, resulting in a resonance and antiresonance absorption profile. For the case of RGO observed here, the energy of the NH stretches is too high to efficiently couple to the phonon continuum, and is also too high in energy to couple to intraband electron-hole pair excitations. Thus, the most likely excitations that can couple to the adsorbate vibrations in this energy range are the electron-hole pair excitations due to transitions between the valence and conduction bands. While the numerous overlapping bands in this region made it difficult to attribute exactly which surface species participates in this process, simple arguments suggest that only the  $\text{NH}_2$  groups formed from the dissociation of  $\text{NH}_3$  can contribute. The calculations and experimental spectra shown here indicate that  $\text{NH}_3$  and  $\text{NH}_4^+$  are predominantly physisorbed to RGO, by either van der Waals forces or hydrogen bonding. The physisorbed molecules not participating in hydrogen bonding are sufficiently far from the substrate that the tunneling process described above is unlikely. The carbonyl groups that contribute to hydrogen bonded  $\text{NH}_3$  have more localized electronic states, whereas mobile electrons are needed to participate in the damping of the adsorbate vibrations. The remaining majority species are the  $\text{NH}_2$  groups, which we described as being chemically bonded either on top of the carbon planes (Fig. 5.5B) or at defects (Fig. 5.5C). Both of these groups produce asymmetric and symmetric stretching vibrations in the spectral region under consideration. Symmetry arguments can be used to identify which absorption bands are most likely contributing to the asymmetric lineshape. Smith and Kevan[48] suggested, following analysis from Langreth,[46] that where there is electronic coupling to adsorbate vibrations, the

symmetries of the vibration and electronics states must be similar with respect to the surface mirror planes. Thus, the delocalized  $\pi$  electronic states (that are even with respect to the surface mirror planes) can only couple to the symmetric stretches of both types of adsorbed  $\text{NH}_2$  groups since the asymmetric stretches are odd with respect to the mirror planes. It is impossible from the analysis presented here, though, to conclusively state which species of  $\text{NH}_2$ , if not both, contribute to the electronic coupling. This model, however, does explain the uncharacteristically large absorption strength in the NH stretching region, which has its origin in the electronic component of the dynamical dipole moment of the coupled electron-vibration excitation.

### 5.3.5 Spatially Dependent Adsorption Distribution

IR imaging using an IR focal plane array (FPA) detector was performed to study the morphology of the  $\text{NH}_3/\text{RGO}$  system. Fig. 5.11A shows an IR image obtained from the raw absorbance at  $3300\text{ cm}^{-1}$ , of a multilayer RGO sample following exposure to  $\text{NH}_3$ . The absorption at this wavelength is dominated by the background electronic absorption of direct transitions between the RGO valence and conduction bands. This image may be used to visualize the shape and thickness of the sample, where the strength of the background absorption scales linearly with thickness. The image in Fig. 5.11A shows substantial variations in film thickness, providing a means to study the adsorption capacity of RGO as a function of film thickness. Fig. 5.11B shows a chemical image of the sample in Fig. 5.11A integrated over  $3000\text{--}3410\text{ cm}^{-1}$ , with a baseline used at the integration limits. The use of the baseline eliminates the background absorption and shows only the absorption due to the adsorbates' stretching modes. The resulting image is quite noisy at the single pixel level ( $0.54 \times 0.54\ \mu\text{m}^2$  projected sample area) due to the extremely weak vibrational absorption of the adsorbates as compared with the much stronger electronic absorption that additionally produces a severe modulation of the

baseline in the spectral region of interest. Despite the large level of noise, it is clear that the absorption is strongest in the central (thicker) region of the sample, and decreases with decreasing thickness at the periphery of the sample. To further illustrate this point, average spectra generated from the central and peripheral regions of the sample are shown in Fig. 5.11C. The red curve is generated by averaging all of the spectra within the solid white oval at the center of the flake shown in Fig. 5.11A, and the black curve is generated by averaging all of the spectra in the peripheral region shown by the dashed white oval in Fig. 5.11A. The spectra have been baseline corrected and smoothed for clarity. The bands due to the adsorbates appear somewhat different here than in the differential spectra of Fig. 5.1 due to a combination of the subtraction of the strongly varying electronic background and lower SNR of the FPA detector, but the previously assigned bands are still apparent. Upon examination, the absorption strength of the adsorbate stretching vibrations from the thick region is seen to be greater than that from the thin region. This has a very simple explanation: in the thicker regions, the space between the layers is sufficiently large to allow intercalation of the  $\text{NH}_3$  molecules. If the adsorption were taking place only on the surface of the flakes, a uniform absorption over the distribution of the sample would be expected. The higher quantity of adsorbates observed in the thicker region of the sample provides further confirmation that a Langmuir-type adsorption is dominant over a multilayer adsorption process. If the majority response were due to the continuous growth of a multilayer at the surface, a uniform distribution of the adsorbates over the thick and thin regions of the sample would be observed. A multilayer adsorption process between the RGO multilayers is also not possible due to the limited space between adjacent layers. The chemical image in Fig. 4B thus indicates that the adsorption onto multilayer RGO can be considered as a Langmuir process on each independent layer. The fact that thicker flakes can host more  $\text{NH}_3$

molecules/molecular fragments has a significant implication for sensor design: Since larger/thicker flakes will have an overall smaller resistance and if each layer can contribute as an independent single layer RGO sensor, the overall SNR will be better for thicker RGO films than for monolayer films.

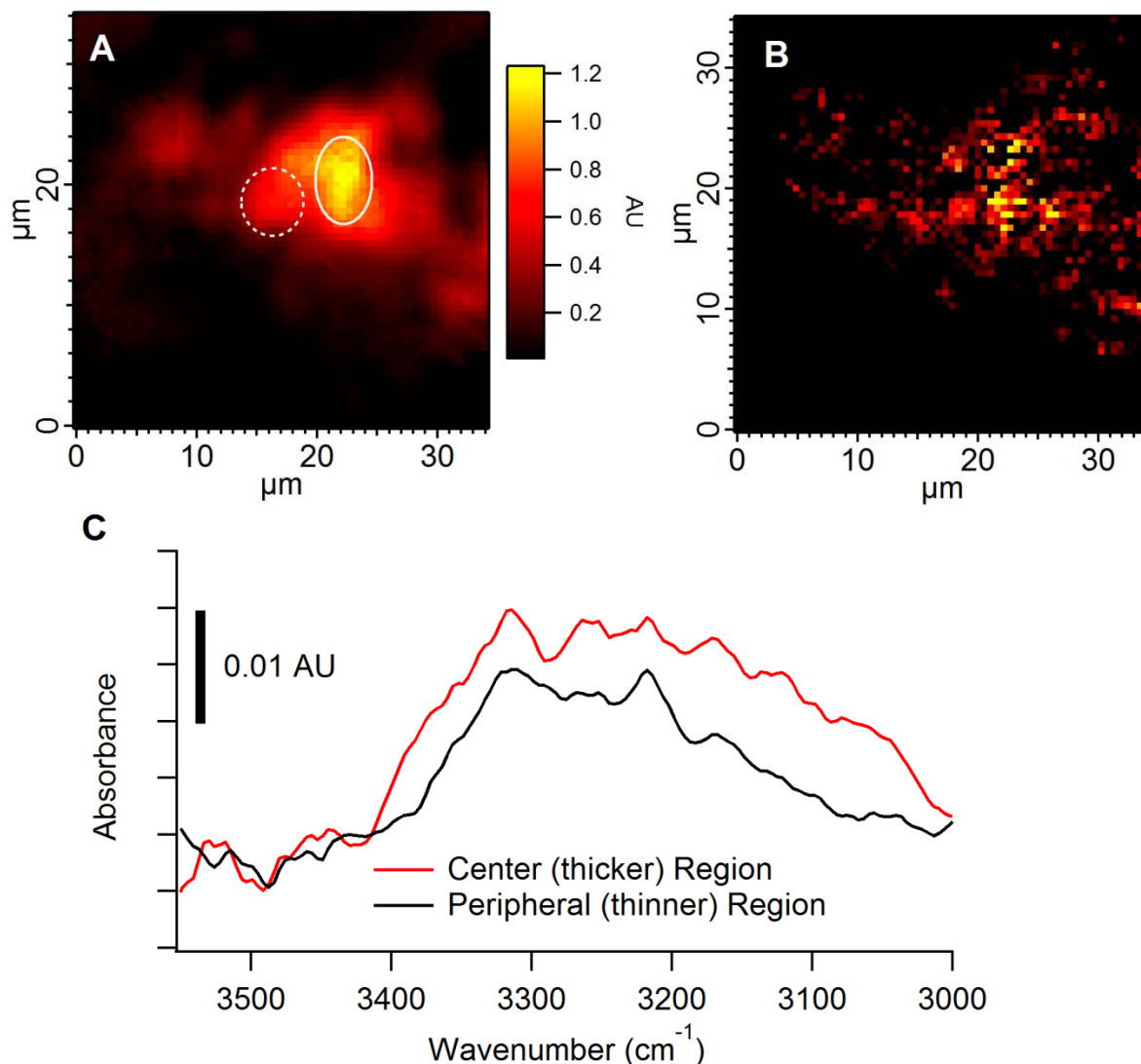


**Fig. 5.11: IR spectral imaging of NH<sub>3</sub>/RGO.** A) Raw absorbance at 3300 cm<sup>-1</sup> of NH<sub>3</sub>-covered RGO showing the distribution and profile of the RGO sample. The relative strength of the absorption is an indication of the local sample thickness. The reference for this measurement is the clean diamond window. B) Integrated absorbance from the image in A) over the spectral regions 3000-3410 cm<sup>-1</sup> (with same baseline). The reference for this measurement is again the clean diamond window. The data indicate the strongest NH functional group absorption is present at the central (thicker) region of the

sample, and the NH functional group absorption strength becomes weaker with decreasing thickness at the periphery of the sample. C) Comparison of spectra averaged from the central (thick) region and a peripheral (thin) region. The spectra have been baseline corrected to remove the electronic background and a 7-point smoothing was applied for clarity. The spectra demonstrate stronger absorption of the NH bands in the central thick region than in the thinner peripheral regions.

## 5.4 Conclusions

Structural and chemical defects introduced to the graphene lattice, such as those in RGO, act as highly reactive centers for  $\text{NH}_3$ . Four intuitive physical models are presented to account for the predominant contributions observed in the vibrational absorption spectrum. The calculations and experiments given here show that both epoxide groups and carbon vacancies can contribute to dissociation of the  $\text{NH}_3$  molecule, and such heterogeneity can result in a wide variety of adsorbed species. Calculations and the change in the background IR absorption suggest that all of these different surface species produce a small net electron donor effect. These data can facilitate understanding of how  $\text{NH}_3$  molecules interact with the RGO, which will be critical in furthering the development of RGO applications.

## 5.5 References

1. Schedin, F., et al., *Detection of individual gas molecules adsorbed on graphene*. Nature Materials, 2007. **6**(9): p. 652-655.
2. Stankovich, S., et al., *Graphene-based composite materials*. Nature, 2006. **442**(7100): p. 282-286.
3. Dikin, D.A., et al., *Preparation and characterization of graphene oxide paper*. Nature, 2007. **448**(7152): p. 457-460.
4. Park, S., et al., *Colloidal Suspensions of Highly Reduced Graphene Oxide in a Wide Variety of Organic Solvents*. Nano Letters, 2009. **9**(4): p. 1593-1597.

5. Mkhoyan, K.A., et al., *Atomic and Electronic Structure of Graphene-Oxide*. Nano Letters, 2009. **9**(3): p. 1058-1063.
6. Gomez-Navarro, C., et al., *Atomic Structure of Reduced Graphene Oxide*. Nano Letters, 2010. **10**(4): p. 1144-1148.
7. Gomez-Navarro, C., et al., *Electronic transport properties of individual chemically reduced graphene oxide sheets*. Nano Letters, 2007. **7**(11): p. 3499-3503.
8. Fowler, J.D., et al., *Practical Chemical Sensors from Chemically Derived Graphene*. Acs Nano, 2009. **3**(2): p. 301-306.
9. Lu, G.H., L.E. Ocola, and J.H. Chen, *Gas detection using low-temperature reduced graphene oxide sheets*. Applied Physics Letters, 2009. **94**(8).
10. Lu, G., L.E. Ocola, and J. Chen, *Reduced graphene oxide for room-temperature gas sensors*. Nanotechnology, 2009. **20**(44): p. 445502.
11. Lu, G.H., et al., *Toward Practical Gas Sensing with Highly Reduced Graphene Oxide: A New Signal Processing Method To Circumvent Run-to-Run and Device-to-Device Variations*. Acs Nano, 2011. **5**(2): p. 1154-1164.
12. Feibelman, P.J., *Thoughts on starting the Hydrogen Economy*. Physics Today, 2005. **58**(6): p. 13-14.
13. Zhou, S.Y., et al., *Metal to insulator transition in epitaxial graphene induced by molecular doping*. Physical Review Letters, 2008. **101**(8).
14. Liu, Z.H., et al., *Room-temperature Fano resonance tunable by chemical doping in few-layer graphene synthesized by chemical-vapor deposition*. Physical Review B, 2010. **82**(15).
15. Crowther, A.C., et al., *Strong Charge-Transfer Doping of 1 to 10 Layer Graphene by NO<sub>2</sub>*. Acs Nano, 2012. **6**(2): p. 1865-1875.
16. Nasse, M.J., et al., *Demountable Liquid/Flow Cell for in Vivo Infrared Microspectroscopy of Biological Specimens*. Applied Spectroscopy, 2009. **63**(10): p. 1181-1186.

17. Nasse, M.J., et al., *High-resolution Fourier-transform infrared chemical imaging with multiple synchrotron beams*. Nature Methods, 2011. **8**(5): p. 413-U58.
18. Nasse, M.J., et al., *Multi-beam synchrotron infrared chemical imaging with high spatial resolution: Beam line realization and first reports on image restoration*. Nuclear Instruments & Methods in Physics Research Section a-Accelerators Spectrometers Detectors and Associated Equipment, 2011. **649**(1): p. 172-176.
19. Giannozzi, P., et al., *QUANTUM ESPRESSO: a modular and open-source software project for quantum simulations of materials*. Journal of Physics-Condensed Matter, 2009. **21**(39).
20. Perdew, J.P. and A. Zunger, *Self-interaction correction to density-functional approximations for many-electron systems*. Physical Review B, 1981. **23**: p. 5048-5079.
21. Lowdin, P., *On the Non-Orthogonality Problem Connected with the Use of Atomic Wave Functions in the Theory of Molecules and Crystals* Journal of Chemical Physics, 1950. **18**(3): p. 365-375.
22. Mao, S., H.H. Pu, and J.H. Chen, *Graphene oxide and its reduction: modeling and experimental progress*. Rsc Advances, 2012. **2**(7): p. 2643-2662.
23. Li, Z.Q., et al., *Dirac charge dynamics in graphene by infrared spectroscopy*. Nature Physics, 2008. **4**(7): p. 532-535.
24. Mak, K.F., et al., *The evolution of electronic structure in few-layer graphene revealed by optical spectroscopy*. Proceedings of the National Academy of Sciences of the United States of America, 2010. **107**(34): p. 14999-15004.
25. Li, Z.Q., et al., *Band Structure Asymmetry of Bilayer Graphene Revealed by Infrared Spectroscopy*. Physical Review Letters, 2009. **102**(3).
26. Zhang, Y.B., et al., *Direct observation of a widely tunable bandgap in bilayer graphene*. Nature, 2009. **459**(7248): p. 820-823.
27. Lui, C.H., et al., *Observation of an electrically tunable band gap in trilayer graphene*. Nature Physics, 2011. **7**(12): p. 944-947.



28. Mak, K.F., et al., *Measurement of the Optical Conductivity of Graphene*. Physical Review Letters, 2008. **101**(19).
29. Wooten, F., *Optical properties of solids*. 1972: Academic Press.
30. Li, J.L., et al., *Oxygen-driven unzipping of graphitic materials*. Physical Review Letters, 2006. **96**(17).
31. Nguyen, M.-T., R. Erni, and D. Passerone, *Two-dimensional nucleation and growth mechanism explaining graphene oxide structures*. Physical Review B, 2012. **86**(11).
32. *NIST Chemistry Webbook*. NIST Chemistry Webbook, 2012.
33. Lakhlifi, A. and J.P. Killingbeck, *Dynamic and spectroscopic studies of single molecules physisorbed on graphite substrates. 2. Application to the ammonia molecule*. Journal of Physical Chemistry B, 2005. **109**(22): p. 11322-11331.
34. Bolina, A.S. and W.A. Brown, *Studies of physisorbed ammonia overlayers adsorbed on graphite*. Surface Science, 2005. **598**(1-3): p. 45-56.
35. Petit, C., M. Seredych, and T.J. Bandosz, *Revisiting the chemistry of graphite oxides and its effect on ammonia adsorption*. Journal of Materials Chemistry, 2009. **19**(48): p. 9176-9185.
36. Tang, S.B. and Z.X. Cao, *Adsorption and Dissociation of Ammonia on Graphene Oxides: A First-Principles Study*. Journal of Physical Chemistry C, 2012. **116**(15): p. 8778-8791.
37. Bellamy, L.J. and R.L. Williams, *Spectrochimica Acta*, 1957. **A9**: p. 341.
38. Ugeda, M.M., et al., *Missing Atom as a Source of Carbon Magnetism*. Physical Review Letters, 2010. **104**(9).
39. Stuart, B.H., *Infrared Spectroscopy: Fundamentals and Applications*. 2004, Chichester: John Wiley & Sons.
40. Acik, M., et al., *The Role of Intercalated Water in Multilayered Graphene Oxide*. ACS Nano, 2010. **4**(10): p. 5861-5868.

41. Acik, M., et al., *The Role of Oxygen during Thermal Reduction of Graphene Oxide Studied by Infrared Absorption Spectroscopy*. Journal of Physical Chemistry C, 2011. **115**(40): p. 19761-19781.
42. Bagri, A., et al., *Structural evolution during the reduction of chemically derived graphene oxide*. Nature Chemistry, 2010. **2**(7): p. 581-587.
43. Tsyganenko, A.A., D.V. Pozdnyakov, and V.N. Filimonov, *Infrared study of surface species arising from ammonia adsorption on oxide surfaces*. Journal of Molecular Structure, 1975. **29**: p. 299-318.
44. Hirschmugl, C.J., et al., *ADSORBATE-SUBSTRATE RESONANT INTERACTIONS OBSERVED FOR CO ON CU(100) IN THE FAR INFRARED*. Physical Review Letters, 1990. **65**(4): p. 480-483.
45. Chabal, Y.J., *Electronic Damping of Hydrogen Vibration on the W(100) Surface*. Physical Review Letters, 1985. **55**(8): p. 845-848.
46. Crljen, Ž. and D.C. Langreth, *Asymmetric line shapes and the electron-hole pair mechanism for adsorbed molecules on surfaces*. Physical Review B, 1987. **35**(9): p. 4224-4231.
47. Langreth, D.C., *Energy Transfer at Surfaces: Asymmetric Line Shapes and the Electron-Hole-Pair Mechanism*. Physical Review Letters, 1985. **54**(2): p. 126-129.
48. Smith, K. and S. Kevan, *Nonadiabatic adsorbate vibrational damping and surface electronic structure: H on W(001)*. Physical Review Letters, 1990. **64**(5): p. 567-570.

## Chapter 6: Bonding and Interactions at the NO<sub>2</sub>/Reduced Graphene Oxide Interface

The adsorption of NO<sub>2</sub> onto reduced graphene oxide (RGO) was investigated using *in situ* IR Microspectroscopy and DFT calculations. As for the case of NH<sub>3</sub> adsorption, the numerous possible adsorption sites lead to several distinct species of NO<sub>x</sub> on the surface. Physisorption occurs at graphitic regions while molecular chemisorption takes place at defects containing dangling bonds. Adsorption at the epoxide O-top sites leads to the formation of physisorbed NO<sub>3</sub> anions, and adsorption near carbonyl groups results in formation of NO<sub>3</sub> complexes that are chemisorbed to the carbon. A significant perturbation to the electronic structure is manifested as a broadband modulation of the background IR absorption. This is attributed to the reaction of NO<sub>2</sub> with the epoxide groups to form physisorbed NO<sub>3</sub>, causing an increase in the density of states near the Fermi energy and a lowering of the effective mass of these states.

## 6.1 Introduction

Nitrogen dioxide is among the most common toxic environmental pollutants, forming during combustion reactions in power plants and automobile exhaust. As such, tremendous effort has gone into developing substrate materials that are capable of both detecting the presence of  $\text{NO}_2$  in small quantities and changing its oxidation state into a more benign form. Devices based on graphene are proving to be a competitive alternative for the room temperature  $\text{NO}_2$ -based gas sensors. This is due to the high mobility of carriers and the ease with which the carrier density in graphene sheets may be modulated to produce a measureable signal. For example, adsorption of  $\text{NO}_2$  onto epitaxial graphene on SiC in ultra-high vacuum (UHV) has been shown to induce a metal-insulator transition by tuning the charge carriers from electrons to holes and exposing the small band gap induced by the substrate. [1] Despite this relatively large modulation of the transport properties under UHV conditions, operation under ambient atmospheric conditions requires competition for adsorption sites between the small concentration of the target molecules of interest with the much larger amount of atmospheric molecules including water, oxygen, and  $\text{CO}_2$ . It is thus desirable to use substrates which possess a strong, selective interaction with  $\text{NO}_2$ . In addition, the use of graphene derived from epitaxial growth on SiC or from mechanical exfoliation of graphite is extremely cost-prohibitive. Graphene oxide (GO) [2, 3] and reduced graphene oxide (RGO), [4] on the other hand, are inexpensive and contain numerous oxygen functional groups and structural defects to the carbon lattice. [5, 6] These chemically active defects have the potential to enhance the interaction between the substrate and targeted adsorbates and correspondingly enhance the modulation of transport properties following adsorption. RGO also has the advantage over GO of high conductivity. [7] Due to these attractive properties, RGO has been demonstrated to perform at a high level in a variety of

sensing applications.[8-18] However, as discussed in detail in Chapter 4, RGO is highly nonuniform, with varying stoichiometry, and spatially heterogenous chemical and atomic structure. [6] It has thus been difficult to understand the adsorbate bonding configuration and substrate-adsorbate interactions that give rise to the modulation of the transport properties. In this work, *in situ* synchrotron infrared microspectroscopy studies of NO<sub>2</sub> adsorption on RGO are presented in conjunction with density functional theory (DFT) calculations to model the adsorption. Based on correlations between experimental measurements and theoretical modeling, the majority surface species present following exposure of RGO to NO<sub>2</sub> are identified, and their collective effects on the local electronic structure are discussed.

## 6.2 Experimental

RGO suspensions in *N,N*-dimethylformamide (DMF) were prepared as described previously[4]. Samples for IR microspectroscopy were prepared for transmission experiments by depositing a small quantity of the RGO dispersion onto IR transparent diamond windows. For the *in situ* measurements, the substrates were placed in a custom flow cell [19] that employs 0.5 mm thick, 3 mm diameter, IR transparent diamond windows for transmission measurements. IR microspectroscopy was performed at the synchrotron radiation center, using the multi-beam IRENI [20, 21] beamline in the spectral range 8,000-650 cm<sup>-1</sup>. Transmission measurements were performed *in situ* by collecting background single beam spectra on the sample using a 74× objective of NA=0.65. Measurements were taken on the RGO sample in the flow cell before and during exposure to NO<sub>2</sub>. The flow cell was pumped on by an external exhaust system, producing a weak vacuum environment. 100 ppm NO<sub>2</sub> diluted in Ar was subsequently pumped through the flow cell at a flow rate of 63 mL/min. Ar was chosen as an inert balance gas of the diluted mixture to mimic UHV conditions and highlight only the surface chemistry of the target gases

and not that of ambient atmospheric components. Single beam spectra were recorded at the exact same position as the reference spectra to produce differential absorption spectra during exposure to the gases, highlighting only changes due to the adsorption. Individual spectra were collected for approximately 3 minutes at  $8 \text{ cm}^{-1}$  spectral resolution.

Plane-wave density functional theory (DFT) calculations and geometry optimization were performed with the QUANTUM ESPRESSO package[22] using the Perdew-Zunger local density approximation (LDA) [23] for the exchange-correlation potential. Ultrasoft pseudopotentials with a plane-wave cutoff of 30 Ry ( $\sim 408 \text{ eV}$ ) for the wavefunction and 300 Ry ( $\sim 4082 \text{ eV}$ ) for the charge density were used to represent the interaction between ionic cores and valence electrons. A convergence threshold of  $10^{-8} \text{ eV}$  was set for the energy self-consistency and the forces were relaxed to  $0.005 \text{ eV}/\text{\AA}$ . Integration over the Brillouin zone was performed on a regular  $12 \times 12 \times 1$  Monkhorst-Pack  $\mathbf{k}$ -point grid. The computational unit cell consists of a  $3 \times 3$  graphene supercell with a single  $\text{NO}_2$  molecule adsorbed at different sites. The unit cell for defective graphene has one vacancy and that for RGO has one epoxide group in a  $3 \times 3$  supercell. A vacuum region of  $12 \text{ \AA}$  was considered to separate the layer and its image in the direction perpendicular to the graphene plane. The adsorption energy,  $E_a$ , is defined as the difference between the energy of the system with a bound  $\text{NO}_2$  molecule and the sum of the energy of the isolated molecule and the graphene layer. The charge transfer from  $\text{NO}_2$  to graphene, defective graphene and RGO was calculated on the basis of Löwdin population analysis.[24]

## 6.3 Results and Discussion

### 6.3.1 Differential IR Absorption of NO<sub>2</sub>/RGO

The structure and composition of RGO was discussed at length in Chapter 4; in brief, RGO can vary in composition based on the preparation method, [25] but is well known to differ dramatically from the structure of pristine graphene.[6, 26] Furthermore, irrespective of its synthesis, RGO always contains some degree of residual oxidation. [25] For the case of hydrazine-reduced GO presented here,[4] the nature of the residual oxygen groups was illuminated by IR absorption measurements shown in Chapter 4. The absorption spectrum of the RGO substrate used for the experiments in which NO<sub>2</sub> was adsorbed is shown here in Fig. 4.16-4.17. Based on the analysis in Chapter 4, it was found that the onset of the absorption edge occurred at  $\approx 0.22$  eV ( $1800$  cm<sup>-1</sup>). The spectrum was taken *in situ* immediately before exposing the sample any NO<sub>2</sub> molecules.

Fig. 6.1A shows a differential absorption spectrum of RGO following a 29 min exposure to 100 ppm NO<sub>2</sub> diluted in Ar at a flow rate of 63 mL/min, at which point the absorption bands are saturated. The differential absorbance here is the logarithm of the ratio of the transmittance of the RGO exposed to NO<sub>2</sub> to the transmittance of the RGO prior to exposure. For clarity, the bands due to atmospheric absorption and gas-phase NO<sub>2</sub> have been subtracted. Several absorption bands are observed below  $2000$  cm<sup>-1</sup> in conjunction with a significant modulation in the broadband IR absorption; spectral weight is transferred from higher to lower energies resulting in negative absorbance at frequencies above  $4500$  cm<sup>-1</sup> and positive absorbance below  $4500$  cm<sup>-1</sup>. This shift in the spectral weight is discussed in detail below, and the vibrational absorption bands in the mid-IR fingerprint region are considered first. For ease of interpretation, the emphasis is on the most diagnostic spectral region,  $1000$ - $1700$  cm<sup>-1</sup>, the region in which the

N-O bond stretching vibrations occur. Fig. 6.1B shows an enlargement of the spectrum in Fig. 6.1A in the N-O stretching region. The absorption profile in this region consists of several overlapping bands sitting on a very broad background. To identify more clearly how many bands are present, the region from 800-17070  $\text{cm}^{-1}$  was baseline corrected and fitted with several Gaussian absorption bands (Fig. 6.2). In this system there is substantial inhomogeneous broadening and fairly low SNR; however, the curve fitting approach provides the most effective assessment of the predominant absorption bands present. The peak positions of the most significant bands are located at 1700, 1560, 1495, 1425, 1367, 1235, 1150, 1060, and 975  $\text{cm}^{-1}$ . In making the band assignments, it is instructive to consider existing literature on  $\text{NO}_2$  adsorption on pure graphite and soot. Muckenhuber and Grothe [27] performed diffuse reflectance infrared fourier transform spectroscopy (DRIFTS) to study  $\text{NO}_2$  adsorption on graphite and various types of soots and carbon black in high-vacuum conditions. Several of the bands observed in their work are consistent with bands observed in Figs. 6.1-6.2, and their assignments were supported by isotopic substitution. In particular, a strong absorption band was observed at 1230  $\text{cm}^{-1}$  on soot and graphite samples, assigned to a C-O vibration of chemisorbed C-O-N=O species. Interestingly, this band was only observed on graphite when the samples reacted at 400°C, suggesting a large activation barrier for adsorption in this configuration. The corresponding N=O stretch for this species was observed at 1485  $\text{cm}^{-1}$ . A bands at 1560  $\text{cm}^{-1}$  was also observed and assigned to R- $\text{NO}_2$  groups where R could represent either extended aromatic structure or disordered carbon network.

Based on the known assignments for the  $\text{NO}_2$ /soot and  $\text{NO}_2$ /graphite systems, the role of oxygen in RGO and the remaining bands not observed in these systems can be more clearly distinguished. The assignments of the bands observed in the data in Fig. 6.1 are given in table



6.1. Before discussing the assignments of the bands observed in the data shown here, the atomic structure of RGO is first considered in conjunction with first principles modeling. The approach toward modeling the substrate is identical to that considered in Chapter 5; RGO is decomposed into graphitic regions, oxidized (epoxide) regions, and defective regions (carbon vacancy).

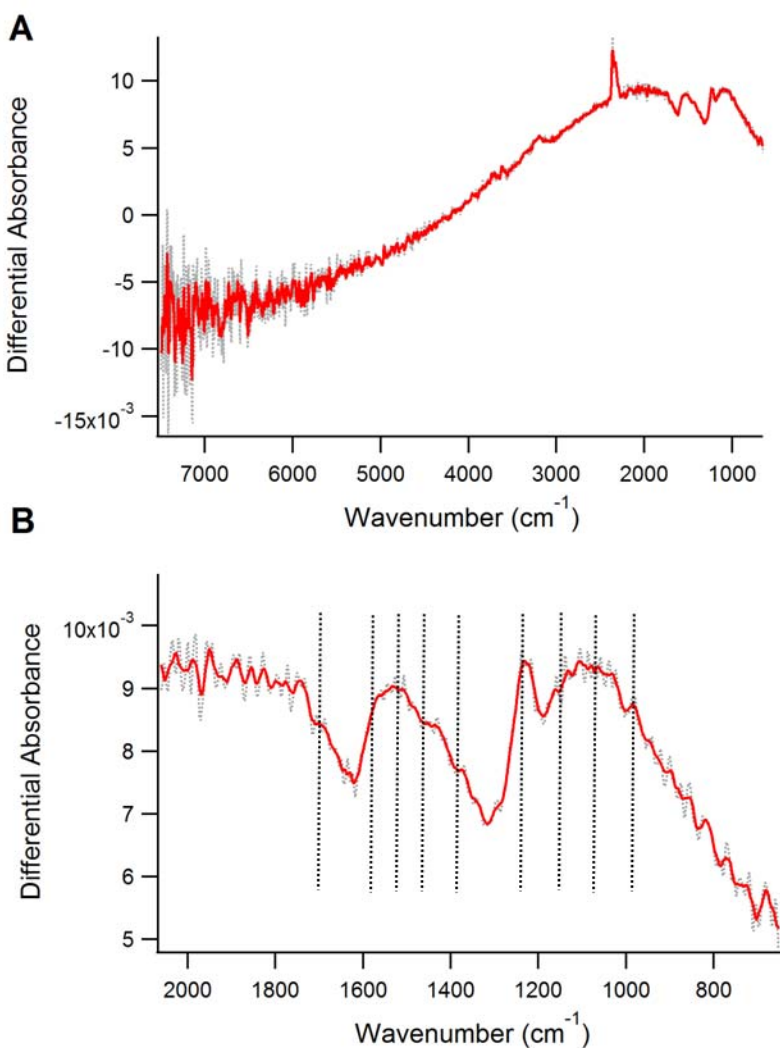


**Fig. 6.1:** Differential absorption of the  $\text{NO}_2/\text{RGO}$  system over the entire mid-IR (A) and the fingerprint region (B). The spectrum is generated using the clean RGO as the reference spectrum for the adsorbate-covered RGO. The absorption bands contributing to the spectrum are indicated by the dashed lines.

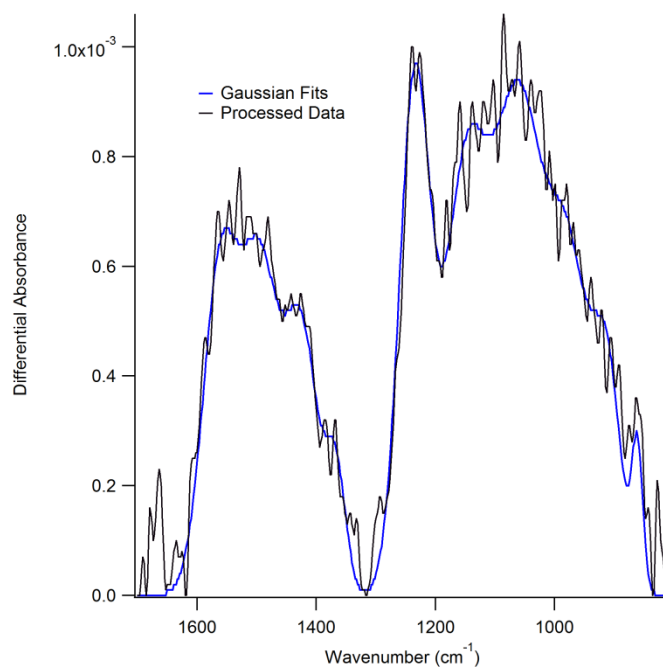


**Fig. 6.2:** Gaussian curve fits to baseline corrected data from Fig. 6.2.

Surface Species	Bands Observed	Functional Group Assignment
Physisorbed NO <sub>2</sub>	1560 cm <sup>-1</sup>	NO <sub>2</sub> Asymmetric Stretching
Physisorbed N <sub>2</sub> O <sub>4</sub>	1700 cm <sup>-1</sup> 1367 cm <sup>-1</sup>	NO <sub>2</sub> Asymmetric Stretching NO <sub>2</sub> Symmetric Stretching
Physisorbed NO <sub>3</sub> <sup>-</sup>	1425 cm <sup>-1</sup> 1150 cm <sup>-1</sup> 1060 cm <sup>-1</sup>	NO <sub>3</sub> Asymmetric Stretch NO <sub>3</sub> Asymmetric Stretch NO <sub>3</sub> Symmetric Stretch
Chemisorbed NO <sub>2</sub> <sup>-</sup>	1495 cm <sup>-1</sup> 1235 cm <sup>-1</sup>	N=O Stretching N-O Stretching

**Table 6.1:** Assignments of observed bands in the fingerprint region to N<sub>x</sub>O<sub>y</sub> species formed following exposure of RGO to NO<sub>2</sub>.

### 6.3.2 Correlating IR Measurements with Theoretical Modeling

First, the case of NO<sub>2</sub> adsorption on regions that are predominantly graphene-like is considered. DFT calculations, in agreement with previous reports, [28, 29] suggest molecular physisorption of NO<sub>2</sub> at these regions. The optimized structure (adsorption energy = 0.3 eV) shows that the most energetically favorable configuration consists of the molecule adsorbed at the carbon bridge site, with the oxygen atoms pointing toward the graphene sheet (Fig 6.4A). The nitrogen atom is 3.35 Å above the carbon plane indicating physical adsorption between the graphene sheet and NO<sub>2</sub>. Other adsorbate geometries, such as NO<sub>2</sub> physisorbed in a C<sub>2v</sub> configuration at the C-top and 6-fold hollow sites, had very similar adsorption energies to the

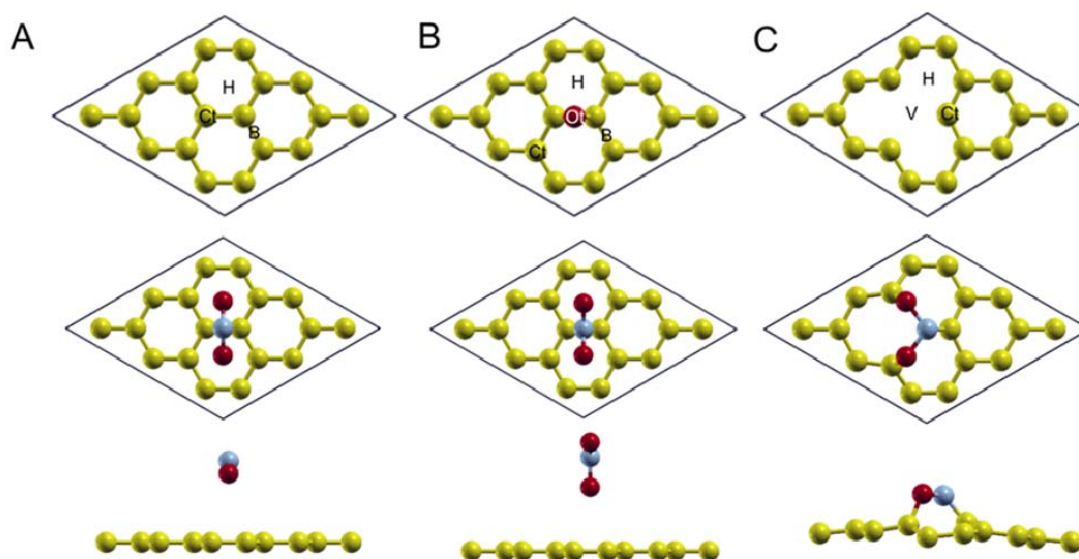


**Fig. 6.3:** Representative structural models used for modeling the interaction of NO<sub>2</sub> with various structures in RGO. A) Adsorption at graphitic regions can be described by physisorption of NO<sub>2</sub> over the bridge sites. B) Starting from the O-top site, NO<sub>2</sub> can react with an epoxide group to form physisorbed NO<sub>3</sub>. C) Adsorption at a single carbon vacancy results in a C<sub>2v</sub> bonding configuration in which each atom in the NO<sub>2</sub> bonds to a carbon atom at the defect.

structure in 6.3A and are also likely to represent subpopulations of adsorbates that are indistinguishable from one another in the IR experiments. The calculated total density of states (TDOS) for the structure in Fig. 6.3A before and after adsorption of NO<sub>2</sub> is shown in Fig. 6.4. The electronic states of the substrate are overall very similar with and without the presence of NO<sub>2</sub>, but the position of the Fermi level following adsorption of NO<sub>2</sub> is redshifted as compared to the clean substrate. This indicates hole doping of the substrate and small fractional charge transferred to the NO<sub>2</sub>. Thus a minor redshift of the molecular vibrational frequencies is expected as compared to the gas phase values (asymmetric and symmetric stretching at 1618 and 1318 cm<sup>-1</sup>, respectively [30]). This situation

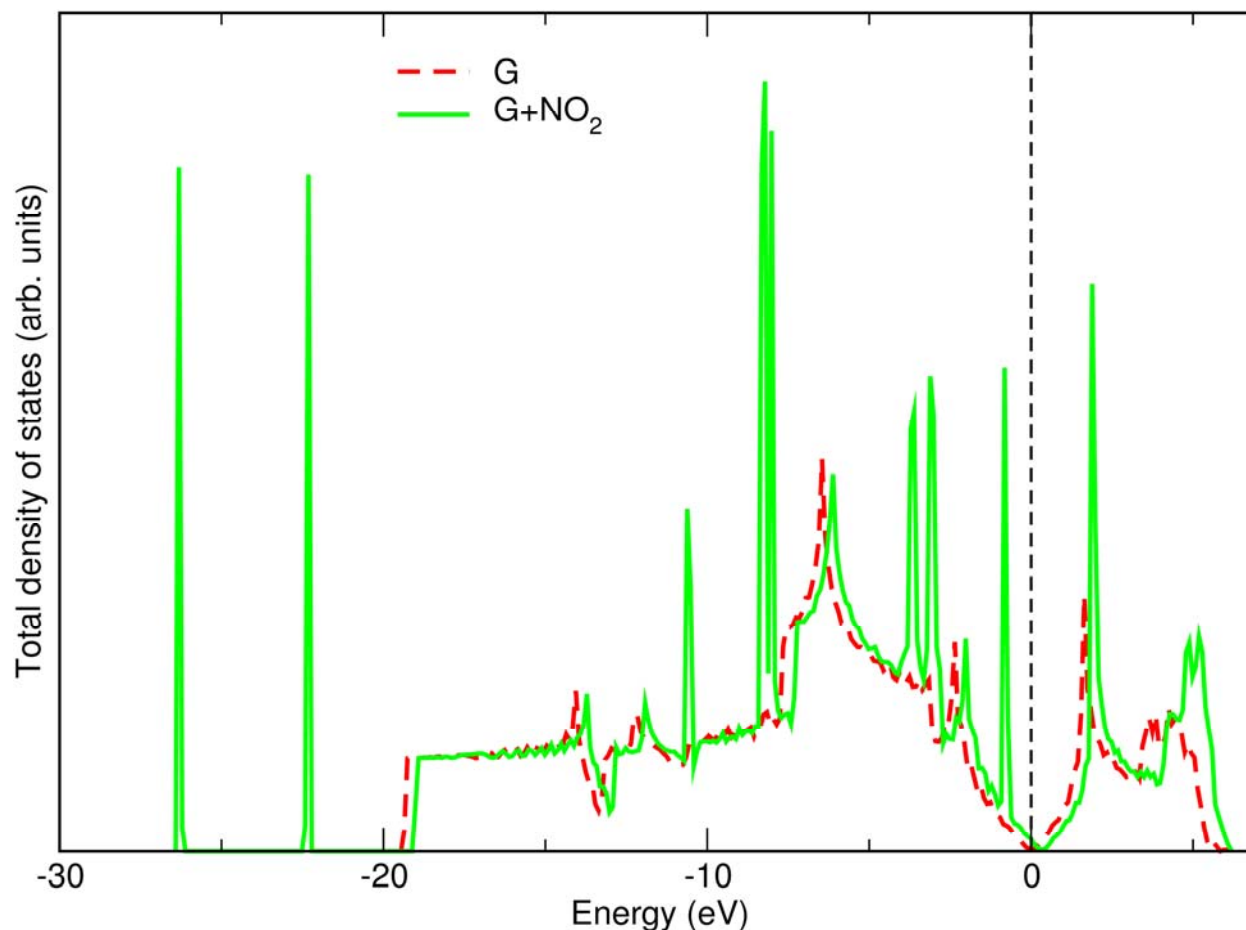


**Fig. 6.4:** Calculated TDOS for the  $3 \times 3$  graphene substrate with (dashed red) and without (solid green) the physisorbed  $\text{NO}_2$  as in Fig. 6.4A.

most closely corresponds to the band that is observed at  $1560 \text{ cm}^{-1}$ , which is assigned to the  $\text{NO}_2$  asymmetric stretching mode (the exact frequency of this band was difficult to assess due to the imperfect subtraction of the gas-phase  $\text{NO}_2$  spectrum). The far weaker symmetric stretching mode is seen as the weak shoulder at  $1300 \text{ cm}^{-1}$  sitting on the much larger band at  $1235 \text{ cm}^{-1}$ .

Previously published reports [1] have indicated that adsorption of  $\text{NO}_2$  on pristine graphite or graphene surfaces results in dimerization of the molecule to form physisorbed  $\text{N}_2\text{O}_4$ ; this scenario also is supported by our experimental data. The bands at  $1700$  and  $1375 \text{ cm}^{-1}$

provide a unique fingerprint of the  $\text{N}_2\text{O}_4$  and are typical of the frequencies for this molecule observed on numerous other surfaces.[31] Thus graphitic regions of the surface can host  $\text{NO}_2$  in both its molecular and dimerized forms.

Next, adsorption at an epoxide site is considered. When the molecule initially starts close to the O-top site with the N atom pointing toward the oxygen, the energetically favorable pathway involves a breaking of the epoxide C-O-C bonds in favor of the formation of an adsorbed  $\text{NO}_3$  complex with a significant excess negative charge. Following the epoxide bond breaking, the  $\text{NO}_3$  molecule rises away from the carbon plane with the final distance between the graphene sheet and the lowest oxygen atom equal to 2.4 Å (Fig. 6.3B). The overall adsorption energy of this process is 1.65 eV. The reaction of the  $\text{NO}_2$  molecule with the epoxide group results in a significant negative charge transferred to the  $\text{NO}_3$  complex, effectively hole-doping the substrate. This is illustrated in Fig. 6.5, where the calculated DOS is shown for the substrate in Fig. 6.3B before and after the reaction with  $\text{NO}_2$ . The data show that following reaction (blue and black curves for spin up and down, respectively), the substrate electronic states are essentially graphene-like (see, *e.g.*, Fig. 4.20), but the Fermi level is redshifted over 1 eV from the Dirac point, indicating the process hole-dopes the substrate. In this relatively high concentration ( $\text{C}_{18}\text{NO}_3$ ) the doping is somewhat exaggerated; however, lower concentrations will have the same effect with a smaller overall shift to the electronic states. The DOS in Fig. 6.5 for this structure also shows a strong resonance centered exactly at  $E_f$ , indicating a partially occupied state. Several calculations were performed with different concentrations of the  $\text{NO}_3$  complex (for example, a  $4\times 4$  supercell was used as the starting structure) and the results indicate that the energy of the resonance was dependent on the concentration. This suggests that it is unlikely that the  $\text{NO}_3$  complex has a half-filled state in the actual experimental conditions.

The free  $\text{NO}_3^-$  ion has a  $D_{3h}$  symmetry, and accordingly has only one doubly degenerate infrared active mode corresponding to the asymmetric stretching of the N-O bonds, in which an N-O bond stretch occurs for 2 O atoms and an N-O bond compression occurs for the third. In the gas phase this mode is observed at  $1356\text{ cm}^{-1}$  [30]. This ion also has one Raman active mode at  $1045\text{ cm}^{-1}$  corresponding to the symmetric stretching of the N-O bonds which is silent in the IR. The adsorbed  $\text{NO}_3$  complex has a lower  $C_{2v}$  symmetry due to the presence of the surface; consequently, the symmetric stretching mode at  $1050\text{ cm}^{-1}$  becomes IR active and the degenerate asymmetric stretch is split into two modes. The degree of the splitting is generally related to the strength of the interaction with the surface. These modes are assigned to the bands at  $1425$ ,  $1150$  and  $1060\text{ cm}^{-1}$ , which are in the typical range of those reported for nitrates chemically adsorbed in the  $C_{2v}$  configuration [31]. In addition, these bands were not observed for  $\text{NO}_2$  adsorption on soot and graphite [27], where oxygen functional groups play a less prominent role. The band at  $1060\text{ cm}^{-1}$  is displaced only  $15\text{ cm}^{-1}$  from its gas-phase frequency, while the bands at  $1150$  and  $1425\text{ cm}^{-1}$  are displaced from the gas-phase value of the degenerate stretch, respectively, by  $206$  and  $70\text{ cm}^{-1}$ , indicating a substantial interaction with the surface. This is somewhat surprising considering that the optimized adsorbate structure has a weak physical bond to the surface. The following mechanism is proposed to account for this interaction: following the reaction of  $\text{NO}_2$  with the epoxide group, the  $\text{NO}_3^-$  ion inherits an excess negative charge, and hole-dopes the substrate. This difference in the charge distribution creates an electric field normal to the surface that acts upon the  $\text{NO}_3^-$  ion. The adsorbed  $\text{NO}_3^-$  feels the effect of the electric field, causing the degenerate mode to split. This is in essence the principle of the vibrational Stark effect [32].

Next the adsorption of  $\text{NO}_2$  at defective regions of the RGO substrate is qualitatively considered. Many types of defective regions in RGO and graphene are possible; [33] here we

focus on unreconstructed defects such as single carbon vacancies, double vacancies, etch holes, and edges. In general, the main feature under consideration is the presence of one or more carbon dangling bonds. These types of defects are the most likely to result in chemisorption of the  $\text{NO}_2$  and to produce distinctive vibrational signatures from the physisorbed species already discussed.

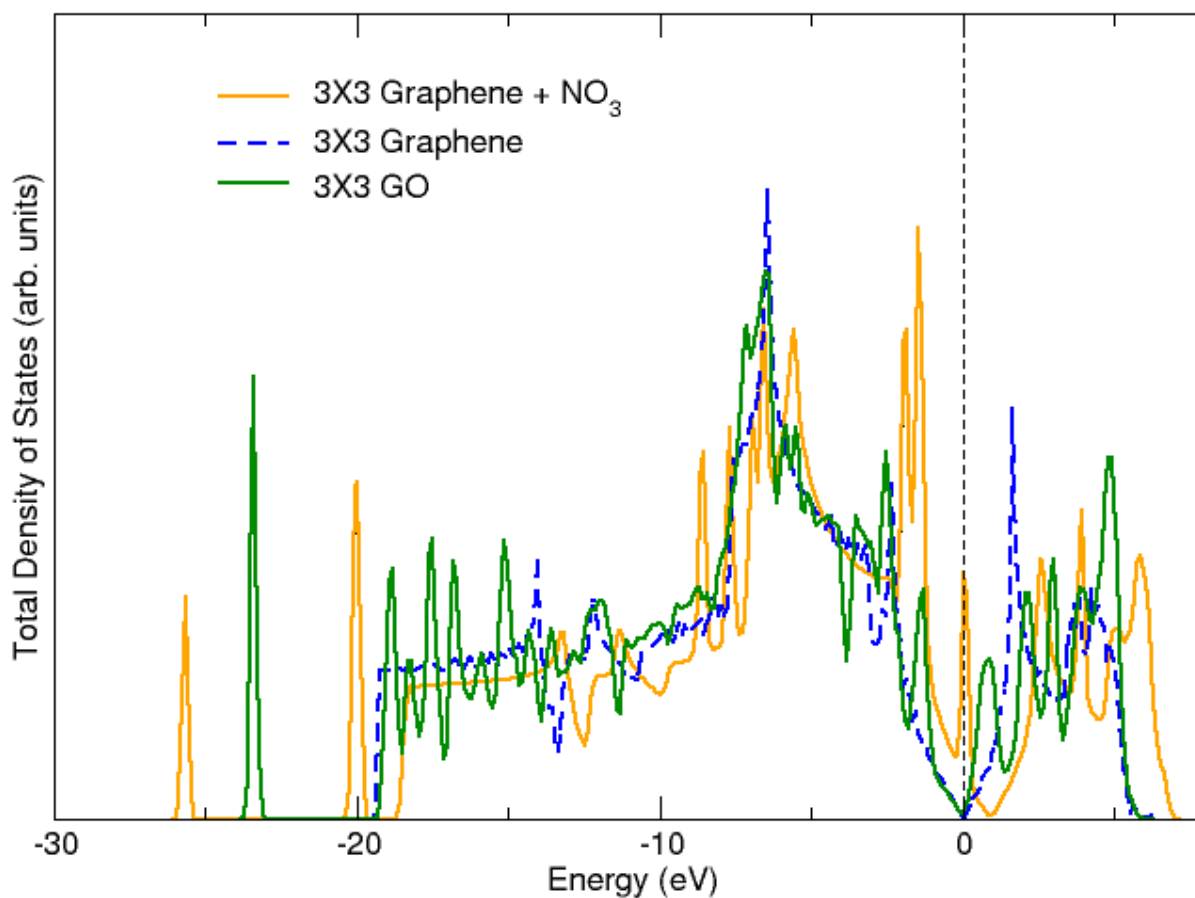


**Fig. 6.5:** Calculated TDOS for the bare substrates in Fig. 6.4A (dashed blue) and Fig. 6.4B (solid green), and for the final structure in Fig. 6.4B after reaction with  $\text{NO}_2$  (solid orange). Note that the strong resonance at 0 eV due to the  $\text{NO}_3$  that appears half-filled was found to vary in energy as a function of  $\text{NO}_3$  concentration.



A reductionist approach toward understanding the highly complicated interaction of the adsorbate with defective sites is taken. As the simplest case of the interaction with such defects, adsorption of  $\text{NO}_2$  onto a single carbon vacancy is used as a template to understand the interaction of the molecule with carbon dangling bonds. The model consists of  $\text{NO}_2$  adsorption at  $3 \times 3$  graphene unit cells containing a single carbon vacancy (Fig. 6.3C), at which the  $\text{NO}_2$  is initially placed. Following relaxation of the models of the substrate structure, the  $\text{NO}_2$  molecule is placed immediately above the vacancy in a  $C_{2v}$  configuration. Upon relaxation, the lowest energy structure has all three of the atoms in  $\text{NO}_2$  bonded at the vacancy as in Fig. 6.3C. This structure is categorized as the *nitro-nitrito* configuration in which the molecule is coordinated to the substrate atoms by both the N atom and one or more O atoms. While this ideal case of a single atomic vacancy is likely not representative of the majority defects of RGO, which contains large holes and edges, the model demonstrates that it is highly favorable for the oxygen and nitrogen atoms in  $\text{NO}_2$  to passivate the dangling bonds. In this case in which three dangling bonds are initially exposed, the adsorption energy for the structure in Fig. 6.3C is 3.79 eV. The ideal case of a single carbon vacancy in an otherwise pristine graphene sheet preserves the  $C_{2v}$  symmetry of the molecule; however, in more general defects such as vacancy clusters, holes and edges of stacked RGO sheets, there will not be three symmetric dangling bonds to host the  $\text{NO}_2$  molecule. In such cases, the  $\text{NO}_2$  molecule can be coordinated by both a nitrogen and oxygen atom (*nitro-nitrito* configuration) or by a single oxygen atom (*nitrito* configuration). These configurations both involve a lowering of the molecular symmetry of the  $\text{NO}_2$  molecule and likely represent the predominant interaction of the target molecules with defective regions of the film. The effect of this symmetry lowering will be to convert the collective symmetric and

asymmetric stretches of the N-O and N=O bonds into single N-O and N=O bond stretching modes. Considering this distinction along with the substantial negative charge transferred to the molecule from the substrate, the features most closely resembling this situation are the bands observed at 1495 and 1235  $\text{cm}^{-1}$ , which are assigned to the N=O and C-O stretches of the  $\text{NO}_2^-$  ion bonded in a configuration C-O-N=O. These assignments are further supported by the fact that these same bands are observed during the reaction of  $\text{NO}_2$  with soot and graphite at elevated temperatures [27]. In addition to defects containing  $sp^2$  dangling bonds, C-O-N=O bonding configurations could result from regions where the substrate has a local  $sp^3$  structure [34], such as in the vicinity of epoxide groups [35] and extended topological defects [6].

The interaction between  $\text{NO}_2$  and the other minority functional groups in the samples consisting of carbonyl groups and even fewer hydroxyl groups is now considered. Tang and Cao[36] showed that  $\text{NO}_2$  chemisorption at the carbonyl groups is slightly favorable (adsorption energy = -0.37 eV) resulting in an  $\text{NO}_3$  complex coordinated to a single carbon atom. This conclusion is not supported by the experimental data shown here. The structure they proposed has an  $\text{O}\cdots\text{NO}_2$  bond length of 4.62 Å, which is larger than the bond lengths in gas-phase  $\text{NO}_2$ , giving the complex a  $\text{C}_{2v}$  symmetry. The chemical bond between the carbonyl group and the  $\text{NO}_2$  adsorbate would certainly cause a large perturbation to the vibrational frequency of the C=O stretching mode. In the data shown in Fig. 4.16, this mode is seen as a sharp, intense feature at 1735  $\text{cm}^{-1}$ , whereas in the differential spectra in Fig. 6.1, there are no vibrational features evident in this frequency region. If the carbonyl groups were so perturbed as suggested by Tang and Cao, either a negative or derivative band at the initial C=O stretching frequency would be observed, yet there is nothing in the data to support this conclusion. The difference between our samples and their structural models could contribute to the discrepancy between their predictions

and the experiments shown here. Their models of the interaction of  $\text{NO}_2$  with substrates containing the carbonyl group contained a  $4 \times 4$  graphene lattice with both a carbonyl and a hydroxyl group, the latter being at best a minority in the samples here. Furthermore, in this model, of all of the other adsorption sites in the supercell besides from the carbonyl group had a greater binding energy. The calculated adsorption energy of our structure of physisorbed  $\text{NO}_2$  was 0.3 eV, which is comparable to their calculated binding energy for adsorption to the carbonyl group. Thus, in the experiments it is more likely that other more favorable adsorption configurations compete with that proposed by model.

There is also a very weak band in the X-H stretching region of the spectrum, at approximately  $3250 \text{ cm}^{-1}$ . A band in this position is unexpected since it is observed in IR spectra of RGO that hydroxyl groups are an extreme minority. The presence and strength of this band was observed to be variable in different experiments, and a number of hypotheses were considered regarding the physical origin of this band. The first possibility involves  $\text{NO}_2$  adsorption at an adsorbed hydroxyl group. DFT calculations were performed and indicate that the interaction of the hydroxyl groups with  $\text{NO}_2$  is based on van der Waals bonding and does not form any new N-H or O-H bonds. Another possibility that was considered is that the band is a consequence of  $\text{NO}_2$  reaction with water molecules to produce  $\text{HNO}_2$  and  $\text{HNO}_3$ . This reaction could take place in the gas phase under the atmospheric conditions reported here, or with minority amounts of adsorbed water on the surface of the sample. These complexes, however, are not likely to account for any of the majority bands observed in the region  $1000\text{-}1700 \text{ cm}^{-1}$  for the following reason: in both the *trans* and *cis* conformations of  $\text{HNO}_2$ , the strongest band in the spectrum occurs for  $790$  and  $850 \text{ cm}^{-1}$ , respectively. The experimental spectra show some very weak intensity in this region, but the absorbance here is far lower than in the  $1000\text{-}1700 \text{ cm}^{-1}$

region, and the bending modes of  $\text{NO}_x$  are expected in this region as well and could account for this intensity. If the strongest bands for  $\text{HNO}_2$  were responsible for this low-frequency ( $<1000\text{ cm}^{-1}$ ) intensity, the absorption in the  $1000\text{-}1700\text{ cm}^{-1}$  would correspondingly be negligible as compared with dominant the features in this region of the spectrum that are assigned to the N-O stretches. From this it is concluded that none of the stronger bands observed in the  $1000\text{-}1700\text{ cm}^{-1}$  region of our experimental spectra can be assigned to the modes of  $\text{HNO}_2$ . Similarly, both the *cis* and *trans* conformations of  $\text{HNO}_3$  have strong bands at  $789$  and  $772\text{ cm}^{-1}$ , respectively. There are no pronounced absorption features in our data that could be assigned to these modes. In addition, the N-H stretching vibrational frequencies observed are much lower than would be expected for  $\text{HNO}_2$  and  $\text{HNO}_3$ . [30]

As an additional demonstration that the bands in the  $1000\text{-}1700\text{ cm}^{-1}$  region are not associated with a nitrogen hydroxide, an illuminating comparison between two identical experiments is shown in Fig. 6.6. The only difference between the two experiments were the samples, which were indistinguishable on the basis of their IR absorption. In the first experiment (spectrum from Fig. 6.1, red curve in 6.6), the feature at  $3250\text{ cm}^{-1}$  can barely be observed, while in the second experiment (blue curve in 6.6) the feature is much more intense than any other bands in the spectrum. The band intensities in the fingerprint region are nearly identical in the two experiments. To further highlight the changes in the two experiments, the difference between the two spectra in Fig. 6.6 was calculated and is shown in Fig. 6.7. In the OH stretching region, two peaks can be discerned at  $\approx 3250$  and  $3500\text{ cm}^{-1}$ , while in the OH bending region, a clear peak is observed at  $1641\text{ cm}^{-1}$ . These bands provide a characteristic fingerprint of adsorbed water molecules. The OH stretching modes are redshifted from their gas-phase values ( $3756$  and  $3656\text{ cm}^{-1}$ ) while the OH bending mode is blueshifted (gas phase value of  $1594\text{ cm}^{-1}$ ). These

shifts are characteristic of hydrogen bonding. In addition, an asymmetric feature is observed at  $1269\text{ cm}^{-1}$  that arises due to a slight frequency mismatch of the  $1235\text{ cm}^{-1}$  band between the two experiments. The data suggest the following interpretation for the presence of the adsorbed water: since the experiments are not performed in UHV, atmospheric water is omnipresent due to minute leaks in the flow cell and tubing. When the flow cell is not being purged with a high volume of dry nitrogen gas, the water molecules can easily infiltrate the flow cell. When the  $\text{NO}_2$  chemisorbs to the surface, it provides active sites to which the water molecules can be coordinated by hydrogen bonding to the oxygen atoms in  $\text{NO}_2$ . This results in a shift of the distinctive mode at  $1235\text{ cm}^{-1}$  and shifts of the OH bending and stretching modes relative to their gas-phase values. The quantity and presence of the water on the surface are dependent on the relative humidity at the time that the experiment is performed. For example, the experiment that yielded the red spectrum in Fig. 6.6 was performed in August of 2012, a period in which an historic draught took place in Wisconsin (particularly Madison). The experiment that yielded the blue spectrum was performed in October 2012, when the relative humidity was higher. Importantly, the data show that environmental effects are relevant in actual sensing applications, as the bonding of water to the adsorbed  $\text{NO}_2$  will distort the electron distribution and impact the acceptor behavior of  $\text{NO}_2$ .

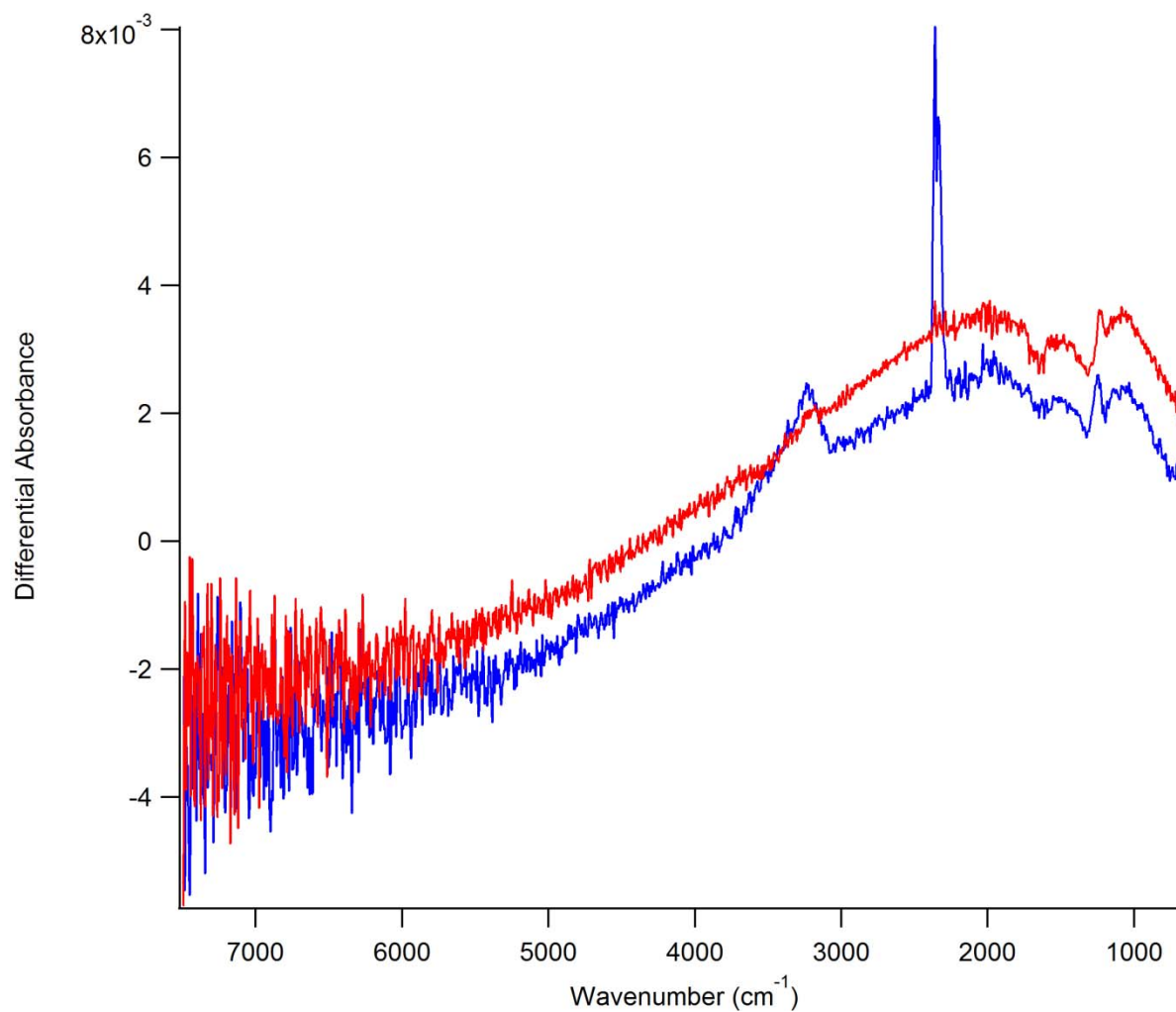


**Fig. 6.6:** Comparison of NO<sub>2</sub>/RGO differential absorption spectra shown for two different experiments spaced months apart. In the red spectrum, the band at 3250 cm<sup>-1</sup> can barely be observed, while it is much stronger in the blue spectrum. Both spectra, however, have very similar absorption features below 2000 cm<sup>-1</sup>. In both measurements, the clean diamond window is used as a reference.

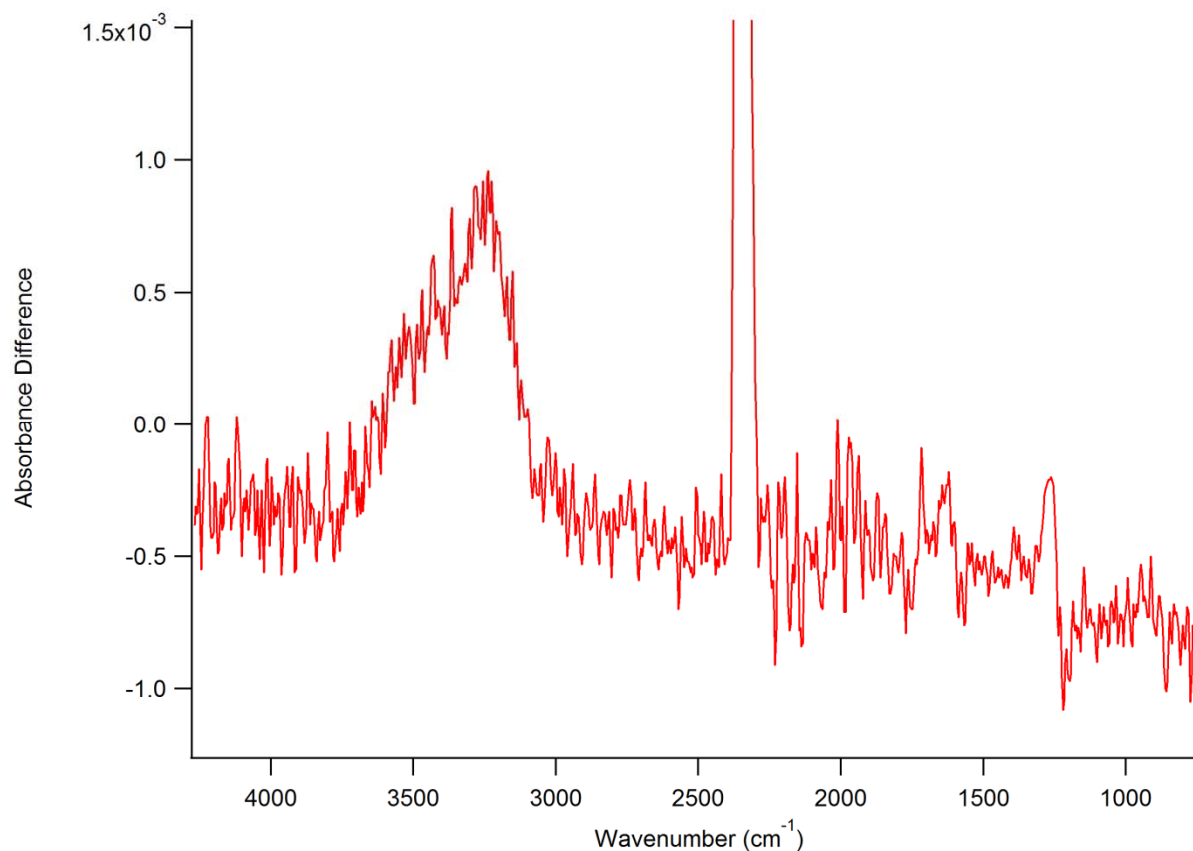


**Fig. 6.7:** Absorption difference between the two differential spectra in Fig. 6.6. The difference spectrum highlights the changes in the OH stretching and bending regions. The asymmetric feature at  $1270\text{ cm}^{-1}$  is due to a relative shift in frequency of this band between the two experiments.

### 6.3.3 Change of the Broadband Absorption

Finally, the modulation of the broadband IR absorbance of the substrate following exposure to  $\text{NO}_2$  is discussed. The spectrum in Fig. 6.1A shows the following behavior: starting from the low-frequency cutoff of the detector ( $650\text{ cm}^{-1}$ ), the differential absorbance is positive and increases with the photon frequency until it reaches a maximum value near  $1900\text{ cm}^{-1}$ . Beyond  $1900\text{ cm}^{-1}$ , the differential absorbance begins to drop, reaching zero at  $4400\text{ cm}^{-1}$  before becoming increasingly negative throughout the observable spectral range. The shape of the differential absorption above  $1900\text{ cm}^{-1}$  is nearly exactly opposite the broadband absorption observed in Fig. 6.1A, which was assigned to excitations across the gap in the oxidized regions

of the sample. The negative absorption in this region suggests a suppression of the excitations across the gap induced by the epoxide groups. This observation, coupled with the fact that the most significant changes to the calculated density of states were caused by the structure of Fig. 6.3B, suggests that this modulation of the broadband absorbance is a result of the interaction of the NO<sub>2</sub> molecules with the substrate epoxide groups. This conclusion is supported by our first-principles calculations. The data in section 4.4.2.3 showed that epoxide groups present in RGO, depending on their concentration, can open a gap in the DOS and result in the absorption onset seen in our IR measurements. The calculation of the TDOS shown in Fig. 6.5 shows that, following the reaction between the NO<sub>2</sub> and epoxide groups, the TDOS near the Fermi level is graphene-like and hole doped resulting from the significant charge transfer to the physisorbed NO<sub>3</sub> complex. Despite the valence and conduction bands being gapless (in the idealized model), this hole doping will have the effect of creating an optical gap, and hence an additional absorption threshold observed in the IR spectrum. The direct excitations across the optical gap give rise to the increased absorption observed in the differential spectra from 650-4000 cm<sup>-1</sup> (Fig. 6.1A). The negative absorbance occurs because the differential absorption spectrum represents the change in absorbance of the initial and final states of the sample. Following removal of the epoxide groups, the absorption due to direct excitations across the gap will be eliminated. The change in absorption will be directly related to the difference between the joint density of states (JDOS) of the initial and final systems. In the vicinity of an M<sub>0</sub>-type critical point, the JDOS carries the functional form  $\rho_{cv} \propto m_r^{3/2} \sqrt{\hbar\omega - E_g}$ , where  $\rho_{cv}$  is the JDOS and  $m_r$  is the reduced effective mass of the valence and conduction band states. Thus the change in absorbance will be proportional to  $\Delta A \times \omega \propto m_{r,f}^{3/2} \sqrt{\hbar\omega - E_{gf}} - m_{r,i}^{3/2} \sqrt{\hbar\omega - E_{gi}}$ . It is important to note that when  $E_{g,f} < E_{g,i}$ , which is the case indicated by our IR data, the change in



absorption can only become negative if the reduced effective mass of the initial state is greater than that of the final state. The negative absorbance above  $4400\text{ cm}^{-1}$  is thus consistent with the model effect of epoxide removal to form a more an electronic state that is more similar to graphene, which has the lowest possible effective mass near the Fermi energy. Even in reality, where the structure is more complex than a simple  $3\times 3$  graphene cell with a single epoxide, the process of removing oxygen to form states with lower effective mass, albeit not identical to those of pure graphene, is consistent with our experimental observations. This effect of lowering the reduced mass has an important implications for the mechanism of RGO based sensors: the generation of available holes will increase the carrier density, and the lowering of the effective mass will increase the carrier mobility and correspondingly the substrate conductivity. Such an effect is consistent with transport measurements on the  $\text{NO}_2/\text{RGO}$  system [10, 14, 17]. Thus the interaction of  $\text{NO}_2$  with the epoxide groups in RGO represents a significant enhancement in the adsorbate-substrate interaction as compared with that of pure graphene.

## 6.4 Conclusions

The adsorption of  $\text{NO}_2$  onto RGO is characterized by several distinct species present on the surface including physisorbed  $\text{NO}_2$  and  $\text{N}_2\text{O}_4$ ,  $\text{NO}_3^-$  and chemisorbed  $\text{NO}_2^-$ . While all of the adsorbates produce an acceptor behavior that could contribute to the observed sensing response, the formation of the charged  $\text{NO}_3$  complex has the largest impact on the electronic structure.

The reaction with the  $\text{NO}_2$  with epoxide groups has a combined effect of lowering the gap in the DOS that is induced by the epoxide groups as well as behaving as an acceptor molecule. The net effect is an increase in the hole concentration as well as the hole mobility.

## 6.5 References

1. Zhou, S.Y., et al., *Metal to insulator transition in epitaxial graphene induced by molecular doping*. Physical Review Letters, 2008. **101**(8).
2. Stankovich, S., et al., *Graphene-based composite materials*. Nature, 2006. **442**(7100): p. 282-286.
3. Dikin, D.A., et al., *Preparation and characterization of graphene oxide paper*. Nature, 2007. **448**(7152): p. 457-460.
4. Park, S., et al., *Colloidal Suspensions of Highly Reduced Graphene Oxide in a Wide Variety of Organic Solvents*. Nano Letters, 2009. **9**(4): p. 1593-1597.
5. Mkhoyan, K.A., et al., *Atomic and Electronic Structure of Graphene-Oxide*. Nano Letters, 2009. **9**(3): p. 1058-1063.
6. Gomez-Navarro, C., et al., *Atomic Structure of Reduced Graphene Oxide*. Nano Letters, 2010. **10**(4): p. 1144-1148.
7. Gomez-Navarro, C., et al., *Electronic transport properties of individual chemically reduced graphene oxide sheets*. Nano Letters, 2007. **7**(11): p. 3499-3503.
8. He, Q.Y., et al., *Centimeter-Long and Large-Scale Micropatterns of Reduced Graphene Oxide Films: Fabrication and Sensing Applications*. Acs Nano, 2010. **4**(6): p. 3201-3208.
9. Sudibya, H.G., et al., *Electrical Detection of Metal Ions Using Field-Effect Transistors Based on Micropatterned Reduced Graphene Oxide Films*. Acs Nano, 2011. **5**(3): p. 1990-1994.
10. Lu, G.H., L.E. Ocola, and J.H. Chen, *Gas detection using low-temperature reduced graphene oxide sheets*. Applied Physics Letters, 2009. **94**(8).
11. Ko, G., et al., *Graphene-based nitrogen dioxide gas sensors*. Current Applied Physics, 2010. **10**(4): p. 1002-1004.
12. Fowler, J.D., et al., *Practical Chemical Sensors from Chemically Derived Graphene*. Acs Nano, 2009. **3**(2): p. 301-306.

13. Li, W.W., et al., *Reduced Graphene Oxide Electrically Contacted Graphene Sensor for Highly Sensitive Nitric Oxide Detection*. *Acs Nano*, 2011. **5**(9): p. 6955-6961.
14. Lu, G., L.E. Ocola, and J. Chen, *Reduced graphene oxide for room-temperature gas sensors*. *Nanotechnology*, 2009. **20**(44): p. 445502.
15. Robinson, J.T., et al., *Reduced Graphene Oxide Molecular Sensors*. *Nano Letters*, 2008. **8**(10): p. 3137-3140.
16. Mao, S., et al., *Specific Protein Detection Using Thermally Reduced Graphene Oxide Sheet Decorated with Gold Nanoparticle-Antibody Conjugates*. *Advanced Materials*, 2010. **22**(32): p. 3521-+.
17. Lu, G.H., et al., *Toward Practical Gas Sensing with Highly Reduced Graphene Oxide: A New Signal Processing Method To Circumvent Run-to-Run and Device-to-Device Variations*. *Acs Nano*, 2011. **5**(2): p. 1154-1164.
18. Mao, S., et al., *Tuning gas-sensing properties of reduced graphene oxide using tin oxide nanocrystals*. *Journal of Materials Chemistry*, 2012. **22**(22): p. 11009-11013.
19. Nasse, M.J., et al., *Demountable Liquid/Flow Cell for in Vivo Infrared Microspectroscopy of Biological Specimens*. *Applied Spectroscopy*, 2009. **63**(10): p. 1181-1186.
20. Nasse, M.J., et al., *High-resolution Fourier-transform infrared chemical imaging with multiple synchrotron beams*. *Nature Methods*, 2011. **8**(5): p. 413-U58.
21. Nasse, M.J., et al., *Multi-beam synchrotron infrared chemical imaging with high spatial resolution: Beam line realization and first reports on image restoration*. *Nuclear Instruments & Methods in Physics Research Section a-Accelerators Spectrometers Detectors and Associated Equipment*, 2011. **649**(1): p. 172-176.
22. Giannozzi, P., et al., *QUANTUM ESPRESSO: a modular and open-source software project for quantum simulations of materials*. *Journal of Physics-Condensed Matter*, 2009. **21**(39).
23. Perdew, J.P. and A. Zunger, *Self-interaction correction to density-functional approximations for many-electron systems*. *Physical Review B*, 1981. **23**: p. 5048-5079.

24. Lowdin, P., *On the Non-Orthogonality Problem Connected with the Use of Atomic Wave Functions in the Theory of Molecules and Crystals* Journal of Chemical Physics, 1950. **18**(3): p. 365-375.
25. Mao, S., H.H. Pu, and J.H. Chen, *Graphene oxide and its reduction: modeling and experimental progress*. Rsc Advances, 2012. **2**(7): p. 2643-2662.
26. Erickson, K., et al., *Determination of the Local Chemical Structure of Graphene Oxide and Reduced Graphene Oxide*. Advanced Materials, 2010. **22**(40): p. 4467-4472.
27. Muckenhuber, H. and H. Grothe, *A DRIFTS study of the heterogeneous reaction of NO<sub>2</sub> with carbonaceous materials at elevated temperature*. Carbon, 2007. **45**(2): p. 321-329.
28. Tang, S.B. and Z.X. Cao, *Adsorption and Dissociation of Ammonia on Graphene Oxides: A First-Principles Study*. Journal of Physical Chemistry C, 2012. **116**(15): p. 8778-8791.
29. Leenaerts, O., B. Partoens, and F.M. Peeters, *Adsorption of H<sub>2</sub>O, NH<sub>3</sub>, CO, NO<sub>2</sub>, and NO on graphene: A first-principles study*. Physical Review B, 2008. **77**(12).
30. *NIST Chemistry Webbook*. NIST Chemistry Webbook, 2012.
31. Hadjiivanov, K.I., *Identification of Neutral and Charged N<sub>x</sub>O<sub>y</sub> Surface Species by IR Spectroscopy*. Catalysis Reviews, 2000. **42**(1-2): p. 71-144.
32. Lambert, D.K., *VIBRATIONAL STARK-EFFECT OF CO ON NI(100), AND CO IN THE AQUEOUS DOUBLE-LAYER - EXPERIMENT, THEORY, AND MODELS*. Journal of Chemical Physics, 1988. **89**(6): p. 3847-3860.
33. Banhart, F., J. Kotakoski, and A.V. Krasheninnikov, *Structural Defects in Graphene*. Acs Nano, 2011. **5**(1): p. 26-41.
34. Dai, J. and J. Yuan, *Physisorption to chemisorption transition of NO<sub>2</sub> on graphene induced by the interplay of SiO<sub>2</sub> substrate and van der Waals forces: A first principles study*. Chemical Physics, 2012. **405**(0): p. 161-166.
35. Huang, B., et al., *Overcoming the Phase Inhomogeneity in Chemically Functionalized Graphene: The Case of Graphene Oxides*. Physical Review Letters, 2013. **110**(8).

36. Tang, S.B. and Z.X. Cao, *Adsorption of nitrogen oxides on graphene and graphene oxides: Insights from density functional calculations*. Journal of Chemical Physics, 2011. **134**(4).

## Chapter 7: Concluding Remarks

This work in this dissertation has been a compilation of different aspects of carbon-based materials science and optical instrumentation/analysis. In particular, I have focused on understanding the role of oxygen atoms incorporated into graphene through various channels and in different structural configurations. The conclusions in this work have involved an intimate collaboration between experiments and theory, and the combined approaches have been used to identify the relationships between oxygen adatoms (epoxide groups), atomic and electronic structure, and reactivity.

Experiments involving *in situ* SAD studies of thermal reduction of GO, while initially motivated by understanding sensor materials, revealed a surprising and exciting ordering on and/or in the sample. This observation led to a number of experiments and theoretical calculations to understand the nature of the ordering and its parent structure. The result of this collaboration found that the structure that was most consistent with experimental measurements and thermodynamic probability was the so-called graphene monoxide, which happened to have many appealing properties. The subsequent discovery of the necessity of the presence of Mo in order to produce the material, however, drew serious questions about the validity of the interpretation of GMO. Ongoing experiments are currently providing increasing evidence that the Mo initially used as the TEM support becomes incorporated into the structure during the reduction process, and a possible interpretation is that there has not been any actual synthesis of GMO. This represents a critical ongoing question that will hopefully be targeted by future x-ray scattering experiments.

Depending on whether the oxygen groups are ordered to form periodic crystal or act as disordered dopants, the introduction of oxygen into the graphene lattice opens a gap in the density of states, rendering it a semiconductor. The semiconducting behavior possessed by both RGO and the hypothetical GMO is attractive for a number of applications, including gas sensing. In addition, the residual oxygen groups in RGO as well as the comparatively large concentration of defective sites RGO as compared to graphene result in a larger interaction with the target molecules. Infrared measurements combined with theoretical modeling further indicate that the residual epoxide groups in RGO are highly active toward  $\text{NH}_3$  and  $\text{NO}_2$ , and this interaction plays a large role in mediating the conductivity (dc and optical) of RGO-based sensors. Thus the very properties that render the transport properties of RGO inferior to graphene make it far superior in applications that require an interaction between the substrate and adsorbate.

The IR measurements thus far, combined with theoretical modeling, have revealed important information on the bonding configuration of adsorbates on RGO. Future directions should focus on understanding similar interactions in hybrid systems where RGO is used as a support for metal and metal oxide nanocrystals. These systems are currently demonstrating great promise for gas sensing applications[1-3], as well as heterogeneous catalysis and photocatalysis[4-7]. In addition, there is great potential for nitrogen-doped graphene in these applications, as it has been demonstrated that the N-dopants eliminate the need for the noble metal nanocrystal component of the catalyst system [8].

## 7.1 References

1. Lu, G.H., et al., *Facile, Noncovalent Decoration of Graphene Oxide Sheets with Nanocrystals*. Nano Research, 2009. **2**(3): p. 192-200.
2. Mao, S., et al., *Tuning gas-sensing properties of reduced graphene oxide using tin oxide nanocrystals*. Journal of Materials Chemistry, 2012. **22**(22): p. 11009-11013.
3. Cui, S., et al., *Indium-doped SnO<sub>2</sub> nanoparticle-graphene nanohybrids: simple one-pot synthesis and their selective detection of NO<sub>2</sub>*. Journal of Materials Chemistry A, 2013. **1**(14): p. 4462-4467.
4. Yang, M., et al., *Graphene Oxide: An Ideal Support for Gold Nanocatalysts*. Journal of Physical Chemistry C, 2012. **116**(42): p. 22336-22340.
5. Khalid, N.R., et al., *Nitrogen doped TiO<sub>2</sub> nanoparticles decorated on graphene sheets for photocatalysis applications*. Current Applied Physics, 2012. **12**(6): p. 1485-1492.
6. Zhang, H., et al., *P25-Graphene Composite as a High Performance Photocatalyst*. Acs Nano, 2010. **4**(1): p. 380-386.
7. Williams, G., B. Seger, and P.V. Kamat, *TiO<sub>2</sub>-graphene nanocomposites. UV-assisted photocatalytic reduction of graphene oxide*. Acs Nano, 2008. **2**(7): p. 1487-1491.
8. Long, J.L., et al., *Nitrogen-Doped Graphene Nanosheets as Metal-Free Catalysts for Aerobic Selective Oxidation of Benzylic Alcohols*. Acs Catalysis, 2012. **2**(4): p. 622-631.



## Curriculum Vitae

### **Eric C. Mattson**

#### **Education**

PhD (Physics); University of Wisconsin-Milwaukee May 2013 Grad. GPA 3.926  
BSc (Physics); University of Wisconsin-Milwaukee December 2007 UG GPA: 3.579

#### **Positions and Appointments**

2011 Graduate Student Member, Synchrotron Radiation Center User Advisory Committee  
2008-Present Research Assistant, University of Wisconsin-Milwaukee  
(under the direction of Professor Carol Hirschmugl)  
2007-2008 Teaching Assistant, University of Wisconsin-Milwaukee

#### **Books**

M. J. Nasse, **E. C. Mattson**, C. Gohr, A. K. Rosenthal, S. Ratti, M. Giordano, and C. J. Hirschmugl, "Biological Kinetics Under the Microscope: Pathological Mineralization, IRENI, and *in vivo* Capabilities," in Vibrational Spectroscopic Imaging for Biomedical Applications; edited by Gokulakrishnan Srinivasan, McGraw Hill (2009).

#### **Peer Reviewed Publications**

1. "Effect of Numerical Aperture, Spatial Oversampling and Deconvolution on Spatial Resolution in Widefield Infrared Spectromicroscopy," **E. C. Mattson**, M. Unger, S. Clede, C. Policar, and C. J. Hirschmugl, submitted to *Analyst*
2. "Exploring Adsorption and Reactivity of Ammonia on Reduced Graphene Oxide," **E. C. Mattson**, K. Pande, M. Unger, S. M. Cui, G. H. Lu, M. Gajdardziska-Josifovska, M. Weinert, J. H. Chen, and C. J. Hirschmugl, accepted in *Journal of Physical Chemistry C*
3. "Multiple Morphologies of Gold-Magnetite Hybrid Nanoparticles are Effectively Functionalized with Protein for Cell-Targeting," E. S. Krystofiak, **E. C. Mattson**<sup>\*</sup>, P. M. Voyles, C. J. Hirschmugl, M. Gajdardziska-Josifovska, and J. A. Oliver, Accepted in *Microscopy and Microanalysis*  
<sup>\*</sup>ESK and ECM Contributed equally
4. "Fast and Selective Room-temperature Ammonia Sensors Using Silver Nanocrystal Functionalized Carbon Nanotubes," S. M. Cui, H. H. Pu, G. H. Lu, Z. H. Wen, **E. C. Mattson**, C. J. Hirschmugl, M. Gajdardziska-Josifovska, M. Wenert, and J. H. Chen, *ACS Applied Materials and Interfaces*, 4 (2012) 4898

5. "Ag Nanocrystal as a Promoter for Carbon Nanotube-based Room Temperature Gas Sensors," S. M. Cui, H. H. Pu, **E. C. Mattson**, G. H. Lu, S. Mao, M. Weinert, C. J. Hirschmugl, M. Gajdardziska-Josifovska, and J. H. Chen, *Nanoscale*, 4 (2012) 5887
6. "Restoration and Spectral recovery of Midinfrared Chemical Images," **E. C. Mattson**, M. J. Nasse, M. Rak, K. M. Gough, and C. J. Hirschmugl, *Analytical Chemistry*, 84 (2012) 6173-6180.
7. "Tailoring Nanomaterial Products through Electrode Material and Oxygen Partial Pressure in a Mini-arc Plasma Reactor," S. Cui, **E. C. Mattson**, G. Lu, C. J. Hirschmugl, M. Gajdardziska-Josifovska, and J. H. Chen, *Journal of Nanoparticle Research*, 14 (2012) UNSP-744.
8. "Evidence of Nanocrystalline Semiconducting Graphene Monoxide During Thermal Reduction of Graphene Oxide in Vacuum;" **E. C. Mattson**, H. Pu, S. Cui, M. A. Schofield, S. H. Rhim, G. H. Lu, M. J. Nasse, R. S. Ruoff, M. Weinert, M. Gajdardziska-Josifovska, J. H. Chen, and C. J. Hirschmugl, *ACS Nano*, 5 (2011) 9710.
9. "Fast High Resolution Fourier Transform Infrared Chemical Imaging with Multiple Synchrotron Beams;" M. J. Nasse, M. J. Walsh, **E. C. Mattson**, R. Reininger, A. Kajdascy-Balla, V. Macias, R. Bharghava, and C. J. Hirschmugl, *Nature Methods*, 8 (2011) 413.
10. "Multi-beam Synchrotron Infrared Chemical Imaging with High Spatial Resolution: Beamline Realization and First Reports on Image Restoration;" M. J. Nasse, **E. C. Mattson**, R. Reininger, T. Kubala, S. Janowski, and C. J. Hirschmugl, *Nuclear Instruments and Methods in Physics Research A*, 649 (2011) 172.
11. "Structure of Tin Oxide-Graphene Oxide Hybrid Nanomaterials for Gas Sensors;" **E. C. Mattson**, S. Cui, G. H. Lu, J. H. Chen, C. J. Hirschmugl, and M. Gajdardziska-Josifovska, *Microscopy and Microanalysis*, 16 (2010) 1706.
12. "Hyperspectral Data Restoration in Synchrotron-based Infrared Microspectroscopic Imaging;" **E. C. Mattson**, M. J. Nasse, and C. J. Hirschmugl, *Microscopy and Microanalysis*, 16 (2010) 764.
13. "Characterization of Articular Calcium-containing Crystals by Synchrotron FTIR;" A. K. Rosenthal, **E. C. Mattson**, C. M. Gohr, and C. J. Hirschmugl, *Osteoarthritis and Cartilage* 16 (2008) 1395.
14. "Association Between Crystals and Cartilage Degeneration in the Ankle;" C. Muehleman, J. Li, T. Aigner, L. Rappoport, **E. C. Mattson**, C. J. Hirschmugl, K. Masuda, and A. K. Rosenthal, *Journal of Rheumatology* 35 (2008) 1108.
15. "Promotion of Articular Cartilage Matrix Vesicle Mineralization by Type I Collagen;" B. Jubeck, C. M. Gohr, M. Fahey, E. Muth, M. Matthews, **E. Mattson**, C. Hirschmugl, and A. K. Rosenthal, *Arthritis and Rheumatism*, 58 (2008) 2809.
16. "Feasibility of a Tetracycline-binding Method for Detecting Basic Calcium Phosphate Crystals;" A. K. Rosenthal, M. Fahey, C. Gohr, T. Burner, I. Konan, L. Daft, **E. Mattson**, C. Hirschmugl, L. M. Ryan, and P. Simkin, *Arthritis and Rheumatism*, 58 (2008) 3270.

### Conference Presentations

1. "Understanding Molecular Adsorption on Graphene-based Hybrid Nanostructures by *In Situ* Infrared Microspectroscopy," **E.C. Mattson**, K. Pande, S. M. Cui, M. Unger, M. A. Schofield, G. H. Lu, M.

- Gajdardziska-Josifovska, M. Weinert, J. H. Chen, and C. J. Hirschmugl, 2012 AVS International Symposium and Exhibition.
2. "Understanding Molecular Adsorption on Graphene-based Hybrid Nanostructures by *In Situ* Infrared Microspectroscopy," **E.C. Mattson**, K. Pande, S. M. Cui, M. Unger, M. A. Schofield, G. H. Lu, M. Gajdardziska-Josifovska, M. Weinert, J. H. Chen, and C. J. Hirschmugl, 2012 Synchrotron Radiation Center Users' Meeting
  3. "Understanding Gold Growth on Magnetite Nanoparticles Using Probe-Corrected Scanning Transmission Electron Microscopy," **E. C. Mattson**, E. S. Krystofiak, P. M. Voyles, M. Gajdardziska-Josifovska, and J. A. Oliver, 2012 Microscopy and Microanalysis Meeting
  4. "Water-driven Growth of Graphene Monoxide Revealed by *In Situ* Infrared and Electron Microscopy, Diffraction and Spectroscopy;" **E. C. Mattson**, J. Zhu, M. A. Schofield, G. H. Lu, S. M. Cui, H. H. Pu, S. H. Rhim, M. Weinert, J. H. Chen, C. J. Hirschmugl, and M. Gajdardziska-Josifovska, 2012 Microscopy and Microanalysis Meeting
  5. "Formation, Structure, and Dynamics of Graphene Monoxide/Graphene Thin Films;" **E.C. Mattson**, H. Pu, S. Cui, M. A. Schofield, S. H. Rhim, G. H. Lu, M. J. Nasse, M. Weinert, M. Gajdardziska-Josifovska, J. H. Chen, and C. J. Hirschmugl, Synchrotron Radiation Center User's Meeting (Stoughton, WI -- September 2011).
  6. "Synthesis, Structure, and Morphology of Magnetic Core-Shell Nanoparticles;" **E. C. Mattson**, E. S. Krystofiak, C. J. Hirschmugl, P. M. Voyles, M. Gajdardziska-Josifovska, and J. A. Oliver, Microscopy and Microanalysis (Nashville, TN -- August 2011).
  7. "Real Time Observations of Structural Ordering in Graphene Oxide During Thermal Reduction in Vacuum;" **E. C. Mattson**, H. H. Pu, S. M. Cui, M. A. Schofield, S. H. Rhim, G. H. Lu, M. Weinert, M. Gajdardziska-Josifovska, J. H. Chen, and C. J. Hirschmugl, Microscopy and Microanalysis (Nashville, TN -- August 2011).
  8. "Structural Anomalies in Thermally Reduced Graphene Oxide Illuminated by Infrared Synchrotron Radiation;" **E.C. Mattson**, H.H. Pu, S.M. Cui, M.A. Schofield, S.H. Rhim, G.H. Lu, M. Weinert, M. Gajdardziska-Josifovska, J.H. Chen, and C.J. Hirschmugl, International Conference on Advanced Vibrational Spectroscopy (Sonoma, CA -- June 2011).
  9. "*In Situ* Studies of Carbon-based Gas Nanosensors;" **E. C. Mattson**, S. Cui, G. H. Lu, M. A. Schofield, J. H. Chen, M. Gajdardziska-Josifovska, and C. J. Hirschmugl, Synchrotron Radiation Center Users Meeting (Stoughton, WI -- October 2010).
  10. "Structure of Tin Oxide-Graphene Oxide Hybrid Nanomaterials for Gas Sensors;" **E. C. Mattson**, S. Cui, G. H. Lu, J. H. Chen, C. J. Hirschmugl, and M. Gajdardziska-Josifovska, Microscopy and Microanalysis (Portland, OR, August 2010).
  11. "Data Restoration in Synchrotron- based Infrared Microspectroscopic Imaging;" **E. C. Mattson**, M. J. Nasse, and C. J. Hirschmugl, Microscopy and Microanalysis (Portland, OR, August 2010).

### Awards and Recognition

1. Finalist for Morton Traum Surface Science Student Award, 2012 American Vacuum Society International Symposium and Exhibition
2. Microscopy Society of America Presidential Student Award, 2012
3. Recipient of the 2011-2012 UW-Milwaukee Graduate School Fellowship

4. Best Poster Award, 2011 International Conference on Advanced Vibrational Spectroscopy
5. Student Travel Award, Midwest Microscopy and Microanalysis Society
6. Best Poster Award, 2011 Microscopy and Microanalysis Meeting
7. 2011 Aladdin Lamp Award for Excellence in Synchrotron Radiation Research